NASA/TP-2001-210831

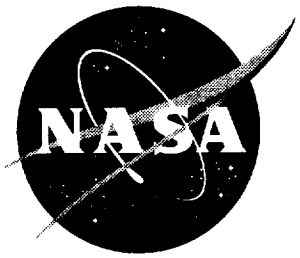

In-Flight Characterization of the Electromagnetic Environment Inside an Airliner

Karl J. Moeller, Kenneth L. Dudley, and Cuong C. Quach
Langley Research Center, Hampton, Virginia

Sandra V. Koppen
Lockheed Martin Engineering & Sciences, Hampton, Virginia

National Aeronautics and
Space Administration

Langley Research Center
Hampton, Virginia 23681-2199

March 2001

Acknowledgments

The EME flight experiment required the participation of a large number of people at many different locations. Contributors include Robert Johnk and Arthur Ondrejka of the National Institute of Standards and Technology (NIST); Ly Dao of the U.S. Air Force Phillips Laboratory; Andy Poggio and Richard Zacharias of the Lawrence Livermore National Laboratory; Bruce Hunter and Gordon Thompson of the Voice of America; Mike Hatfield of the Naval Surface Warfare Center; Theodore Bugtong of the NASA Wallops Flight Facility; Al Christman of Grove City College; Norris Beasley and Charles Howell of NYMA, Inc.; and various people in the Aircraft Support Branch and the Operations Engineering Branch, especially Mike Basnett. This experiment would not have been possible without the planning efforts performed by Chuck Meissner, Peter Padilla and Hal Carney, all formerly of the Assessment Technology Branch; Larry Corsa of Hewlett-Packard; Dave Walen, formerly of Boeing; Richard Hess of Honeywell; Rod Perala of EMA, Inc.; and Pete Saraceni of the FAA. The reduction and analysis of the collected data would not have been possible without the advocacy provided by Mike Goode of the Systems Integration Branch, Celeste Belcastro of the Assessment Technology Branch, and Carrie Walker of the Airframe Systems Program Office. The authors would like to thank Brian Bailie of NCI Information Systems for his assistance in developing many of the figures in this report. The authors would also like to thank Constantine Balanis of Arizona State University and Charles Bunting of Old Dominion University for their helpful suggestions in the development of this manuscript. A special thanks to Truong Nguyen of NASA for insightful technical discussions during the experiment data reduction phase, Jay Ely and Delores Williams of NASA for assistance during the final publication process, and individual contributions by Max Williams, Rueben Williams, and Stephen Scearce of the NASA Langley Research Center, Electromagnetic Research Branch, High Intensity Radiated Fields Laboratory.

Available from:

NASA Center for AeroSpace Information (CASI)
7121 Standard Drive
Hanover, MD 21076-1320
(301) 621-0390

National Technical Information Service (NTIS)
5285 Port Royal Road
Springfield, VA 22161-2171
(703) 605-6000

Contents

Symbols

$\mathbf{A}$	rotation matrix used in ECEF to antenna coordinate transformation
a	Earth's equatorial radius
$\mathbf{a_E}$	vector in the direction of the electric field
$\mathbf{B}$	rotation matrix used in antenna to ground track coordinate transformation
b	Earth's polar radius
$\mathbf{C}$	rotation matrix used in ground track to aircraft coordinate transformation
$\mathbf{E}$	electric field
EH	ellipsoid height (see page 19)
f	flattening (see page 19)
G_{ant}	antenna gain at boresight
$\hat{\mathbf{k}}$	unit vector in the direction of propagation of the incident wavefront
LAT	latitude
LON	longitude
N	North
n	radius of curvature of prime vertical (see page 19)
P_{ant}	power at the antenna input terminals
$\mathbf{pairl}_{\mathbf{ant}}$	position of the aircraft in the antenna's coordinate system
$\mathbf{pairl}_{\mathbf{ECEF}}$	position of the aircraft in the ECEF coordinate system
$\mathbf{pantl}_{\mathbf{air}}$	position of the antenna in the aircraft's coordinate system
$\mathbf{pantl}_{\mathbf{g.t.}}$	position of the antenna in the ground track coordinate system
R	distance between the aircraft and the antenna
s	eccentricity (see page 19)
W	power density of the field illuminating the aircraft

$\hat{\mathbf{z}}$	unit vector in the direction of the aircraft's z-axis
$\mathbf{z_{pro}}$	projection of aircraft's z-axis onto incident wavefront
α	angle defining the polarization of the incident wavefront
α_1	angle of first rotation about z-axis encountered in ECEF to antenna coordinate transformation
α_2	angle of second rotation about z-axis axis encountered in ECEF to antenna coordinate transformation
α_3	angle of rotation about z-axis encountered in antenna to ground track coordinate transformation
α_v	angle of rotation about z-axis encountered in ground track to aircraft coordinate transformation
β	angle of rotation about y-axis encountered in ECEF to antenna coordinate transformation
β_p	angle of rotation about y-axis encountered in ground track to aircraft coordinate transformation
γ_r	angle of rotation about x-axis encountered in ECEF to antenna coordinate transformation
η_0	impedance of free space

Abstract

In 1995, the NASA Langley Research Center conducted a series of experimental measurements that characterized the electromagnetic environment (EME) inside a Boeing 757 airliner while in flight. Measurements were made of the electromagnetic energy coupled into a commercially configured aircraft as it was flown in close proximity to ground-based radio frequency (RF) transmitters operating at approximately 26, 173, and 430 MHz. The goal of this experiment was to collect data for the verification of analytical predictions of the internal aircraft response to an external stimulus. This paper describes the experiment, presents the data collected by it, and discusses techniques used to compute both the magnitude of the electric field illuminating the aircraft and its direction of propagation relative to a coordinate system fixed to the aircraft. The latter is determined from Global Positioning System (GPS) and aircraft Inertial Reference Unit (IRU) data. The paper concludes with an examination of the shielding effectiveness of the test aircraft, as determined by comparison of the measured internal EME and computed external EME.

1. Introduction

Digital technology has brought about significant advances in the control of flight, communications, and navigation functions of aircraft. New generation transport aircraft, such as the Boeing 777 and the Airbus A320, are "fly-by-wire" (FBW), a term which refers to the electronic links between the pilot's controls and the aircraft's flight surfaces that replace what had been mechanical links. Older generation aircraft are now built or retrofitted with flight management and navigation computers, flight data computers, engine control computers, digital autopilots, and computers to control collision avoidance and windshear warning systems. This trend is expected to continue in the future, with digital avionics employed to perform increasingly complex functions such as stability augmentation, gust load alleviation, and satellite-guided navigation.

Unlike avionics systems of the past, these systems are flight critical—their reliable operation is required in order to safely fly the aircraft. This fact raises concern about the vulnerability of these systems to electromagnetic interference (EMI). A history of EMI-induced system failures in military and commercial electronic systems is one of the reasons for this concern. EMI sources of particular concern are man-made radio frequency (RF) sources generated external to the aircraft, such as radar and radio transmitters. These potential sources of EMI are collectively known as HIRF or High Intensity Radiated Field sources. Some literature refers to this as HERF. A variety of definitions have been used with this acronym.

The National Aeronautics and Space Administration (NASA) Langley Research Center in Hampton, Virginia, has responded to this concern by developing a multifocused research program to study the coupling of HIRF into aircraft and the effects of that coupled energy on avionics systems. This paper reports on the results of one element of this research program, the experimental measurement of the electromagnetic environment (EME) inside a commercially configured airliner exposed to HIRF during flight.

1.1. HIRF Defined

HIRF encompasses man-made sources of electromagnetic radiation generated external to the aircraft considered as possibly interfering with safe flight. The easiest way to distinguish HIRF from other types of EMI is to state what it is not. HIRF does not include interference among on-board systems; this type of interference is referred to as an Electromagnetic Compatibility or EMC issue. HIRF also does not include EMI effects caused by portable electronic devices (PEDs) carried by passengers, such as cellular telephones, laptop computers, and portable radios. Rapid increases in the technology of personal communications causes concern about the potential EMI threat posed by PEDs however. More information on this subject can be found in [1] and [2]. HIRF does not include the effects of lightning, nor the effects of static electricity generated on the airplane; this is called Electrostatic Discharge or ESD. The effect of lightning on aircraft and avionics systems is similar to that produced by low frequency HIRF (kHz frequency range). For a review of this subject, see [3].

HIRF sources are only those emitters that intentionally generate emissions. Non-intentional (and in some cases non-licensed) emissions in the passband of aircraft navigation and communication systems have been known to cause interference problems, sometimes with serious consequences,[1] but are not considered HIRF. These types of emissions are regulated by the Federal Communications Commission (FCC). HIRF sources include radio and TV transmitters, airport and weather radar, and various military systems, both ground-based and airborne, such as surveillance radar, electronic warfare (EW) systems, and electromagnetic weapons. A discussion of the potential terrorist threat posed by the existence of electromagnetic weapons can be found in [5]. Concern about this threat has been heightened recently by the reported use of an electromagnetic weapon to disrupt transactions at an European financial institution [6].

1.2. Aviation Incidents Attributed to HIRF

The earliest HIRF-induced avionics failures to receive widespread attention were the crashes of five Army Blackhawk helicopters between 1981 and 1987, reported by the Knight Ridder News Service in 1987. In each case, the helicopter was reportedly flying near a radio transmitter when it suddenly dove straight into the ground [7]. Subsequent investigation and testing showed that the helicopter's rear wing (the stabilator) control system was vulnerable to EMI [8, 9]. Although most of the Blackhawk's flight control system is conventional (mechanically linked with hydraulic assist), the stabilator control system is FBW.

In 1991, the Knight Ridder News Service reported on the crash of an F-111 aircraft and the aborted missions of five others that occurred during a U.S. strike on Libya in 1986 [10]. Air Force officials blamed this on EMI generated by other U.S. aircraft participating in the strike. That same year, Aviation Week magazine reported that the in-flight breakup of seven Piper Malibu business aircraft was suspected by the National Transportation Safety Board (NTSB) to be due to HIRF induced upset of the autopilot system. The NTSB reported that it had received about 300 reports from users of the autopilot system installed in the Piper Malibu complaining of sudden and unusual excursions, particularly in the pitch axis [11]. Also in 1991, Lee [12] reported that a 1983 crash of a British-made Tornado fighter was found to be the result of the HIRF induced upset of the aircraft's air data computer. The electric field level near the crash site, which was near a Voice of America station, was later measured at 70 volts per meter.

---

[1] An example of this is Korean Air Flight 801, a 747 that crashed near Agana, Guam, in August 1997. A cockpit indicator failed to alert the crew that the glideslope system at Agana had been turned off, contributing to crew confusion in a crash that was blamed on "pilot error." A navigation systems expert with the FAA blamed "spurious radiation" for the misleading readout [4].

In 1994, Shooman [13] reported that a number of carriers were experiencing intermittent avionics upsets when operating in the Caribbean. British Airways, Air Canada, Air Jamaica, and Ward Air reported that as many as seven non-critical systems were affected simultaneously during landing, on the ground, and in the clearance process before and during takeoff. Subsequent testing conducted by Fuller [14] implicated high powered radiation from shipboard and/or airborne surveillance operated by U.S. military forces conducting drug traffic surveillance in the Caribbean and southern United States. Shooman also reported that an airship flying in close proximity to a Voice of America station in 1990 suffered a double engine failure and was forced to execute an emergency landing. Subsequent investigation showed that the engine ignition system was susceptible to EMI [15].

Shooman's report also discussed the results of a NASA-funded study which conducted an anonymous survey of crew members and EMI experts to collect first-hand experiences of undesired avionics upsets in which EMI was the suspected cause. The motivation for this study was concern that HIRF events may be under-reported because of political, business or liability reasons, or because they are either too minor to report (a momentary fluctuation in an instrument) or too major to report (a crash of undetermined cause). Shooman, who specializes in applying probabilistic measures to issues of safety and risk, determined that the frequency of EMI events in which HIRF was identified by the respondents as the cause is on the order of one every ten thousand flights. This rate of occurrence is on the order of that associated with lightning-induced upsets, upsets due to EMC problems, and equipment failure on commercial aircraft.

Most recently, Scarry [16] has proposed that HIRF may have been a factor in the crash of TWA Flight 800, a Boeing 747 which suffered a mid-air explosion off the coast of Long Island, New York, in July 1996. She postulates that ships and aircraft in the vicinity of the explosion may have been responsible for the HIRF and identifies 10 military planes and ships and a civilian airliner (USAir Flight 217) that were active in the area in which TWA 800 was flying.

1.3. Regulatory Response and Threat Definition

In 1986, the Federal Aviation Administration (FAA) requested the Society of Automotive Engineers (SAE)[2] to define the electromagnetic environment (EME) resulting from ground-based, shipborne, and airborne HIRF emitters and to draft certification requirements for the protection of aircraft against HIRF. In the fall of 1987, the SAE Aircraft Radiated Environments Subcommittee (AE4R) was formed to establish the HIRF environment and compliance criteria and develop a user's guide to certification through analysis and testing. This committee was composed of industry and government representatives from both the U.S. and Europe. In December of 1989, the FAA issued its first regulatory requirement for HIRF, an interim policy established until a final rule can be issued, which requires that critical avionics on new aircraft be shielded to withstand an illumination of 100 V/m over a frequency range from 10 kHz to 18 GHz, following test procedures established by the RTCA. The RTCA, established in 1935 as the Radio Technical Commission for Aeronautics, is another organization involved with aviation standards. The RTCA document DO-160 specifies all forms of environmental testing that avionic equipment must meet, including temperature, humidity, pressure, and vibration. Starting in 1977, electromagnetic susceptibility was addressed by this document, at that time as an EMC issue, which was also considered an environmental problem. In 1981, this section of the document was amended to include lightning and EMI extensions of the original EMC testing standards. In 1989, the RTCA added another amendment to include testing guidelines for HIRF.

[2] The SAE is one of several organizations that sets standards for the aviation industry.

In June of 1992, the AE4R committee forwarded a completed advisory circular to the FAA. In response to industry requests, the FAA did not immediately submit the advisory circular to the public rule-making process, but instead formed an Aviation Rulemaking Advisory Committee (ARAC) to assure that regulatory documents in the United States would be identical to those used by the European Joint Airworthiness Authority (JAA). In 1994, a working group of ARAC known as the "Electromagnetic Effects Harmonization Working Group" (EEHWG) was formed to take inputs from the SAE and their counterpart in Europe (EUROCAE, the European Organization for Civil Aviation Equipment) and produce common regulatory requirements. The EEHWG delivered its first drafts of an advisory circular and a "Notice of Proposed Rulemaking" (NPRM) to the FAA in August 1997. Under the Federal Aviation Act of 1958, the FAA must follow a public rulemaking process in order to add regulations to the U.S. Code of Federal Aviation Regulations (FARs). This process requires that NPRMs be reviewed for economic impact and published for public comment before they can be made law. The rulemaking process for HIRF is not expected to be complete until 2000. In the meantime, the FAA has issued a Flight Standards Bulletin (FSAW 97-16A) which establishes inspection requirements for in-service aircraft with HIRF protection.

In addition to developing the advisory circular and NPRM, the EEHWG has established HIRF environments calculated from 500,000 emitters based in the US and Europe. The HIRF environment proposed for certifying safety critical systems in fixed wing aircraft and helicopters is shown in Table 1.1. As this table suggests, the HIRF frequency spectrum divides into distinctly different halves around 400 MHz. Below this frequency, most high-power use of the electromagnetic spectrum is by communication and navigation devices which radiate signals that are weakly directional and continuously on the air. This includes AM and HF or "short wave" broadcasts, and FM and television broadcasts. Most high-power use of the spectrum above 400 MHz is by radar, satellites, and weapons systems. Radiation associated with these systems is generally narrow in beamwidth and often pulsed. In spite of the much higher peak power levels associated with signals in the GHz range, experience has shown that the region of greatest sensitivity for electrical and electronic systems on aircraft is between a few MHz and few hundred MHz [14].

Table 1.1. HIRF Certification Environment Proposed by the EEHWG [17]

Frequency	Field Strength (V/m)	
	Peak	Average
10 kHz – 2 MHz	50	50
2 MHz – 30 MHz	100	100
30 MHz –100 MHz	50	50
100 MHz – 400 MHz	100	100
400 MHz – 700 MHz	700	50
700 MHz – 1 GHz	700	100
1 GHz –2 GHz	2000	200
2 GHz – 6 GHz	3000	200
6 GHz – 8 GHz	1000	200
8 GHz – 12 GHz	3000	300
12 GHz –18 GHz	2000	200
18 GHz – 40 GHz	600	200

A reasoning for this behavior can be constructed by arguing that all electrical systems are complex combinations of electrical loops connecting sources to loads. In most cases, the wires forming the loop are much longer than the separation between those wires. One example is the path of a circuit on a printed circuit board, which may be 10 to 20 inches in length, but separated from the conducting backside of the board, which is the circuit's return path, by only the thickness of the board. Another example is the path from a power supply to a light on an aircraft wing; the wiring typically follows the inner surface of the wing and is co-routed with a return path wire. One would expect that fields which illuminate these circuits would not couple well if the circuit length was much less than a quarter wavelength long. The lowest frequency at which circuits are a quarter wavelength long can be estimated from the maximum dimensions of the system. For large aircraft, this frequency is around a few MHz.

As the frequency of illumination increases, the electromagnetic response of the aircraft varies up and down as the system passes through various resonances. Baum [18] writes,

> "Beginning with the lowest resonances associated with the major dimensions of the system (e.g., fuselage and wing lengths for an aircraft) and interior electrical wiring (cable shields and internal wires) of similar length, one goes up through resonances associated with shorter wires and dimensions of interior cavities. Then there are dimensions of doors, windows, boxes for electronic equipment, spacing between hinges and rivets, etc. For typical systems, the resonance region extends up to about 1 GHz, corresponding to half- or quarter-wave resonance of the smallest dimensions involved in the system construction, this coming from the smallest sizes with which human beings usually work, related to the size of a hand."

As the frequency of illumination increases above the resonance region, Baum models the the aircraft system using a circuit analogy—a source and a resistive load connected by a conducting wire above a ground plane. Once the frequency increases to a point where the spacing between wire and ground plane is a significant fraction of a wavelength, the current on the wire becomes attenuated. This attenuation increases with frequency, and eventually disconnects the source from the load. For typical circuit geometries, the current begins to fall off sharply over a few hundred MHz.

1.4. Problem Statement

Whether these arguments are accepted or not, the EME inside the aircraft must be known before the voltage levels on aircraft wiring can be determined. Unfortunately, the internal EME which results from the illumination of the aircraft exterior by HIRF defies simple analysis. If an aircraft is considered as a metal cavity with several apertures, then the problem is to determine the electromagnetic penetration into the cavity from external sources. Calculation of the penetration into simple cavities with single apertures has been performed, but an aircraft is an extraordinarily complex cavity with many apertures. The interior of an aircraft contains compartments, subcompartments, and partitioned substructures, any of which can potentially exhibit localized cavity resonance or mutually couple to one another. Significant analytical effort would be required to characterize these and other effects in order to determine the EME inside an aircraft. Typically, experimental testing is the tool of choice used to understand the relationship between internal and external fields. The aircraft manufacturing industry employs a combination of laboratory testing of avionic equipment to determine equipment susceptibility and on-the-ground field testing of aircraft to determine the relationship between the EME outside and inside the aircraft where the avionic equipment is located (see Figure 1.1). This approach has its roots in nuclear electromagnetic pulse research conducted at the Lawrence Livermore National Laboratory [19], the Sandia National

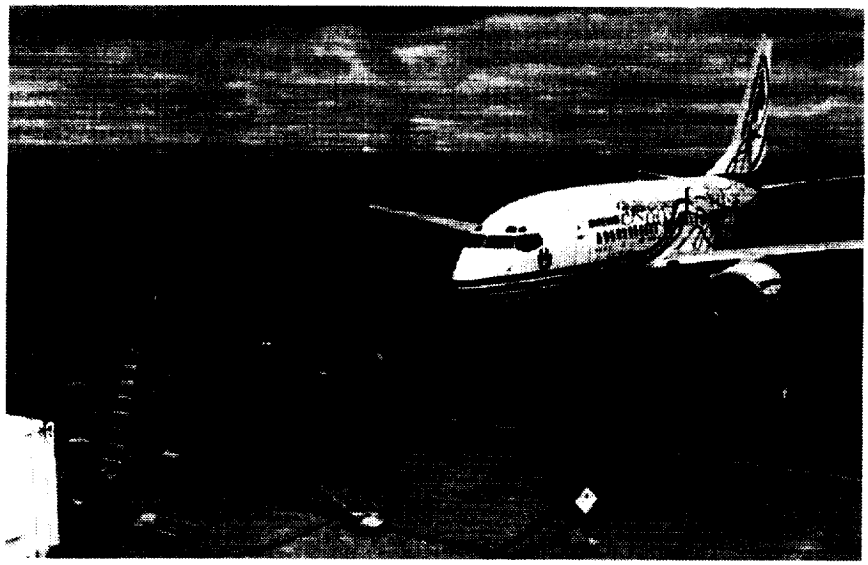

Figure 1.1. Field measurement of airframe attenuation performed in 1997 to satisfy part of the FAA-required HIRF certification plan for the Boeing 737-300. Photograph courtesy of The Boeing Company.

Laboratory [20], and the Air Force Phillips Laboratory (formerly the Air Force Weapons Laboratory) [18]. It assumes that the problem can be separated into the multiplication of two factors, aircraft shielding effectiveness (which is a measure of the attenuation due to the airframe) and equipment coupling efficiency. This concept requires that the avionic equipment not couple back into the aircraft in a way that affects shielding effectiveness.

This approach has several weaknesses. On-the-ground tests of shielding effectiveness may expose one or more significant coupling paths into the aircraft, but there is no way of knowing if all of the EMI-relevant coupling paths have been discovered. It is not possible to illuminate the aircraft from below, for example, which is the direction of illumination one would expect for many HIRF sources. Some of the coupling paths that are present during ground tests may or may not be present during flight. Wheel bay doors are open during ground tests but not during flight, for example. Finally, measurements may provide no aid in assessing the shielding effectiveness of aircraft during the design process. This is important because design changes to improve aircraft shielding must take place before the aircraft is built, as it is cost-prohibitive to do so afterwards.

1.5. Response to Problem

In 1992, NASA began funding a research program which addresses these weaknesses. NASA's program began with an industry-government workshop [21] to provide a forum for the presentation of electric and electronic system technology needs and requirements for future generations of commercial aircraft, from both industry and government-regulatory viewpoints. This workshop culminated in the identification of a number of research topics in need of NASA support. Among these topics were the development of analytical techniques to determine the shielding effectiveness of aircraft, and the pursuit of a measurement program to collect data for the verification of these techniques.

In 1995, the NASA Langley Research Center conducted a series of experimental measurements to characterize the EME inside an airliner during flight. The test object for these measurements was a commercially configured Boeing 757 owned by NASA. This aircraft was instrumented with an array of

sensors positioned so as to characterize the electromagnetic coupling characteristics and shielding effectiveness of three compartments of the aircraft: the flight deck (or cockpit), the avionics bay (located in the belly of the aircraft, behind the nosewheel bay), and the passenger cabin. The aircraft was then flown in close proximity to a number of ground-based RF transmitters operating in the "few MHz to few hundred MHz" range, which was identified as the frequency range of greatest concern during the aforementioned 1992 workshop. These transmitters were located at a Voice of America (VOA) station near Greenville, North Carolina, and at the NASA Wallops Flight Facility on Wallops Island, Virginia. This effort is referred to collectively as the "the EME flight experiment" or "the flight experiment" throughout the remainder of this report.

1.6. Outline

The goal of the research reported here is to measure the EME inside a transport aircraft during flight, so as to initiate the assimilation of information about coupling and shielding behavior for transports. It is anticipated that this information will be useful for the corroboration of analytical predictions of internal aircraft response to external stimuli. This effort has resulted in unique contributions in the characterization of coupling response for aircraft, in the characterization of the ground-based source antennas used in the experiment, and in the determination of the geometrical relationship between antennas, electromagnetic fields, and aircraft.

Section 2 provides details concerning the EME flight experiment and the interpretation and analysis of the measured data. The measurements of internal EME reported here are the first for a large aircraft in flight exposed to ground-based sources operating in the critical "few MHz to few hundred MHz" frequency range. Analysis of the measurements confirms the existence of several suspected coupling paths and has revealed some unexpected new ones. Section 3 discusses the problem of determining the fields external to the aircraft. Section 4 relates calculated values of the external EME to the measured internal EME to determine shielding effectiveness. A summary of findings is presented in Section 5.

2. Internal EME

This section describes certain details of a series of experimental measurements conducted by the NASA Langley Research Center that characterized the electromagnetic environment (EME) inside an airliner during flight. This measurement series, known as the EME flight experiment, was conducted over several days in February 1995. In this experiment, a commercially configured Boeing 757 aircraft, owned by NASA (see Figure 2.1), was instrumented with an array of sensors placed inside the aircraft and flown in close proximity to ground-based RF sources operating at approximately 26, 173, and 430 MHz. The aircraft was illuminated by the ground-based sources and the resulting electric field levels were measured by the array of sensors. The goal of this experiment was to collect coupling and shielding behavior data for transport aircraft. Possible future uses of these data include the corroboration of analytical predictions of internal aircraft response to external stimuli.

This section describes the sensors used to characterize the EME inside the aircraft, the instrumentation used to collect sensor data, and the paths flown by the aircraft past the ground-based sources. These flight paths determine the location of the aircraft relative to the ground-based source. Since this information is needed for simulation of the experiment, the calculations used to determine it are discussed here as well. The section concludes with an examination of some of the data collected by the experiment. Details about the ground-based sources will be discussed in Section 3.

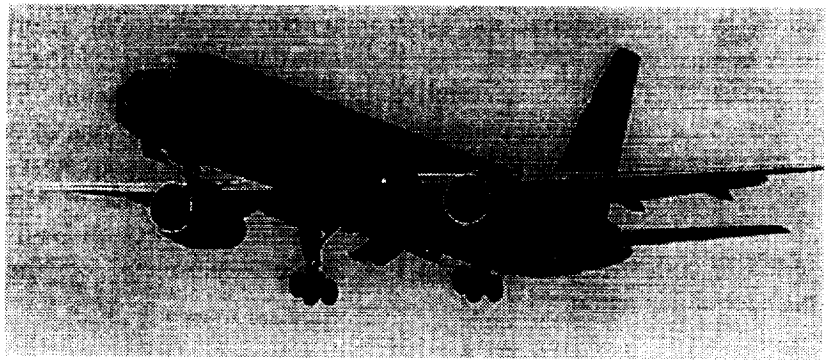

Figure 2.1. The NASA-owned Boeing 757. This aircraft is a standard-body airliner with a length of 155 ft, a wingspan of 125 ft, and seating for 194 passengers.

2.1. EME Sensors

Six RF sensors, illustrated in Figure 2.2, were used as probes to directly measure the electromagnetic environment inside the aircraft. These sensors consisted of three linear electric-field sensors known as D-Dot sensors, a long wire antenna, and two current probes. Sensors were positioned so as to characterize the three main compartments of the aircraft: the flight deck (or cockpit), the main electronics bay (in the belly of the aircraft), and the passenger cabin.

2.1.1. D-Dot Sensors

D-Dot sensors are most commonly used to measure EMP phenomena. At sufficiently low frequencies, these sensors produce output voltages that are proportional to the time derivative of an impinging electric field [22]. At higher frequencies, this derivative property is lost and the sensor operates as an electrically small antenna. The D-Dot sensors used for the flight experiment were model AD-60 manufactured by Prodyn Technologies of Albuquerque, New Mexico. The sensor consists of a solid metal central element supported by a plastic cylindrical shell (see Figure 2.3). The sensor is

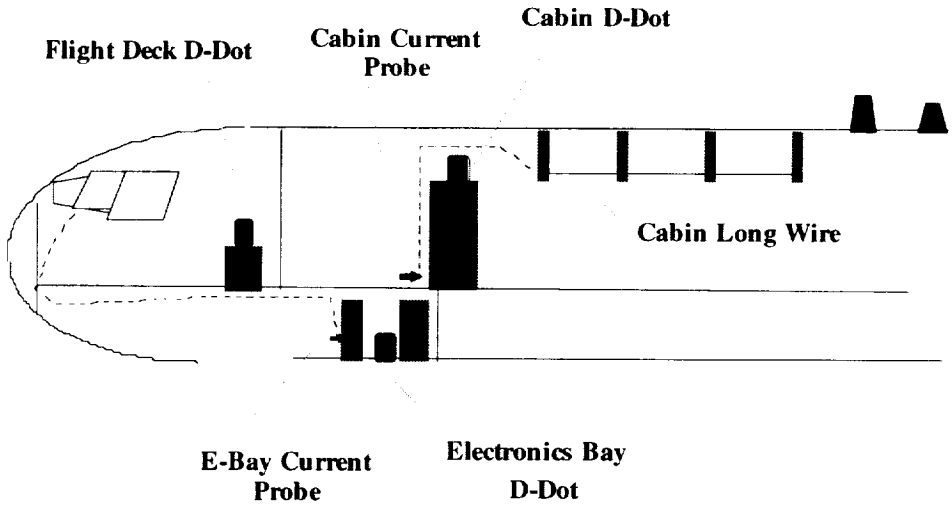

Figure 2.2. Sensor locations.

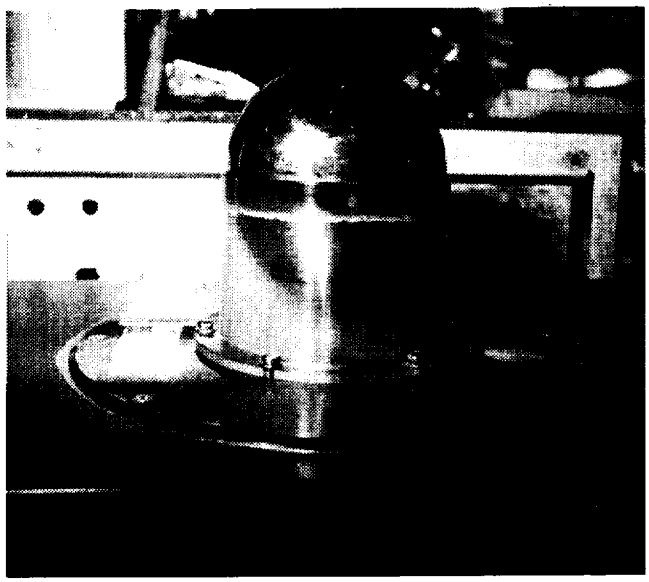

Figure 2.3. D-Dot sensor used in the EME flight experiment, electronics bay mounting shown. The overall height of this sensor is 6.1 in.

designed to be used on a large, highly conducting ground plane. A coaxial cable connector is mounted on the opposite side of the ground plane from the element, with the cable's outer conductor connected to the ground plane and the center conductor connected to the element.

One vertically oriented D-Dot sensor was positioned in each of the aircraft's three main compartments: the flight deck, the electronics bay, and the passenger cabin. The Flight Deck D-Dot was mounted on a metal box located aft of the first officer's seat (see Figure 2.4), the Electronics Bay D-Dot was mounted in the main electronics equipment bay which is located just aft of the nosewheel bay, and

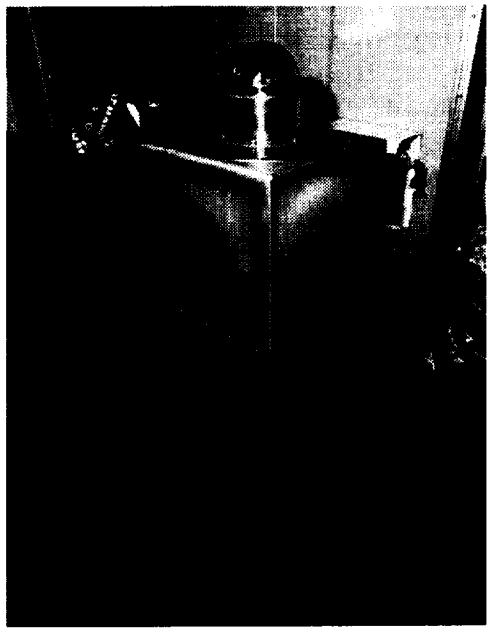

Figure 2.4. D-Dot sensor mounted in the flight deck.

the Cabin D-Dot was mounted on top of one of the equipment racks housing the data acquisition system in the passenger cabin (see Figure 2.5).

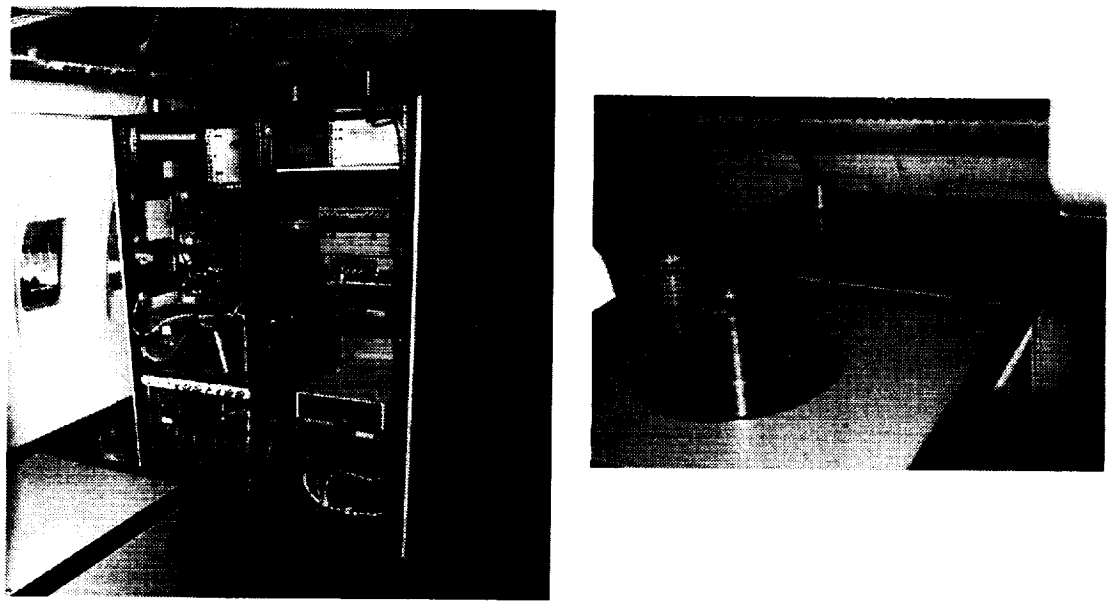

Figure 2.5. Two views of the D-Dot sensor mounted in the passenger cabin.

During the planning stages of the experiment, it was assumed that computer simulations would be able to predict the sensor terminal voltages. This approach may be viable at higher frequencies, where the D-Dot responds like an antenna (the AD-60 operates as an electrically small antenna above 300 MHz, as will be seen below). Reasonable results may be expected from a coarse model of the sensor in this case. At low frequencies, however, the sensor response exhibits a differentiating property that is a result of fine geometric detail of a very small scale relative to the rest of the aircraft. Since it would be very difficult to include this fine detail within a much coarser model of the aircraft, it was decided to calibrate the D-Dots to extract the impinging field strength from the measured terminal voltage. An effort was initiated with the National Institute of Standards and Technology (NIST), in Boulder, Colorado, to calibrate the D-Dots in the configurations and at the frequencies used in the flight experiment. This effort was performed in 1995 by the Department of Commerce for the NASA Langley Research Center and was documented in a working paper by R. T. Johnk and A. R. Ondrejka entitled, *Time-Domain Calibrations of D-Dot Sensors.*

For this calibration, a D-Dot sensor was mounted in a number of vertically oriented configurations (see Figure 2.6). Each configuration was illuminated by a vertically polarized wave of known amplitude and the output voltage from the D-Dot was recorded as a function of frequency. Reference incident fields were generated both by a TEM cell and a cone and ground plane system. A TEM cell is a closed transmission line system that, in this case, generated incident reference fields between 25 MHz and 100 MHz. A cone and ground plane system is an open, conical antenna driven against a very large ground plane. This system generates an axially symmetric TEM spherical wave originating from the base of the cone that is usable, in this case, above 50 MHz.

D-Dot sensors are specified by the manufacturer to be mounted on an electrically large ground plane. Figure 2.6(a) illustrates the sensor mounted in this configuration and Figure 2.7 shows the resulting voltage response as a function of frequency. As can be seen from this figure, the sensor exhibits a

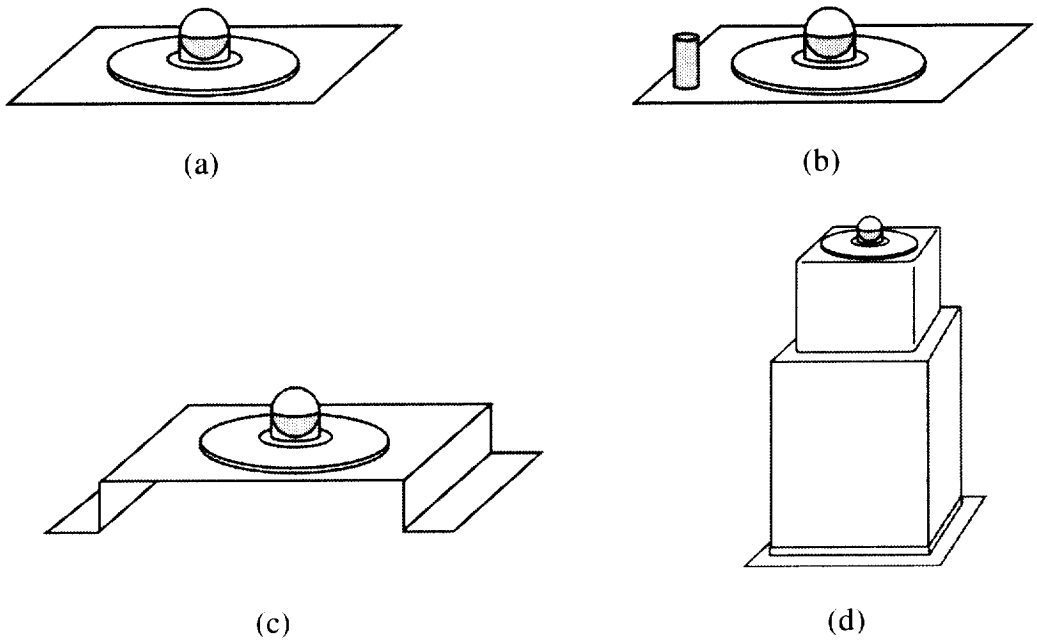

Figure 2.6. D-Dot sensor mounts calibrated by NIST. Mount (a) is a baseline mounting, (b) is intended to be representative of the passenger cabin mounting, (c) is a mounting similar to that used in the electronics bay, and (d) is the mounting used in the flight deck.

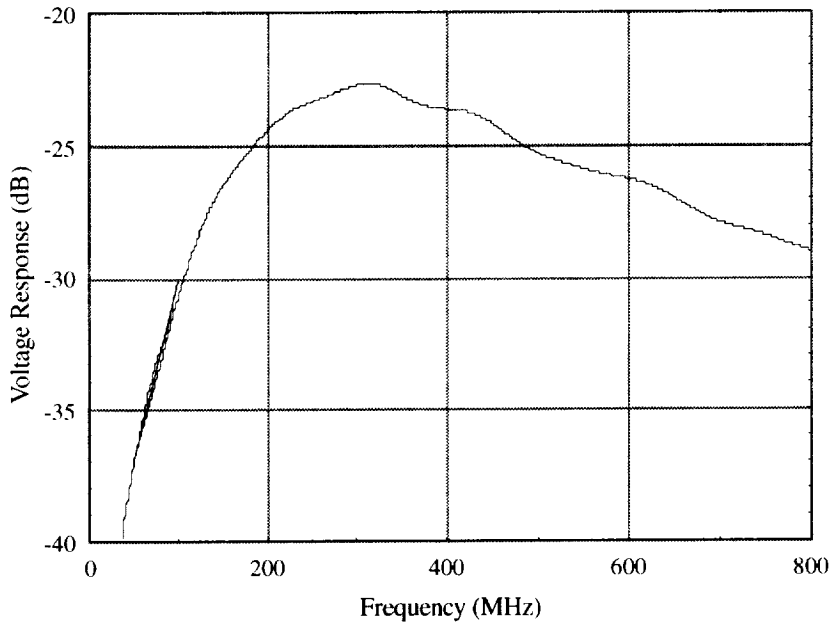

Figure 2.7. D-Dot response for baseline configuration. Both the TEM cell (25 MHz to 100 MHz) and the cone and ground plane (50 MHz and up) measurements are shown.

low-frequency differentiating property that breaks down above 200 MHz. In this figure and those that follow, the voltage response shown is that due to an illuminating electric field with a field magnitude of 1 V/m. The voltage response of the sensor is shown in dB, referenced to 1 V (0 dB = 1 V), e.g., a calibrated voltage response for –25 dB indicates that the sensor produces a voltage of 0.056 V.

Figure 2.6(b) illustrates the D-Dot mounted next to a metal post, as was the case for the sensor in the passenger cabin. Both the metal post and the sensor were located on top of an equipment rack during the flight experiment, but the equipment rack was too large to be included in the calibration measurement. As an alternative, the metal post and the D-Dot were mounted to a large ground plane. The configuration was oriented both with the post located between the incident wave front and the D-Dot, and with the post on the opposite side of the D-Dot. In neither case were pronounced differences observed from the baseline calibration.

Figure 2.6(c) illustrates the D-Dot mounted on an elevated platform (approximately 4 inches high) similar to that used in the electronics bay. The vertical portions of the platform were solid in the narrow dimension and open in the wide dimension and, as a result, the platform forms an open resonant structure. Measurements were performed both with the narrow and the wide portions of the platform facing the incident wave front. Figure 2.8 shows that the response of the sensor is shifted from the baseline calibration by as much as 4.5 dB and shows there are considerable differences between the two platform orientations. While it is possible to determine the orientation of the radiation incident upon the aircraft during the flight experiment, it is not possible to know its orientation when it illuminates the D-Dot inside the aircraft. These calibration measurements can therefore be used only to estimate a range of possible calibration factors associate with the electronics bay D-Dot measurements.

Figure 2.6(d) illustrates the D-Dot mounted on the metal box that was located just aft of the first officer's seat in the flight deck. The frequency response of the sensor in this configuration, shown in Figure 2.9, deviates substantially from the baseline calibration, especially at lower frequencies. NIST attributed this to resonances of the box and stated that no reliable statement of calibration uncertainty can be made in this case. Large uncertainties must therefore be assumed for the low-frequency data collected by the D-Dots in the flight deck and the cabin (since this sensor is also mounted atop a large box-like structure).

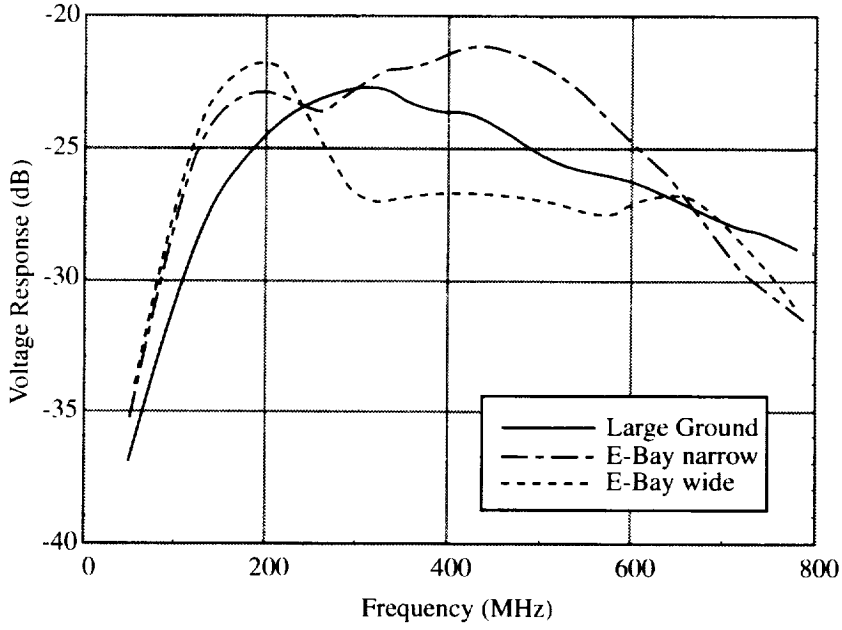

Figure 2.8. D-Dot response for electronics bay and baseline configurations.

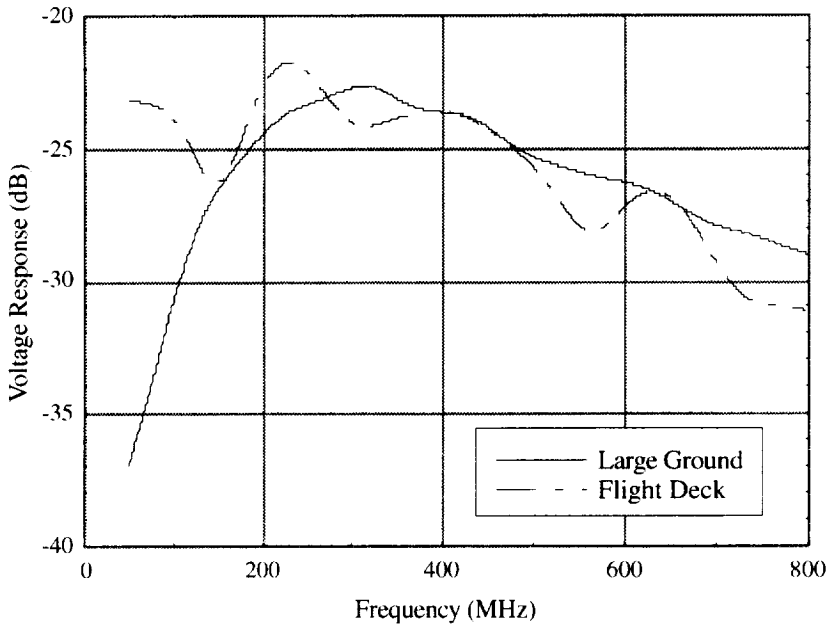

Figure 2.9. Response of D-Dot in flight deck configuration compared to baseline.

Of interest, but not addressed by the NIST calibration, is the polarization sensitivity of the D-Dots. Although these sensors are believed by the manufacturer to be sensitive only to the polarization oriented in the direction of the sensor, no known measurement of the sensitivity of these sensors to cross-polarized radiation has been made, and nothing can be said about the effect of the mounting structure on polarization sensitivity. This is of concern because the polarization to which the D-Dots were exposed during the flight experiment was arbitrary and not necessarily aligned with the sensor.

The NIST calibration measurements and the lack of information about D-Dot polarization sensitivity suggest that the appropriate calibration factors to apply to the voltages measured at the D-Dot sensor terminals cannot be determined with good precision, particularly at the lower frequencies. In spite of this, calibration factors were applied to the measured voltages, to enable analysis and reporting of the data. The selected calibration factors are documented in Table 2.1.

Table 2.1. Calibration Factors Applied to D-Dot Voltages
[Estimates of calibration uncertainty are shown in parentheses]

	26 MHz	173 MHz	430 MHz
Flight Deck D-Dot	−25 (±4) dB	−25 (±1) dB	−23.9 (±0.9) dB
Cabin D-Dot	−30 (±4) dB	−25 (±1) dB	−23.9 (±0.9) dB
E-Bay D-Dot	−40.9 (±0.7) dB	−23.1 (±1.1) dB	−24.3 (±3.1) dB

2.1.2. Cabin Long Wire Sensor

The Cabin Long Wire (CLW) sensor was a 20 foot long wire positioned along the longitudinal axis of the aircraft and suspended from the ceiling of the passenger cabin by dielectric standoffs (see Figure 2.10). This wire was connected to the center conductor of a 50 ohm coaxial cable whose outer conductor was connected to a small strip of metal (a 1 by 14 inch rectangle). This sensor was not

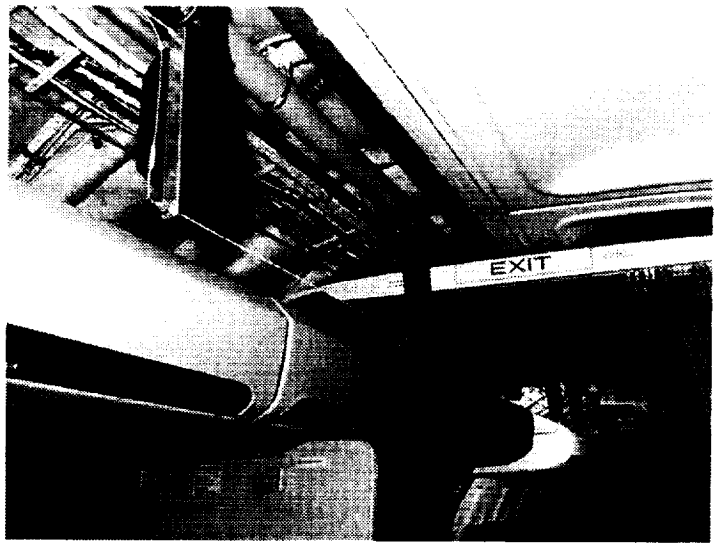

Figure 2.10. Cabin Long Wire (CLW) sensor. Both the wire and the small strip of metal, used in lieu of a ground plane, can be seen in this photograph.

calibrated to measure the electric field strength but was intended instead to be included as part of the aircraft in computer simulations of the flight experiment. A spectrum analyzer recorded the voltage between the cable's center and outer conductor. This sensor proved to be responsive to signals across the test spectrum.

2.1.3. Current Probes

The current probes were model I-320 manufactured by Prodyn Technologies of Albuquerque, New Mexico. These current probes were clamp-on devices that were used to sense currents induced onto the shielding of wire bundles in the aircraft (see Figure 2.11). Two I-320 current probes were used for this experiment. One was located in the main electronics bay and was coupled to a cable that ran from the electronics bay along the interior left side of the aircraft fuselage to the flight deck windscreen heat mesh embedded in the captain's window. This sensor was used to sense currents that were theorized to be induced onto cable bundles from external electromagnetic energy impinging on the nose of the aircraft and entering the window apertures of the aircraft's flight deck. The other current probe was located in the passenger cabin and was used to sense currents on the shielded outer conductor of the semi-rigid coaxial cable feeding the CLW sensor. Calibration information for these sensors was provided by the U.S. Air Force Phillips Laboratory (courtesy Ly Dao of the U.S. Air Force Phillips Laboratory, Kirtland Air Force Base, NM).

In both cases, the cables to which the current probes were attached are part of a bundle of cables held together with cable ties. The exact path followed by the probed cable and its neighbors was not documented. It is therefore not practical to perform a computer simulation of the measurement performed by these probes. The data collected by these probes are useful for qualitative analysis however, as will be seen below.

Figure 2.11. Current probe sensor located in the passenger cabin.

2.2. Flight Instrumentation

The response of all six EME sensors was recorded during flight by a real-time data acquisition system. This system consisted of two equipment racks containing the measurement instruments, a signal switch matrix, a signal amplifier, and a control computer. Figure 2.12 illustrates this system. Signals from the EME sensors were multiplexed through the switch matrix (see Figure 2.13) such that the response of each sensor was recorded in turn by both a spectrum analyzer set to zero span and one channel of an oscilloscope. The zero span spectrum analyzer measurement established the absolute amplitude of the signal at the frequency of interest, while the oscilloscope measured the time signature of the signal, which was of interest for cases in which the aircraft was illuminated by a pulsed source.

In addition to the sensor measurement instrumentation, the data acquisition system included a Global Positioning System (GPS) receiver and a VXI (IEEE standard 1155) bus controller used to access the aircraft's internal data bus (an ARINC standard 429 bus). The GPS receiver established the aircraft's location (latitude, longitude, and altitude), while the VXI bus controller was used to acquire the aircraft's attitude (pitch, roll, and yaw) from the aircraft's own flight instruments.

More detailed information about the instrumentation and the data collection process can be found in reports written by Dudley [23] and Koppen [24].

2.3. Flight Profiles

A number of flight paths were flown past each ground-based source to ensure that electromagnetic energy impinged upon the aircraft at various angles of incidence. Flights directed towards (inbound) and away from (outbound) the sources were executed to illuminate the nose and tail of the aircraft, respectively. Crossbound flight paths were executed to illuminate the side of the aircraft.

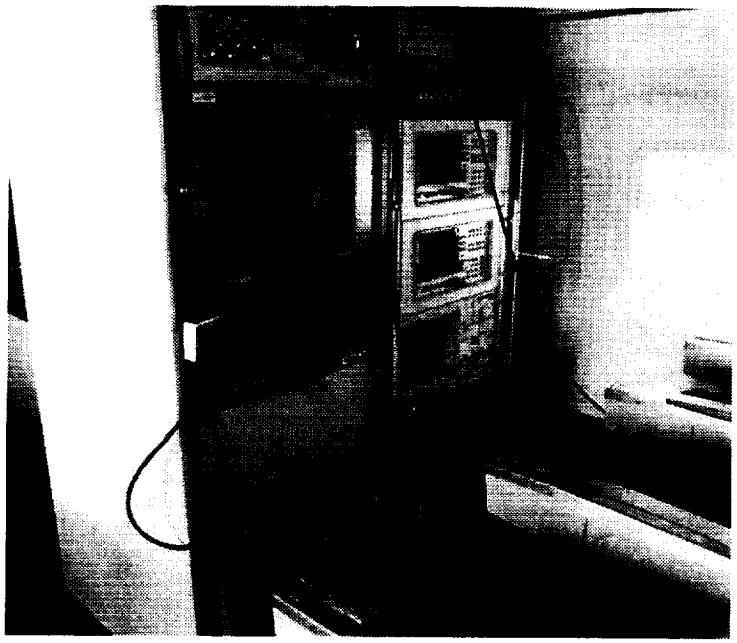

Figure 2.12. Front view of the equipment comprising the data acquisition system. The left rack contains the control computer and a signal amplifier. The right rack contains a GPS receiver, two spectrum analyzers, a two channel oscilloscope, and a VXI bus controller.

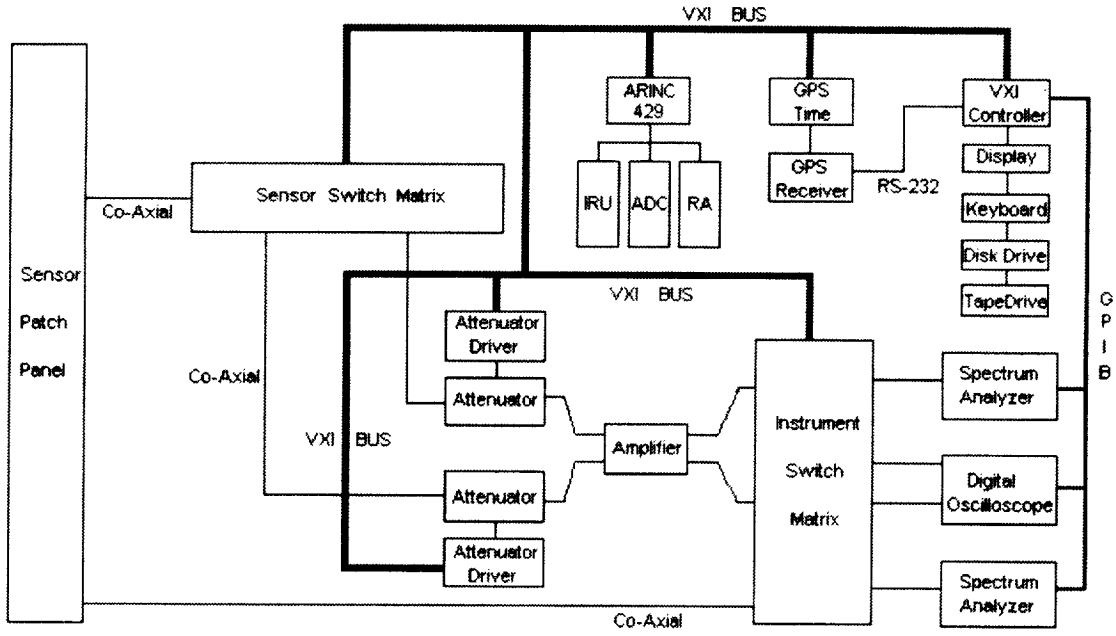

Figure 2.13. Schematic of data acquisition system.

Each inbound, outbound, and crossbound path was executed three times, with the aircraft in different configurations each time. These configurations were designated "clean," "flaps," and "flaps & gear." The "clean" configuration was flown with the aircraft's wing flaps and slats trimmed to neutral and the landing gear up with the bay doors closed. The "flaps" configuration was flown with the aircraft's flaps extended to 15 degrees. This flap setting also caused the slats to be deployed. The "flaps & gear" configuration was flown with the flaps and slats extended as before, and with the gear bay doors open and the landing gear down. These three configurations were executed to help define EME coupling apertures and to determine if changes in the aircraft configuration significantly affected shielding effectiveness.

Flight paths flown against the 26, 173, and 430 MHz sources are illustrated in Figures 2.14, 2.15, and 2.16, respectively. The 26 MHz source was fixed in the horizontal polarization, with the main beam pointing at a compass heading of 94.42°. The 173 MHz source was configurable in both the horizontal and vertical polarizations, and in-flight measurements were made for both cases. For the flight test, this source was aimed at a compass heading of 129°.

Unlike the 25 and 173 MHz sources, the 430 MHz source was not fixed in position, but tracked the aircraft to keep it within the vertically polarized main beam of this source. The flight paths flown against this source differ from the previous two because of this. Flights from the southwest to the northeast first illuminate the left side of the aircraft and, after a turn, the tail of the aircraft. Conversely, flights from the northeast to the southwest illuminate the nose and then the right side.

The flight paths shown in these three figures are derived from measurements of the location of the aircraft for flights conducted in the "clean" configuration. Flight paths for the "flaps" and "flaps & gear" configurations are similar.

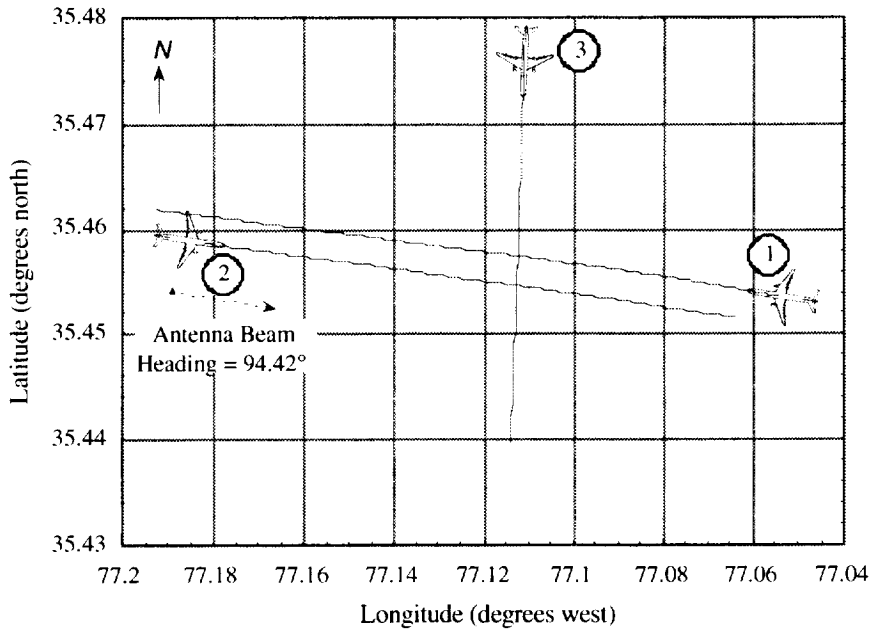

Figure 2.14. Flight paths flown against 26 MHz source. Inbound (path 1), outbound (path 2), and right-side crossbound (path 3) flights were executed at this frequency.

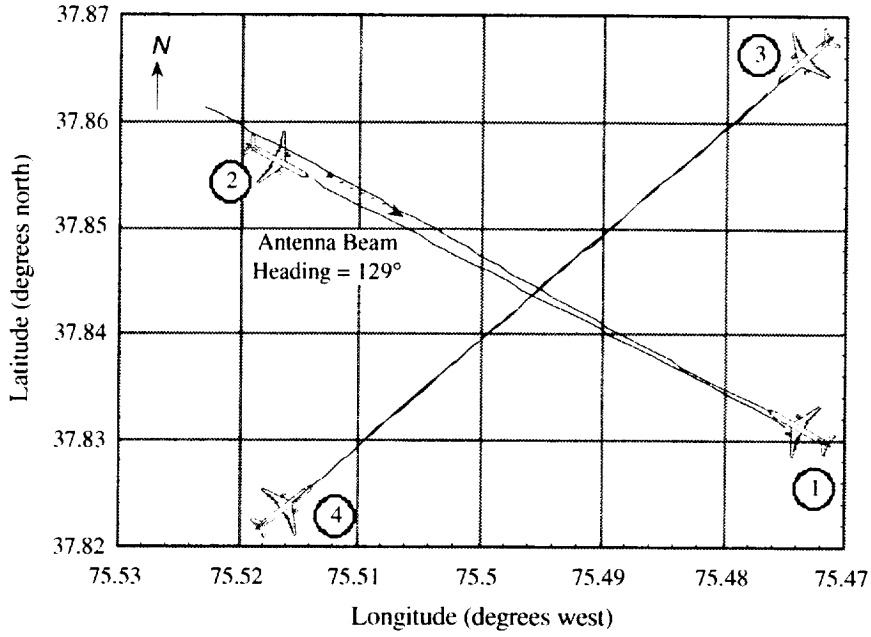

Figure 2.15. Flight paths flown against 173 MHz source: Inbound (path 1), outbound (path 2), right-side crossbound (path 3), and left-side crossbound (path 4).

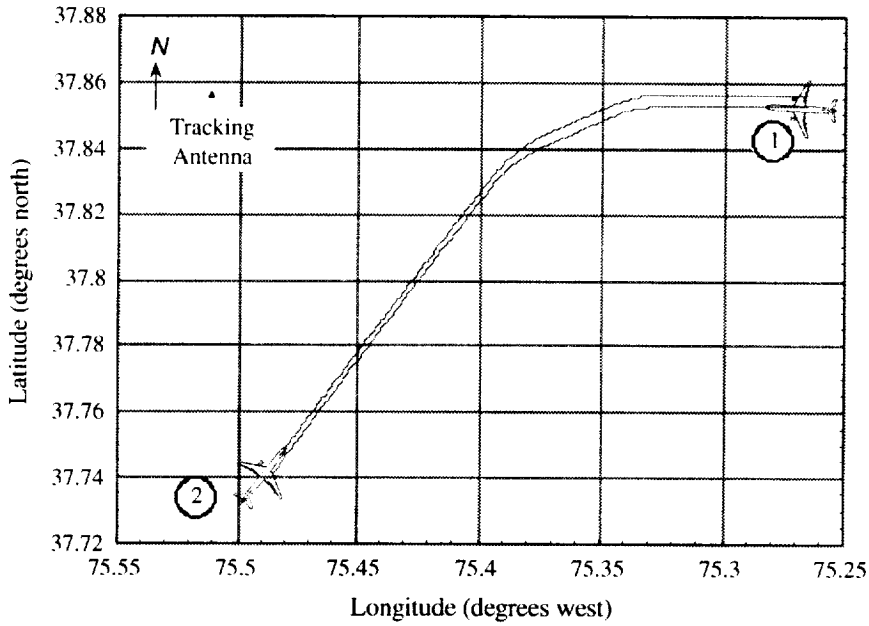

Figure 2.16. Flight paths flown against 430 MHz source: Inbound to right-side crossbound (path 1) and left-side crossbound to outbound (path 2).

2.4. Aircraft Location

The data recorded by the data acquisition system include the response of the EME sensors along with the GPS coordinates of the aircraft. For reporting and analysis purposes, it is desirable to determine the location of the aircraft relative to the ground-based source during measurement. This is somewhat more complicated than it might first appear. The position information collected by the flight experiment is limited to the GPS coordinates of the source antenna and the aircraft. GPS coordinates include latitude, longitude, and "ellipsoid height," where ellipsoid height is the height of the aircraft above a GPS-standard smooth-surface model of the Earth. Ellipsoid height therefore does not necessarily coincide with altitude above the Earth's surface.

Kaplan [25] describes a transformation which converts GPS coordinates to coordinates in an "Earth Centered, Earth Fixed" (ECEF) coordinate system, a Cartesian coordinate system whose origin is located at the center of the Earth (see Figure 2.17). The (x, y, z) location of a point in the ECEF coordinate system may be found from its GPS coordinates of latitude, longitude, and ellipsoid height (LAT, LON, EH) using the following equations:

$$x = (n + \mathrm{EH})\cos(\mathrm{LAT})\cos(\mathrm{LON}) \tag{2.1}$$

$$y = (n + \mathrm{EH})\cos(\mathrm{LAT})\sin(\mathrm{LON}) \tag{2.2}$$

$$z = (n(1 - s) + \mathrm{EH})\sin(\mathrm{LAT}) \tag{2.3}$$

where n and s are given by the following:

$$n = \frac{a}{\sqrt{1 - s \cdot \sin^2(\mathrm{LAT})}} \tag{2.4}$$

$$s = (2f - f^2)^2 \tag{2.5}$$

where a is the Earth's equatorial radius (6 378 137 m) and

$$f = \frac{a - b}{a} \tag{2.6}$$

where b is the Earth's polar radius (6 356 752 m).

Kaplan's equations can be used to determine position vectors for both the aircraft and the source antenna in the ECEF coordinate system. What is desired however, is the position vector for the aircraft in a coordinate system aligned with the source antenna. This information can be found by performing a transformation which employs Euler angles [26]. For this effort, an antenna coordinate system was selected in which the z-axis is normal to the ground beneath the antenna and the x-axis is aligned in the direction of the main beam (see Figure 2.18).

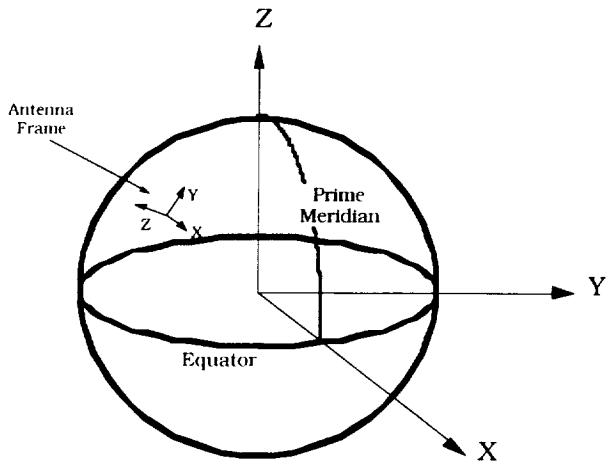

Figure 2.17. ECEF coordinate system. This coordinate systems orients the z-axis through the North pole, and the x-axis through the intersection of the Prime Meridian and the Equator. Also shown is a coordinate system aligned with the source antenna.

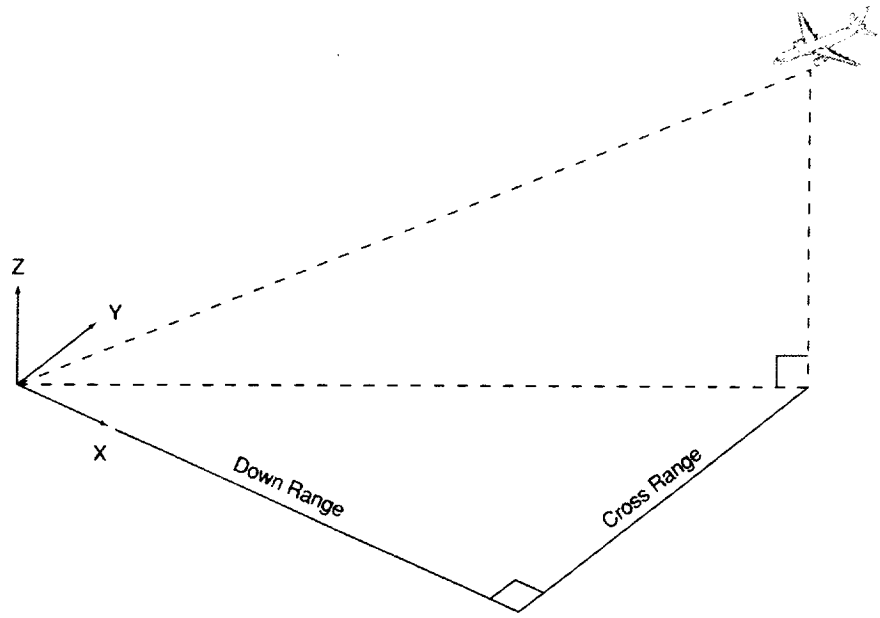

Figure 2.18. Antenna coordinate system. Note that the xy plane is not the Earth's surface, but a plane tangent to the Earth at the antenna location.

The transformation of an aircraft vector in the ECEF coordinate system to an aircraft vector in the antenna coordinate system can be performed as follows:

1. Create a "primed" coordinate system which is congruent with the ECEF system and which contains a "primed" aircraft vector affixed to it.

2. Rotate this primed system counterclockwise about its z-axis by an amount equal to the antenna's longitude east of the prime meridian. This rotation aligns the xz-plane of the primed system with the origin of the antenna coordinate system.

3. Rotate the resulting y-axis of the primed system counterclockwise by (90° − antenna latitude). This aligns the z-axis of the primed system with the z-axis of the antenna coordinate system.

4. Rotate the resulting z-axis counterclockwise by (180° − main beam compass heading). This rotation causes the primed system to be aligned with the antenna system. In the case of the 430 MHz source, a fixed compass heading of 129° was used. With this alignment, the x-axis of the antenna coordinate system is perpendicular to the crossbound portion of the flight path.

5. Translate the resulting coordinate system by an amount defined by the antenna position vector in the ECEF coordinate system. This will bring the primed system and the antenna system into congruence and complete the transformation of the aircraft vector.

This transformation can be performed by subtracting the antenna vector from the aircraft vector in the ECEF coordinate system and then multiplying the (x, y, z) coordinates of the result to a $[3 \times 3]$ rotation matrix. This operation can be written as

$$\mathbf{p}_{air}|_{ant} = \mathbf{A}\,(\mathbf{p}_{air}|_{ECEF} - \mathbf{p}_{ant}|_{ECEF}) \tag{2.7}$$

where $\mathbf{p}_{air}|_{ant}$ is the position vector describing the aircraft location in the antenna's coordinate system, $\mathbf{p}_{air}|_{ECEF}$ is the aircraft location in the ECEF system, $\mathbf{p}_{ant}|_{ECEF}$ is the antenna location in the ECEF system, and $\mathbf{A}$ is the rotation matrix. If the angles of rotation in the transformation described above are denoted by α_1, β, and α_2 ,where α_1 is the z-axis rotation in step 2, β is the y-axis rotation in step 3, and α_2 is the z-axis rotation in step 4, then the rotation matrix $\mathbf{A}$ can be derived by multiplying together matrices which describe these individual rotations [27]. That is

$$\mathbf{A} = \begin{bmatrix} \cos(\alpha_2) & \sin(\alpha_2) & 0 \\ -\sin(\alpha_2) & \cos(\alpha_2) & 0 \\ 0 & 0 & 1 \end{bmatrix} \begin{bmatrix} \cos(\beta) & 0 & -\sin(\beta) \\ 0 & 1 & 0 \\ \sin(\beta) & 0 & \cos(\beta) \end{bmatrix} \begin{bmatrix} \cos(\alpha_1) & \sin(\alpha_1) & 0 \\ -\sin(\alpha_1) & \cos(\alpha_1) & 0 \\ 0 & 0 & 1 \end{bmatrix} \tag{2.8}$$

or

$$\mathbf{A} = \begin{bmatrix} \cos(\alpha_2)\cos(\beta)\cos(\alpha_1) - \sin(\alpha_2)\sin(\alpha_1) & \cos(\alpha_2)\cos(\beta)\sin(\alpha_1) + \sin(\alpha_2)\cos(\alpha_1) & -\cos(\alpha_2)\sin(\beta) \\ -\sin(\alpha_2)\cos(\beta)\cos(\alpha_1) - \cos(\alpha_2)\sin(\alpha_1) & -\sin(\alpha_2)\cos(\beta)\sin(\alpha_1) + \cos(\alpha_2)\cos(\alpha_1) & \sin(\alpha_2)\sin(\beta) \\ \sin(\beta)\cos(\alpha_1) & \sin(\beta)\sin(\alpha_1) & \cos(\beta) \end{bmatrix} \tag{2.9}$$

As can be seen from Figure 2.18, once the location of the aircraft relative to the ground-based antenna has been determined, the EME sensor data can be reported in terms of crossrange and/or downrange distance from the antenna. Crossrange distance is used here to describe aircraft location for flights which illuminated the side of the aircraft (crossbound flights) and downrange distance is used to describe aircraft location for flights which illuminated the nose or tail of the aircraft (inbound or outbound flights). This information is needed in order to compare the EME sensor response with calculations of the field strength illuminating the exterior of the aircraft. More will be said about this subject in the next section. Discussion concerning the application of the transformation described in this section to the data collected by the flight experiment was supplied by Cuong C. Quach, Langley Research Center.

The entire set of measured and reduced EME sensor data collected by the flight experiment may be found in Appendix A. The data may also be accessed from a web page located at `aspo.larc.nasa.gov/emec`.

2.5. Data Discussion and Analysis

In this section, the data collected by the flight experiment are examined and conclusions are drawn about the coupling characteristics of the NASA 757. This subject is of importance in determining the proper application and limitations of analytical techniques and is best introduced by first reviewing the results of earlier studies. Earlier studies of the coupling characteristics of the NASA 757 include one performed by the Lawrence Livermore National Laboratory[3] [28] and another performed by the Naval Surface Warfare Center, Dahlgren Division[4] [29]. These studies were based on measurements which were performed with the aircraft on the ground. The findings of these studies may be summarized as follows:

- *The principal mechanism for coupling of exterior fields into the flight deck is radiation through the cockpit windshield.*

This conclusion was reached as a result of a test in which the cockpit windshield was covered with conductive foil and tape. The aircraft was then illuminated with a vertical electric field over a frequency range of 3 MHz to 1 GHz. This conclusion suggests that analytical predictions of the shielding effectiveness of the flight deck should focus on modeling radiative, as opposed to conductive, coupling paths into this cavity. As was mentioned in Section 1, previous applications of FDTD to aircraft response have focused on the determination of currents induced by external fields onto surfaces and wires.

- *Windows are an effective mechanism for coupling of exterior fields into the passenger cabin only when the frequency of illumination is above 20 MHz.*

The longest dimension of the passenger cabin is approximately 36 meters, which implies a lowest order cavity resonance near 8 MHz. Electromagnetic fields which could induce a fundamental-mode cavity resonance therefore do not couple well into this aircraft.

- *Small-scale geometric detail can be ignored by analytical models.*

This conclusion was reached as a result of tests in which a metallic box, approximately 1 meter on edge, was moved around inside the flight deck. Significant changes in the measured electric field were not observed.

- *The peak field strength coupled into the aircraft is less than 6 dB above the incident field strength.*

Prior to these studies, it had been hypothesized that field levels inside the aircraft could far exceed exterior field levels at frequencies near the resonance of the interior cavities.

---

[3] This effort was performed by the Department of Energy for the NASA Langley Research Center and took place at the U.S. Air Force Phillips Laboratory, Kirtland Air Force Base, Albuquerque, NM, in October 1994.

[4] This effort was performed by the U.S. Navy for the NASA Langley Research Center and took place at NASA Langley in February 1995.

- *Loss mechanisms for fields inside the aircraft include: radiation through apertures, resistive loss in walls, partitions and people, and energy coupled to wires and into loads.*

Although aperture radiation and resistive loss are believed to be the dominant loss mechanisms, tests which studied the impact of opening and closing a single circuit breaker in the electrical system of the aircraft indicate that the electrical system configuration can have a significant effect on the fields inside the aircraft. Tests which studied the impact of personnel and passengers in the aircraft indicate that losses due to people in the aircraft are less important, but not insignificant.

- *Field penetration into the aircraft through gaps around the pressure doors is small.*

This conclusion was reached as a result of tests in which one of the passenger entry/exit doors was sealed with conductive tape.

- *Field penetration through gaps around the electronics bay access door (which is not pressurized) is not small.*

This conclusion was reached as a result of tests in which the access door was sealed with conductive tape. Taping the door gaps was found to increase the shielding effectiveness of the electronics bay by more than 10 dB over broad frequency ranges.

Analysis of the data collected by the flight experiment affords additional insight into the coupling characteristics of the NASA 757, and augments that drawn from ground-based measurements. Conclusions resulting from this analysis are summarized below. A more detailed discussion can be found in [30].

- *Conduction along wires connecting the flight deck to the electronics bay is a significant mechanism for the coupling of external fields into the electronics bay.*

The response of the current probe in the electronics bay (which was coupled to a cable that ran from the heat mesh embedded in the left-side cockpit window) more closely correlates with the response of the D-Dot sensor in the flight deck than with the D-Dot sensor in the electronics bay. This behavior indicates that cable bundles do in fact couple fields impinging upon the nose of the aircraft into the electronics bay, as had been hypothesized prior to the flight test. This conclusion suggests that analytical predictions of the shielding effectiveness of the electronics bay need to include conductive coupling paths into this cavity.

- *Coupling into the passenger cabin increases when the flaps are deployed.*

The sensors located in the passenger cabin exhibited considerable sensitivity to the configuration of the aircraft ("clean" vs. "flaps" or "flaps & gear"). The character of this sensitivity can be seen by comparing the 26 MHz cabin sensor data collected during nose-illuminating inbound flights with the data collected during tail-illuminating outbound flights. Outbound flight measurements of internal EME are approximately three times higher when the flaps are deployed (which is the case in both the "flaps" and "flaps & gear" configuration) than when the flaps are set to the neutral position (the "clean" configuration). This observed sensitivity to configuration during tail illumination can be seen in the data collected from all cabin sensors during illumination from the 26 MHz and 173 MHz horizontally polarized (H-pol) sources. This result is possibly explained by the fact that deploying the flaps opens

apertures into the rear wheel bays of the aircraft (see Figure 2.19). This observation makes it seem likely that significant coupling paths exist which connect the wheel bays to the passenger cabin.

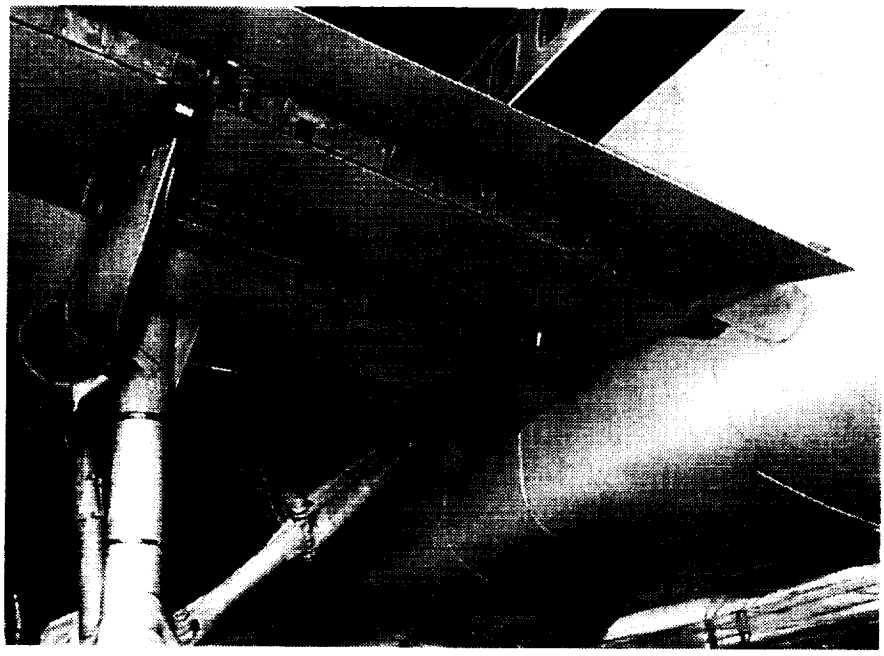

Figure 2.19. Underside view of the NASA 757 with the flaps deployed 15° and the landing gear down. Note the apertures which open into the wheel bay.

- *At 26 MHz, field levels in the passenger cabin are higher than field levels in the flight deck, which in turn are higher than field levels in the electronics bay.*

This behavior is evident for all flight paths and aircraft configurations at this frequency. The free-space wavelength of the 26 MHz illumination is 11.6 m. The minimum wavelength that can be supported within an electromagnetic cavity is limited to the maximum interior dimension of that cavity. The largest interior dimension of the passenger cabin is approximately 36 m. If it can be assumed that the passenger cabin is an electromagnetic cavity, then fields penetrating into the cavity should freely propagate within it in this case. By comparison, the largest interior dimensions of the flight deck and the electronics bay is approximately 3.6 and 3.0 m, respectively, well below the wavelength of illumination. Electromagnetic fields penetrating into these two cavities should therefore be sharply attenuated. These physical observations may explain the relative measured field levels at this frequency.

- *At 173 MHz, fields in the flight deck are as high or higher than in the passenger cabin.*

Field levels in the flight deck are about twice as high as in the passenger cabin when the aircraft is illuminated by vertically polarized radiation at 173 MHz. Recorded field levels are about the same when the aircraft is illuminated by horizontally polarized radiation at this frequency. Since the D-Dot sensors in both the flight deck and the passenger cabin are both vertically oriented, the data collected under vertically polarized case may be a more accurate recording of the effects of radiation into the aircraft. Unlike the 26 MHz case, where the largest interior dimension of the flight deck (approximately 3.6 m) was much less than the free-space wavelength of the illuminating radiation (11.6 m), at 173 MHz the free-space wavelength (1.7 m) is less than the largest flight deck dimension.

3. External EME

In this section, details are provided about the three ground-based sources used to illuminate the NASA 757 during the flight experiment. These details, together with the aircraft location information provided in Section 2, are used to calculate the magnitude of the field external to the aircraft. Calculated external field values are compared with both field measurements and data collected by the flight experiment for corroboration.

In addition to the magnitude of the external illumination, the direction of the arriving illumination, as seen by an observer on the aircraft, must also be determined in order to simulate the experiment computationally. Calculations which determine this from the attitude of the aircraft are therefore provided here as well.

3.1. 26 MHz Source

3.1.1. Description of Antenna

The RF source used to illuminate the aircraft for flight tests conducted at 26 MHz was a large horizontal rhombic antenna located near the southeast corner of a Voice of America (VOA) transmitter site near Greenville, North Carolina. Figure 3.1 illustrates the 2800 acre installation, which includes eleven 500 kW transmitters and 26 antennas. The site is used by the VOA for international short-wave broadcasting. The antenna used for the flight tests is labeled in the figure as BR-17.

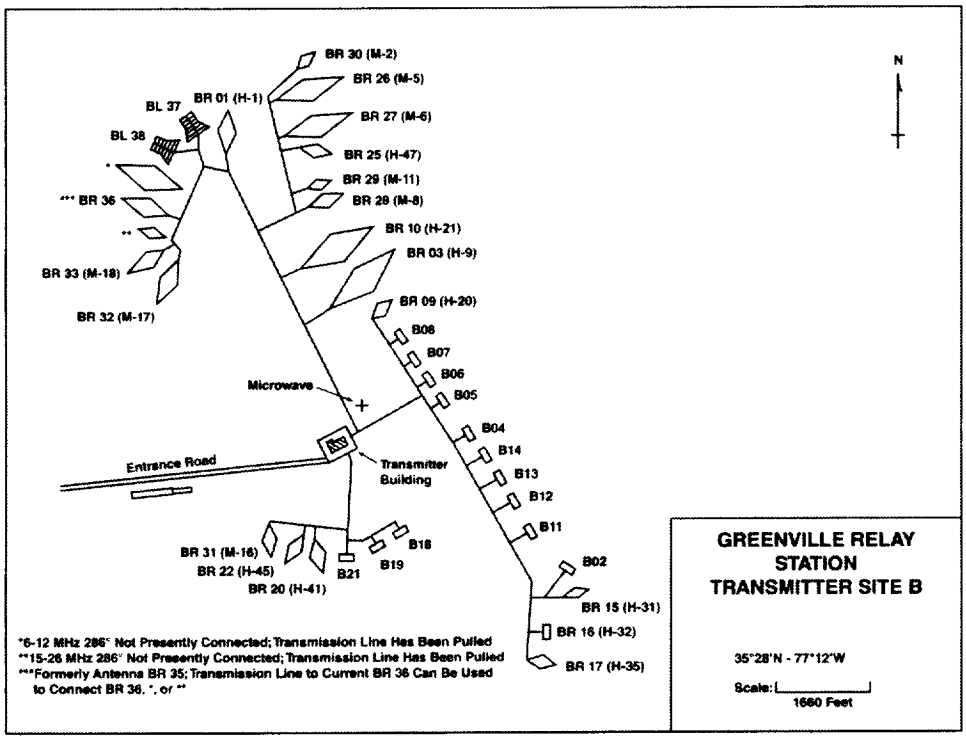

Figure 3.1. Site plan of the Voice of America (VOA) transmitter site at which the illuminating antenna used at 26 MHz was located.

A rhombic antenna [31] is composed of four equal-length wire "legs," each of which are several wavelengths long, oriented in a plane to form a rhombus (see Figure 3.2). The antenna is driven by opening one corner of the rhombus (at either end of the major axis) and applying transmitter power at this feed-point. A bi-directional radiation pattern will result from this configuration, with one large lobe, polarized in the plane of the rhombus, directed outward along each end of the major axis of the antenna. For uni-directional radiation, the antenna must be fed at the "rear" end of the rhombus, and the "front" end must be "terminated." This is accomplished by opening the junction of the two legs at the front of the rhombus and installing a resistive load or termination at this point. For maximum suppression of the "backward" lobe, the value of the termination resistor should be equal to the input impedance of the antenna (typically between 600 and 800 ohms). Note that this resistor will dissipate up to one-half of the power supplied by the transmitter. In the case of the VOA antenna, the resistor is a section of lossy open-wire transmission line that is designed to provide the proper load impedance while having adequate length to safely dissipate the power which otherwise would be radiated off the rear of the antenna.

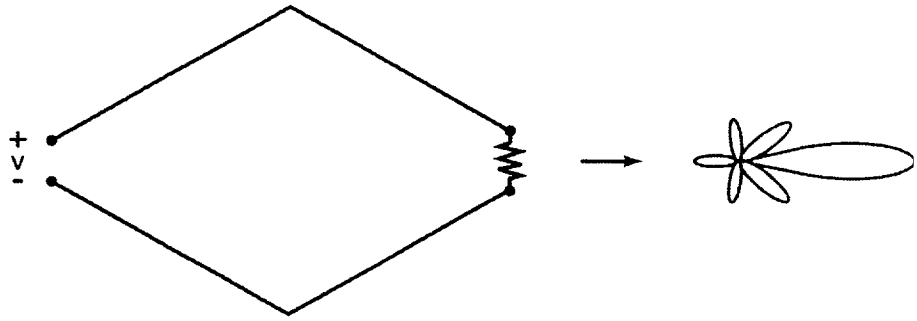

Figure 3.2. Rhombic antenna configuration.

The VOA antenna (see Figure 3.3) is suspended from four steel towers at an average height above the ground of 81 feet. Each tower is grounded at its base, and it is supported by a single set of three steel guy-wires. These guy-wines are one-piece wires, grounded at their lower ends, and there are no insulators at any point. To increase the bandwidth and power-handling capability of the antenna, each leg-wire is actually composed of three separate conductors which are spaced apart in the vertical plane. At the two "side" towers, the wire-to-wire spacing is just over six feet, but the spacing tapers to essentially zero at the feed-point and termination-resistor ends, where the three individual conductors are bonded to large metal plates. Each leg is 298 feet long, when measured along the ground, but the actual wire lengths are greater due to the "sag" in the catenary wire conductors, which amounts to almost 12.5 feet at the middle of each span. The wire conductors are #5 AWG copperweld. At 26 MHz, the skin depth is small enough that essentially all current flows in the copper portion of the wires.

Performance data for the antenna were supplied by the VOA, and this information, which presumably came from the manufacturer, is shown in Table 3.1. This antenna is normally operated over the frequency range from 11 to 26 MHz. Larger rhombics are available on-site for use at lower frequencies.

For the flight experiment, the antenna was driven by a 500 ± 25 kW continuous wave (CW) transmitter operating at a frequency of 25.85 MHz. The power at the antenna terminals is somewhat less than this due to losses in the 300-ohm transmission line. This line is composed of two parallel conductors made from small-diameter copper tubing suspended from copper messenger wires. The distance between transmitter and antenna is more than a mile, but the loss in the air-dielectric "open-wire" line was said to be on the order of 0.3 dB (no measurement was made to confirm this figure).

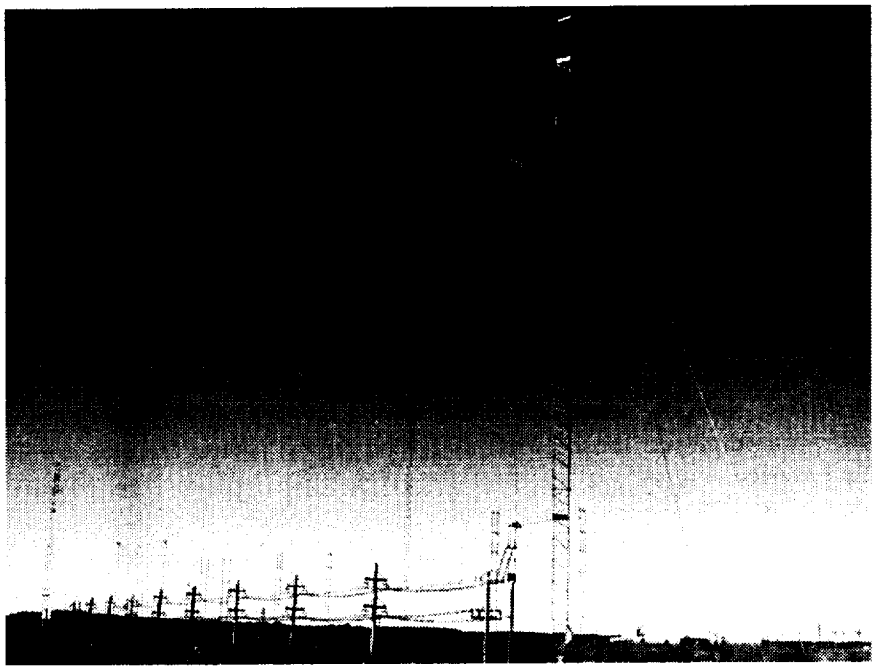

Figure 3.3. View of the VOA BR-17 antenna from the front or terminated end. Only three of the four support towers are visible in this photograph.

Table 3.1. Performance Specifications for the VOA BR-17 Antenna

Frequency (MHz)	Gain (dBi)	Takeoff Angle (degrees)	Horizontal Beamwidth (degrees)
6.1	10	33	38
7.2	12	29	34
9.6	14	22	28
11.8	16	18	25
15.3	18	13	21
17.8	19	11	19
21.6	21	9	16
26.0	23	7	14

3.1.2. Antenna Analysis

Horizontal rhombic antennas have been used since the 1920's for transmission and reception of HF (3–30 MHz) waves via the ionosphere. The far-field radiation characteristics of these types of antennas are well understood [31]. The use of a rhombic antenna to illuminate an aircraft in order to measure the penetration of electromagnetic waves into that aircraft is novel however. In order to make this measurement, the field strength impinging upon the aircraft must first be calculated. This calculation is complicated by the fact that the aircraft was not in the main beam of the antenna for much of the experiment, nor was it in the antenna's far field. Fortunately, numerical simulation techniques are available which permit one to accurately determine the near-field radiation characteristics of wire antennas at arbitrary observation points.

A numerical technique which is particularly well suited to the analysis of HF and VHF wire antennas is solution of the electric field integral equation by the method of moments [32]. This technique was

pioneered in the mid 1960's by Richmond [33], Harrington [34], and others. In this technique, wires and plates are broken down into straight segments and flat patches, each of which are small compared to wavelength (so that an assumption of a constant value of current across the segment/patch is valid). Once the geometry of the structure has been defined, a source is imposed and the technique determines the current on each segment/patch. The electric field at any point in space can then be determined from the sum of the contribution from all segments and patches.

The Numerical Electromagnetics Code (NEC) is a widely used computer program which incorporates the method of moments technique. NEC was developed and is maintained by the Lawrence Livermore National Laboratory in Livermore, California. The code has its origins in programs developed in the early 1970's by Burke, Miller, and Poggio. (See [35].) The 4/26/96 version of NEC 4.1 was used for the work described here. NEC 4, which was first released in 1993, includes catenary wire and buried wire features which were employed for the work described below. These features are not available in earlier versions of the program.

An NEC input file which describes the geometry of the VOA antenna was constructed during a research effort performed at the NASA Langley Research Center in 1995. (This effort was performed by Dr. Al Christman of Grove City College in Grove City, PA, during a Summer Faculty Fellowship at NASA Langley sponsored by the American Society for Engineering Education (ASEE).) The geometry described by this input file includes a description of the four support towers, supporting guy wires for each tower, ground rods for towers and guy wires, the catenary leg-wires, support wires for each leg, and portions of a large curtain antenna located just north of the rhombic (BR-16 in Figure 3.1). Nearly 3,200 wire segments were used to describe these features. A portion of the NEC wire model is illustrated in Figure 3.4.

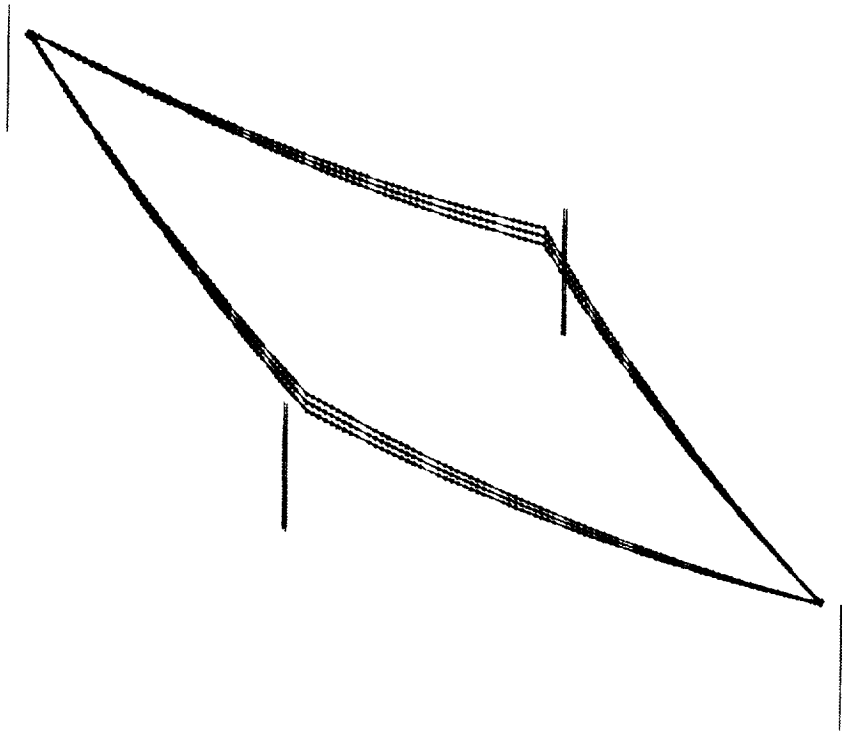

Figure 3.4. NEC simulation of VOA antenna geometry. Currents are illustrated with short arrows. Guy wires, support wires, and ground rods are not shown.

Material parameters for the metals used to construct the antenna are easily obtained. NEC, however, also requires knowledge of the material parameters of the ground. Personnel from SRI International of Arlington, VA, had previously conducted tests at the VOA site in order to determine both the conductivity and dielectric constant of the soil at the site. Although these parameters may vary independently from place to place across the 2800-acre site, only a single value was reported for each of these two parameters. Furthermore, the reported values are for surface soil. The water table is very close to the surface at the VOA site and material parameters could therefore differ substantially only a few feet from the surface. Also, the flight tests were conducted during a period in which the site was heavily saturated with rainwater.

In order to determine the sensitivity of the NEC model to variations from the SRI-reported ground constants, two additional models were constructed in which alternative sets of ground constants were used. These models were then used to calculate the field strength at a collection of common observation points. Both a "high conductivity" soil model, in which the SRI values were doubled, and a "low conductivity" soil model, in which the SRI values were halved, were considered. It was observed that the field strengths predicted by NEC change by less than 10% for either the high or low conductivity case. It was therefore concluded that inaccuracies in the determination of the actual soil conductivity and permittivity do not have a significant impact on the NEC simulation of the VOA antenna.

3.1.3. Predicted Antenna Performance

Figure 3.5 illustrates the far-field radiation patterns calculated by NEC for the VOA antenna when operated at 25.85 MHz. NEC calculates that the antenna gain is 22.78 dBi, which compares favorably with the VOA specification of 23 dBi at 26 MHz. NEC calculates the horizontal beamwidth and takeoff angle of the main beam as 16° and 7°, respectively, which also agree with VOA specifications.

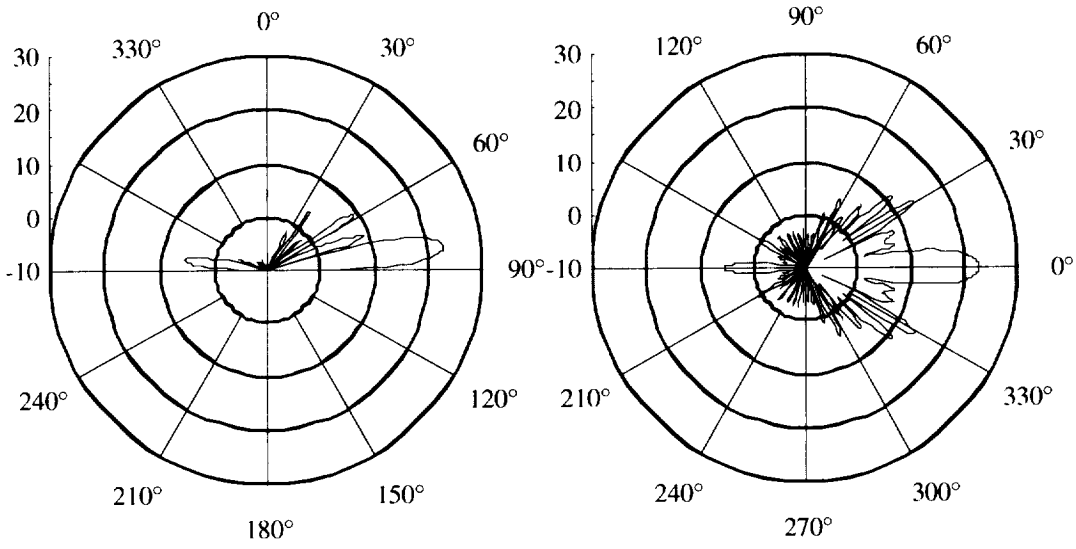

(a) Elevation pattern
(antenna gain vs. θ where ϕ = 0°, 180°)

(b) Azimuthal pattern
(antenna gain vs. ϕ where θ = 83°)

Figure 3.5. NEC predicted far-field illumination patterns for the VOA antenna (antenna gain in dBi).

Although no measurement of the field impinging upon the external surface of the aircraft was made, it seems reasonable to anticipate that the internal sensors will show a response that is proportional to the magnitude of the external field, especially if the direction of the arriving radiation does not change much, which is the case over large portions of the inbound and outbound measurements. Figure 3.6 compares the external field predicted by NEC to the internal field measured by the Cabin Long Wire (CLW) sensor for one of the inbound data runs. As expected, the response measured by the internal sensor as the aircraft approaches the VOA antenna is proportional to the NEC-predicted external field strength, lending confidence to the antenna pattern predicted by NEC.

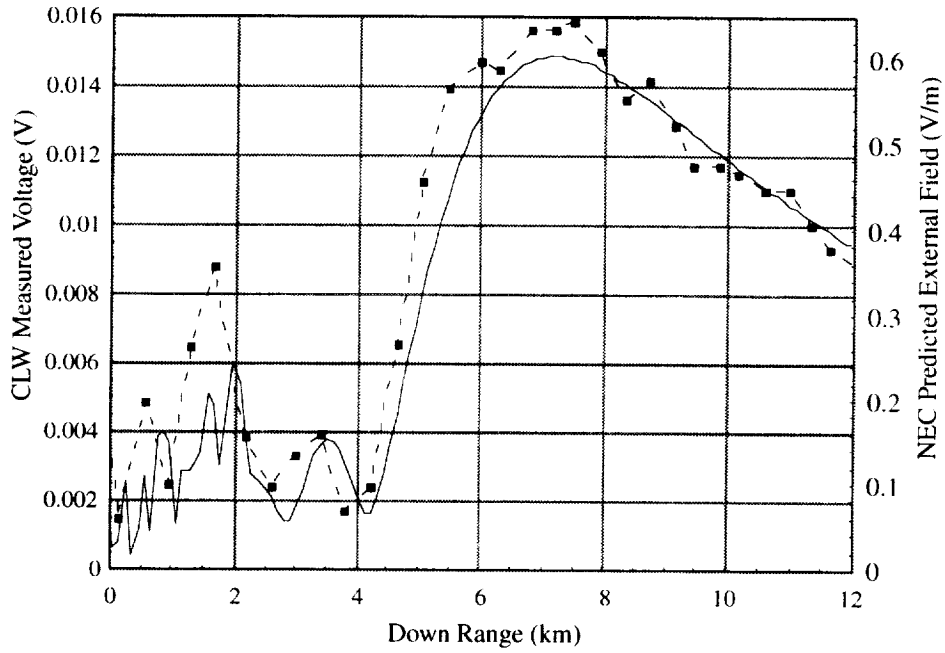

Figure 3.6. NEC predicted external field strength (solid line) vs. measured CLW response (dashed line).

Calculations of the magnitude of the external field strength impinging upon the aircraft for all data runs of the flight experiment in which the VOA antenna was employed may be found in Appendix B. These data may also be accessed from the previously mentioned web page, located at `aspo.larc.nasa.gov/emec`.

3.1.4. Site Survey

Measurement of the power at the input terminals of the VOA antenna is made difficult and potentially dangerous by high transmitter power levels. In lieu of this, measurements of the near-ground electric field intensity resulting from the antenna were made at several locations along an unpaved road which borders the perimeter of the VOA property (see Figures 3.7 and 3.8). These measurements were performed by attaching a three-axis electric field probe to a 6.1 m (20 ft) length of PVC pipe, which was then raised into an upright position and guyed with ropes. At each test point, an attempt was made to orient the probe so that one of its three axes was exactly vertical, while a second axis remained parallel to the major axis of the rhombic. These adjustments were all made by "eye" however, without the use of any surveying instruments. Therefore, in the comparison that follows, the three separate measured field components are ignored and only their vector sum is considered.

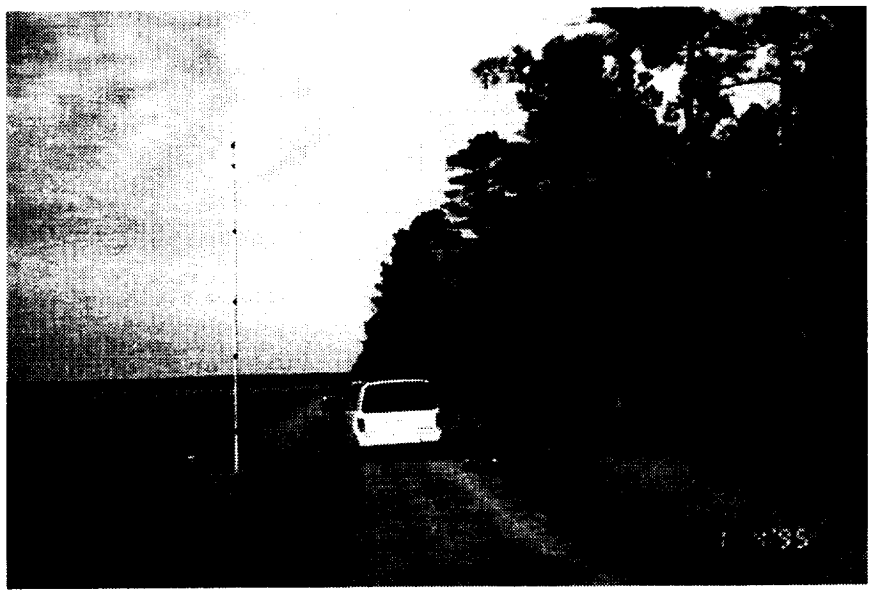

Figure 3.7. View of the location used to probe the near-ground electric field intensity of the VOA antenna.

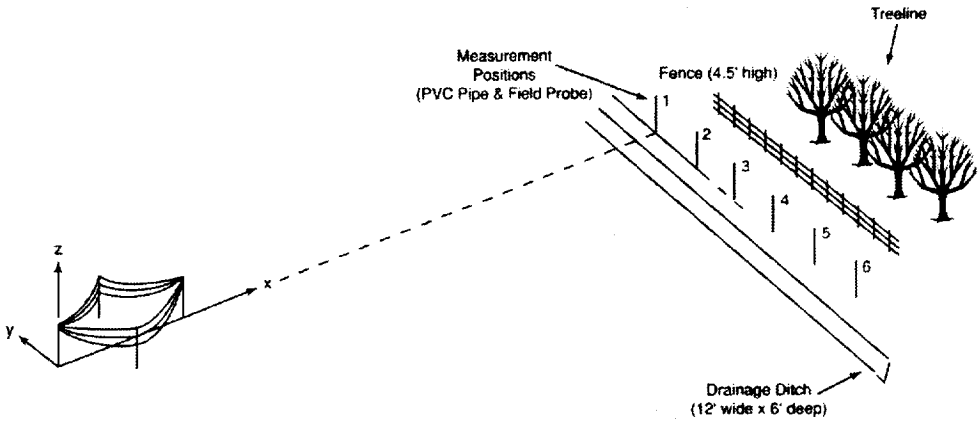

Figure 3.8. VOA near-ground electric field intensity measurement geometry.

A comparison of measured and NEC-predicted values of the electric field at the six measurement points is shown in Figure 3.9. Both measured and NEC-predicted values decrease steadily from the center of the antenna's main beam; the absolute magnitudes differ however. The relative difference is at a maximum at boresight (y = 0, which is measurement position number 1 in Figure 3.8), and becomes progressively smaller as one moves towards the outer test locations, where agreement is quite good.

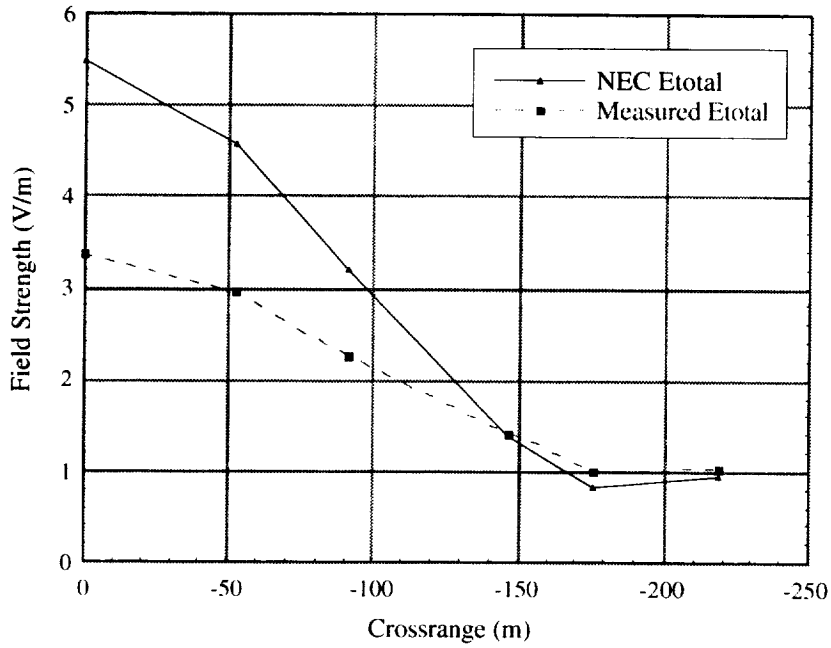

Figure 3.9. NEC predicted electric field intensity vs. measurement at the seven measurement positions shown in Figure 3.8. Crossrange denotes distance along the *y* axis. All measurements shown here were taken 6.1 m (20 ft) above the ground.

The terrain at the VOA site is flat, but is characterized by the presence of numerous drainage ditches, roughly 3.5 m wide and 2 m deep, which are partially filled with water. As Figure 3.8 shows, one of these ditches is parallel to the road along which measurements were made. Each of the measurement locations were displaced laterally from the ditch by only 1.5 m. Figure 3.8 also shows a fence, which marks the VOA property line. This fence delineates the boundary between the "antenna farm," which is grass-covered but essentially treeless, and the surrounding North Carolina countryside, which is heavily forested. The fenceline is parallel to, and roughly 7.5 m away from the points at which electric-field measurements were taken. Although the fenceline can be included in the NEC model of the measurements (doing so was found to produce only a minimal change in the NEC predictions), it is not possible to include terrain features, such as the ditch or the treeline in NEC. Terrain features can alter the propagation of waves impinging upon them. It is reasonable to expect that this effect should reach a maximum at boresight since the direction of propagation of the impinging radiation is perpendicular to the ditch in this case.

In addition to the measurements taken 6.1 m (20 ft) above the ground, the electric field was also measured 3.0 m (10 ft) and 4.6 m (15 ft) above the ground at the test location positioned at boresight (measurement position number 1 in Figure 3.8). Measured and NEC-predicted values at this location are shown in Figure 3.10. These measurements suggest another possible explanation for the discrepancy between prediction and measurement; the antenna and the measurement sites may not be at the same elevation, as was assumed during measurement. An elevation drop of less than 2.5 m from the antenna to the measurement site, located approximately 900 m away, would account for this discrepancy. In addition, the height of the rhombic above the ground, which was determined from construction blueprints, may not have been established with sufficient precision.

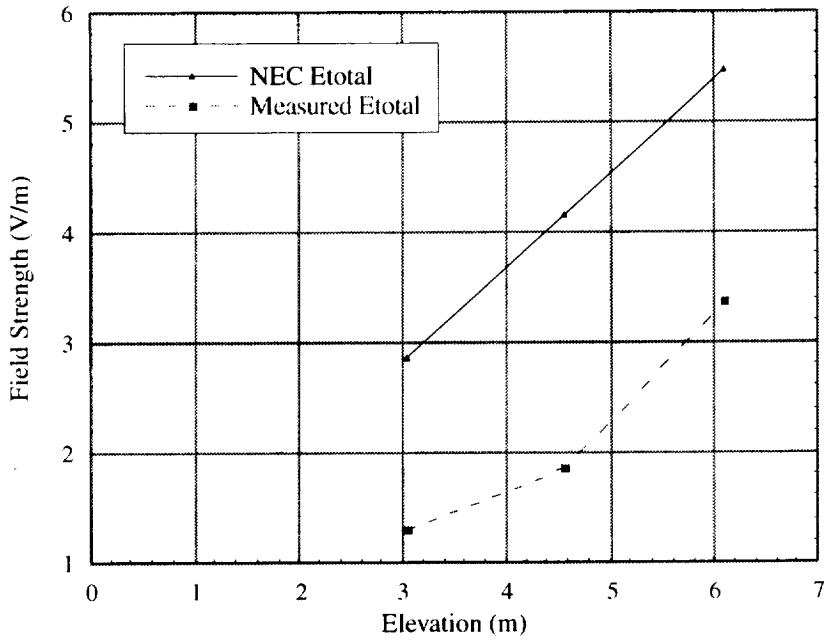

Figure 3.10. NEC predicted electric field intensity vs. measurement at measurement position number 1. Elevation denotes distance along z axis.

The uncertainty associated with calculations of the field external to the aircraft may not be inferred from discrepancies between near-ground calculations and measurement. Much of the discrepancy may be attributed to errors and uncertainty associated with the near-ground measurement. Also, terrain features are likely to have a larger impact on fields closer to the ground, due to the proportionally larger contribution to the total field from surface waves, which are strongly influenced by terrain features.

3.2. 173 MHz Source

3.2.1. Description of Antenna

The RF source used to illuminate the aircraft for flight tests conducted at 173 MHz was a portable log-periodic (LP) antenna driven by a portable 500 W continuous wave (CW) transmitter, both of which were provided by the U.S. Naval Surface Warfare Center–Dahlgren Division (see Figure 3.11). For the flight test, this equipment was located at the NASA Wallops Flight Facility on Wallops Island, Virginia, and operated at a frequency of 173.15 MHz. Data were collected with the antenna positioned in both the vertical and horizontal polarizations. In both cases, the antenna was fixed in position and did not track the aircraft. When fixed in the horizontal polarization, the takeoff angle was set to 50° above the horizon; in the vertical polarization, the takeoff angle was set to 30° above the horizon. These takeoff angles were chosen based on the antenna manufacturer's beamwidth specifications for this antenna, 105° in the H-plane and 60° in the E-plane.

The antenna was manufactured by Amplifier Research Company of Souderton, PA, and is their model AT-1080. It is a 19-element log-periodic dipole array with a 157 cm boom length; the longest element is about 23 cm (see Figure 3.12). The antenna is of aluminum construction and consists of two parallel booms which are square in cross-section (1 inch on edge) and elements made of half-inch diameter tubing, threaded for insertion into the boom. Each boom functions as one conductor of the interelement

transmission line and each element is split in half; one element-half is attached to one boom and the other half-element is attached to the other boom. The free-space radiation pattern resulting from this configuration consists of a broad beam directed along the boom axis and polarized in the plane containing the elements. The manufacturer's specifications for the antenna are shown in Table 3.2.

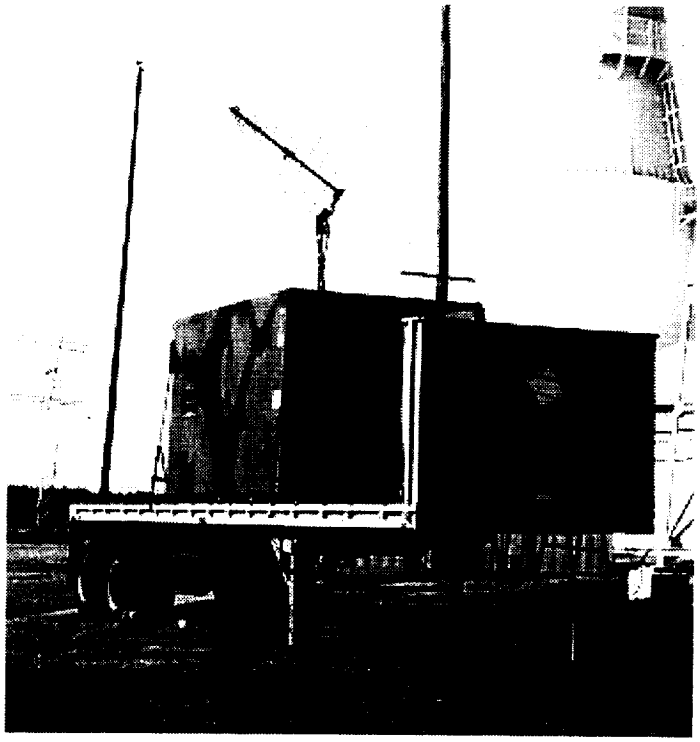

Figure 3.11. View of the log-periodic (LP) antenna positioned in the vertical polarization.

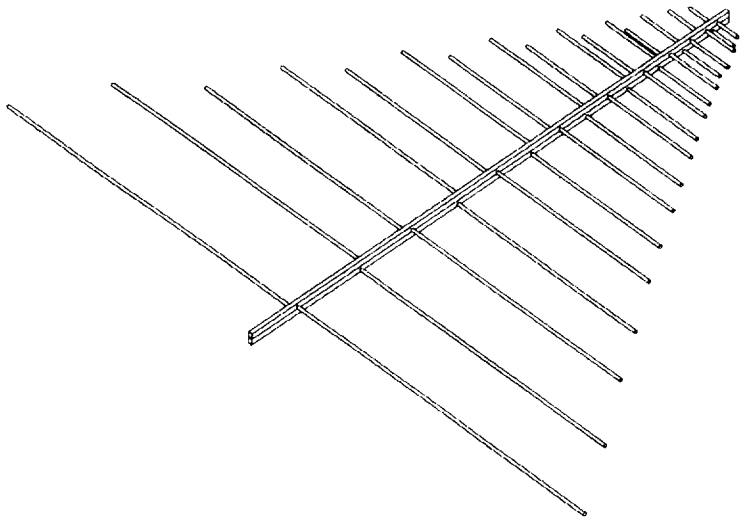

Figure 3.12. Detail of LP antenna construction.

Table 3.2. Performance Specifications for the LP Antenna

Parameter	Manufacturer's Spec.
Gain	7.5 ± 1.0 dBi
Impedance (Ohms)	50 nominal
VSWR	1.5 avg.
E-plane Beamwidth	60° avg.
H-plane Beamwidth	105° avg.

3.2.2. Antenna Analysis

Log periodic dipole arrays were introduced in 1960 and are popular for a variety of applications due to their extremely broad bandwidths (6:1 or more) [31]. Like rhombic antennas, they have been thoroughly studied, but the application here is novel and some analysis is required. NEC, which was used to analyze the VOA rhombic, is also applicable to the analysis of the LP antenna. Although simpler approaches are available which can accurately determine the far-field free-space radiation characteristics of LP antennas, a more advanced approach is required in order to determine the effect of environmental details, such as the metal building and ground beneath the antenna, on the antenna radiation. These environmental details are easily included in an NEC model of the antenna.

A simplified geometrical description of the antenna was used to create an NEC input file. This description consists of straight elements, rather than the actual staggered half-elements. The center wire segment describing each straight element is connected to a 50-ohm transmission line in which the phase is reversed between elements. Only 119 wire segments are needed to describe the antenna this way. The metal transmitter building, located directly beneath the antenna, is described using NEC's surface patch feature. NEC's smooth-surface ground plane feature was used to model the soil beneath the building. The material parameters of the soil (dielectric constant and conductivity) at the LP site were not measured, so assumed approximate values were used. As was the case for the VOA antenna model, variations in the material parameters used to describe the soil were not found to strongly influence NEC's results.

3.2.3. Predicted Antenna Performance

The far-field radiation patterns calculated by NEC for the antenna, when located in free-space (i.e., the building and ground plane are not included in the model) and operated at 173.15 MHz, are shown in Figure 3.13. In this figure, elevation patterns are shown for the two antenna orientations used in the flight experiment; horizontally polarized with a takeoff angle of 50°, and vertically polarized with a takeoff angle of 30°. NEC calculates that the antenna gain resulting from this model is 6.1 dBi, which is somewhat less than the manufacturer's specification of 7.5 ± 1.0 dBi. NEC calculates that the beam width is 132° in the H-plane and 68° in the E-plane, which is somewhat greater than the manufacturer's specifications of 105° and 60°. It is to be noted, however, that the manufacturer specifies only average values to be applied across the entire usable frequency spectrum of 80 to 1000 MHz. In light of this, the NEC-calculated values agree quite well with specifications.

NEC-calculated far-field radiation patterns for the LP antenna positioned above the metal transmitter building and ground surface are shown in Figure 3.14. As can be seen from the figure, the inclusion of the building and, more importantly, the ground in the antenna model results in a predicted antenna performance that deviates substantially, and non-intuitively, from the free-space performance. This deviation includes the intro-duction of additional lobes (scalloping) and, in the horizontally polarized

case, the lack of a clearly recognizable main beam. During the planning phase of the flight experiment, it was anticipated that the aircraft would encounter field levels from this antenna which change slowly with aircraft position. The NEC-calculated patterns show that instead of the anticipated illumination, the aircraft is exposed to external field levels which change very rapidly.

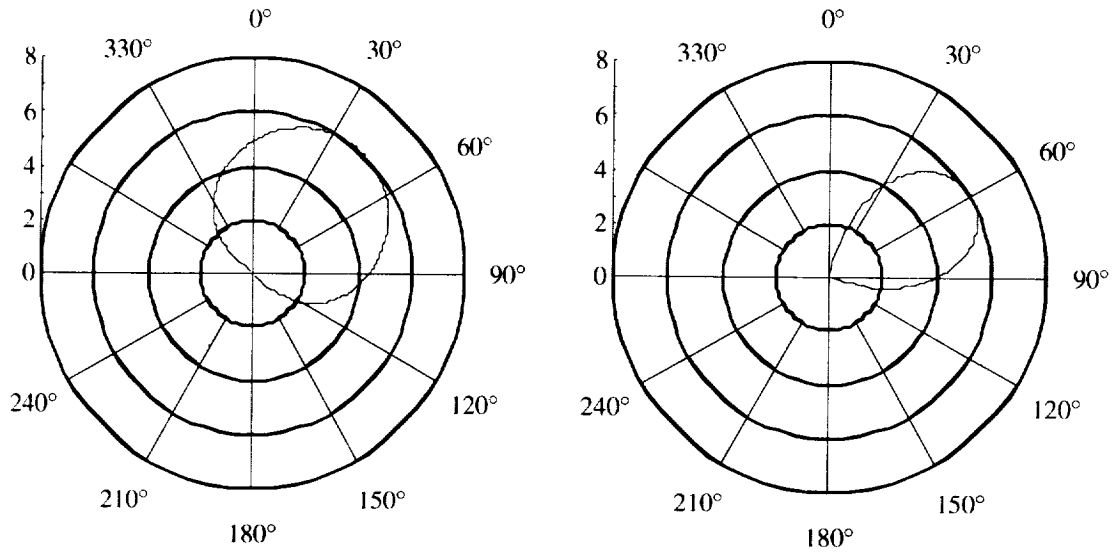

(a) Horizontal polarization.

(b) Vertical polarization.

Figure 3.13. NEC predicted elevation patterns (antenna gain vs. θ, where $\phi = 0°$, 180°) for the LP antenna in free space.

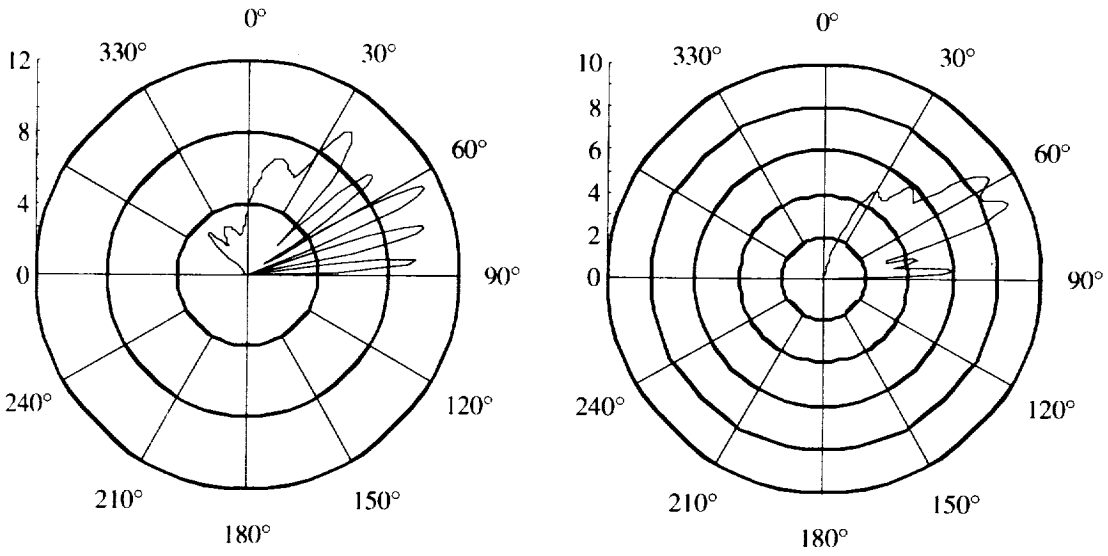

(a) Horizontal polarization.

(b) Vertical polarization.

Figure 3.14. NEC predicted elevation patterns (antenna gain vs. θ, where $\phi = 0°$, 180°) for the LP antenna positioned above building and ground.

As was the case for the flights made in the vicinity of the VOA antenna, the field patterns predicted by the NEC calculations can be confirmed by comparing them with the response of internal sensors during inbound and outbound measurements. Figure 3.15 compares the external field predicted by NEC to the internal field measured by the Cabin Long Wire (CLW) sensor for one of the inbound data runs, "clean" configuration against the horizontally polarized antenna. The relative magnitude of the NEC-predicted field strength compares quite well with the relative response recorded from the CLW sensor for this case. Similar results were found when comparing NEC predictions for the vertically polarized antenna to measured data collected from sensors with polarizations orthogonal to the CLW sensor.

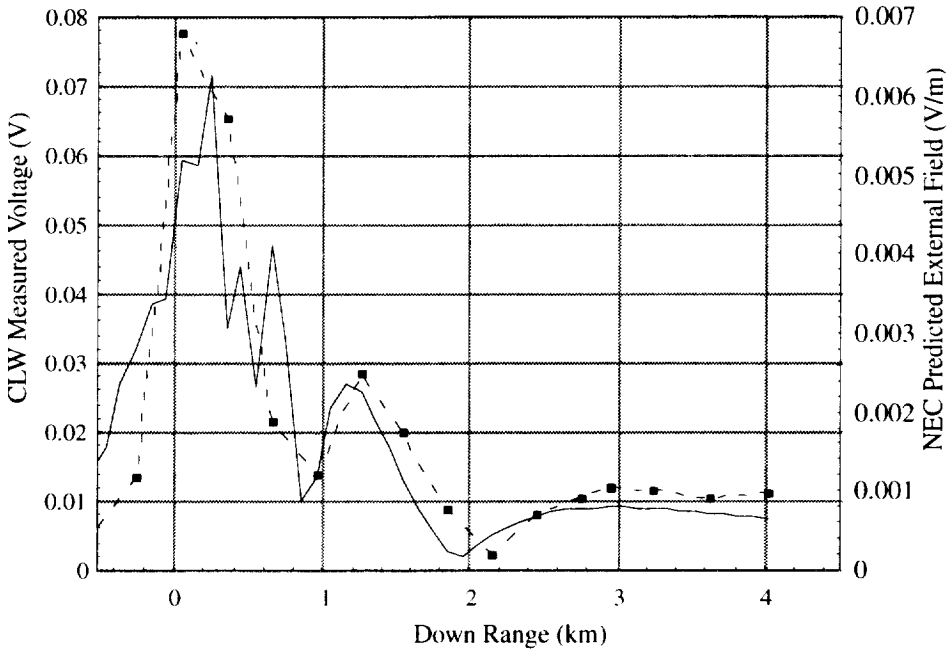

Figure 3.15. NEC predicted external field strength (solid line) vs. measured CLW response (dashed line).

NEC was used to calculate the magnitude of the external field impinging upon the aircraft for all data runs in which the LP antenna was used. The results of these calculations may be found in Appendix B.

3.2.4. Site Survey

Unlike the VOA antenna, the power input to the terminals of the LP antenna was measured with a high degree of confidence during the flight experiment. Nevertheless, the near-ground electric field intensity was measured in the vicinity of the LP antenna since the test equipment necessary to perform this measurement was readily available. A single field measurement was made for both of the antenna orientations. A three-axis probe was attached to a PVC pipe which was estimated to be 2 m long. The pipe was held in position approximately 41.5 m downrange from the antenna. As in the case of the VOA measurements, the probe was positioned without the use of any surveying instruments. The vector sum of the three separate field components recorded by this measurement is shown in Table 3.3 along with NEC-calculated values for the total field strength at this location (total ground wave, including the surface wave).

Table 3.3. NEC-Calculated vs. Measured Electric Field Intensity

Polarization	Measured Field	NEC-calculated Field
Horizontal	4.2 V/m	5.7 V/m
Vertical	2.3 V/m	3.7 V/m

As Table 3.3 shows, NEC predicts field strengths that are somewhat greater than that measured. A study was therefore undertaken to determine the sensitivity of the NEC predictions to a number of modeling parameters. A relatively small change in the antenna takeoff angle (less than 10°) was found to bring the model in agreement with the measurement. The antenna was positioned (both compass heading and takeoff angle) without the aid of surveying instruments and the associated error is estimated to be no better than ±3°. Minor changes to the description of the metal transmitter building beneath the antenna were found to strongly influence the calculation. Measurements of the antenna's position with respect to the metal building and the building's orientation with respect to the antenna were not made, and were estimated from photographs for modeling purposes. As was mentioned earlier, the conductivity and dielectric constant used to describe the ground beneath the antenna was not found to strongly influence results. Effects due to the roughness of the physical ground surface, which cannot be included in the NEC calculation, are believed to have some effect however. In light of these deficiencies, the NEC predictions of field strength would appear to agree quite well with measurement.

The approximate 3 dB discrepancy between near-ground calculations and measurement does not necessarily mean that the uncertainty associated with calculations of the field external to the aircraft is this large. While the variations in modeling parameters discussed above result in large changes in the calculated field values near the ground, they do not result in substantial changes in the calculated field values at selected points along the aircraft's flight path, especially for downrange distances greater than 1 km.

3.3. 430 MHz Source

3.3.1. Description of Antenna

The RF source used to illuminate the aircraft for flight tests conducted at 430 MHz was the Atmospheric Sciences Research Facility (ASRF) UHF radar located at the NASA Wallops Flight Facility on Wallops Island, Virginia (see Figure 3.16). The ASRF UHF radar is a ranging and tracking radar system that tracked the aircraft while data were being collected. The antenna for this system is an 18.3 m (60 ft) parabolic reflector. Radiation from this antenna was fixed in the vertical polarization. Beamwidth and gain specifications for this antenna, which are based on measurement, were provided by NASA Wallops [36] and are discussed below.

This antenna was driven by a pulsed 58 kW (peak) transmitter. A 2 microsecond pulse width modulation at a pulse repetition rate of 640 pulses per second was used. The pulse width was sufficiently long to include hundreds of cycles of the 430 MHz signal. Post-flight data reduction revealed that the responses of the EME sensors reached steady-state levels well before the end of the pulse (see Figure 3.17). Sensor responses reported here are these steady-state levels.

The reader is cautioned that while Figure 3.17 is illustrative of sensor responses to the 430 MHz illumination, time domain information was not used to obtain the data reported here. Steady-state sensor responses at this frequency were instead determined by averaging together peak responses recorded by the zero span spectrum analyzer. Each reported data point in the 430 MHz flight profiles is the average of the

peak pulse response recorded during a 2-second data-collection window and therefore represents the average of approximately 1280 consecutive pulses.

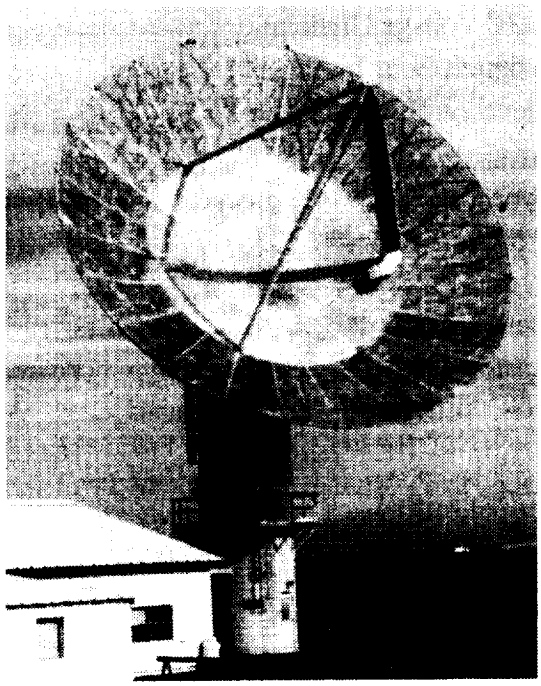

Figure 3.16. ASRF UHF radar.

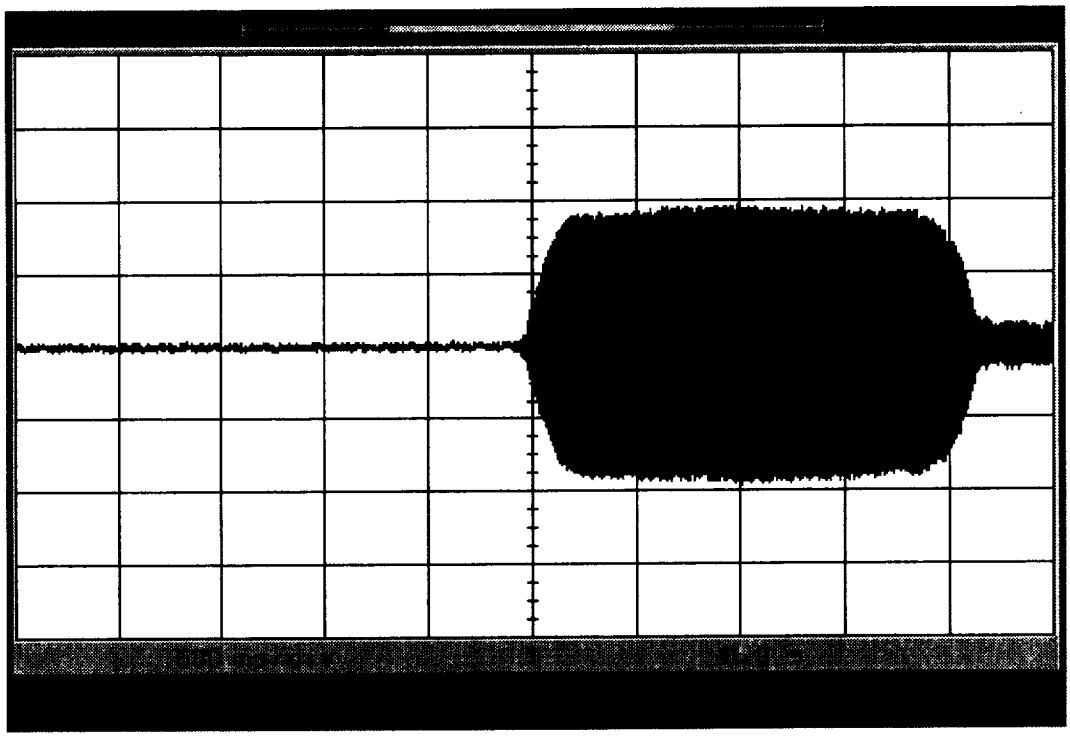

Figure 3.17. Time-domain response of the Flight Deck D-Dot sensor to illumination from the ASRF UHF radar (typical).

3.3.2. Antenna Analysis

The parabolic reflector antenna was first developed in the 1930's for radio astronomy. The technology was further developed in the 1940's for wartime radar applications, and then again in the 1960's for communications applications. In this type of antenna, a feed antenna is placed at the focal point of a parabolic reflector. Classical optics predicts that all rays from the feed travel the same physical distance to the aperture plane, which is the projected area of the reflector onto a plane normal to the optical axis, and produce a beam of parallel rays. This simple picture is modified by diffraction, due to the limited aperture of the optical system, which produces a circularly symmetric pattern consisting of a single major lobe and a characteristic sidelobe structure. The picture is additionally modified by details of the radiation from the feed antenna, blockage due to the feed, scattering from the struts supporting the feed, and other details.

The analysis of the composite result of these effects is typically performed using a computer program. One widely used program is the OSU Reflector Antenna Code (NECREF) [37], developed and maintained by Ohio State University for the U.S. Naval Procurement Office. NECREF uses aperture integration to compute the main beam and near sidelobes, and the Geometrical Theory of Diffraction to compute wide-angle sidelobes and backlobes [38]. Feed blockage is simulated using physical optics [39] and feed strut scattering is calculated by integrating the equivalent current (as determined by the method of moments) along the strut.

3.3.3. Predicted Antenna Performance

The free-space, far-field antenna pattern calculated by NECREF for the ASRF UHF radar antenna is shown in Figure 3.18. NECREF calculates that the antenna gain is 36.7 dBi, which compares favorably with the NASA Wallops specification of 36 dBi. NECREF also calculates that the half-power beamwidth of the main beam is 2.58° in the H-plane and 2.34° in the E-plane, which is slightly less than the Wallops specification of 2.9° in both the E and H planes.

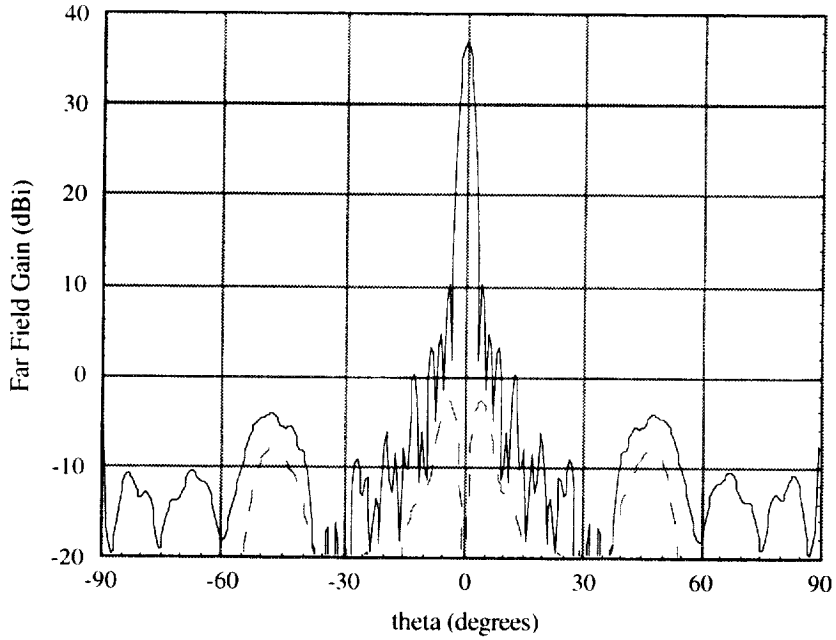

Figure 3.18. Elevation pattern predicted by NECREF for the ASRF UHF radar antenna.

Since the antenna tracked the aircraft while data were collected, only the antenna behavior at boresight is needed in order to determine the magnitude of the external field impinging upon the aircraft. (Wallops personnel stated that the pointing accuracy of the ASRF UHF radar system is less than 0.1°. The reduction in antenna gain corresponding to a pointing error of this magnitude is approximately 0.02 dBi.) This determination can be made by first calculating the power density of the field illuminating the aircraft,

$$W = \frac{P_{ant}\, G_{ant}}{4\,\pi\, R^2} \tag{3.1}$$

where P_{ant} is the power at the antenna input terminals, G_{ant} is the gain at boresight, and R is the distance (or slant range) from the aircraft to the antenna. The magnitude of the electric field, E, can then be found from

$$W = \frac{E^2}{\eta_0} \tag{3.2}$$

where η_0 is the free space wave impedance (377 ohms).

The boresight gain predicted by NECREF is that of an antenna located in free space and does not include ground effects. This is of some concern because the ASRF antenna was slewed to very low elevation angles for this experiment. Elevation angles range from approximately 1.7° to 3.8° above the horizon for the data presented in Appendix A. The ground occupies a portion of the main beam of the free space pattern at the low end of this range. A study was therefore undertaken to determine the effects of the ground on the boresight gain of the ASRF antenna.

The NECREF program does not provide for a means to include a model of the ground with the antenna model. An attempt was therefore made to determine the antenna-over-ground response by adding the antenna's boresight response with the response of the antenna's image below a real-earth ground [40]. Comparison of the results of this attempt with the flight data suggests that this approach may be somewhat inaccurate, however. This may be due to the fact that it does not account for changes in the aperture distribution of the reflector in the presence of the ground (which is in the near-field of the antenna).

NECREF does provide for the inclusion of flat metal plates in the vicinity of the reflector. Antenna models were therefore constructed which use a large flat metal plate as a substitute for the ground. These models can be used to determine the upper-bound on ground effects; the actual effect of the ground should be somewhat less since these models do not account for the finite conductivity of the ground. A large number of models must be used since the geometric relationship between antenna and ground changes with elevation angle. The antenna gain at boresight predicted by these models is shown in Figure 3.19. As can be seen from the figure, these models suggest that the effect of the ground over the range of elevation angles encountered in this experiment is a deviation from the free space gain which is less than 1.3 dBi.

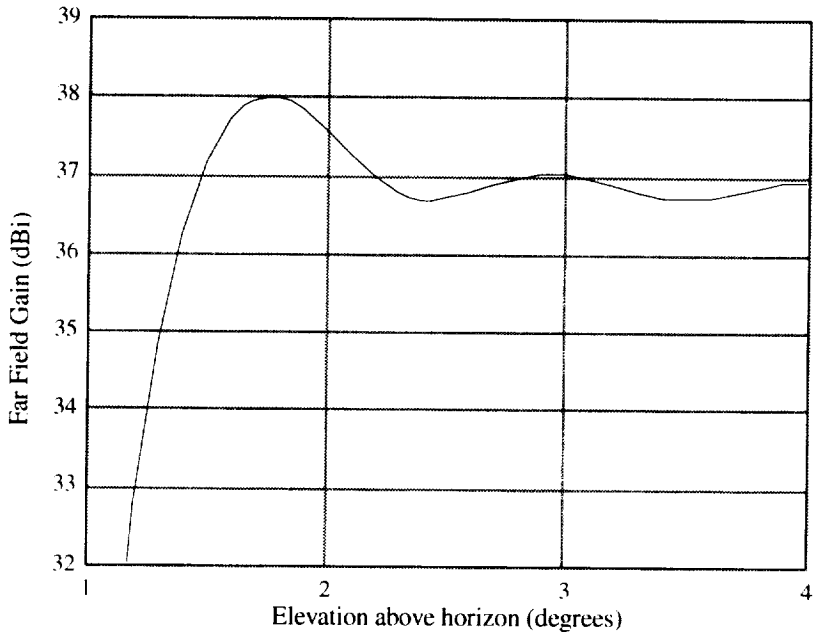

Figure 3.19. Antenna gain at low elevation angles; ground plane effects simulated by including a large PEC plate in the antenna model.

The external field levels predicted by equation 3.2 and the antenna gain values in Figure 3.19 for the 430 MHz data runs may be found in Appendix B. The flight paths flown against the ASRF antenna make it difficult to make a meaningful comparison of the predicted antenna gain pattern with measurement, as was done in Sections 3.1.3 and 3.2.3. The range of elevation angles of the ASRF antenna during the inbound and outbound portions of the 430 MHz flight paths is approximately 1.7° to 2.2°, too small to see the predicted gain fluctuations shown in Figure 3.19 in the measured data. The elevation angle for the crossbound portions of these flights ranges from approximately 3.0° to 3.6°. The relatively small change in predicted antenna gain over this range suggests that the fluctuations in the measured data at this frequency (see Appendix A) are not due to ground effects.

3.4. Incidence Angles

In order to simulate the flight experiment computationally, it is necessary to know not only the magnitude of the field external to the aircraft, but also the orientation of the field (polarization angle) and the direction from which the field originates, as seen by an observer on the aircraft. This information may be determined from the location of the source antenna in a coordinate system fixed to the aircraft. For this effort, an aircraft coordinate system was selected in which the x, y, and z axes are aligned with the roll, pitch, and yaw axes of the aircraft (see Figure 3.20).

The aircraft, and therefore the coordinate system affixed to it, is a dynamic system whose attitude changes due to pilot inputs and wind gusts. Attitudinal information about the aircraft was collected by the flight experiment from the aircraft's flight instruments and includes the compass heading of the aircraft's ground track, as well as the rotation of the body axes relative to a coordinate system aligned with the ground track (roll, pitch, and yaw angles). Typical body axis rotations recorded during data runs are ±1° of roll, 0° to 5° of pitch, and ±1.5° of yaw.

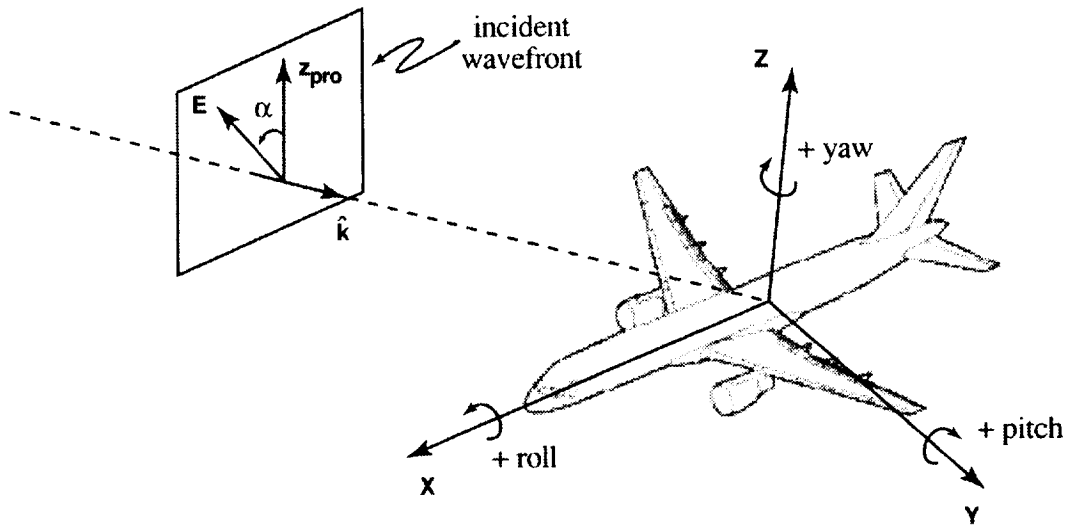

Figure 3.20. Aircraft coordinate system. The incident wavefront is defined by the vector $\hat{\mathbf{k}}$ and the angle α.

In order to find a vector which describes the location of the antenna in the aircraft coordinate system, a transformation procedure was employed which is similar to that described in Section 2:

1. Create a "primed" coordinate system which is congruent with the antenna coordinate system.

2. Rotate this primed system counterclockwise about its z-axis by an amount equal to the difference between the compass heading of the aircraft's ground track and the main beam compass heading described in Section 2.

3. Translate the primed system by an amount defined by the negative of the aircraft's position vector in the antenna's coordinate system.

This procedure can be written

$$\mathbf{pantl}_{g.t.} = \mathbf{B}\,(-\mathbf{pairl}_{ant}) \tag{3.3}$$

where $\mathbf{pantl}_{g.t.}$ is the position vector describing the antenna location in a coordinate system aligned with the aircraft's ground track, $\mathbf{pairl}_{ant}$ is the aircraft location in the antenna's coordinate system (see equation 2.7), and **B** is a rotation matrix which is defined by the z-axis rotation in step 2. Let α_3 describe that rotation; then

$$\mathbf{B} = \begin{bmatrix} \cos(\alpha_3) & \sin(\alpha_3) & 0 \\ -\sin(\alpha_3) & \cos(\alpha_3) & 0 \\ 0 & 0 & 1 \end{bmatrix} \tag{3.4}$$

In order to locate the antenna in the coordinate system affixed to the aircraft's body axes, roll, pitch, and yaw rotations must be applied to the $\mathbf{pantl}_{\mathbf{g.t.}}$ position vector. This operation can be described by

$$\mathbf{pantl}_{\mathbf{air}} = \mathbf{C}\,(\mathbf{pantl}_{\mathbf{g.t.}}) \tag{3.5}$$

where

$$\mathbf{C} = \begin{bmatrix} \cos(-\alpha_y) & \sin(-\alpha_y) & 0 \\ -\sin(-\alpha_y) & \cos(-\alpha_y) & 0 \\ 0 & 0 & 1 \end{bmatrix} \begin{bmatrix} \cos(-\beta_p) & 0 & -\sin(-\beta_p) \\ 0 & 1 & 0 \\ \sin(-\beta_p) & 0 & \cos(-\beta_p) \end{bmatrix} \begin{bmatrix} 1 & 0 & 0 \\ 0 & \cos(\gamma_r) & \sin(\gamma_r) \\ 0 & -\sin(\gamma_r) & \cos(\gamma_r) \end{bmatrix} \tag{3.6}$$

or

$$\mathbf{C} = \begin{bmatrix} \cos(-\alpha_y)\cos(-\beta_p) & -\cos(-\alpha_y)\sin(-\beta_p)\sin(\gamma_r)+\sin(-\alpha_y)\cos(\gamma_r) & \cos(-\alpha_y)\sin(-\beta_p)\cos(\gamma_r)+\sin(-\beta_p)\sin(\gamma_r) \\ -\sin(-\alpha_y)\cos(-\beta_p) & \sin(-\alpha_y)\sin(-\beta_p)\sin(\gamma_r)+\cos(-\alpha_y)\cos(\gamma_r) & -\sin(-\alpha_y)\sin(-\beta_p\cos(\gamma_r)+\cos(-\beta_p)\sin(\gamma_r) \\ \sin(-\beta_p) & \cos(-\beta)\sin(\gamma_r) & \cos(-\beta_p)\cos(\gamma_r) \end{bmatrix} \tag{3.7}$$

where γ_r, β_p, and α_y are the roll, pitch, and yaw angles recorded from the aircraft's flight instruments. The angles $-\beta_p$ and $-\alpha_y$ are used in this expression because roll, pitch, and yaw are defined for the flight instruments about a coordinate system which has a downward directed z-axis, rather than the upward directed z-axis shown in Figure 3.21.

The vector $\mathbf{pantl}_{\mathbf{air}}$ can be used to define the direction of the arriving radiation as seen by an observer on the aircraft. For data reporting purposes, this has been performed using the (θ, ϕ) components of the spherical coordinates of this vector. The angle θ is referenced from the aircraft's z-axis and is defined from 0° to 180°, while ϕ is referenced from the aircraft's x-axis and is defined, for reporting purposes, from −180° to +180°. This definition results in positive and negative values of ϕ indicating radiation arriving from the left and right sides of the aircraft, respectively.

The vector $\mathbf{pantl}_{\mathbf{air}}$ can also be used to define the polarization of the incident field. As is illustrated in Figure 3.21, polarization is defined by α, the angle between the electric field and the projection of the aircraft's z-axis onto the plane which is orthogonal to the direction of propagation. The direction of propagation, $\hat{\mathbf{k}}$, can be defined as the unit vector of $\mathbf{pantl}_{\mathbf{air}}$. $\mathbf{z}_{\mathbf{pro}}$, a vector in the direction of the projection of the aircraft's z-axis onto the plane orthogonal to $\hat{\mathbf{k}}$, may be found from

$$\mathbf{z}_{\mathbf{pro}} = \hat{\mathbf{k}} \times \hat{\mathbf{z}} \times \hat{\mathbf{k}} \tag{3.8}$$

where $\hat{\mathbf{z}}$ is a unit vector in the direction of the aircraft's z-axis. The orientation of the electric field, $\mathbf{E}$, may be defined by the cross product of $\hat{\mathbf{k}}$, with either

1. a unit vector in the direction of the antenna's z-axis, as seen by an observer on the aircraft (for horizontally polarized antennas), or

2. a unit vector in the direction of the antenna's y-axis, as seen by an observer on the aircraft (for vertically polarized antennas).

That is, the direction of **E** is defined by the vector $\mathbf{a_E}$ where

$$\mathbf{a_E} = \hat{\mathbf{k}} \times \left(\mathbf{C}\,\mathbf{B} \begin{bmatrix} 0 \\ 0 \\ 1 \end{bmatrix} \right) \tag{3.9}$$

for horizontally polarized antennas, or

$$\mathbf{a_E} = \hat{\mathbf{k}} \times \left(\mathbf{C}\,\mathbf{B} \begin{bmatrix} 0 \\ 1 \\ 0 \end{bmatrix} \right) \tag{3.10}$$

for vertically polarized antennas. The orientation of the α, finally, may be found from the dot product of $\mathbf{a_E}$ with $\mathbf{z_{pro}}$:

$$\cos\alpha = \frac{\mathbf{a_E} \cdot \mathbf{z_{pro}}}{\|\mathbf{a_E}\| \, \|\mathbf{z_{pro}}\|} \tag{3.11}$$

The angles θ, ϕ, and α have been calculated for all aircraft locations in every data run performed by the flight experiment. Representative values may be found in Appendix B. A complete listing may be found on the aforementioned web page located at `aspo.larc.nasa.gov/emec`.

x4. Shielding Effectiveness

In this section, the internal EME data collected by the flight experiment (which were the subject of Section 2) and the external EME computations (which were computed using NEC or NECREF) are used to draw conclusions about the shielding effectiveness (SE) of the NASA 757. SE is commonly determined in electromagnetic inteference (EMI) problems in which the electronic system of concern is located within a metal enclosure with apertures. SE is defined as the ratio of the internal EME to the external EME and is an expression for the attenuation of fields due to the metal enclosure. As was discussed in Section 1.3, a HIRF environment has been proposed for certifying safety critical electronics in aircraft. This environment is the external EME to which the aircraft is exposed. The SE of the aircraft of interest must be applied to the HIRF environment in order to determine the field levels to which the safety critical electronics must be certified. The SE of aircraft is not well known, so the interior fields to which electronics inside are exposed is not well characterized [41].

In the figures that follow, SE is determined by dividing the measured internal EME (presented in Appendix A) by the computed external EME (presented in Appendix B). Note that the appendices are organized so that all of the internal EME data collected on each flight path are presented on a single page of Appendix A, while all of the relevant external EME computations for that flight path appear on a corresponding single page of Appendix B. Note that the results of the external EME computations are total field values; all three components of the computed electric field are summed. Since the only components present at far field distances from the antenna are those transverse to the direction of

propagation, summing the three computed components results in the magnitude of the incident plane wave. The internal EME measurements, by contrast, are samples of only one component of the electric field. This is because D-Dot sensor measurements are used to determine the internal EME (calibration information relating the sensor response to the magnitude of the electric field is not available for the other sensors used in the flight experiment). All three of the D-Dot sensors used in the flight experiment were oriented to be responsive to that component of the electric field which is aligned with the z-axis of the aircraft's coordinate system. The x- and y-axis components were not measured. The comparison of the external total field to one component of the internal field presented in this section reveals useful information about changes in aircraft response with position and configuration, but it may not give a complete or accurate description of SE.

4.1. Shielding Effectiveness at 26 MHz

Figure 4.1 illustrates the SE of the aircraft for the incidence and polarization angles encountered during the "inbound, clean" flight path flown against the VOA antenna. In this figure, the flight originates 12 km down range from the antenna. At this distance, the illumination is directed towards the nose of the aircraft, from a point slightly below the xy plane of the aircraft's coordinate system. As the flight progresses towards 0 km, the angle θ increases from near 100° to approximately 120° at 3 km, after which θ rapidly increases, indicating that the external field illuminates the underside of the aircraft for the remainder of the flight. As the figure shows, the SE provided by the airframe for this illumination is approximately 65 dB in the flight deck and electronics bay and 35 dB in the passenger cabin. Interestingly, the SE of the flight deck appears to be greater when the nose is illuminated than when underside is illuminated.

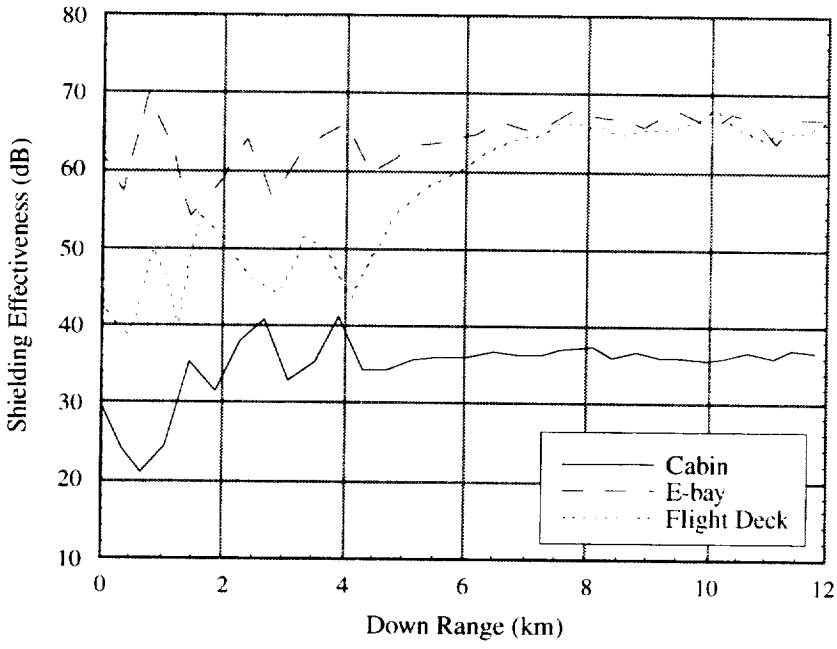

Figure 4.1. Shielding effectiveness for the illumination encountered during the "26 MHz, inbound, clean" flight path.

The SE plotted in the figure shows variations on the order of ±5 dB for down range values less than 4 km. This may be due to errors in the calculation of the sidelobe structure of the VOA antenna. As Figure B1 (in Appendix B) illustrates, the aircraft is in the main beam of the antenna only for down range values greater than 4 km. Calculations of the external illumination resulting from the sidelobe structure of the antenna are likely to be subject to much greater error than calculations of the illumination resulting from the main beam.

The SE resulting from the "outbound, clean" flight is illustrated in Figure 4.2. The illumination resulting from this flight is primarily directed towards the tail of the aircraft. This flight originates over the antenna, at 0 km down range, and progresses towards increasing down range distance, with the external fields illuminating first the underside of the aircraft and then the tail. Comparison with Figure 4.1 shows that SE is approximately 10 dB greater for tail-incident illumination than for nose-incident. Like Figure 4.1, Figure 4.2 suggests that the SE of the flight deck is somewhat lower when the illumination originates below the aircraft vis-à-vis illumination originating in the xy plane of the aircraft's coordinate system.

As was noted in Section 2.5, the field levels recorded during tail-incident illumination were somewhat higher when the flaps were deployed. The impact of this may be seen by comparing Figure 4.2 with the SE resulting from the "outbound, flaps" flight, illustrated in Figure 4.3. As can be seen from the figures, the SE of the passenger cabin and electronics bay drops by about 10 dB when the flaps are deployed.

The SE resulting from the "crossbound, clean" flight is illustrated in Figure 4.4. The illumination resulting from this flight is directed towards the right side of the aircraft. This flight originates at a cross range distance of approximately +2 km. The aircraft was within the main beam of the antenna only for cross range distances less than approximately ±1 km, which can be confirmed by examining Figure B7. The angle θ is approximately 100° throughout the flight, and ϕ spans approximately 20° as the aircraft

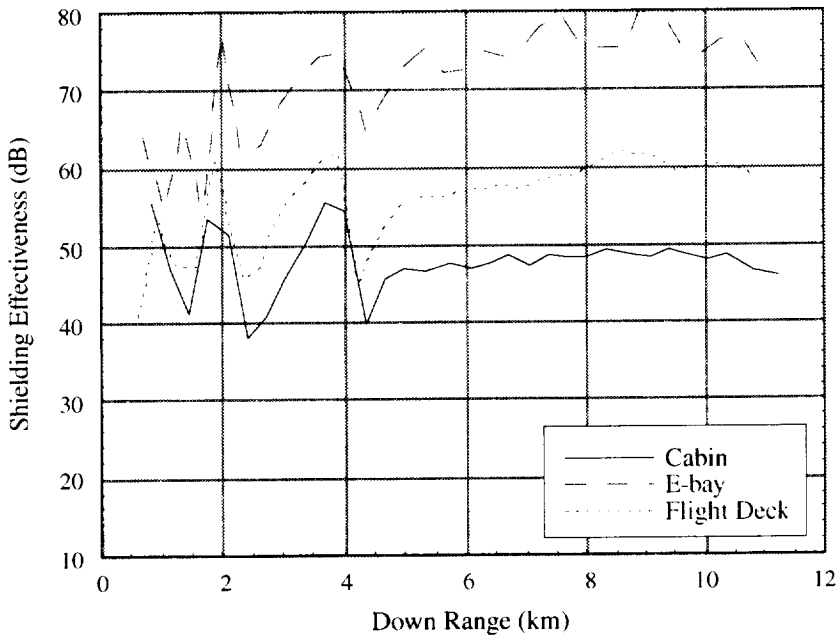

Figure 4.2. SE for the illumination encountered during the "26 MHz, outbound, clean" flight path.

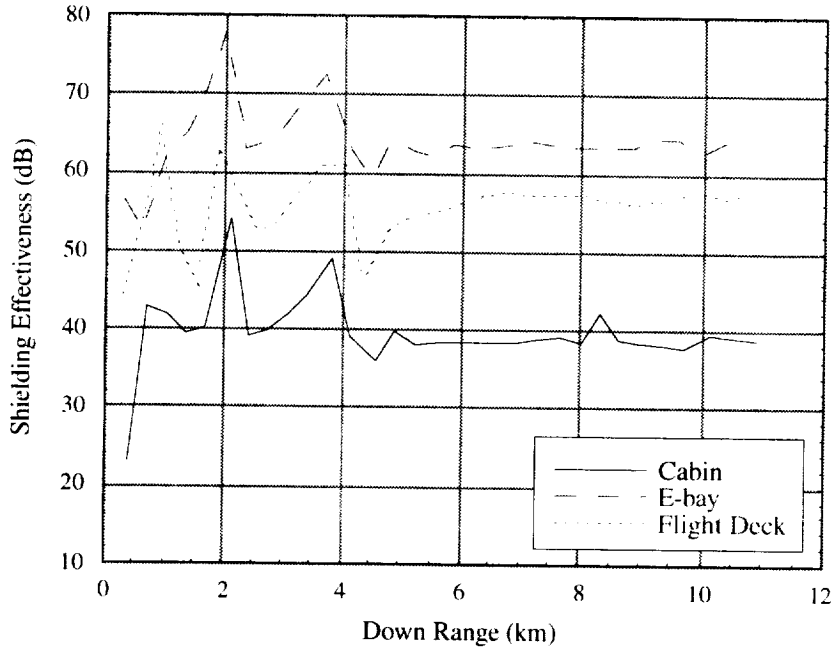

Figure 4.3. SE for the illumination encountered during the "26 MHz, outbound, flaps" flight path.

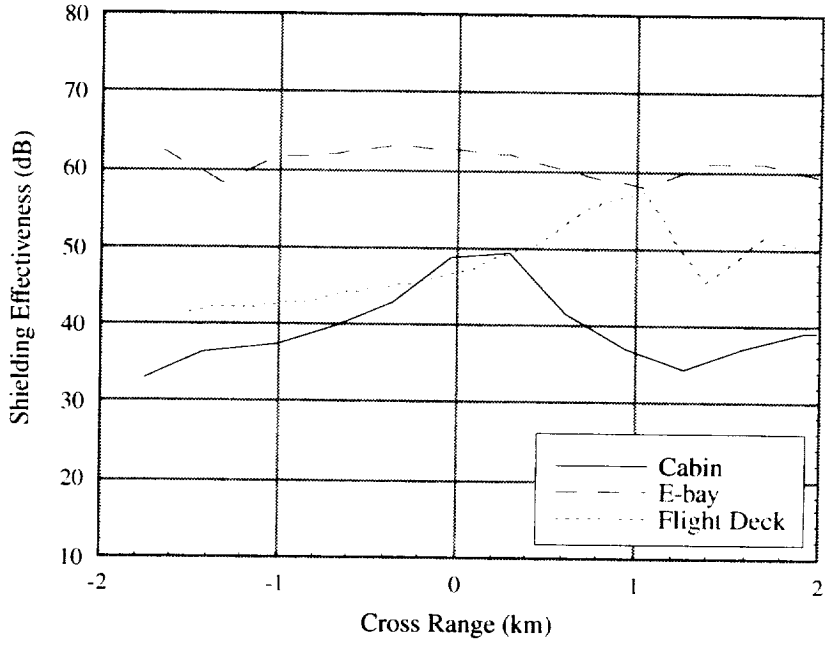

Figure 4.4. SE for the illumination encountered during the "26 MHz, crossbound, clean" flight path.

crosses the main beam. The SE provided by the airframe for this illumination is approximately 60 dB in the electronics bay, 50 dB in the flight deck, and between 35 and 50 dB in the passenger cabin. The SE of the flight deck, is somewhat less than that recorded as a result of illumination directed towards the nose or tail. The variation in the SE of the passenger cabin is not representative of the response recorded by the other sensors in the cabin and may be due to the location of the cabin D-Dot sensor, which was placed near the ceiling of the cabin, as can be seen in Figure 2.5.

4.2. Shielding Effectiveness at 173 MHz

Figure 4.5 illustrates the SE of the aircraft for the incidence and polarization angles encountered during the "inbound, clean" flight paths flown against the LP antenna. Results for both polarizations of the antenna (horizontal and vertical) are shown in this figure. In both cases, the flight path originates approximately 4 km down range from the antenna and progresses towards 0 km. The angle θ increases from near 95° at 4 km down range, to 110° at 1 km, and reaches a maximum near 170° as the aircraft flies over the antenna. The figure suggests that SE is strongly sensitive to polarization. For illumination which is directed towards and slightly below the nose of the aircraft (those portions of the flights between 4 and 2 km in downrange), SE varies by as much as 10 dB with polarization.

As was discussed in Section 3.2.3, the field level illuminating the aircraft during these flight paths changed rapidly with down range position. In the case of the horizontally polarized LP antenna, the aircraft was never illuminated by a discernible main beam, but instead encountered a series of narrow lobes, as can be seen by examining Figure B10. Errors in the calculation of the external EME resulting from the antenna and illuminating the aircraft may account for the ±5 dB variations in SE shown in Figure 4.5. Small errors in the location and depth of the nulls between the narrow lobes of the illumination pattern could produce variations of this magnitude.

The SE resulting from the measurements and calculations associated with the "outbound, clean" flight paths is illustrated in Figure 4.6. This figure suggests that for illumination directed towards and slightly below the tail of the aircraft, the passenger cabin provides approximately the same level of shielding as when the illumination is directed towards the nose, the electronics bay provides 5 dB more shielding, and the flight deck approximately 20 dB more shielding. These observations are consistent with those in Section 2.5, in which it was observed that the cockpit windshield is the principal mechanism for coupling into the flight deck, and that fields in the cockpit are coupled to the electronics bay via wires.

The SE resulting from the measurements and calculations associated with the "right crossbound, clean" and the "left crossbound, clean" flight paths are illustrated in Figures 4.7 and 4.8. Results for both polarizations of the LP antenna are shown in these figures. When the LP antenna was oriented in the horizontal polarization, the aircraft was within the antenna's main beam for cross range distances less than ±1 km, which can be confirmed by examining Figures B16 and B19. When the LP antenna was vertically polarized, the aircraft encountered an illumination which was approximately uniform, as can be confirmed from Figures B28 and B31. The angle θ is approximately 115° in all cases shown here, and ϕ spans approximately 55° for ±1 km of cross range.

These figures suggest that for illumination directed towards and slightly below the side of the aircraft, the SE of the passenger cabin is on the order of that observed for illumination directed towards the nose or tail (i.e., 20 dB), but with a much larger variation than the ±5 dB observed in those cases. Part of this variation may be attributed to changes in the response of the aircraft over the large range of incidence angles represented by these figures. Separation of variations due to the aircraft response from variations due to measurement and incident field calculation errors is not straightforward however. Likewise, the

SE of the electronics bay and the flight deck is on the order of that observed in the previous figures, but with a larger ±15 dB variation.

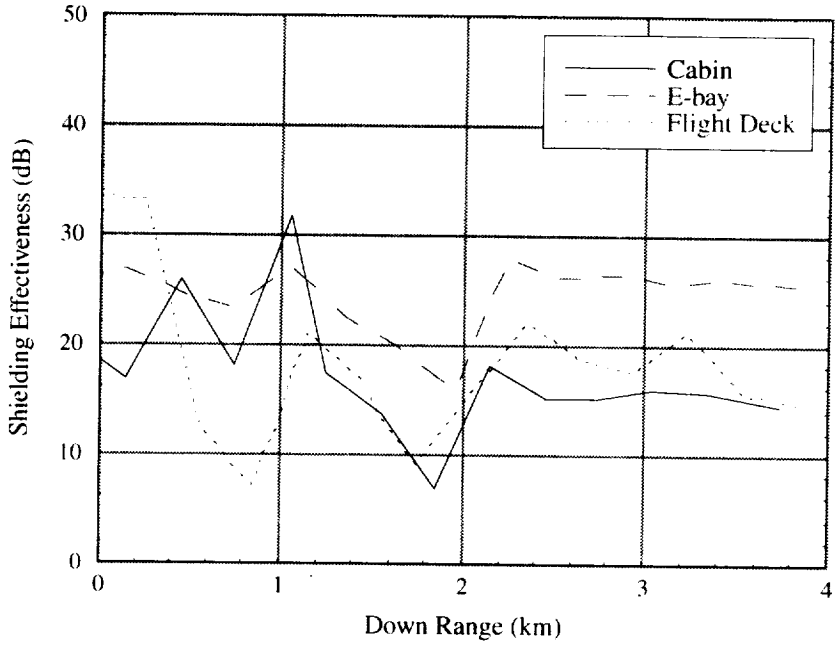

(a) H-pol.

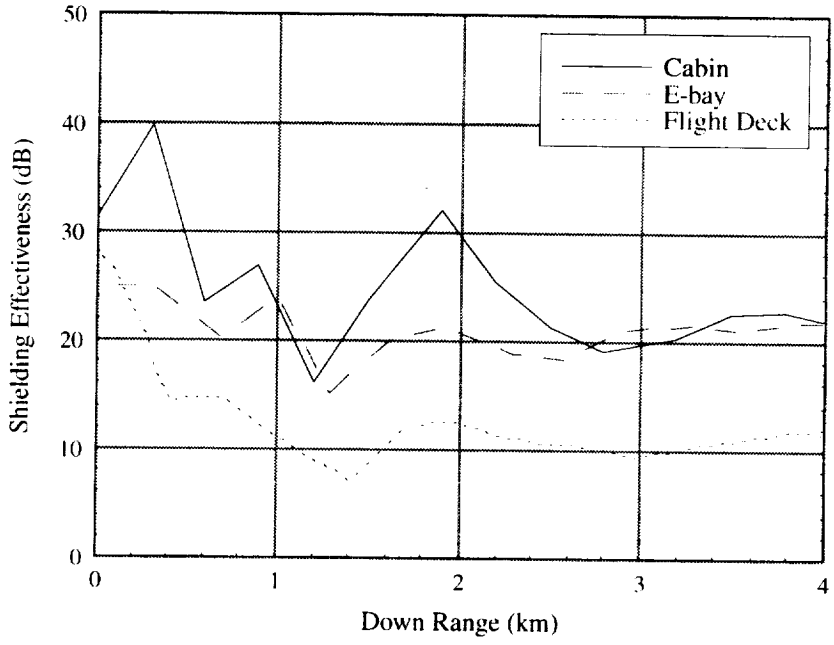

(b) V-pol.

Figure 4.5. SE for the illumination encountered during the "173 MHz, inbound, clean" flight paths.

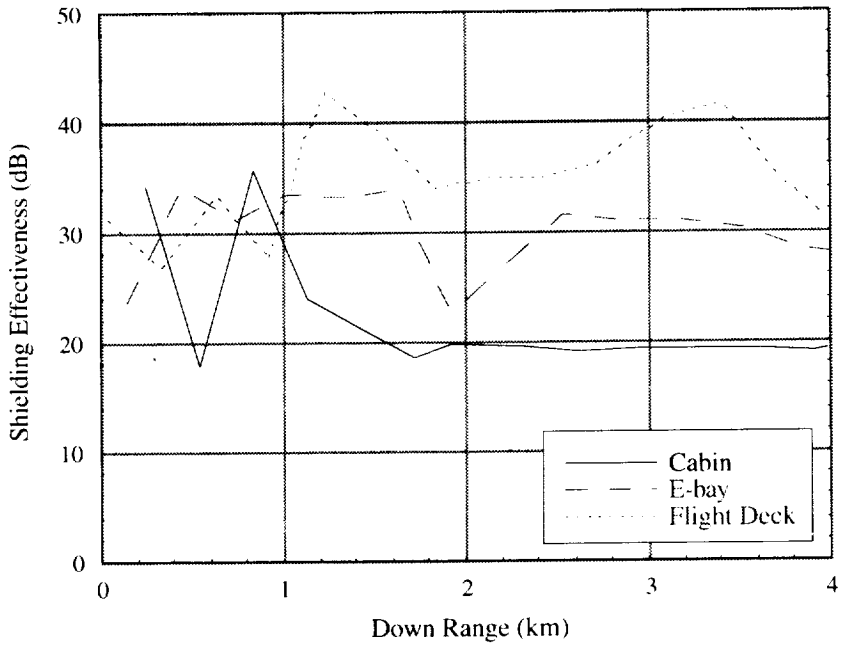

(a) H-pol.

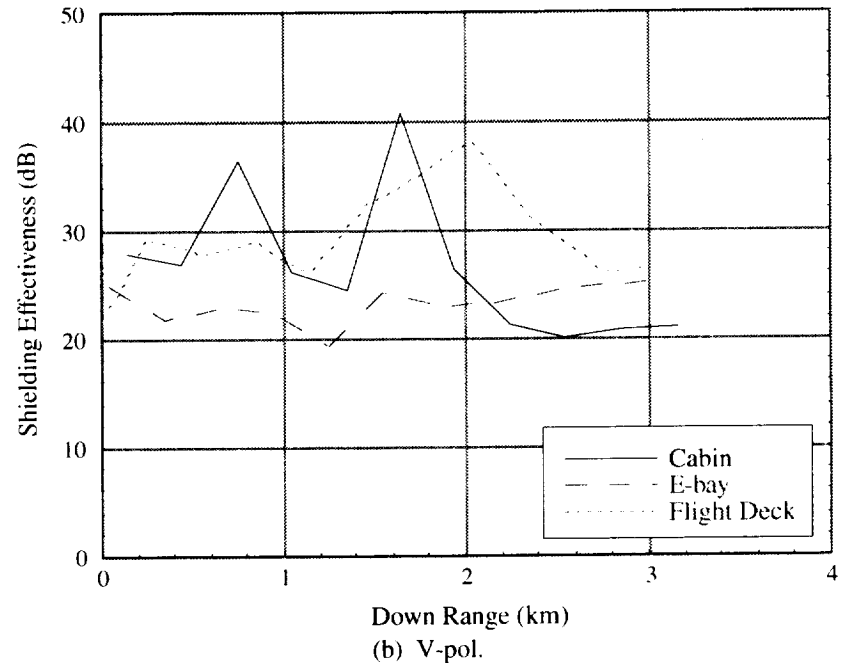

(b) V-pol.

Figure 4.6. SE for the illumination encountered during the "173 MHz, outbound, clean" flight paths.

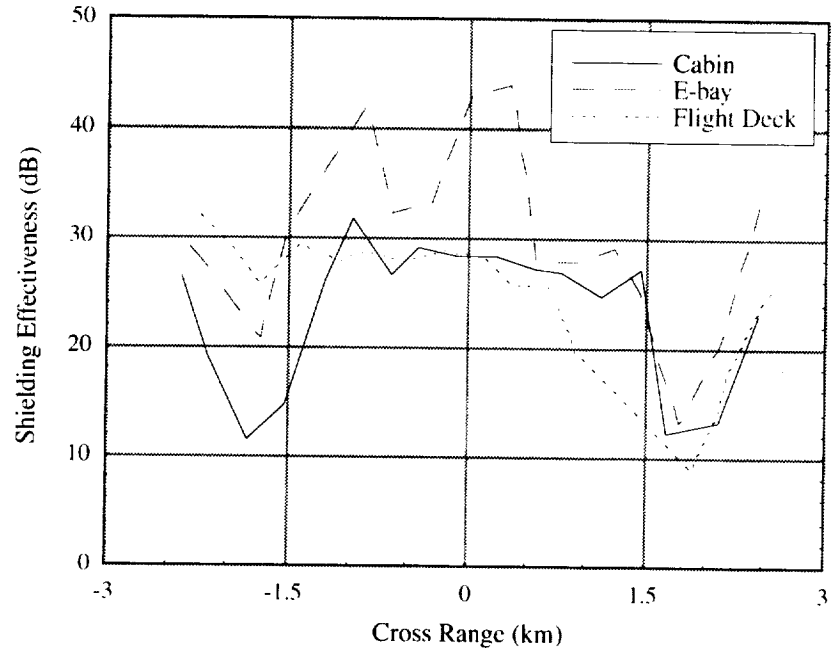

(a) H-pol.

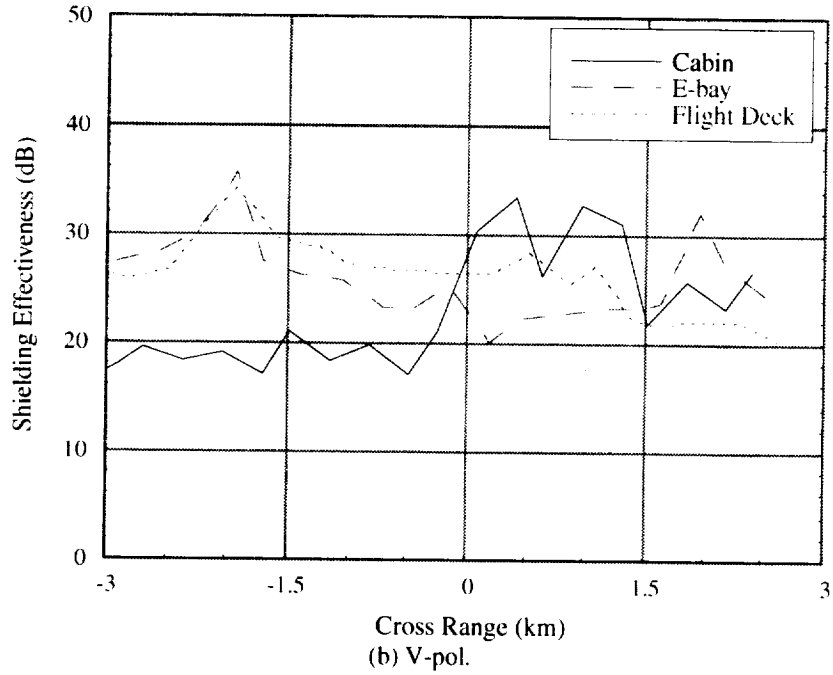

(b) V-pol.

Figure 4.7. SE for the illumination encountered during the "173 MHz, right crossbound, clean" flight paths.

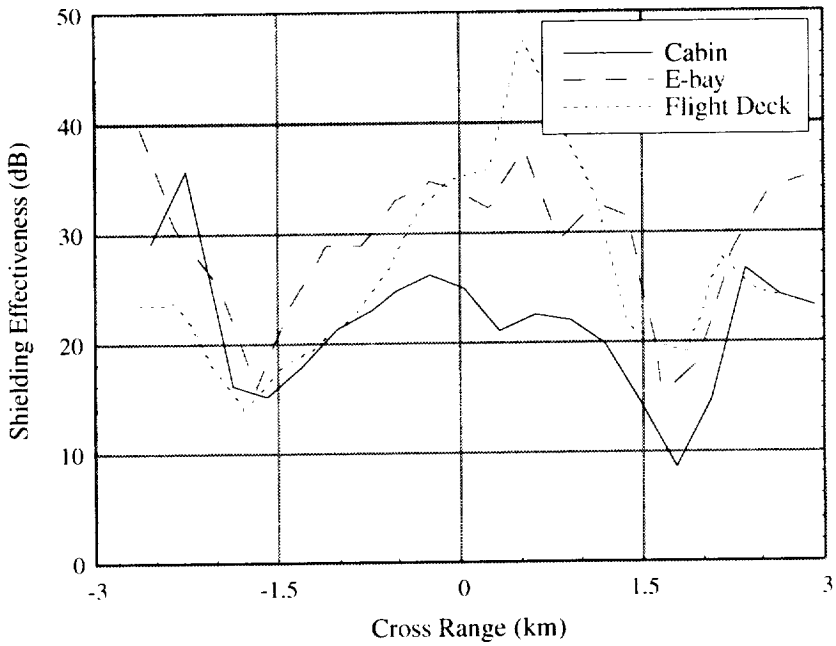

(a) H-pol.

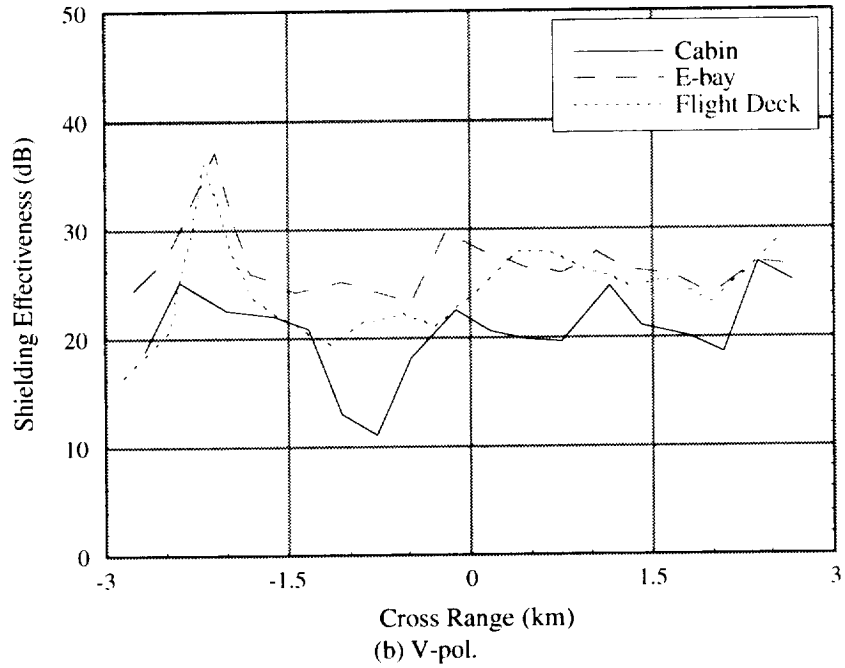

(b) V-pol.

Figure 4.8. SE for the illumination encountered during the "173 MHz, left crossbound, clean" flight paths.

4.3. Shielding Effectiveness at 430 MHz

Figure 4.9 illustrates the SE of the aircraft for the incidence and polarization angles encountered during the "inbound to right crossbound, clean" flight path flown against the NASA Wallops ASRF radar. In this figure, the flight originates at a cross range of approximately 14 km, which corresponds to a down range distance of approximately 18 km. At this distance, the illumination is directed towards the nose of the aircraft, with θ near 90°. The SE provided by the airframe for this direction of illumination is approximately 20 dB in the passenger cabin and approximately 5 dB in the flight deck.

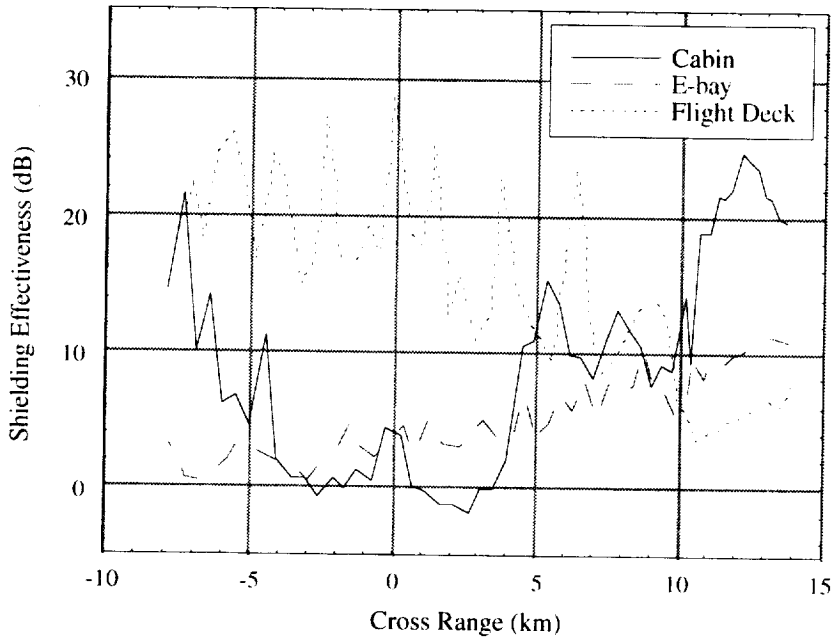

Figure 4.9. SE for the illumination encountered during the "430 MHz, inbound to right crossbound, clean" flight path.

At a cross range of approximately 11 km, which corresponds to down range of 14 km, the aircraft began a banked turn to the left, which ended at a cross range of approximately 8 km. The roll angle of the aircraft during the turn peaked at approximately −15°, exposing the forward right underside (θ = 110°, ϕ = −10° to −50°) of the aircraft to the illumination. Interestingly, the SE of the cabin decreases approximately 10 dB as a result.

After the turn was complete, the aircraft flew in a crossbound direction, with ϕ spanning ±40° about ϕ = −90°. As was observed at 173 MHz, the variation in SE is much larger along the crossbound direction. Unlike the 173 MHz case, it can be concluded that these variations are most likely not due to changes in the antenna response, as was discussed in Section 3.3.3. Instead, the SE variations observed in the figure are most likely due to changes in the response of the aircraft over the large range of incidence angles that are represented by it. At this frequency, the aircraft can be viewed as an electromagnetic cavity which can support a large number of modes. Changes in the incidence angle of the arriving illumination results in changes in the excitation of the modes within the cavity, a process which is known as "mode stirring." Scearce and Bunting [42] show that mode stirring accounts for the variations in the internal EME, and consequently SE, that were measured during the crossbound portions of the 430 MHz

flight tracks. As was the case for the 173 MHz data, these variations cannot be easily separated from measurement and incident field calculation errors.

In spite of the large variations, it can be observed that the SE of the cabin decreases to a minimum of approximately 0 dB, which occurs when the illumination is side-incident (near the $\phi = -90°$ direction). Also, it can be observed that the SE of the flight deck is higher than the cabin for most of this flight portion.

Figure 4.10 illustrates the SE of the aircraft for the "left crossbound to outbound, clean" flight path. This flight originates at a cross range of approximately −8 km, where the aircraft began a crossbound track which ends near +8 km, at which point the aircraft began a banked turn to the right, ending near +11 km and followed a tail-illuminating outbound path. Most of the observations made about the crossbound portion of Figure 4.9 can also be made about the crossbound portion of Figure 4.10. The SE of the cabin decreases to a minimum which occurs when the illumination is directed in the side-incident ($\phi = 90°$). The SE of the flight deck decreases as the illumination moves from nose-incident to tail-incident. The outbound portion of Figure 4.10 suggests that the SE of the electronics bay is considerably lower for tail-incident illumination than for nose-incident illumination.

5. Conclusions

The goal of the research conducted by the EME flight experiment was to provide a source of shielding effectiveness data which may be used for the corroboration of analytical predictions of internal aircraft response to external stimuli. This objective has been satisfied. The measurements of internal response presented in this report are the first reported for a large aircraft which is in flight. The data are of sufficient quality so as to provide a library for the validation of analysis methods and associated computer codes concerned with aircraft shielding effectiveness (SE). The data library reveals the SE behavior of

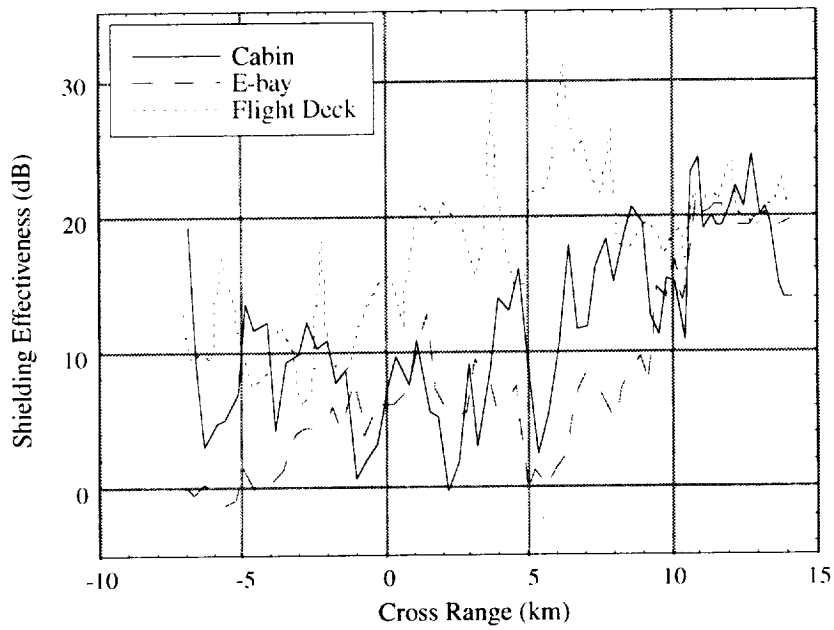

Figure 4.10. SE for the illumination encountered during the "430 MHz, left crossbound to outbound, clean" flight path.

the NASA 757 for a wide variety of illumination directions, polarization angles, and aircraft configurations. Importantly, the frequencies at which these data were collected fall in that band which is considered to pose the greatest threat to aircraft electronics from HIRF.

The effort required to reduce and analyze the collected data was considerably greater than anticipated during the planning stages of the experiment. One of the reasons for this was the need to analytically determine the external field levels impinging upon the aircraft. Another was that the direction of propagation and polarization of the electromagnetic fields illuminating the aircraft needed to be determined in a reference frame fixed to the aircraft. Both of these requirements resulted in the development of novel solutions. The determination of aircraft position and field orientation which was presented here is believed to be the first reported which relies on GPS and aircraft attitude measurements alone. This technique is applicable to other measurements involving ground-based antennas and flying aircraft, such as the measurement of the far-field response of aircraft-mounted antennas.

Lessons Learned: Section 2 discussed the sensors and instrumentation used to characterize the EME inside the aircraft. Among the sensors chosen by experiment planners were the electric field sensors known as D-Dot sensors. When mounted on a large ground plane, D-Dot sensors exhibit a differentiating property over a limited bandwidth (which is what makes them useful for the study of pulse phenomena). The differentiating property of the sensor was not needed for this experiment and is in fact undesirable since it is a result of fine geometric detail that is difficult to include in analytical models of the flight experiment. This fact led to the need to perform calibration measurements of the sensor. The calibration measurements performed by NIST indicate that the mounting surfaces on which the D-Dots were deployed were too small to act as effective ground planes. An additional problem with D-Dot sensors is the lack of information about the polarization sensitivity. A relatively large uncertainty is therefore associated with the data collected by the D-Dot sensors. Alternate sensors which should be considered for future experiments include 3-axis field probes (such as those manufactured by Amplifier Research), magnetic field sensors (known as B-dot sensors), and wire monopole probes. The use of a total-field sensor, such as a 3-axis probe, could have reduced the data reduction requirements for this experiment since it would have eliminated the need to determine the polarization of the arriving illumination. Wire monopole probes could easily be included in analytical models if the dimensions of both the wire and the ground plane were on the order of one tenth of the longest wavelength of interest.

Another of the sensors used to measure the EME inside the aircraft was the CLW sensor described in Section 2.1.2. This sensor proved to be responsive to signals across the frequency spectrum encountered in the experiment and therefore should be included in future experiments. Experiment planners chose to measure the voltage generated between the end of the sensor and a small strip of metal which acted as a partial ground plane. Like the D-Dot, the geometrical details of this metal strip are too fine to be easily included in analytical models of the aircraft. A more useful measurement would result from measuring the voltage between the CLW and a much larger ground plane. A better alternative might be to dispense with the ground plane, cut the CLW sensor in half, and measure the voltage between the two wire sections. Another effective alternative might be to measure the current generated along the wire at one or more locations.

Current probes, such as the Prodyn I-320s described in Section 2.1.3, are potentially the most useful sensors available for experiments of the type described here. Future experiment planners should take care to place these sensors on structures that can be easily included in analytical models.

Experiment planners had anticipated that signals recorded from antennas placed on the exterior of the aircraft, which are normally used for navigation and communications functions, could be used to

determine the magnitude of the EME immediately outside of the aircraft. Experiment planners were restricted by aircraft operational requirements which prohibited substantial modification of the aircraft exterior. Unfortunately, this approach proved impractical. Among the reasons for this is that the far-field patterns of these antennas (which is what is needed to determine the relationship between recorded voltage and impinging external field amplitude) are not available. These antennas incorporate proprietary designs, a fact which inhibits the ability to determine their performance by experimental or analytical modeling. Another reason why these antennas are ill-suited for measuring external EME is that they are located on top of the aircraft. This location results in very low received signal strength for fields originating below the aircraft. A navigation antenna which is of interest, but which was not utilized for this experiment, is a long wire antenna embedded in the vertical stabilizer of the aircraft. Future experiments should investigate the use of this antenna. If possible, calibrated sensors should be placed on external surfaces, preferably under the nose radome and on the underside of the aircraft.

The determination of the aircraft's position relative to ground-based antennas and incident fields proved to be a much more involved and time-consuming process than was originally planned. Part of the reason for this was a poor understanding of the format in which aircraft position had been recorded. In addition to GPS measurements, the flight instrumentation recorded aircraft position information from the aircraft's internal data bus. These data are generated by the aircraft's barometric altimeter and inertial reference unit (which is a laser gyroscope). These instruments have an accuracy of approximately 200 meters when calibrated prior to takeoff, and are subject to drift at a rate of up to 2000 meters per hour during flight. GPS measurements, by comparison, are accurate to 100 meters in "uncorrected" form. Measurement accuracy can be improved to 1 meter by making a "differential correction," which requires the existence of accurately surveyed points in the vicinity of the measurement. Under certain conditions, the measurement accuracy of differential GPS can be reduced to 10 cm. Members of the NASA Langley Flight Operations and Support Division performed both the required survey and the correction to the GPS measurements, but the results and significance of this activity were not understood until well into the data reduction effort. Another problem was confusion as a result of conflict among documents over the location of the ground-based antennas. Part of the reason for this was that the GPS survey team initially did not understand that this information was of interest. Better coordination among experiment participants could have saved considerable time and effort during the data reduction phase of the experiment.

Section 3 discussed the determination of the external EME illuminating the aircraft through analytical means. The confirmation of this analysis through site surveys, in which the near-ground electric field strength was measured, was met with limited success. Although the calculated values appear very reasonable, the site survey measurements must be used to estimate the uncertainty associated with the analysis, especially for the VOA antenna analysis, since the power fed to this antenna was not measured. The discrepancy between analysis and measurement in this case results in a relatively large uncertainty associated with the calculations of the field levels illuminating the aircraft. The discrepancy may be attributed to the uncertainty in the locations at which the site survey was conducted relative to the antenna, and in the inability of analysis to predict the effects of all of the terrain features near the antenna. Future experiments should attempt to sample the electric field at points well above the ground. Great care should be taken in establishing the position, relative to the antenna, at which these measurements are made.

Appendix A

EME Sensor Measurements

This appendix documents the EME sensor measurements taken for the 26, 173, and 430 MHz flights in the form of two plots per flight. It is arranged first by frequency of illumination, then by flight path (inbound, outbound, crossbound), and finally by aircraft configuration ("clean", "flaps", "flaps & gear"). Table A1 cross-references the illumination parameters to the sensor measurements. Note that the 430 MHz data are plotted against cross-range position even though each flight contains both side and end-on exposure. As a result, the end-on portion of these flights is projected to a disproportionately short part of the plot in Figures A68 through A78.

Table A1. Organization of This Appendix

Test Frequency	Antenna Polarization	Flight Path	Figure
26 MHz	Horizontal	Inbound	Figures A1 to A6
		Outbound	Figures A7 to A12
		Right Crossbound	Figures A13 to A18
173 MHz	Horizontal	Inbound	Figures A19 to A24
		Outbound	Figures A25 to A30
		Right Crossbound	Figures A31 to A36
		Left Crossbound	Figures A37 to A42
	Vertical	Inbound	Figures A43 to A48
		Outbound	Figures A49 to A54
		Right Crossbound	Figures A55 to A60
		Left Crossbound	Figures A61 to A66
430 MHz	Vertical	Inbound to Right Crossbound	Figures A67 to A72
		Left Crossbound to Outbound	Figures A73 to A78

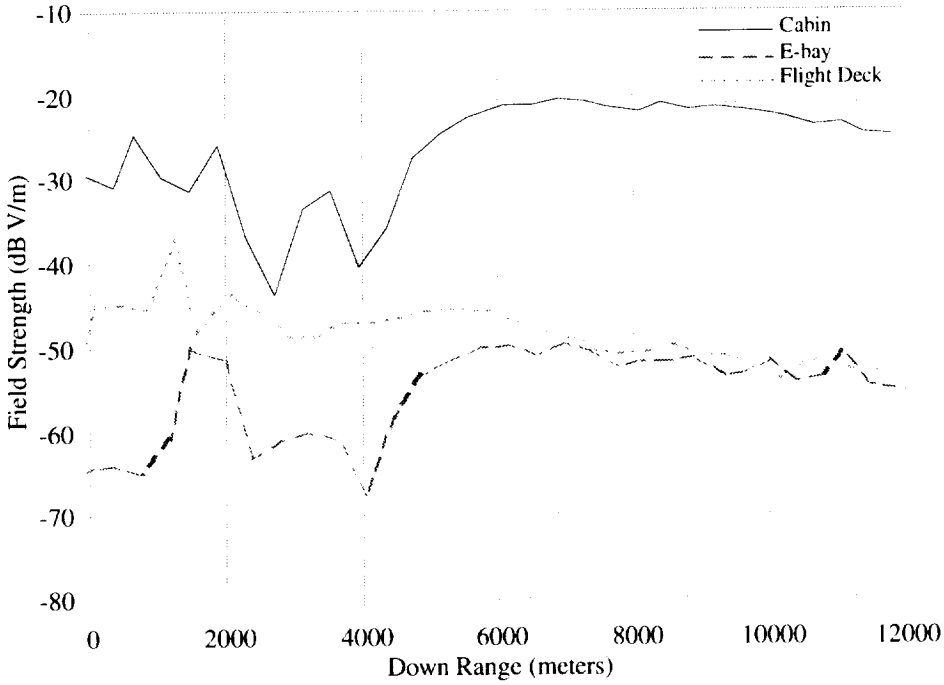

Figure A1. D-Dot measurements. 26 MHz; inbound; "clean."

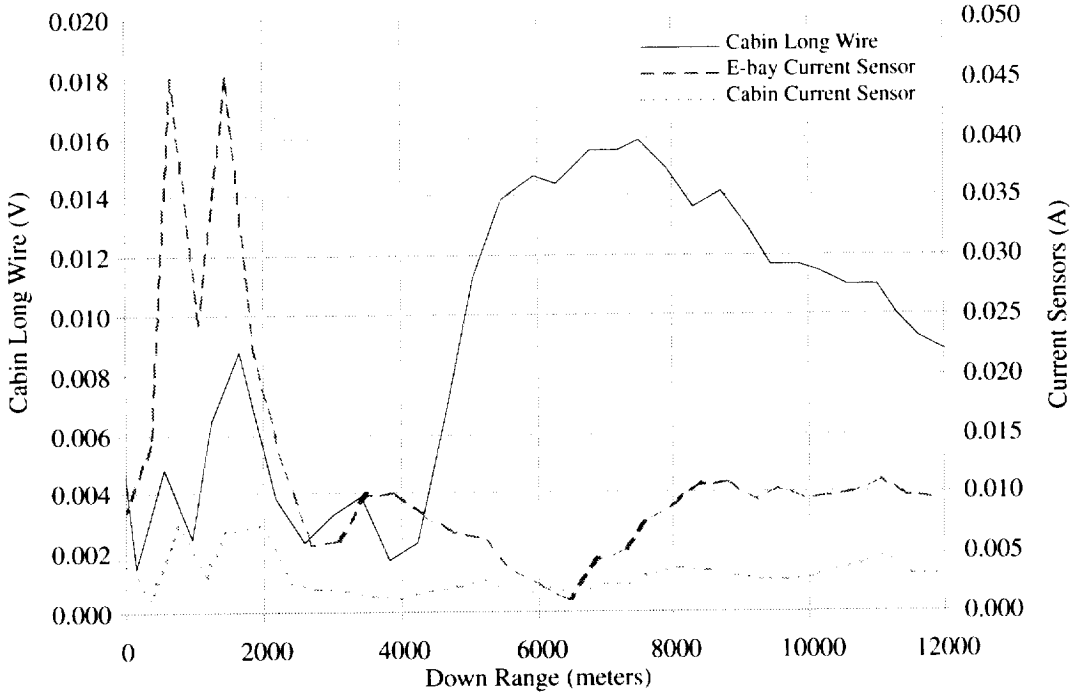

Figure A2. CLW and current sensor measurements. 26 MHz; inbound; "clean."

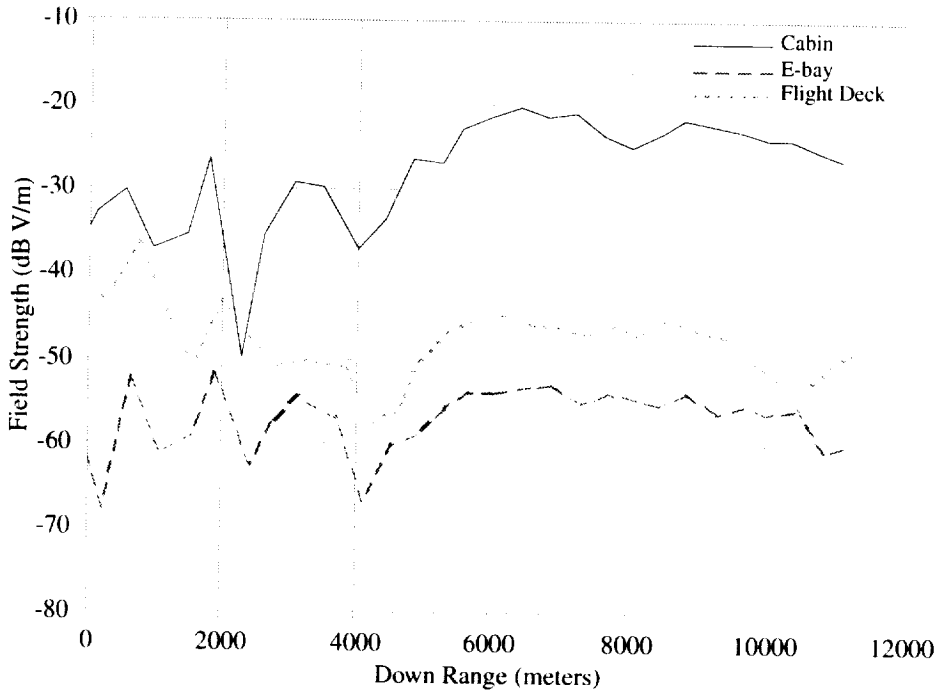

Figure A3. D-Dot measurements. 26 MHz; inbound; "flaps."

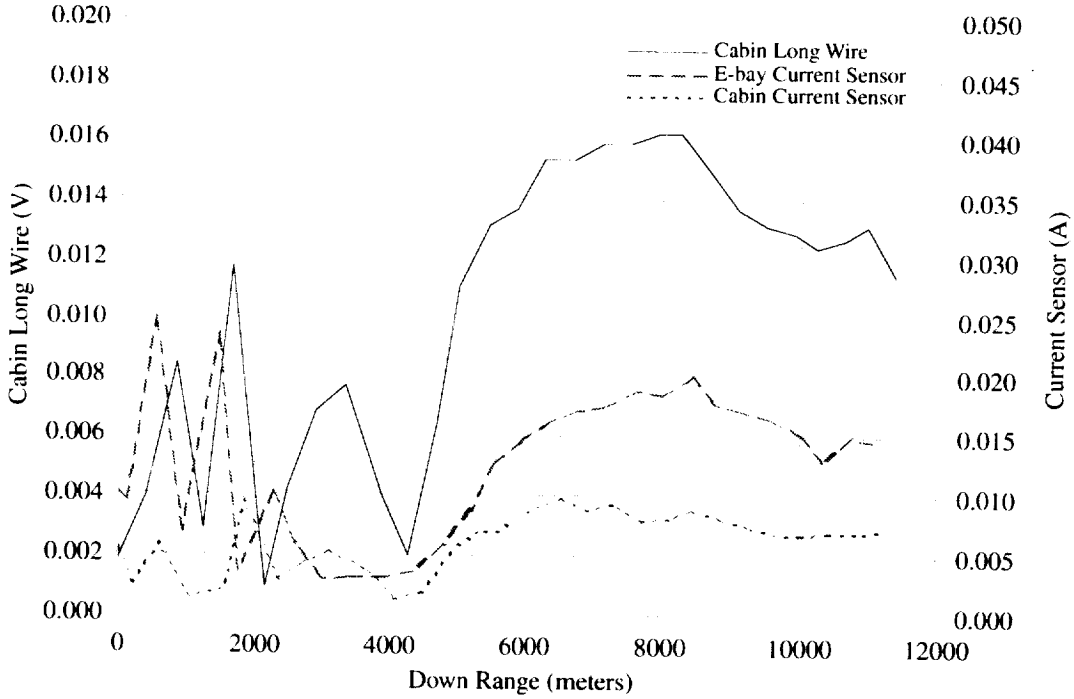

Figure A4. CLW and current sensor measurements. 26 MHz; inbound; "flaps."

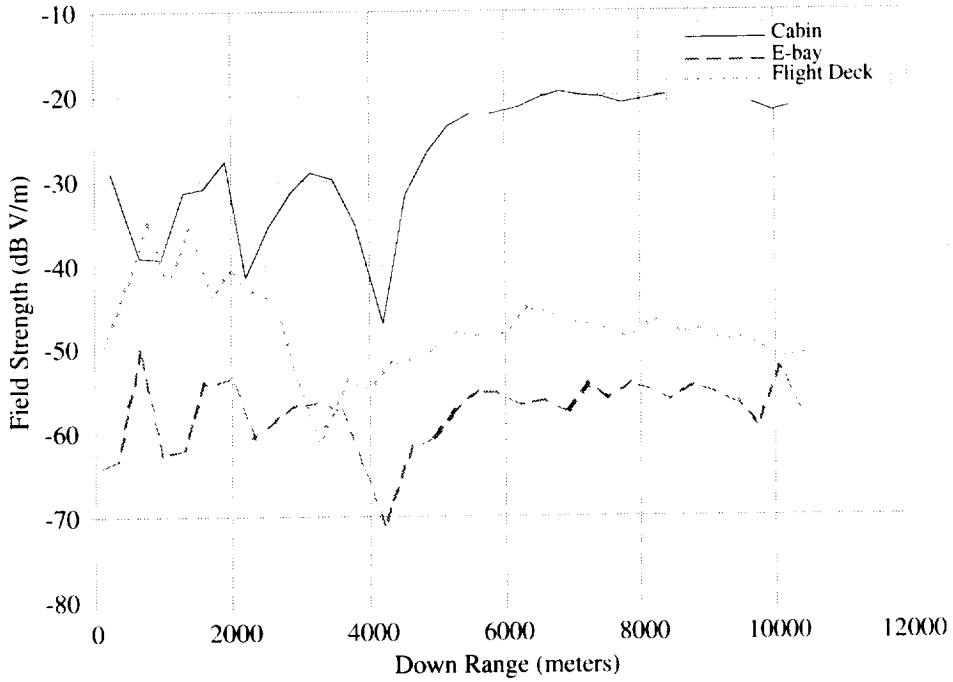

Figure A5. D-Dot measurements. 26 MHz; inbound; "flaps & gear."

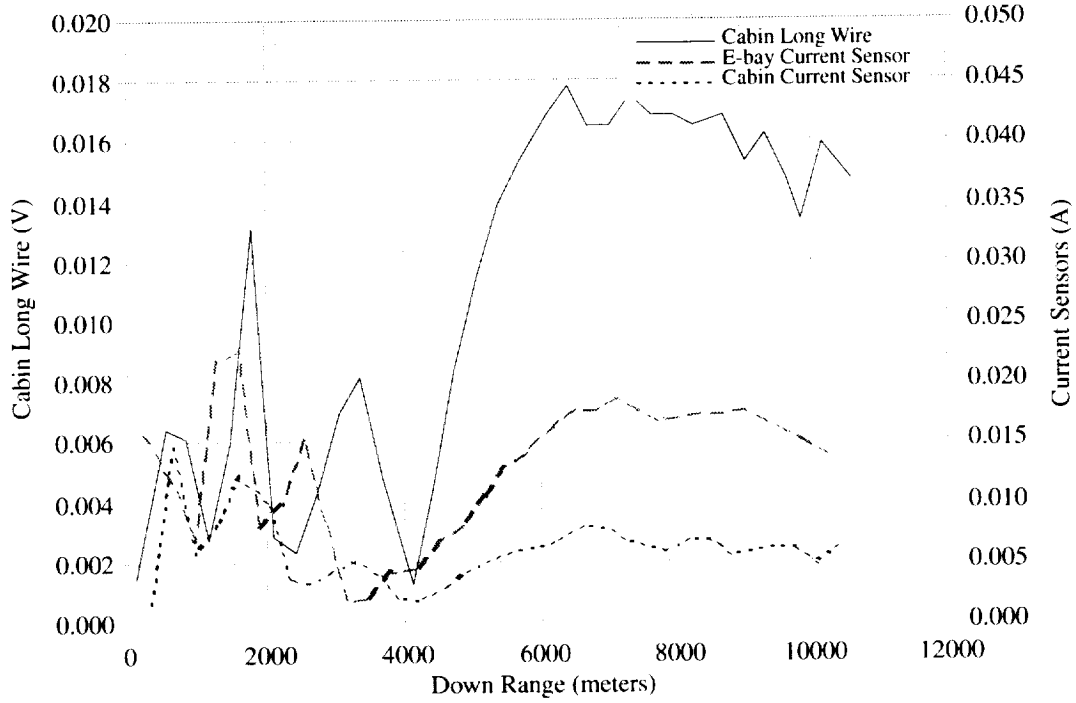

Figure A6. CLW and current sensor measurements. 26 MHz; inbound; "flaps & gear."

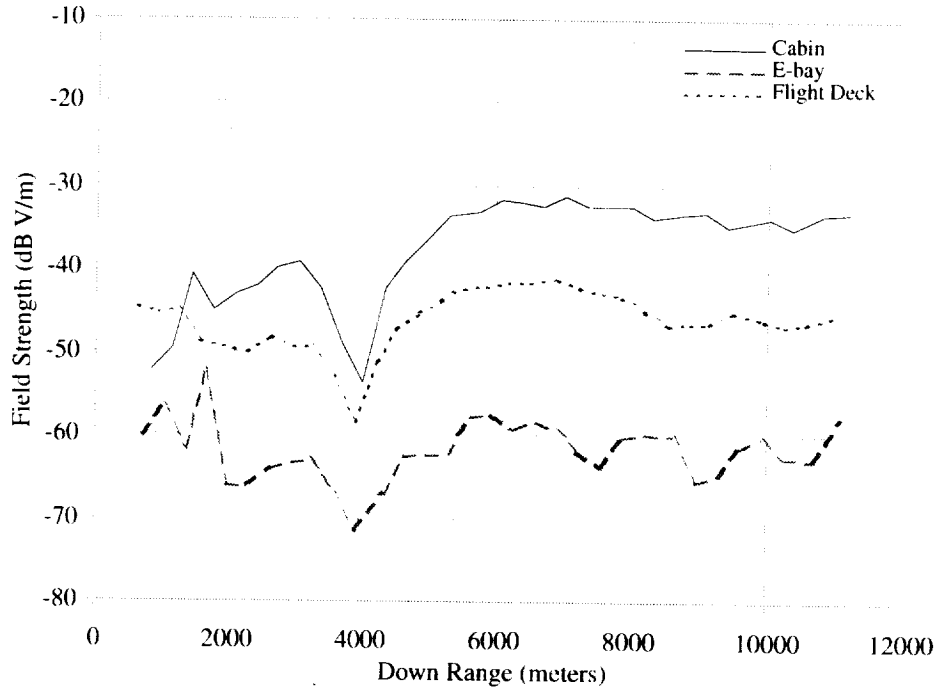

Figure A7. D-Dot measurements. 26 MHz; outbound; "clean."

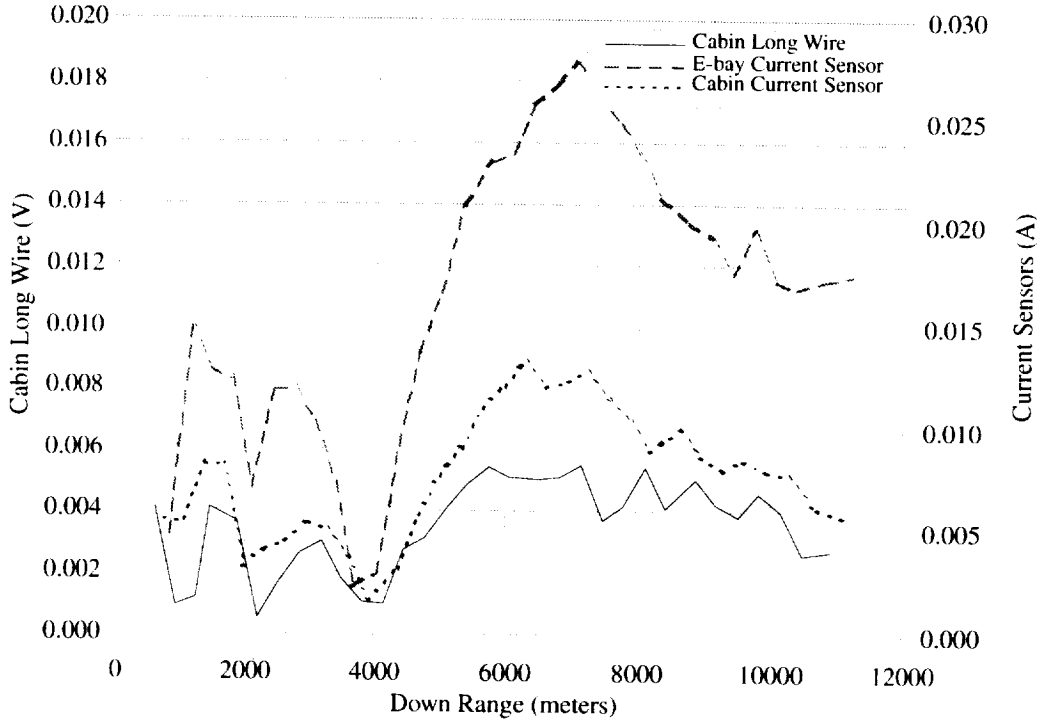

Figure A8. CLW and current sensor measurements. 26 MHz; outbound; "clean."

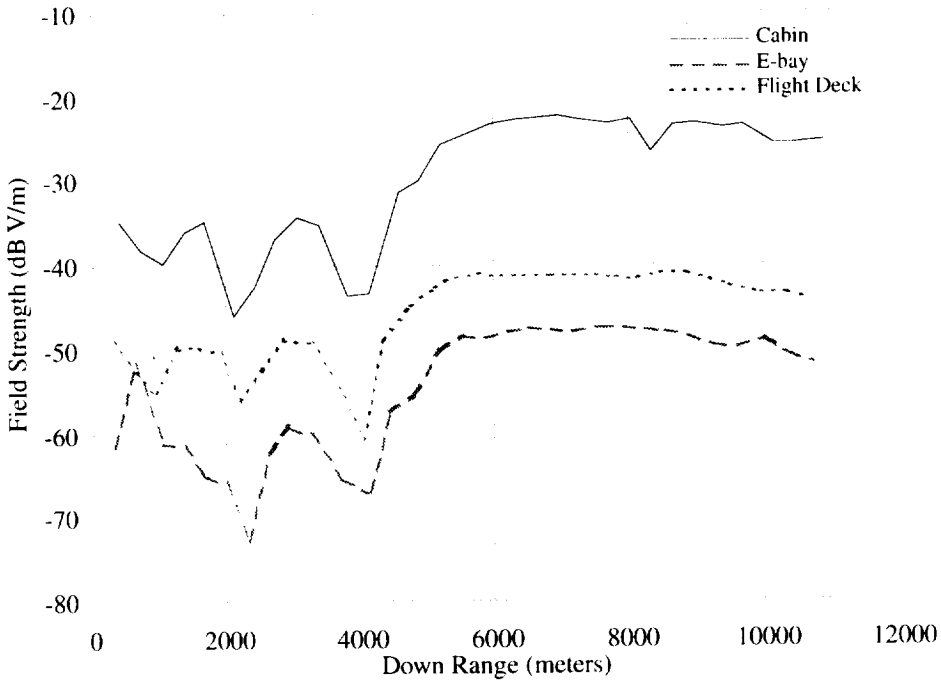

Figure A9. D-Dot measurements. 26 MHz; outbound; "flaps."

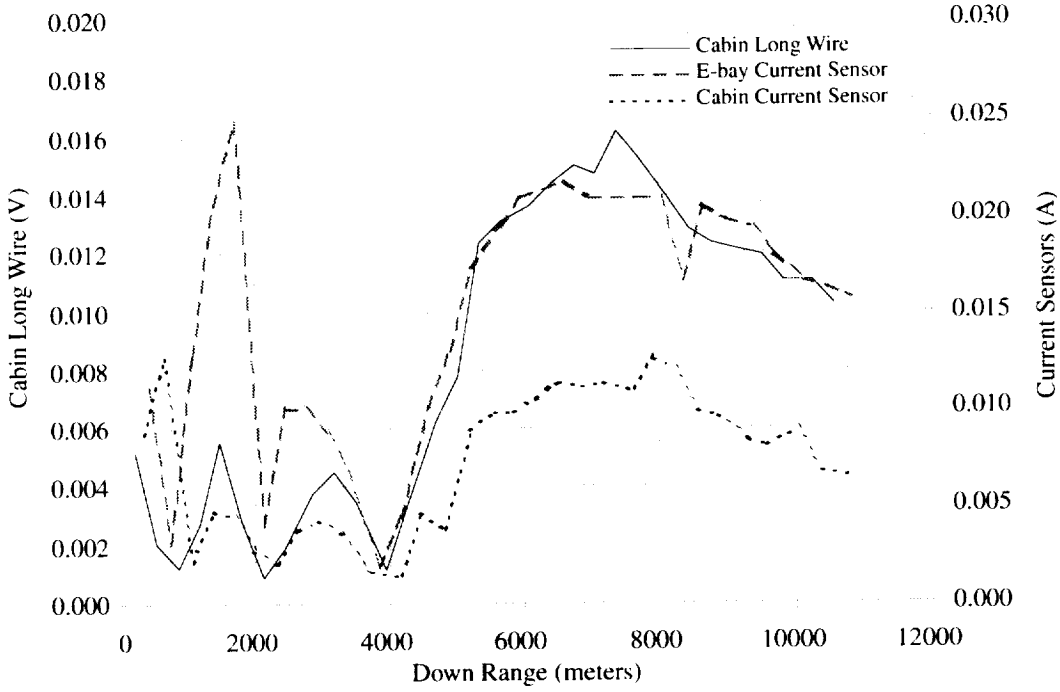

Figure A10. CLW and current sensor measurements. 26 MHz; outbound; "flaps."

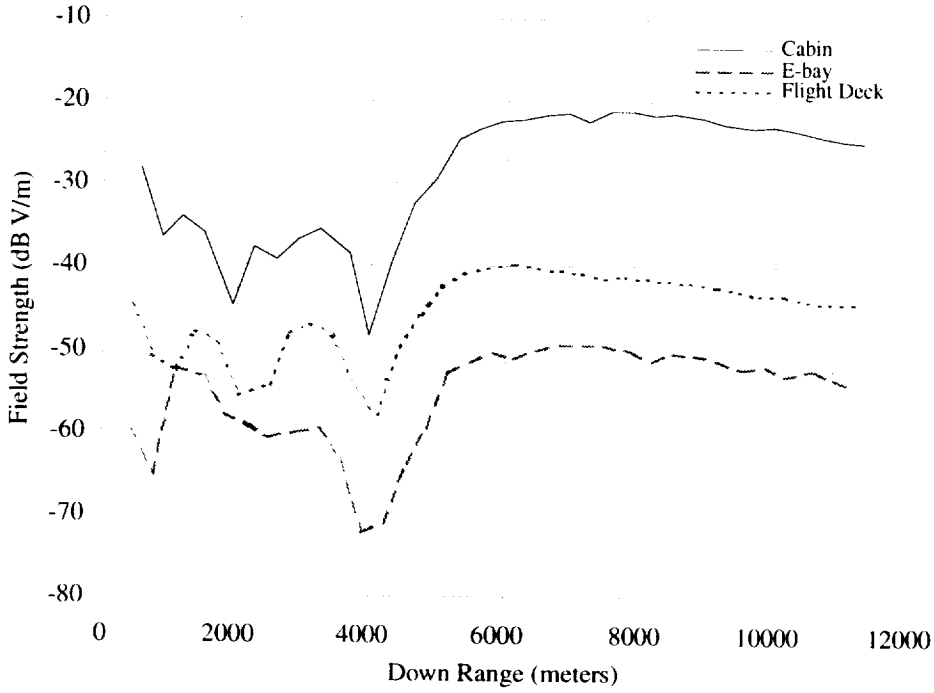

Figure A11. D-Dot measurements. 26 MHz; outbound; "flaps & gear."

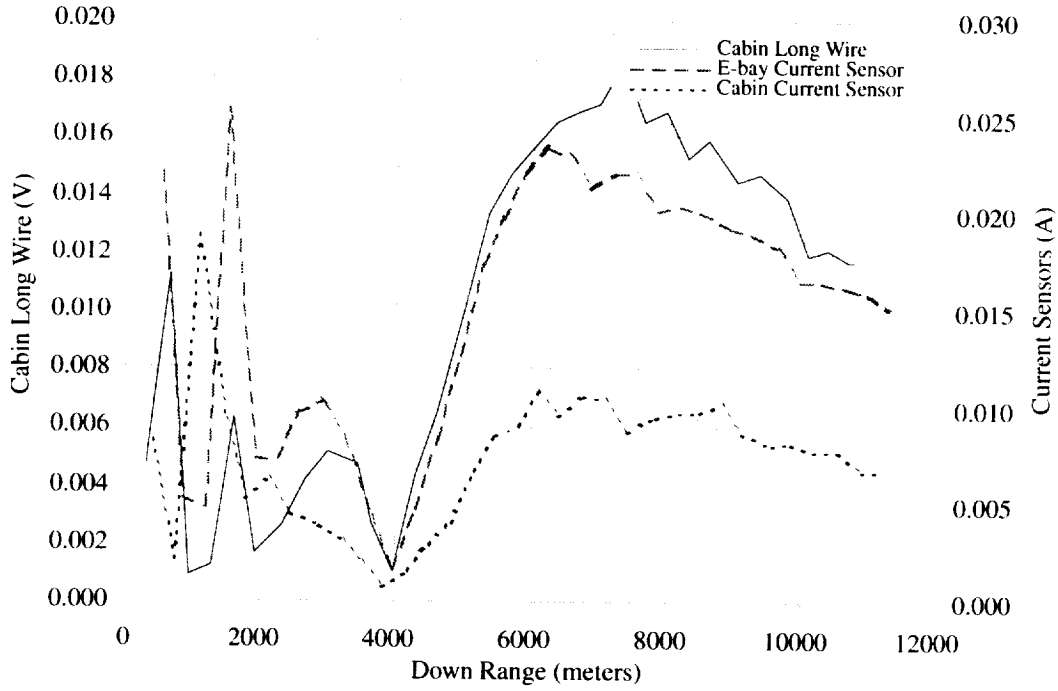

Figure A12. CLW and current sensor measurements. 26 MHz; outbound; "flaps & gear."

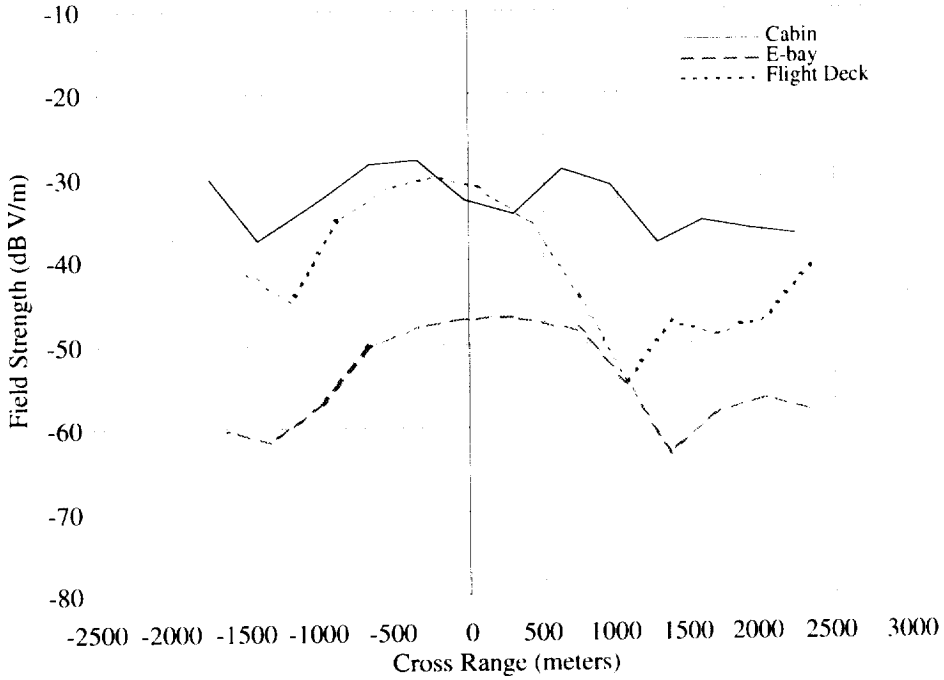

Figure A13. D-Dot measurements. 26 MHz; crossbound; "clean."

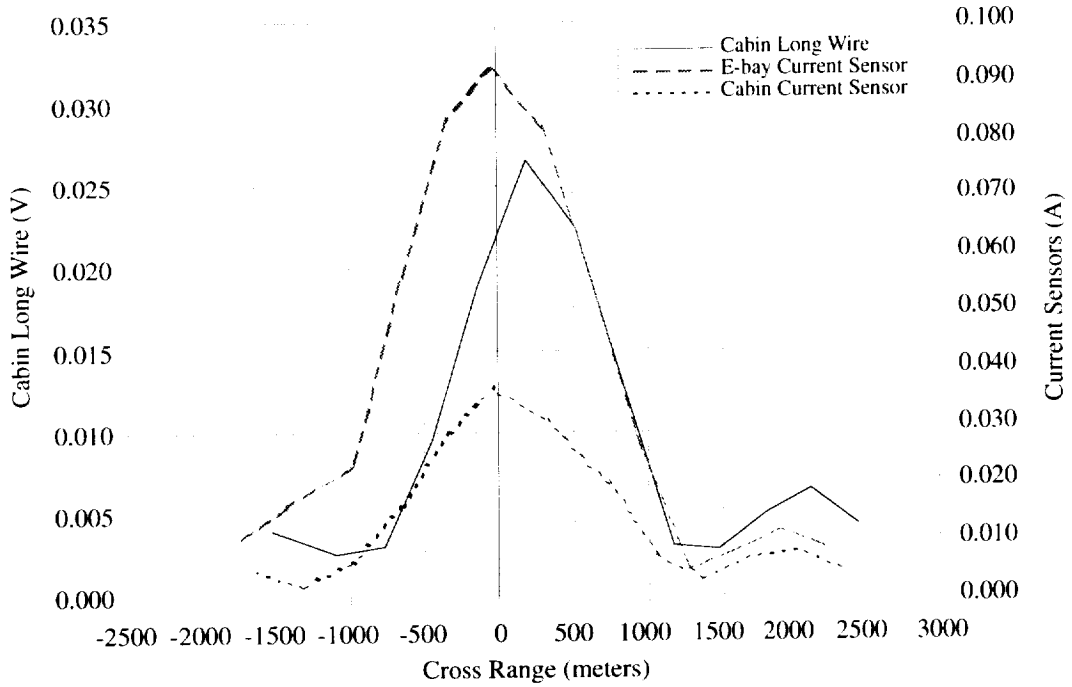

Figure A14. CLW and current sensor measurements. 26 MHz; crossbound; "clean."

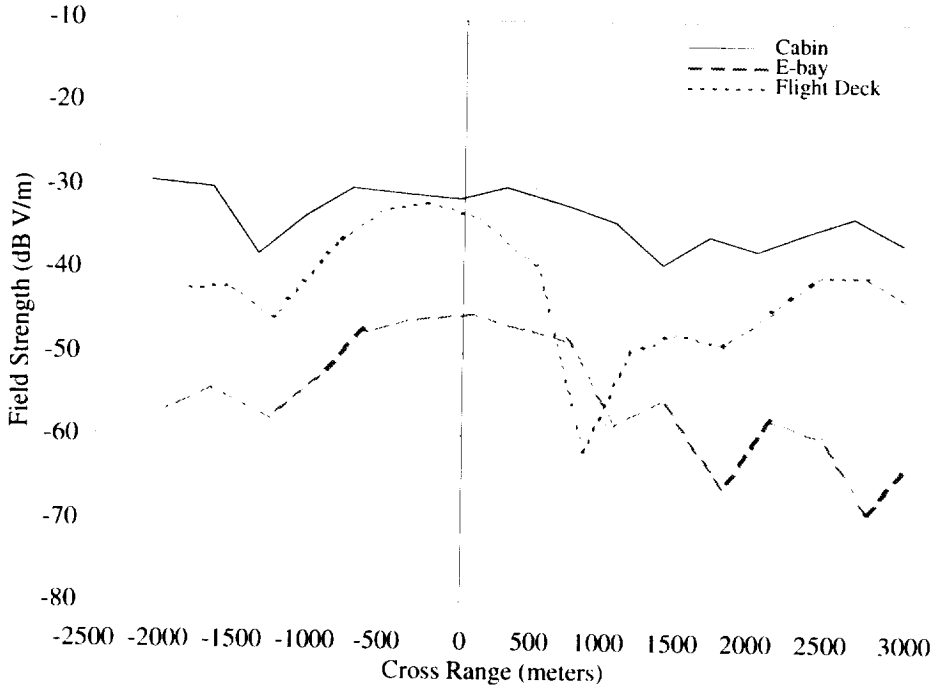

Figure A15. D-Dot measurements. 26 MHz; crossbound; "flaps."

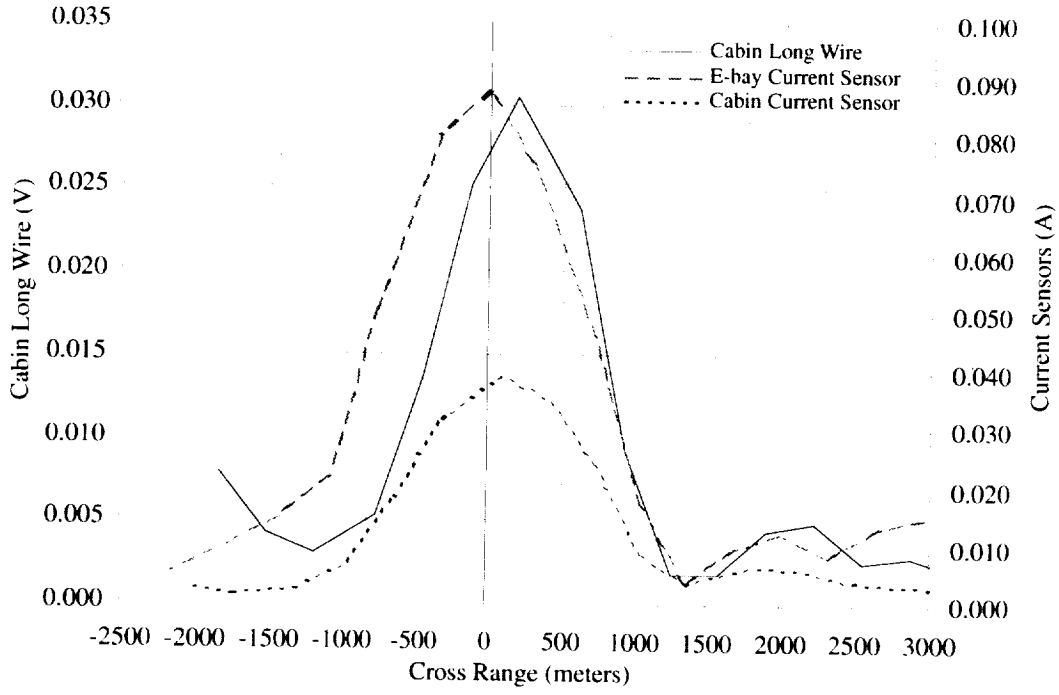

Figure A16. CLW and current sensor measurements. 26 MHz; crossbound; "flaps."

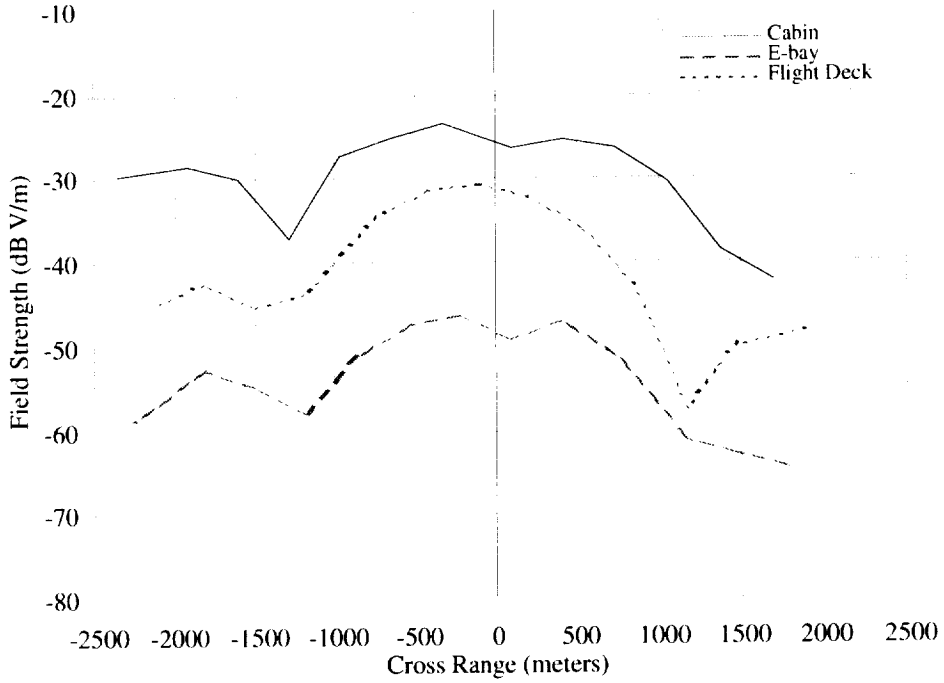

Figure A17. D-Dot measurements. 26 MHz; crossbound; "flaps & gear."

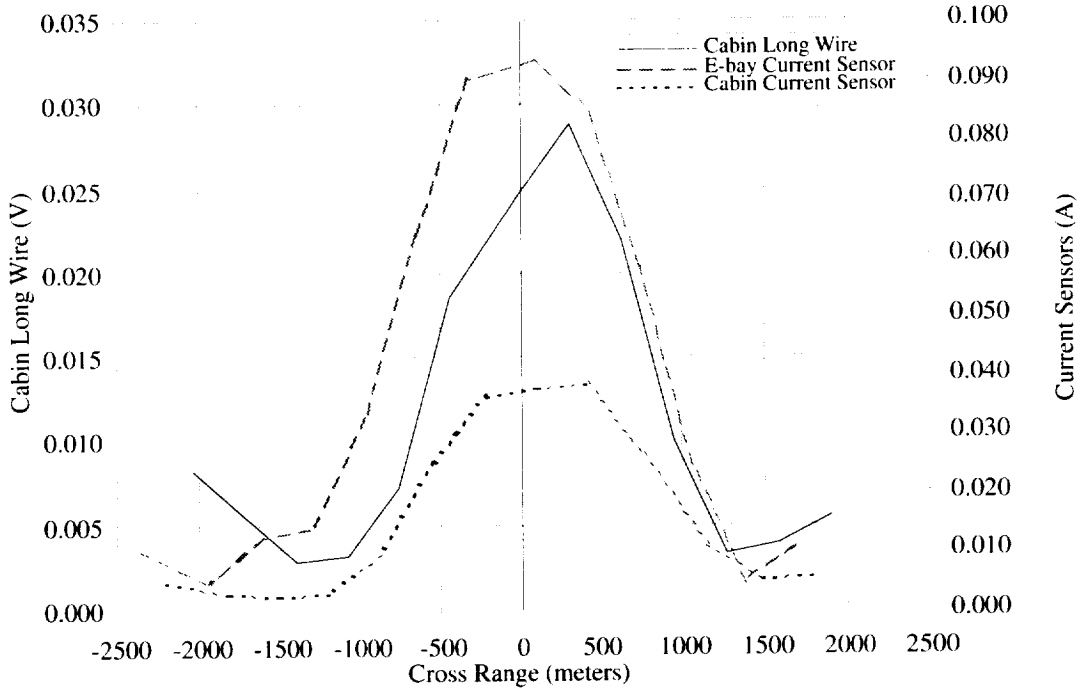

Figure A18. CLW and current sensor measurements. 26 MHz; crossbound; "flaps & gear."

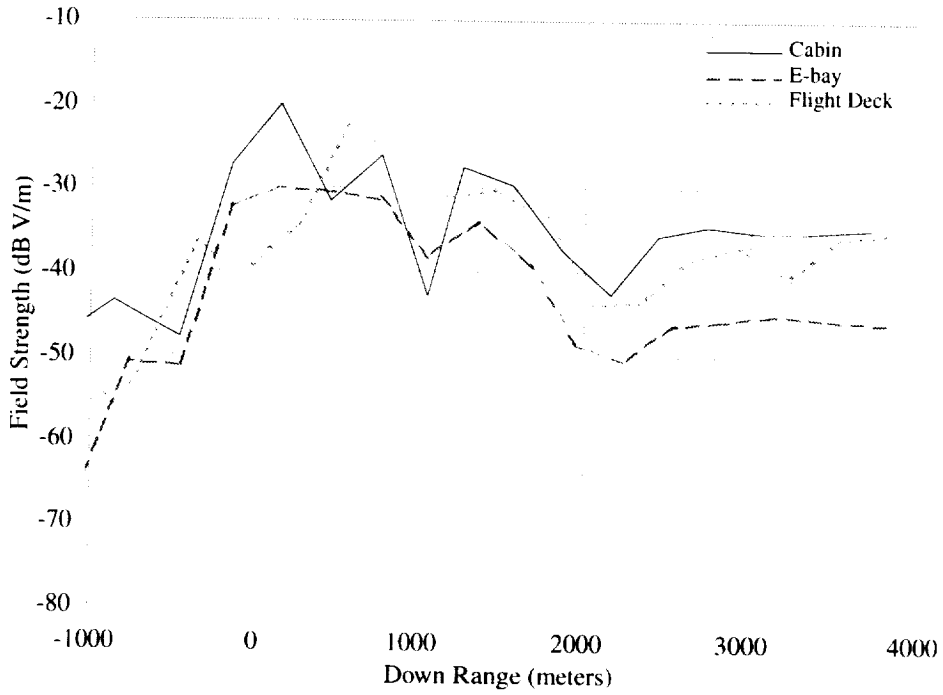

Figure A19. D-Dot measurements. 173 MHz; H-pol; inbound; "clean."

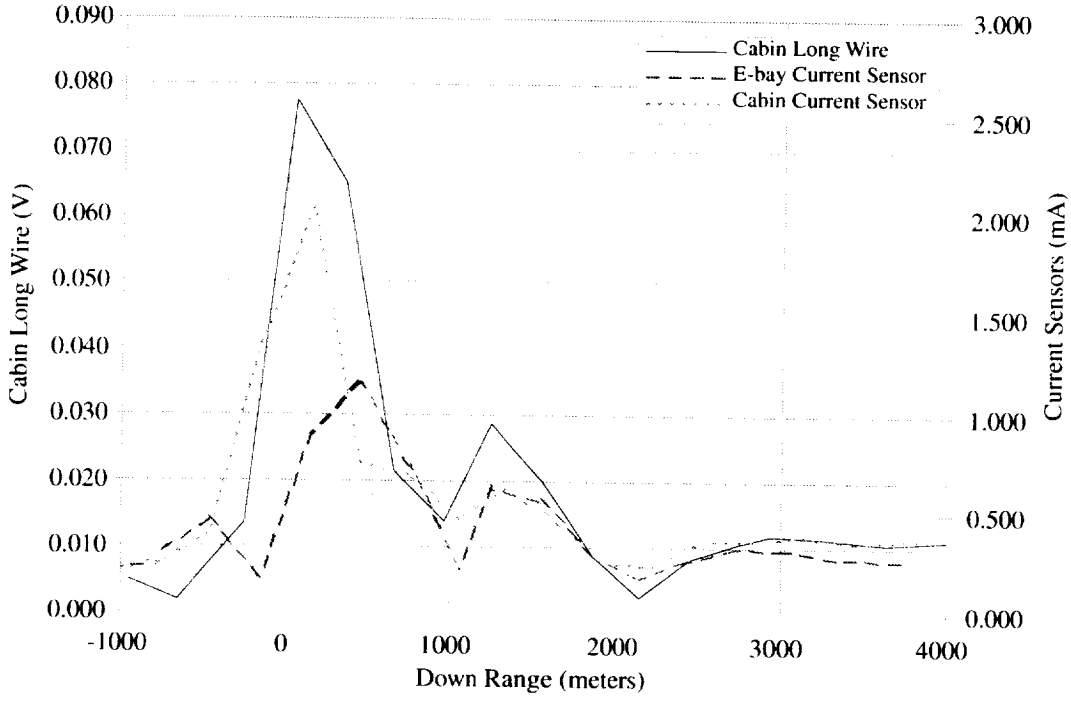

Figure A20. CLW and current measurements. 173 MHz; H-pol; inbound; "clean."

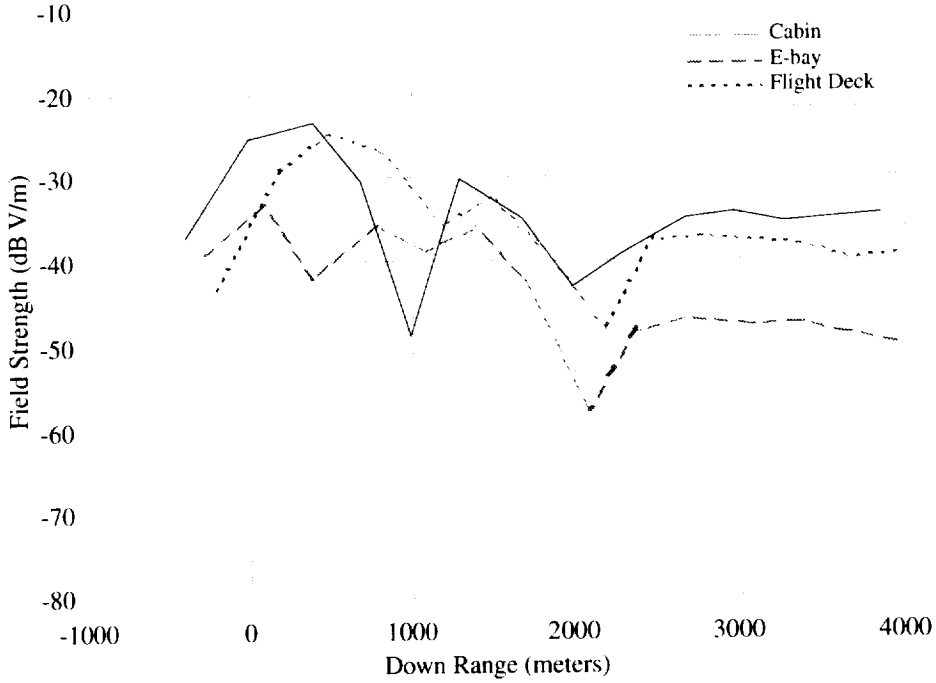

Figure A21. D-Dot measurements. 173 MHz; H-pol; inbound; "flaps."

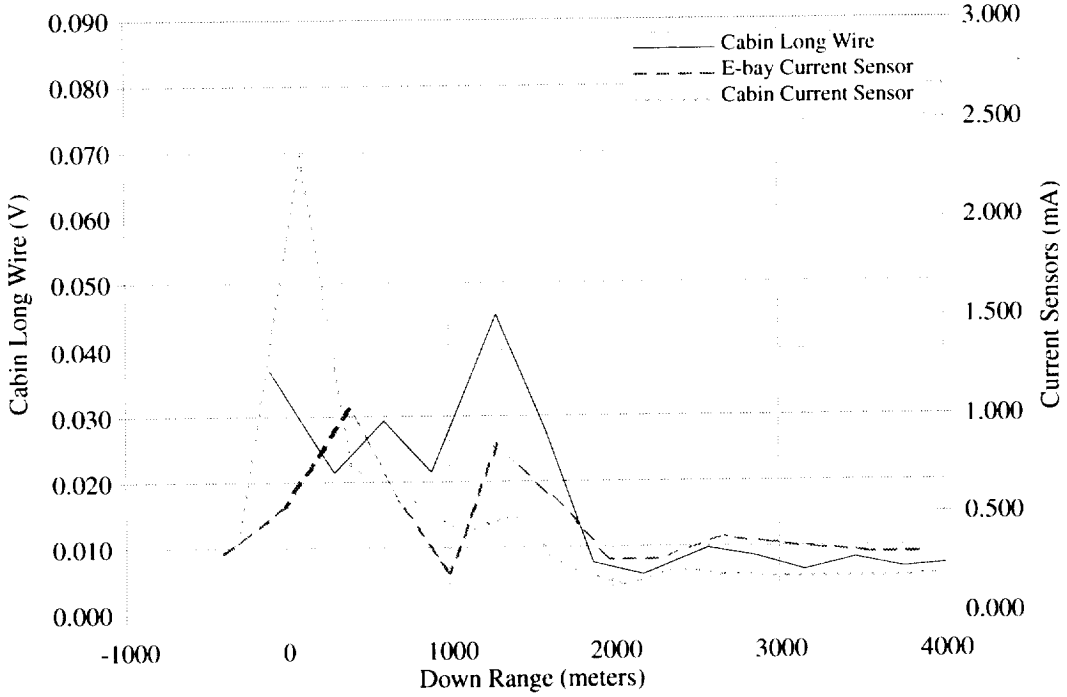

Figure A22. CLW and current measurements. 173 MHz; H-pol; inbound, "flaps."

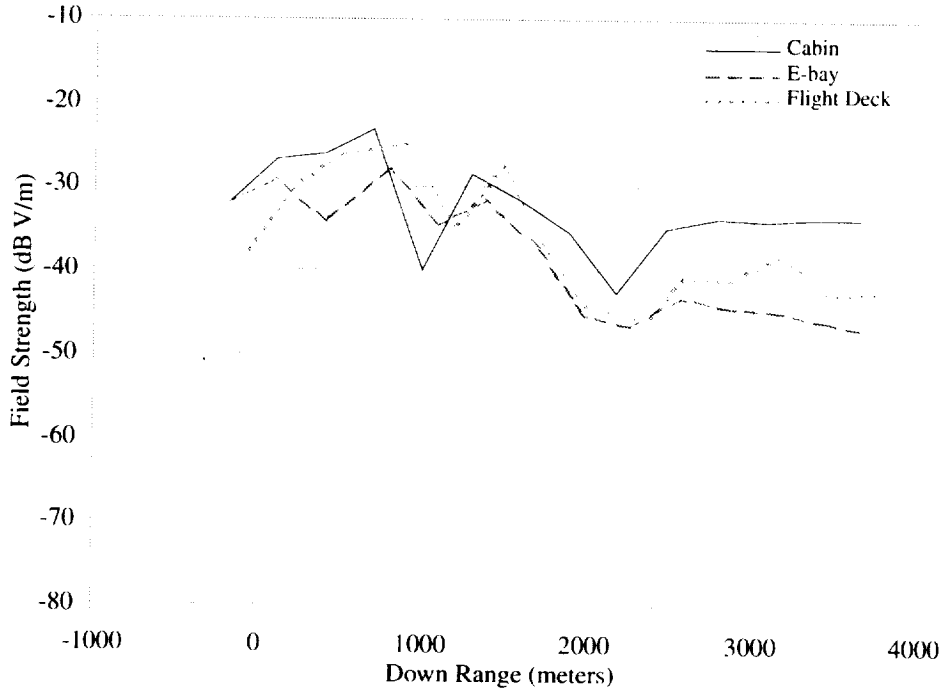

Figure A23. D-Dot measurements. 173 MHz; H-pol; inbound; "flaps & gear."

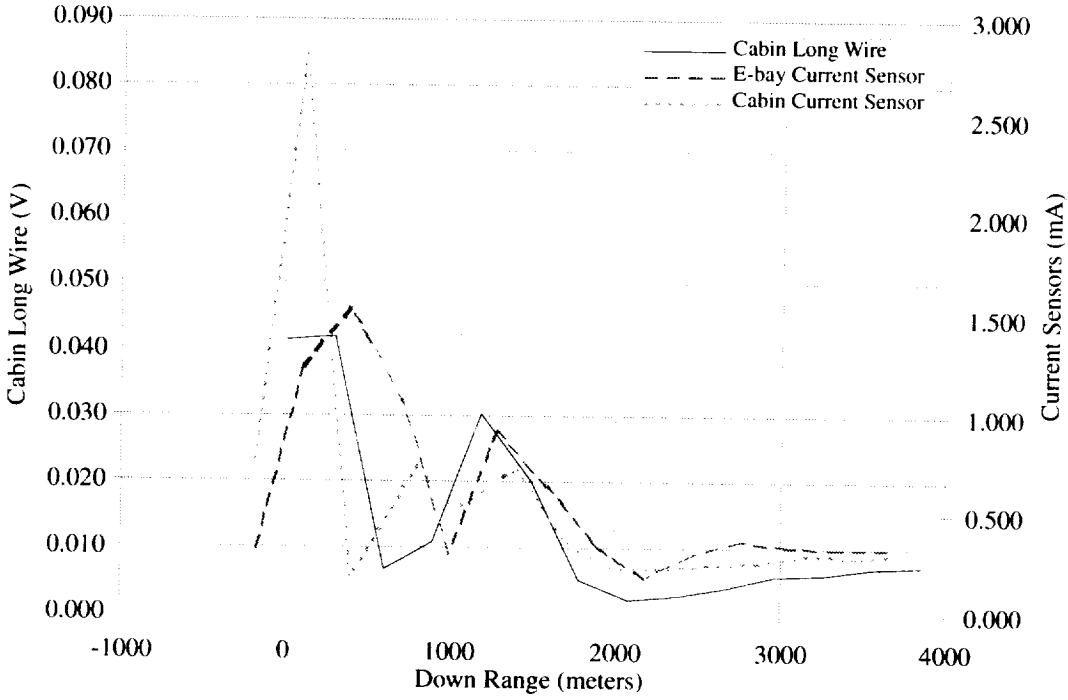

Figure A24. CLW and current measurements. 173 MHz; H-pol; inbound; "flaps & gear."

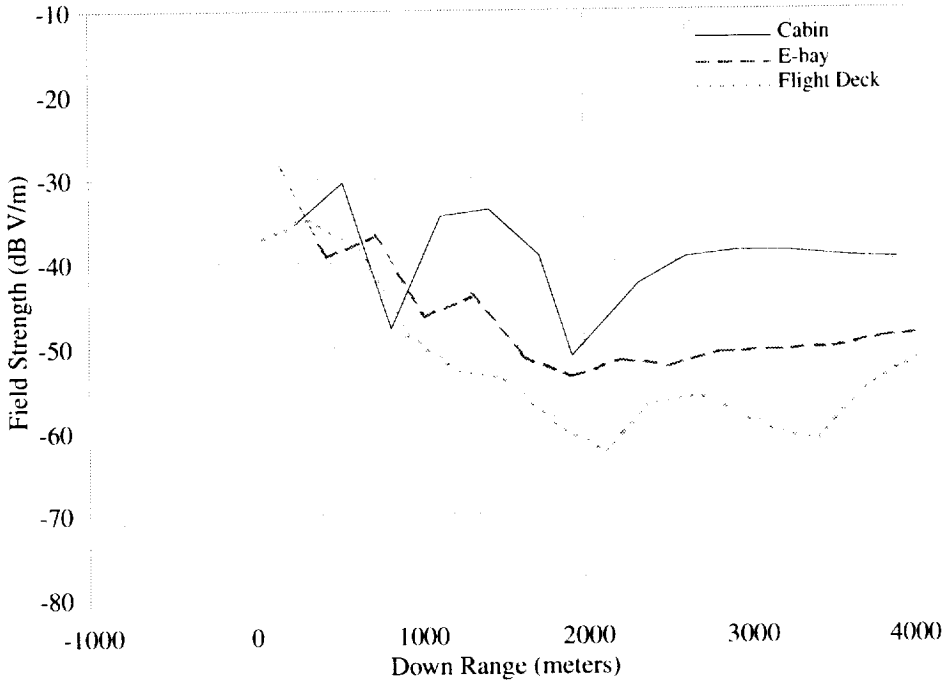

Figure A25. D-Dot measurements. 173 MHz; H-pol; outbound; "clean."

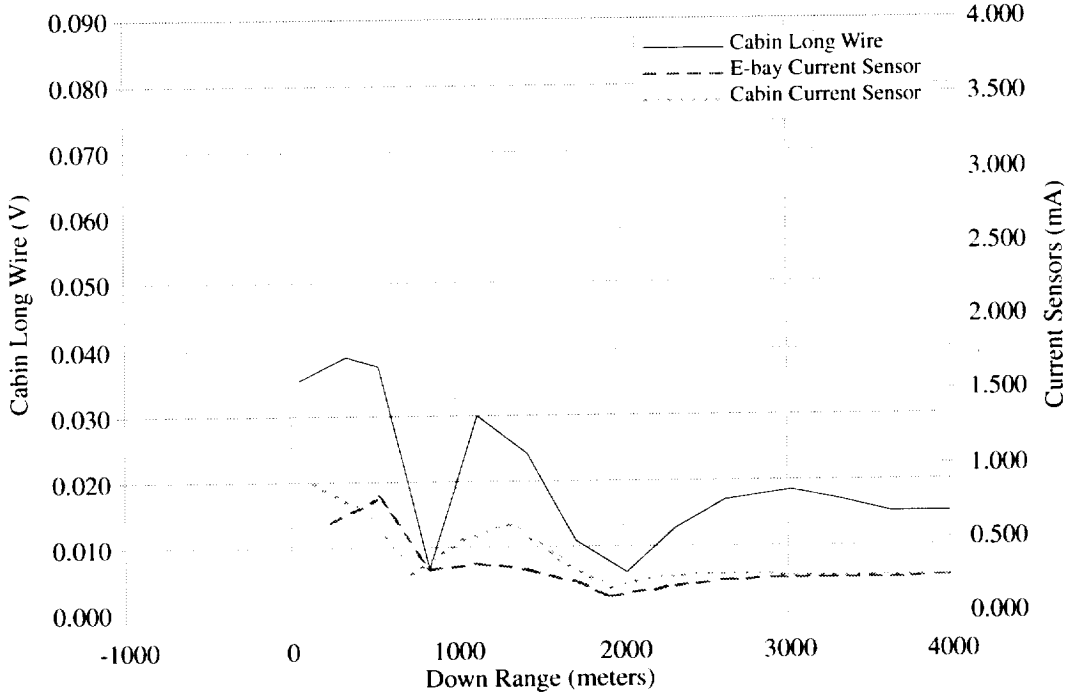

Figure A26. CLW and current measurements. 173 MHz; H-pol; outbound; "clean."

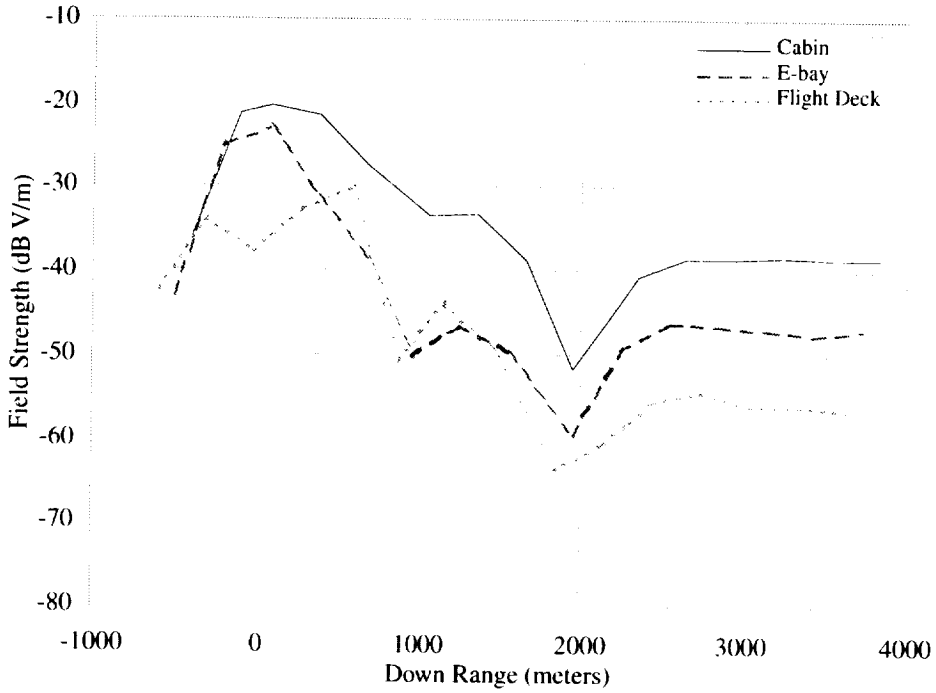

Figure A27. D-Dot measurements. 173 MHz; H-pol; outbound; "flaps."

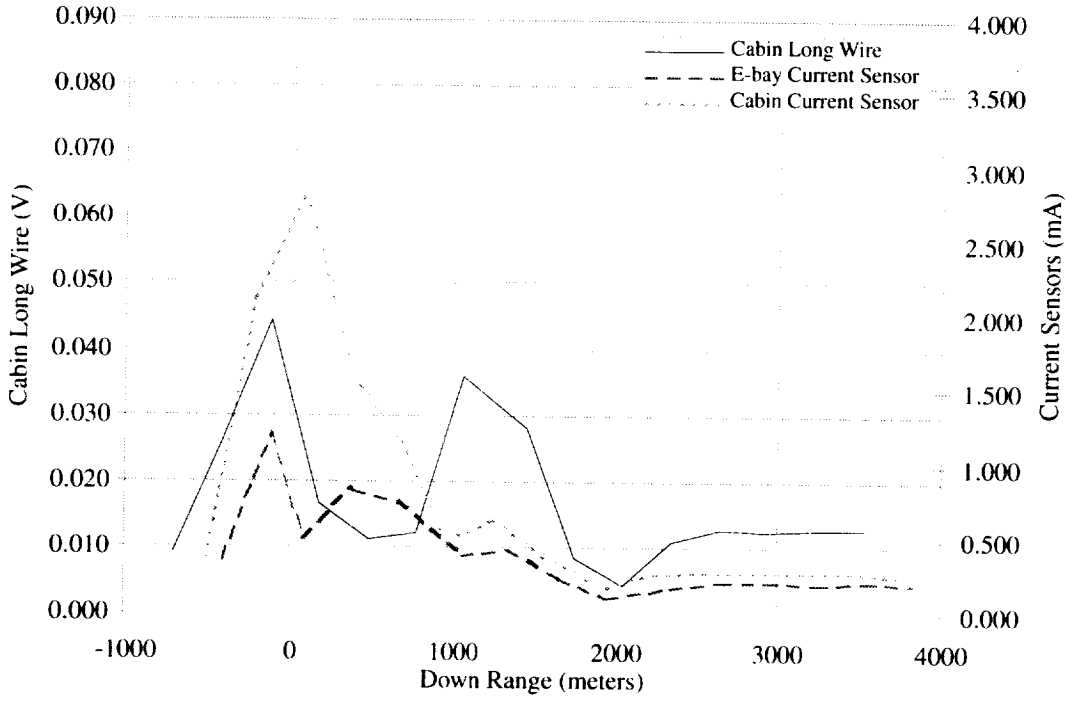

Figure A28. CLW and current measurements. 173 MHz; H-pol; outbound; "flaps."

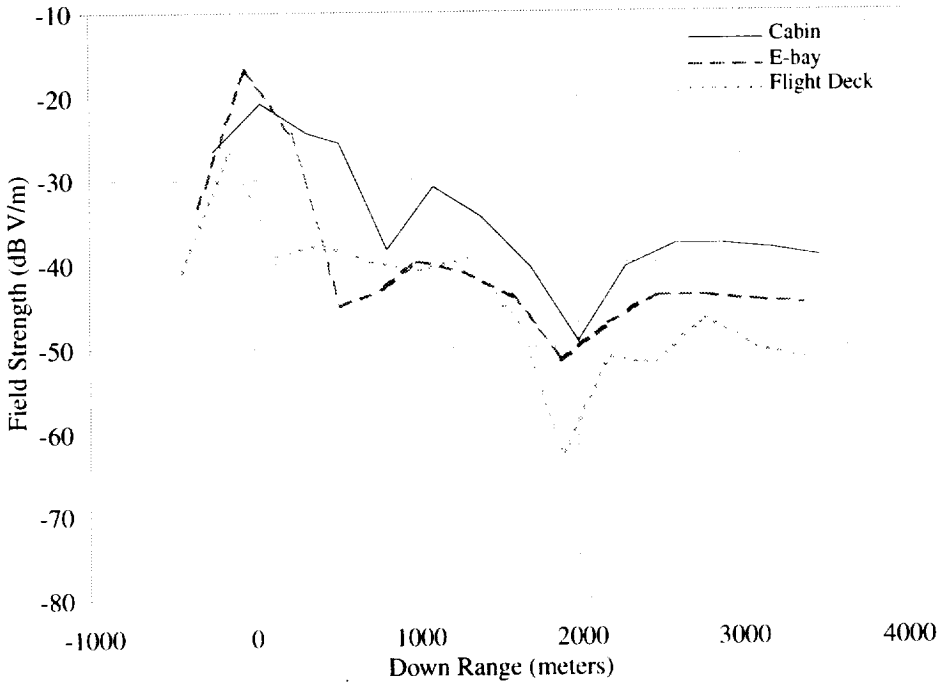

Figure A29. D-Dot measurements. 173 MHz; H-pol; outbound; "flaps & gear."

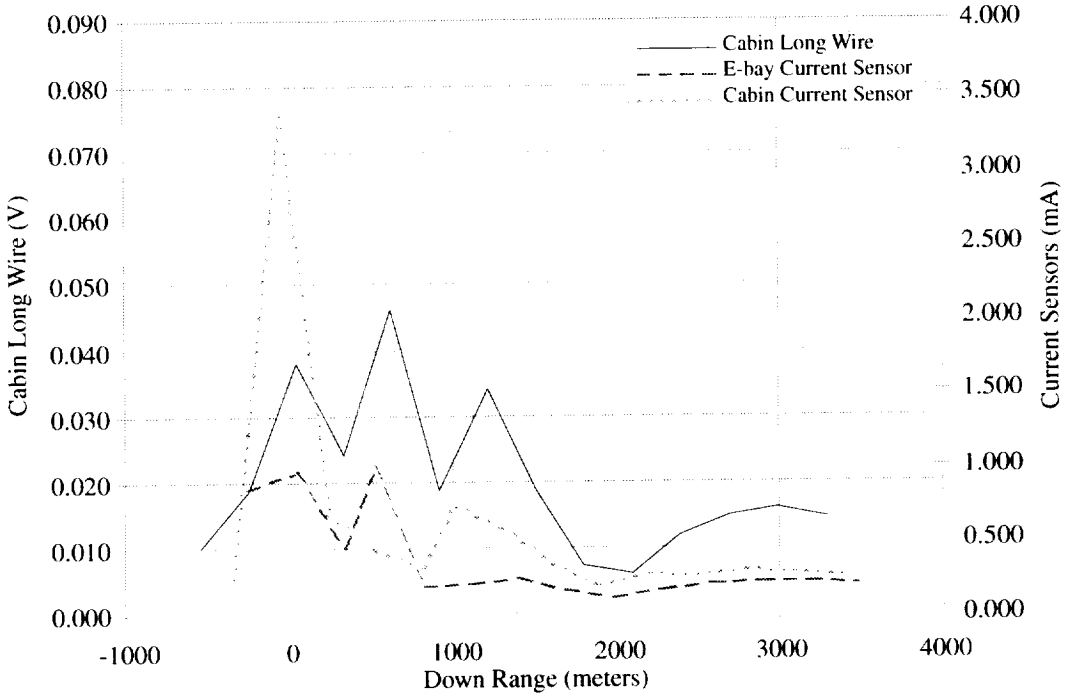

Figure A30. CLW and current measurements. 173 MHz; H-pol; outbound; "flaps & gear."

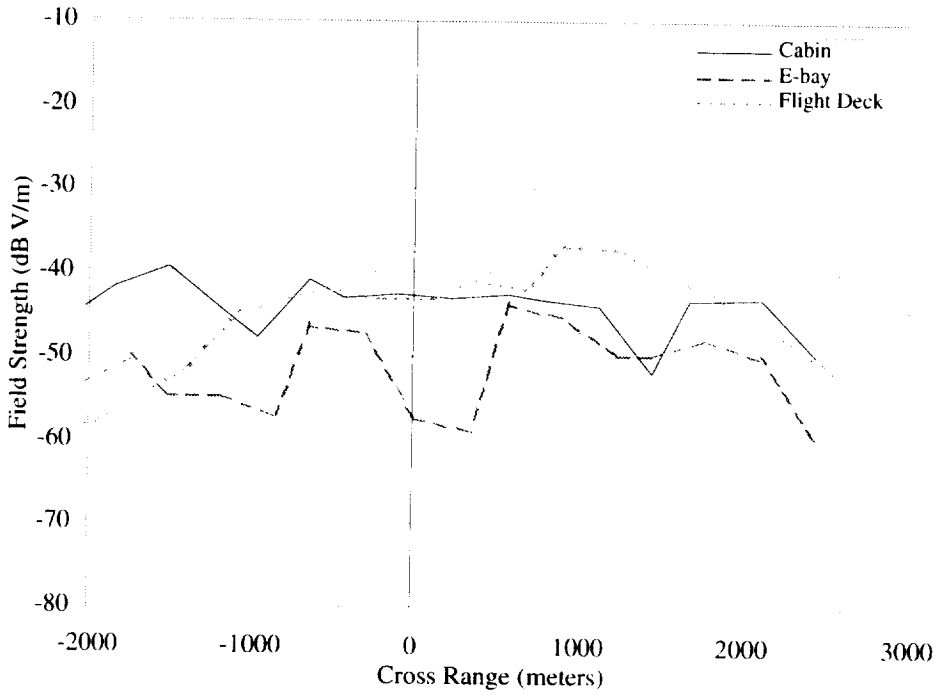

Figure A31. D-Dot measurements. 173 MHz; H-pol; crossbound: right incident; "clean."

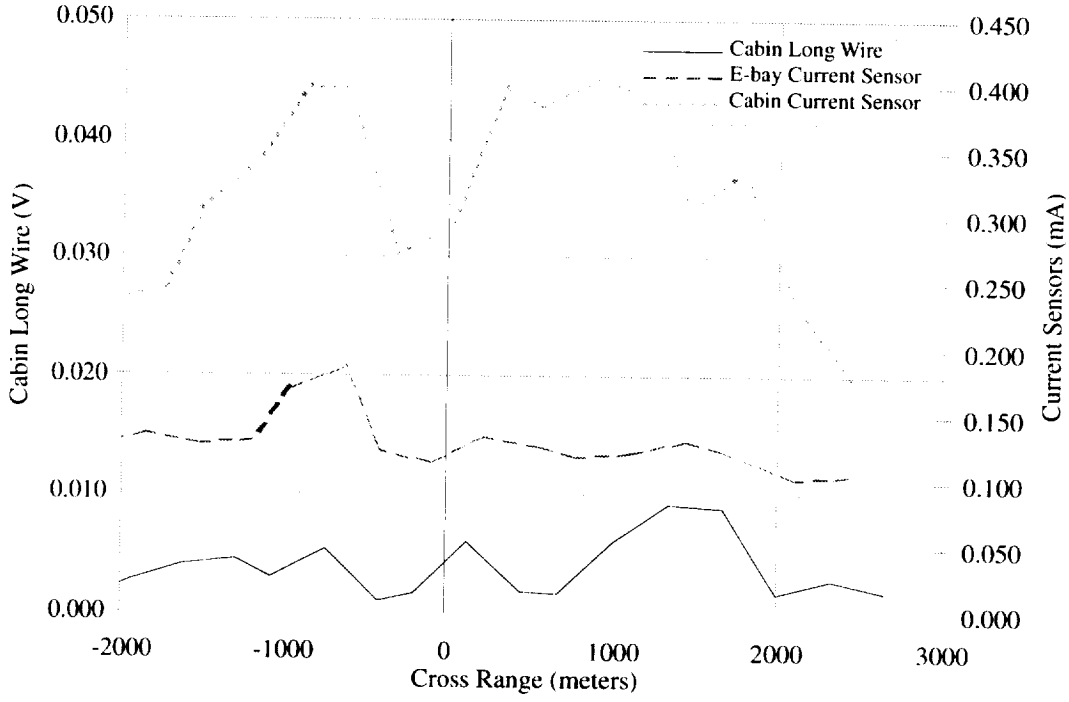

Figure A32. CLW and current measurements. 173 MHz; H-pol; crossbound; right incident; "clean."

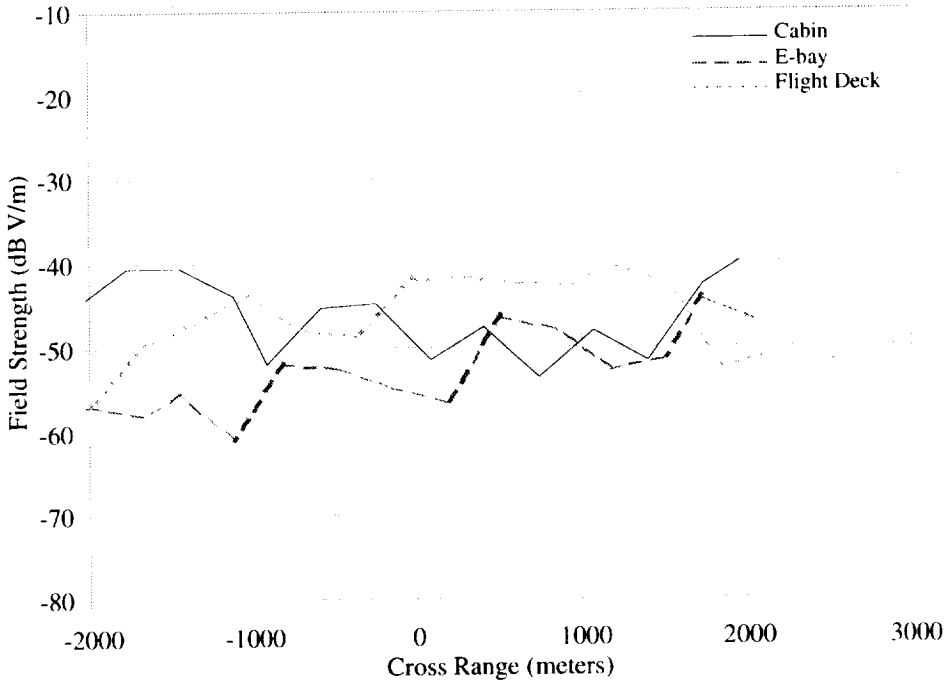

Figure A33. D-Dot measurements. 173 MHz; H-pol; crossbound; right incident; "flaps."

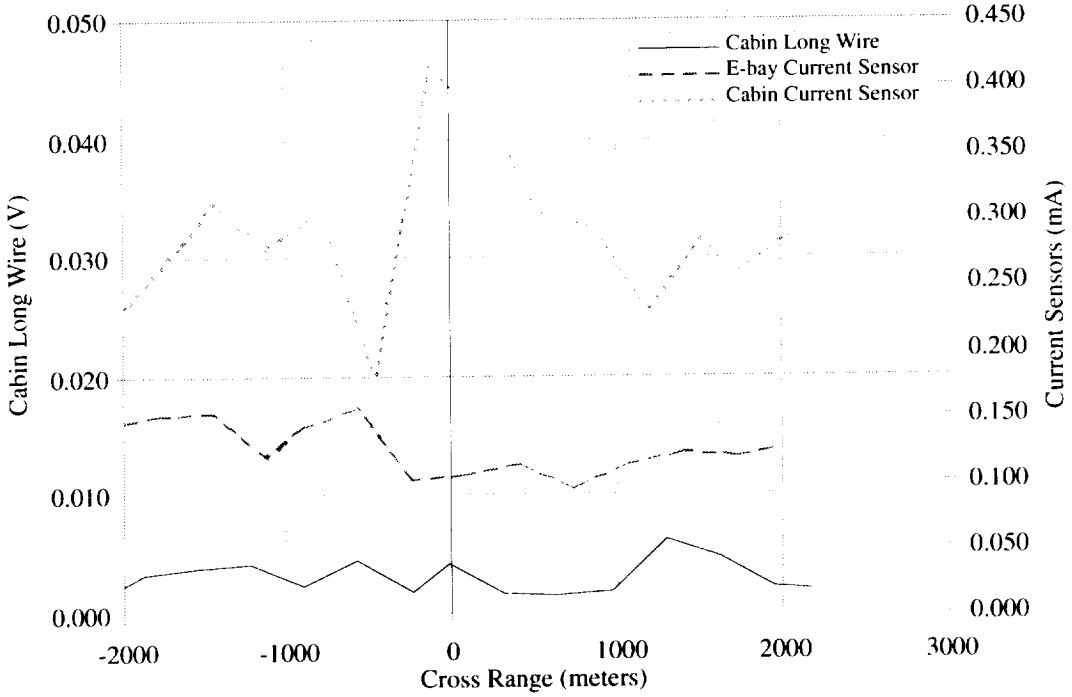

Figure A34. CLW and current measurements. 173 MHz; H-pol; crossbound; right incident; "flaps."

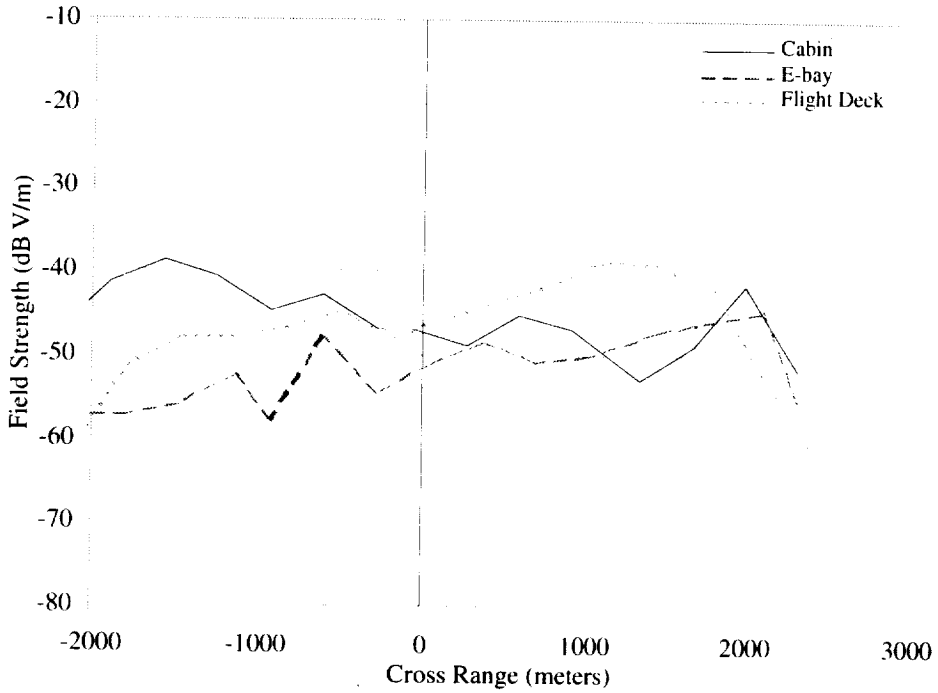

Figure A35. D-Dot measurements. 173 MHz; H-pol; crossbound; right incident; "flaps & gear."

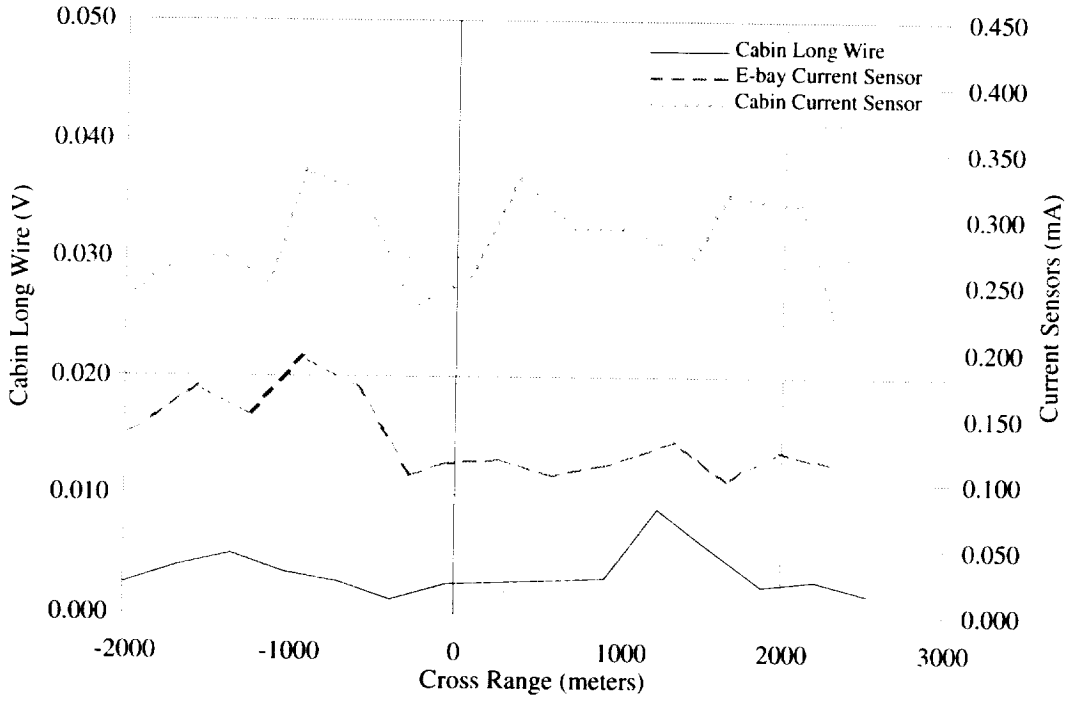

Figure A36. CLW and current measurements. 173 MHz; H-pol; crossbound; right incident; "flaps & gear."

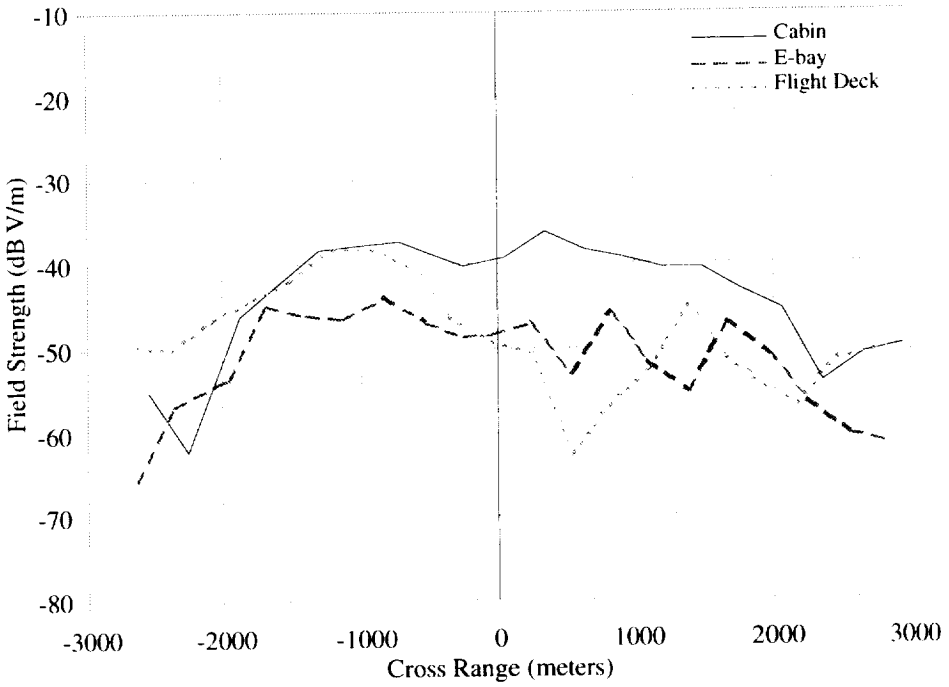

Figure A37. D-Dot measurements. 173 MHz; H-pol; crossbound; left incident; "clean."

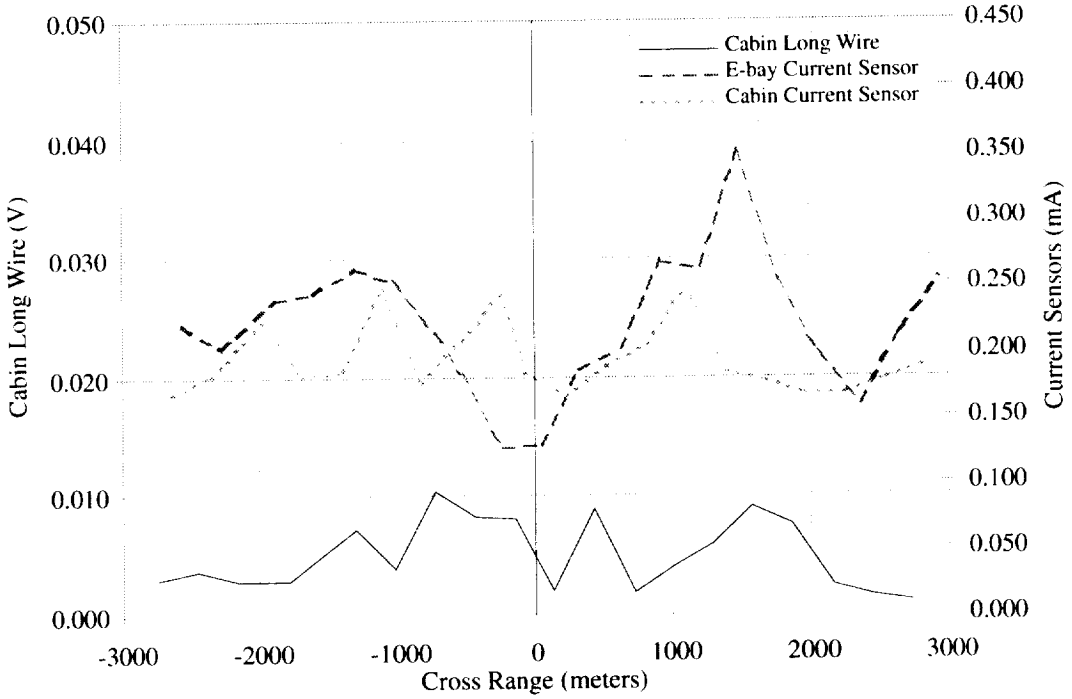

Figure A38. CLW and current measurements. 173 MHz; H-pol; crossbound; left incident; "clean."

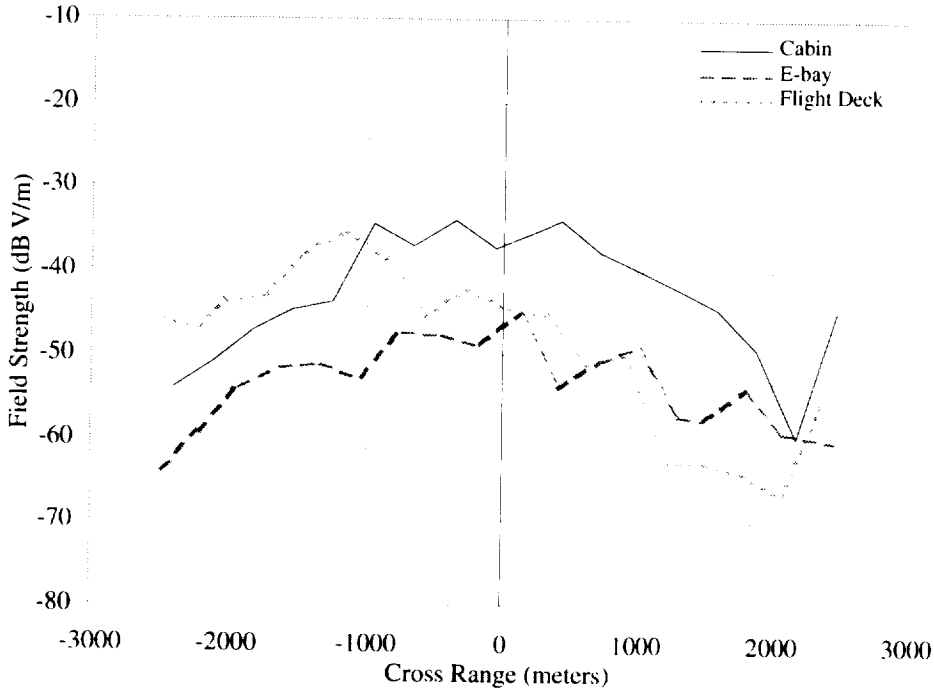

Figure A39. D-Dot measurements. 173 MHz; H-pol; crossbound; left incident; "flaps."

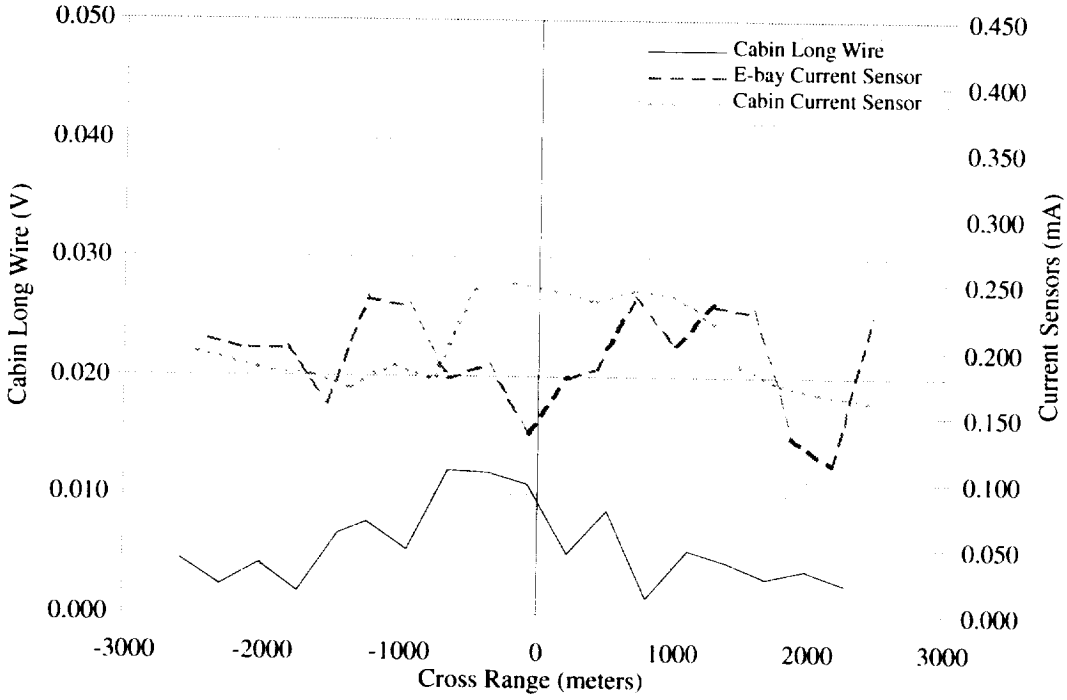

Figure A40. CLW and current measurements. 173 MHz; H-pol; crossbound; left incident; "flaps."

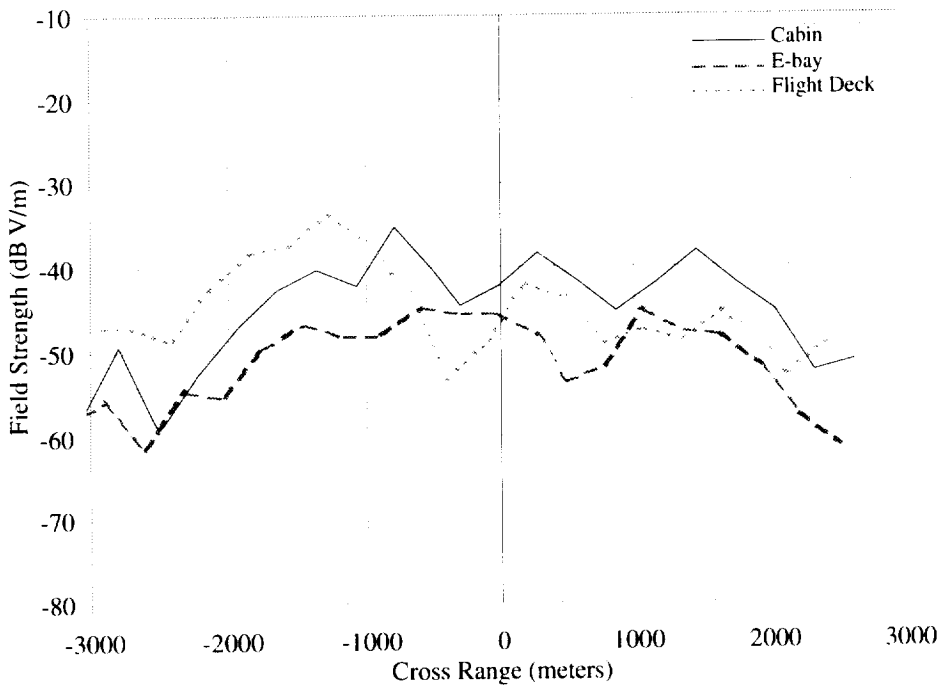

Figure A41. D-Dot measurements. 173 MHz; H-pol; crossbound; left incident; "flaps & gear."

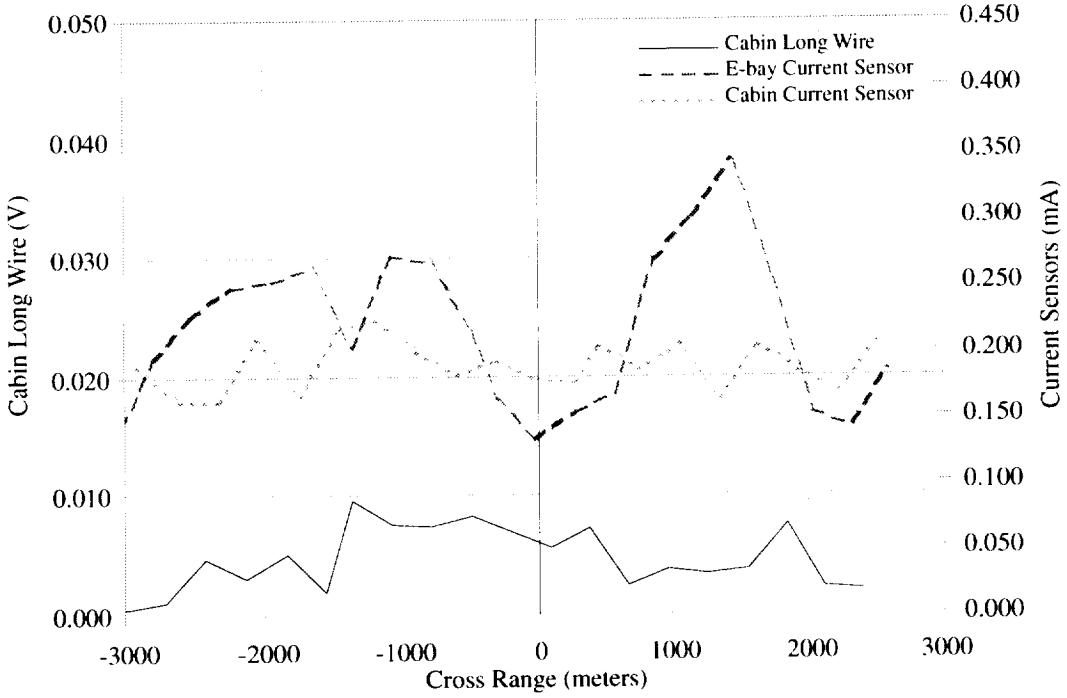

Figure A42. CLW and current measurements. 173 MHz; H-pol; crossbound; left incident; "flaps & gear."

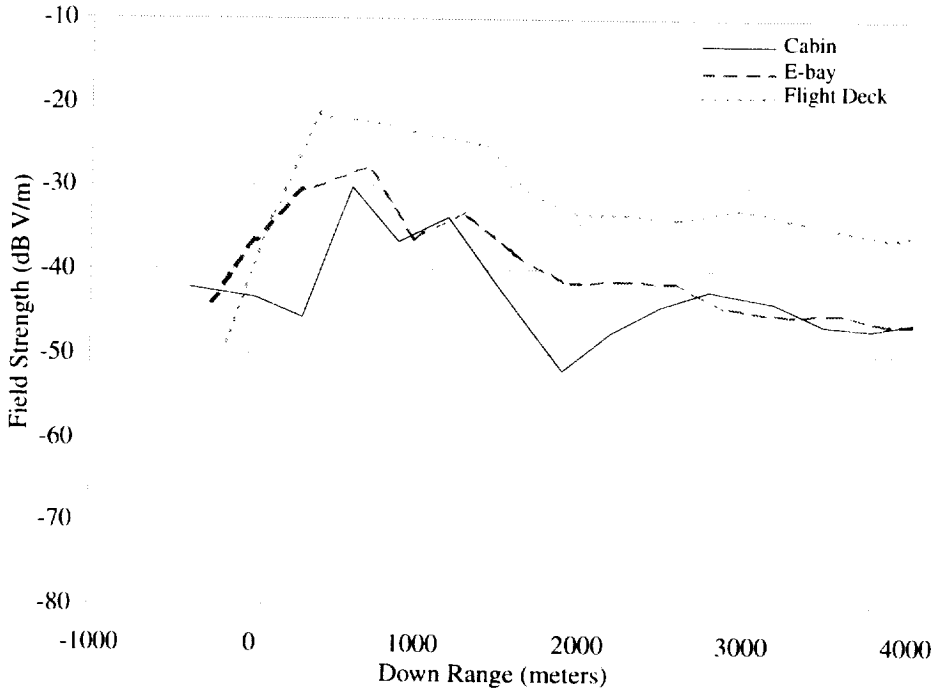

Figure A43. D-Dot measurements. 173 MHz; V-pol; inbound; "clean."

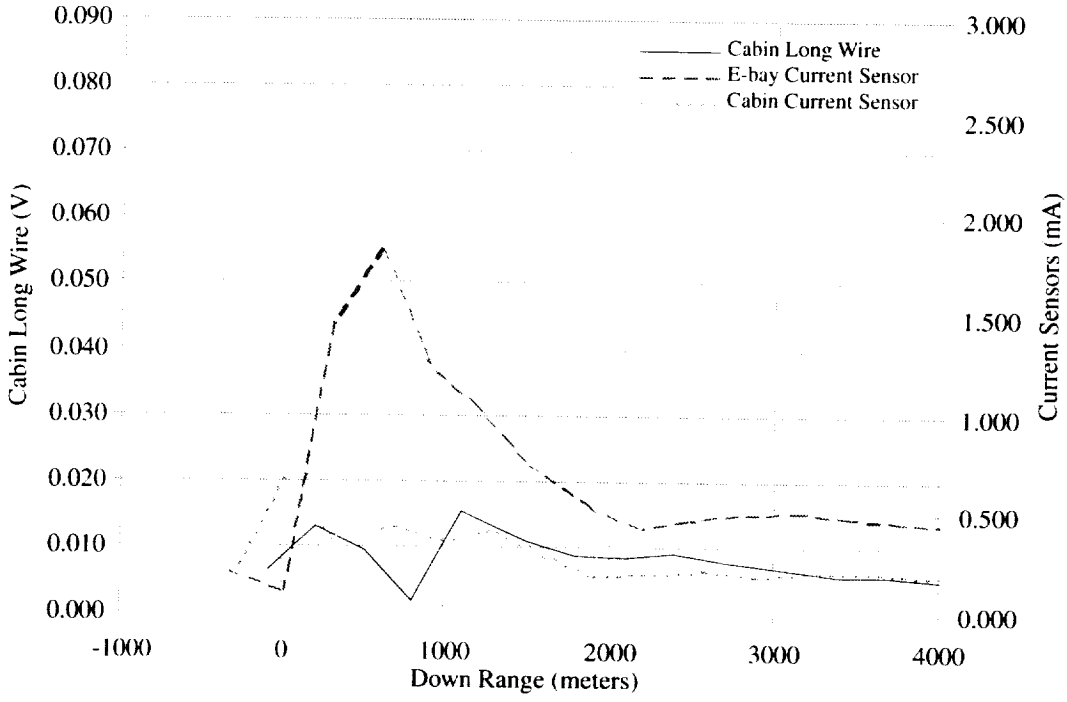

Figure A44. CLW and current measurements. 173 MHz; V-pol; inbound; "clean."

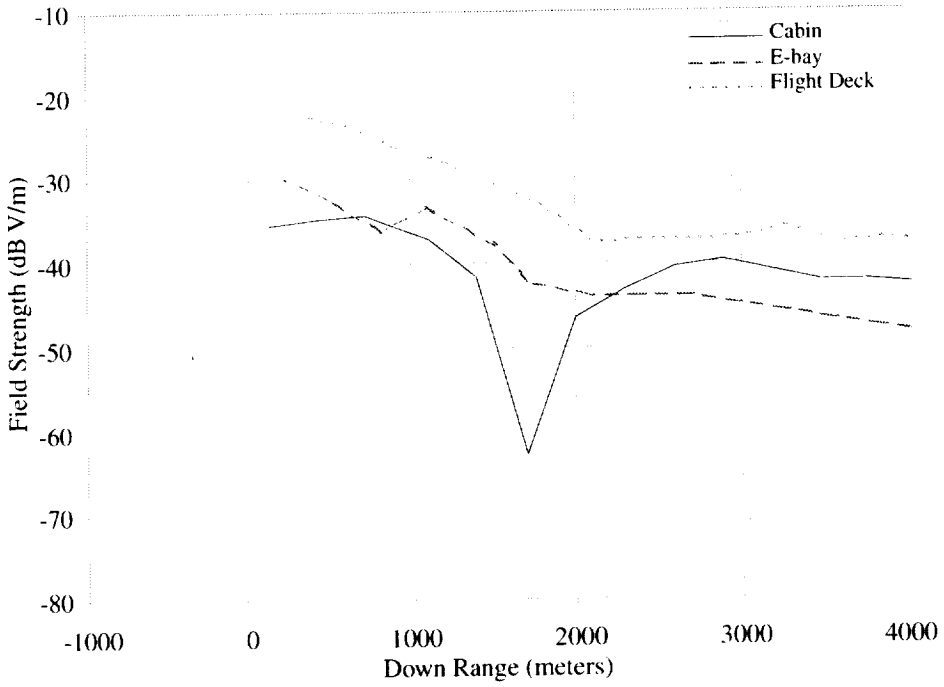

Figure A45. D-Dot measurements. 173 MHz; V-pol; inbound; "flaps."

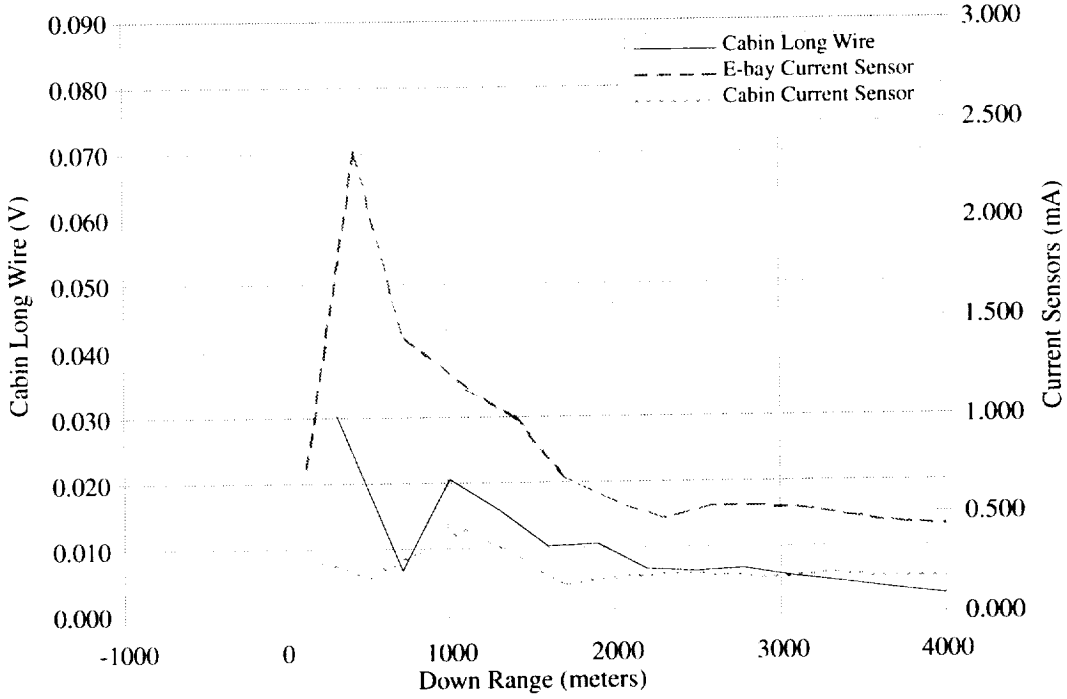

Figure A46. CLW and current measurements. 173 MHz; V-pol; inbound; "flaps."

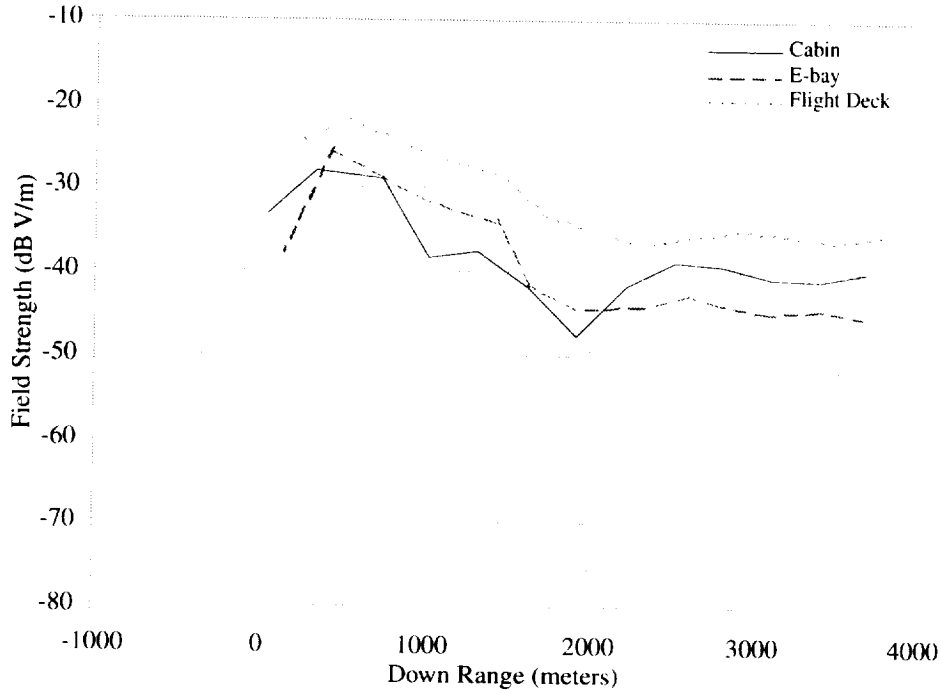

Figure A47. D-Dot measurements. 173 MHz; V-pol; inbound; "flaps & gear."

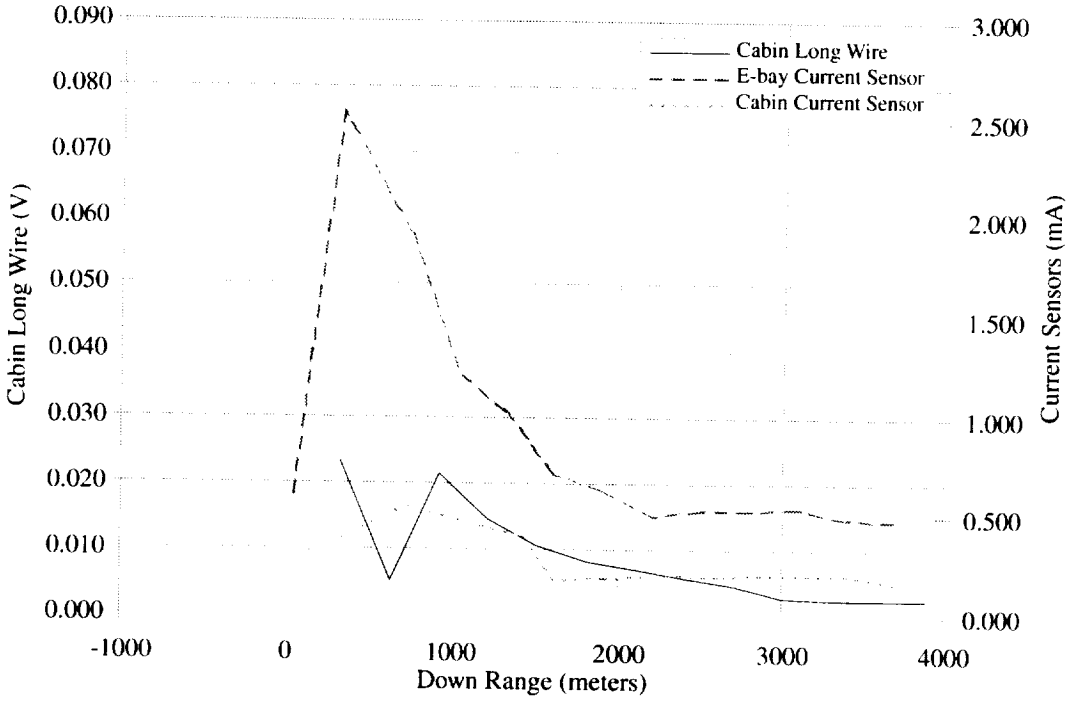

Figure A48. CLW and current measurements. 173 MHz; V-pol; inbound; "flaps & gear."

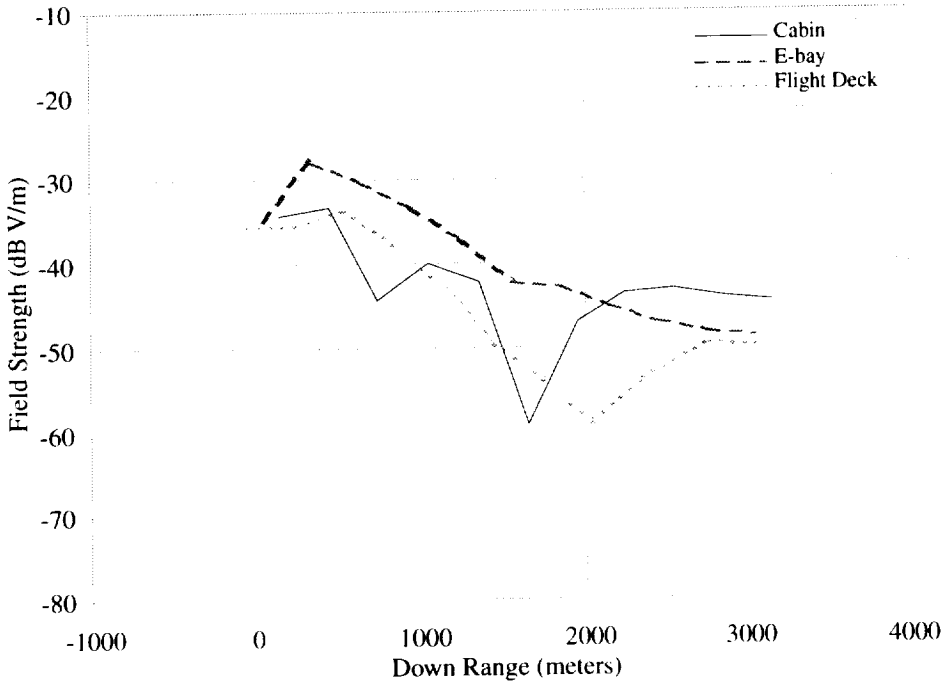

Figure A49. D-Dot measurements. 173 MHz; V-pol; outbound; "clean."

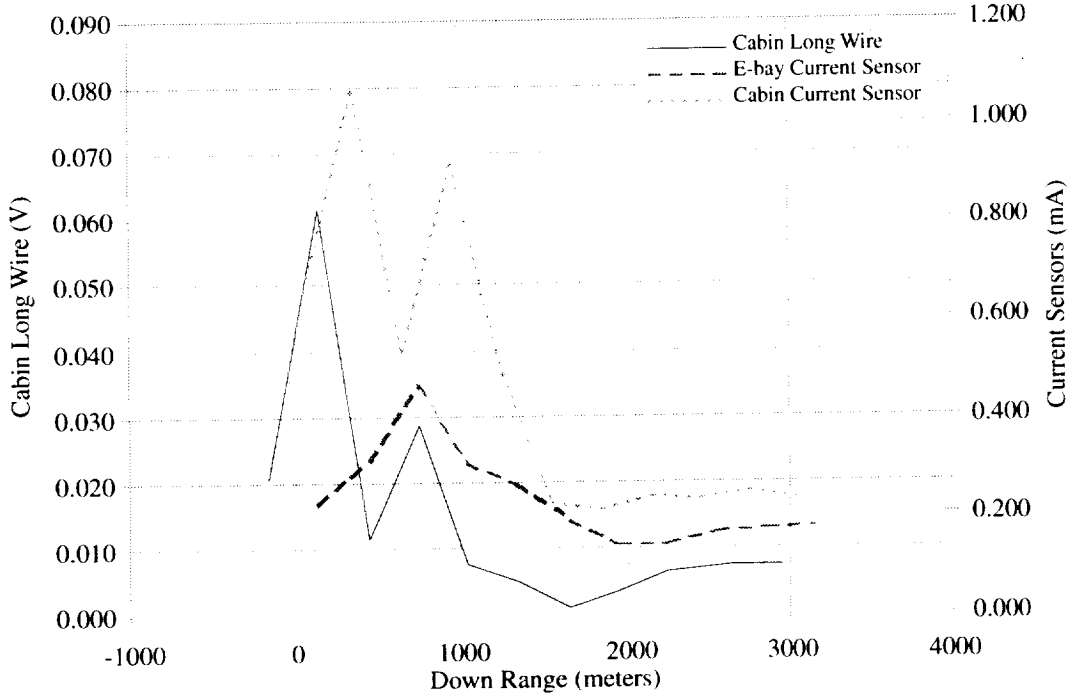

Figure A50. CLW and current measurements. 173 MHz; V-pol; outbound; "clean."

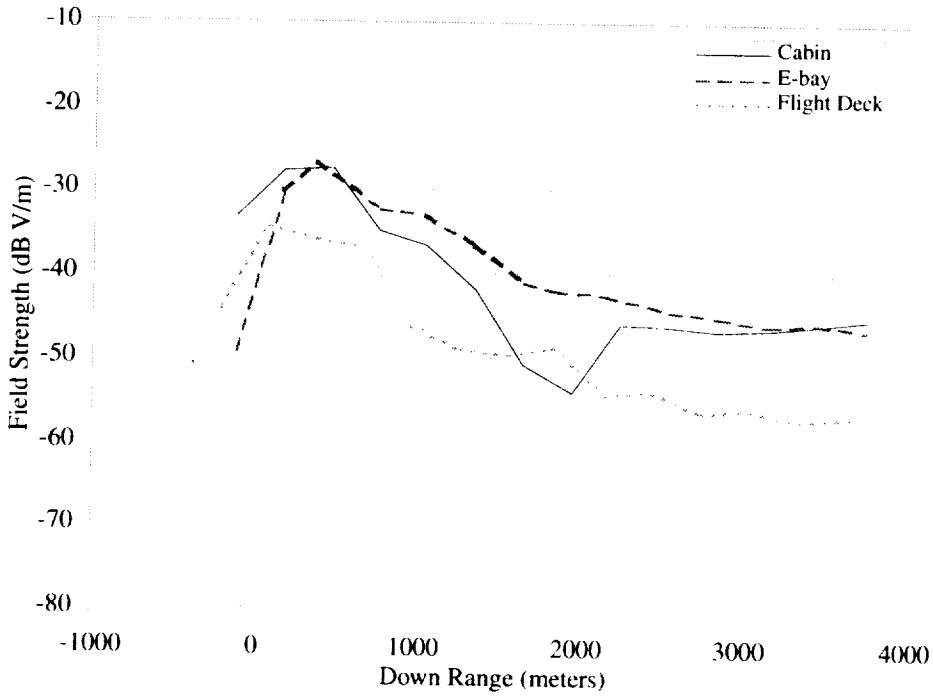

Figure A51. D-Dot measurements. 173 MHz; V-pol; outbound; "flaps."

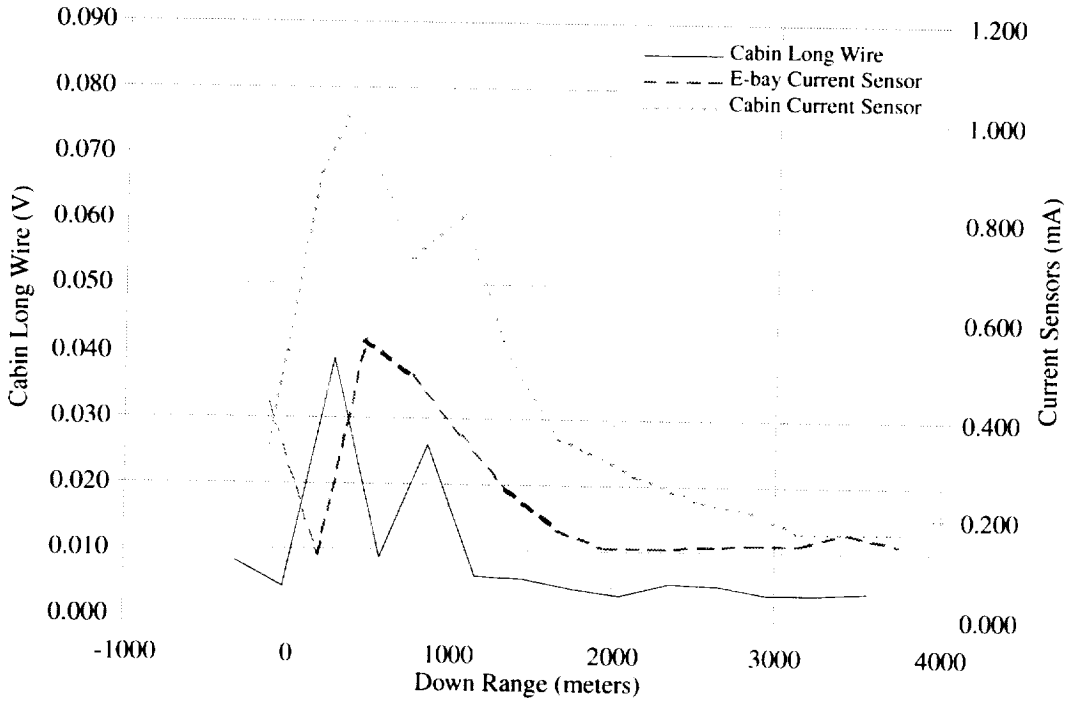

Figure A52. CLW and current measurements. 173 MHz; V-pol; outbound; "flaps."

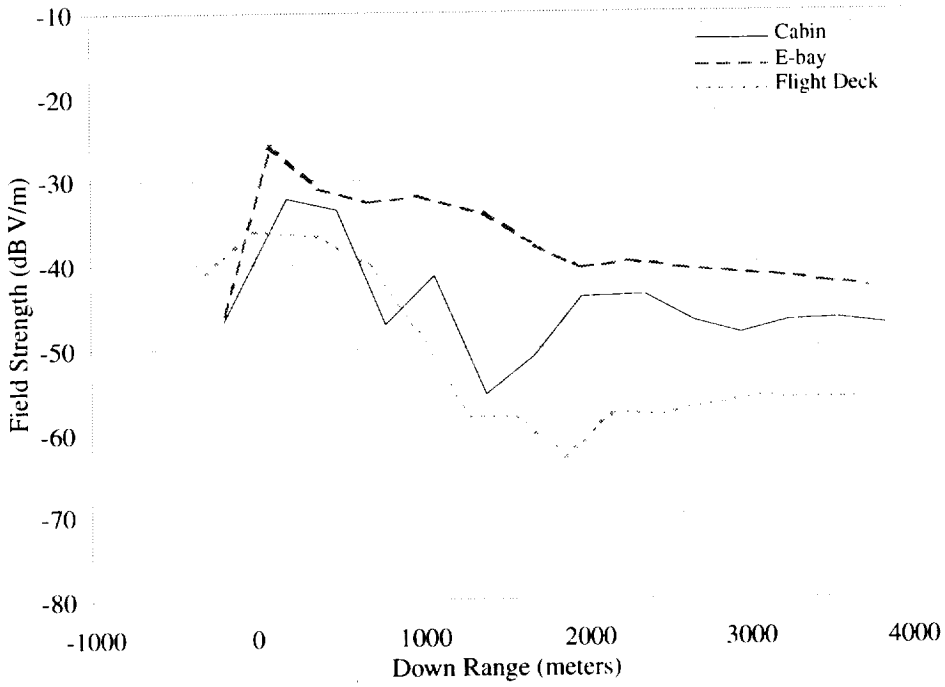

Figure A53. D-Dot measurements. 173 MHz;V-pol; outbound; "flaps & gear."

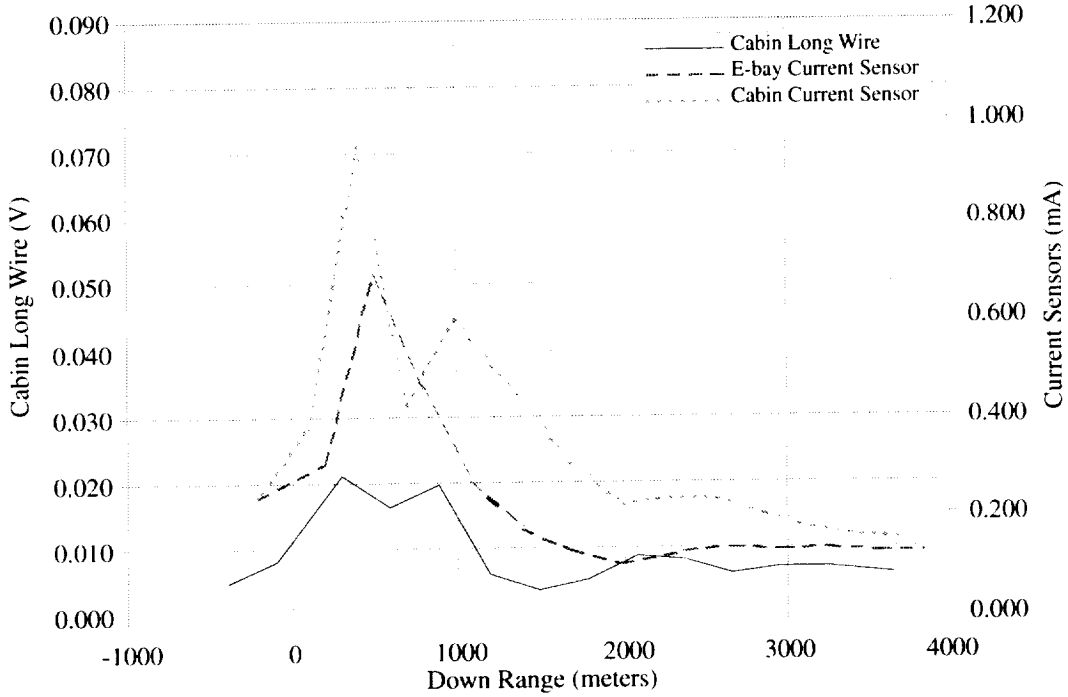

Figure A54. CLW and current measurements. 173 MHz; V-pol; outbound; "flaps & gear."

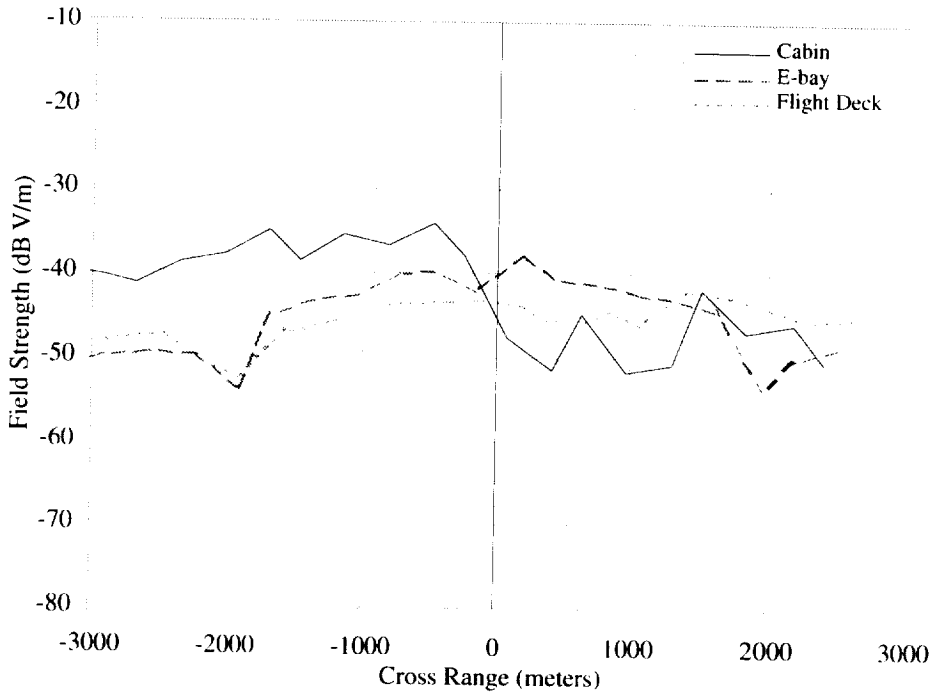

Figure A55. D-Dot measurements. 173 MHz; V-pol; crossbound; right incident; "clean."

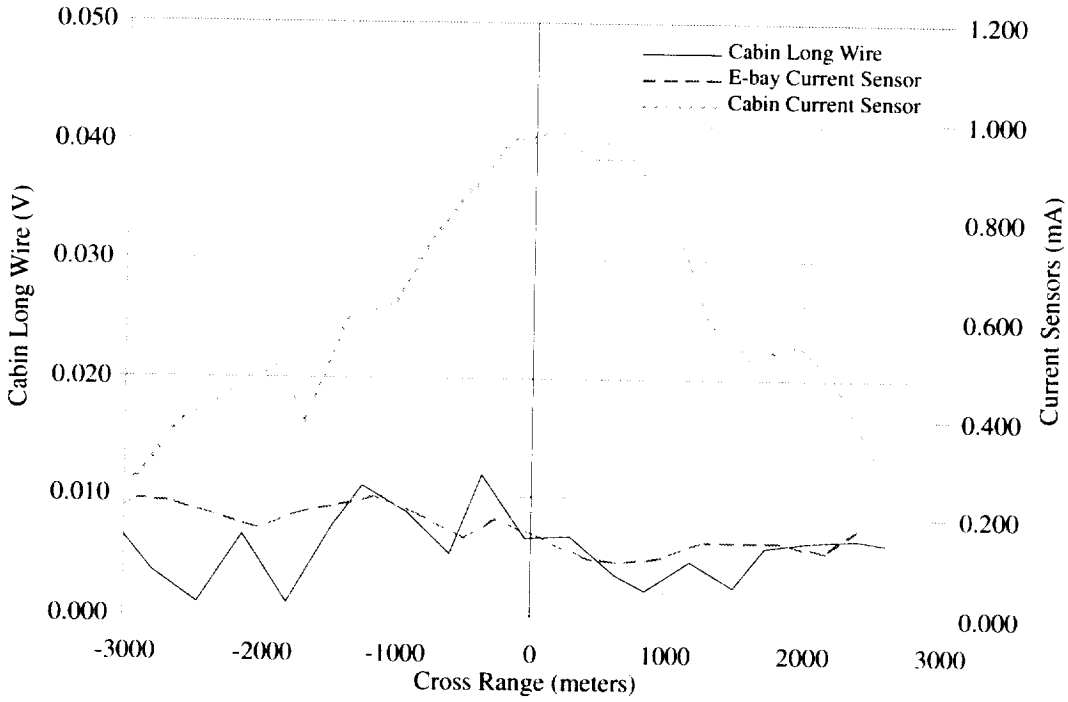

Figure A56. CLW and current measurements. 173 MHz; V-pol; crossbound; right incident; "clean."

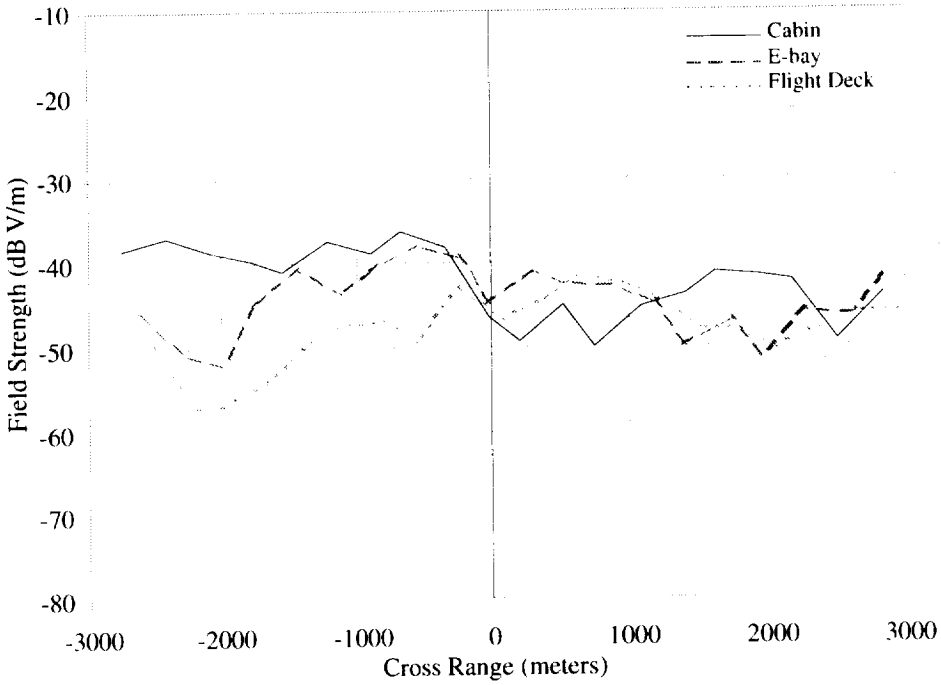

Figure A57. D-Dot measurements. 173 MHz; V-pol; crossbound; right incident; "flaps."

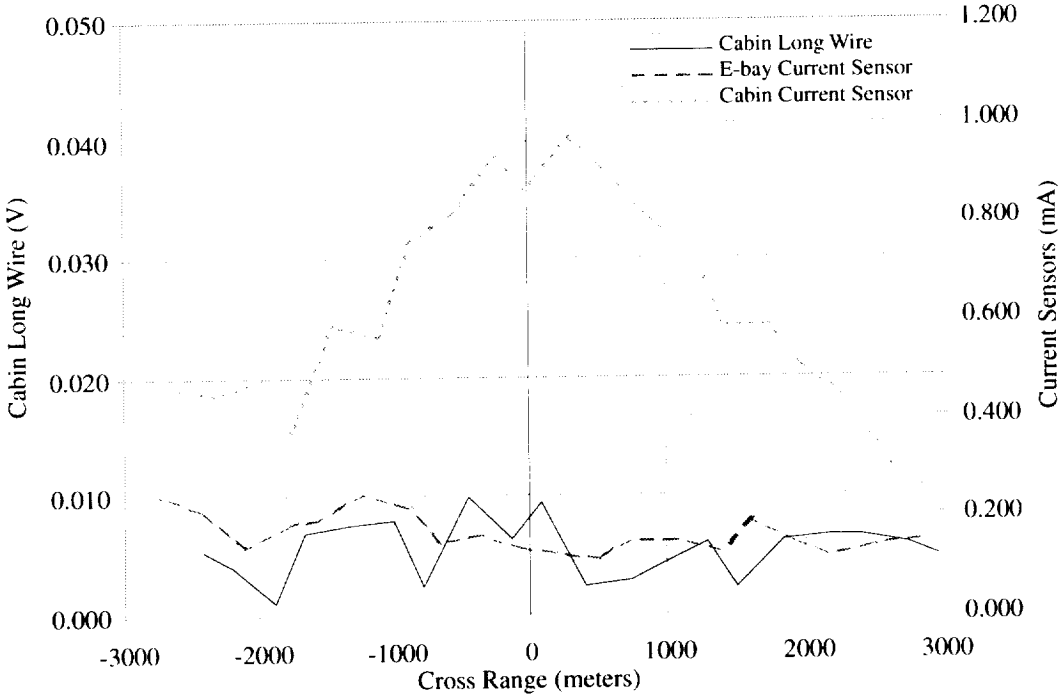

Figure A58. CLW and current measurements. 173 MHz; V-pol; crossbound; right incident; "flaps."

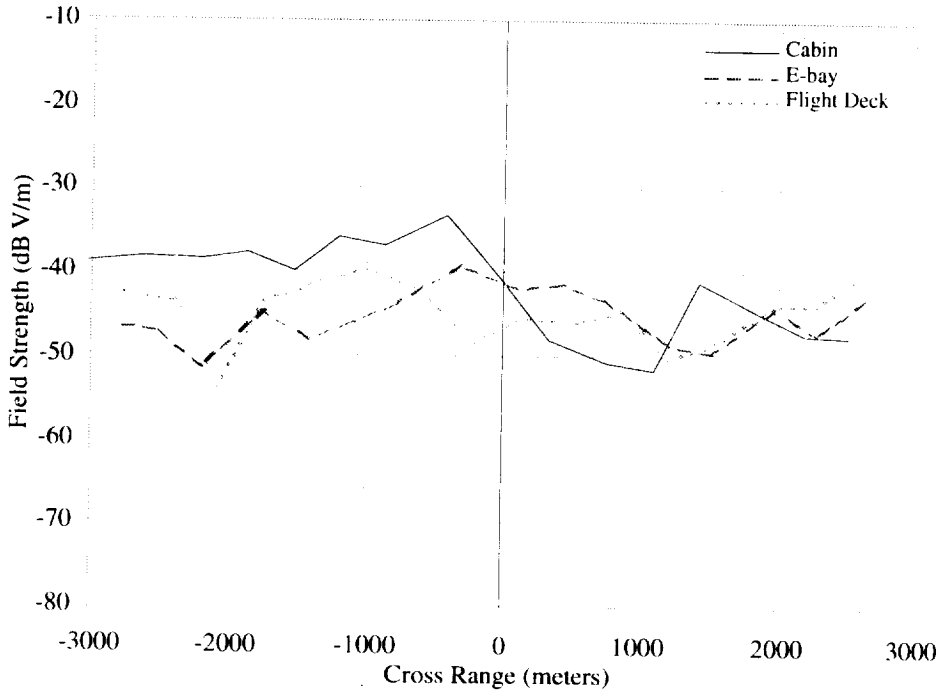

Figure A59. D-Dot measurements. 173 MHz; V-pol; crossbound; right incident; "flaps & gear."

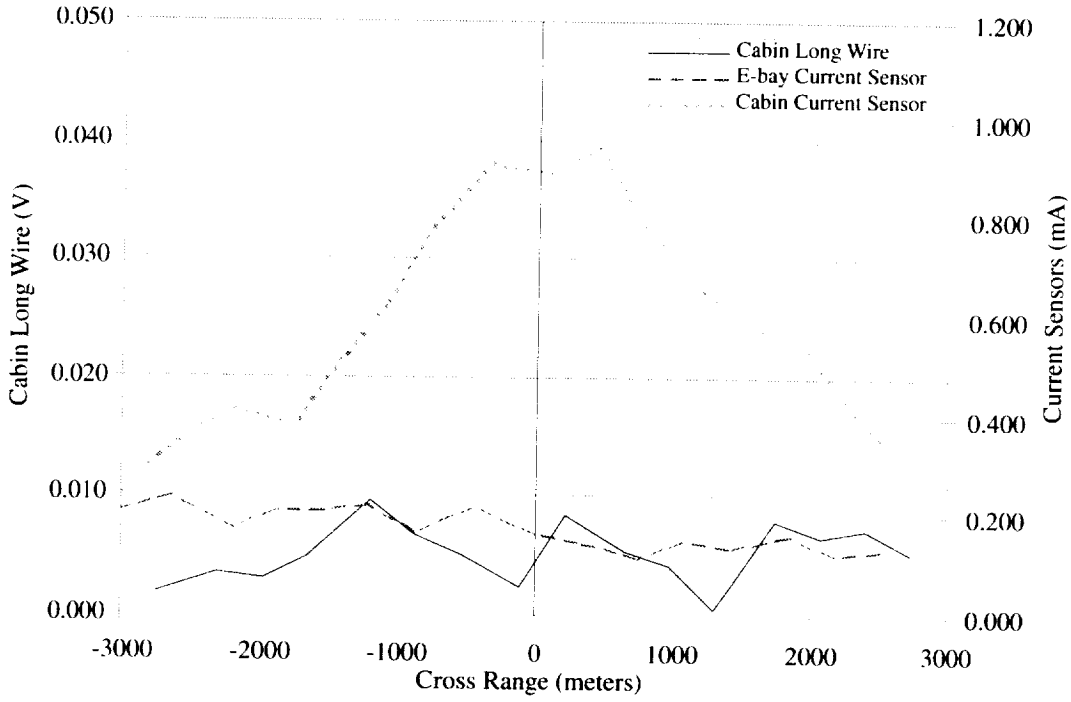

Figure A60. CLW and current measurements. 173 MHz; V-pol; crossbound; right incident; "flaps & gear."

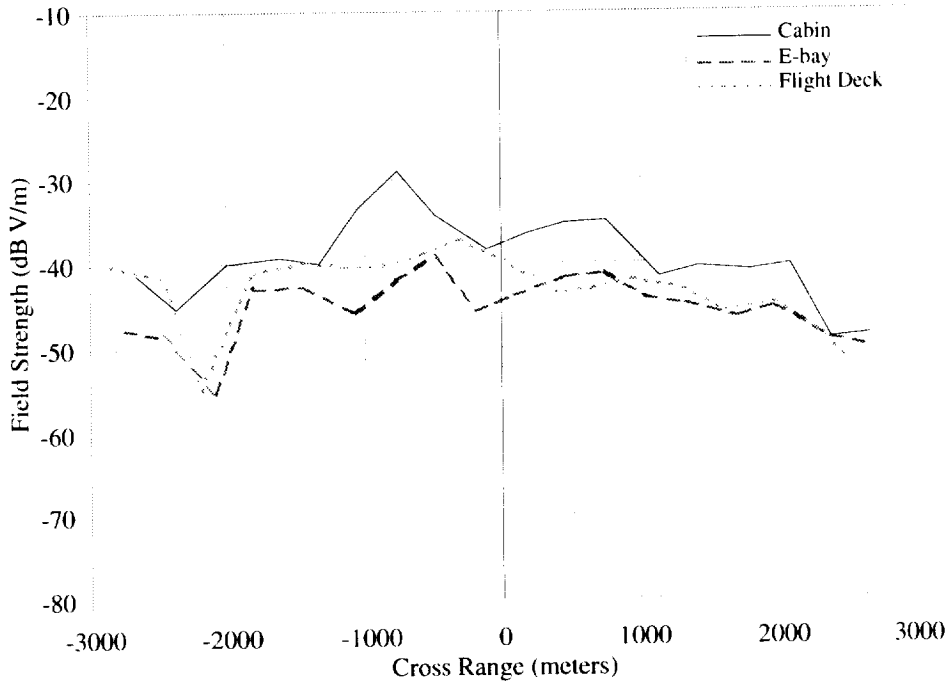

Figure A61. D-Dot measurements. 173 MHz; V-pol; crossbound; left incident: "clean."

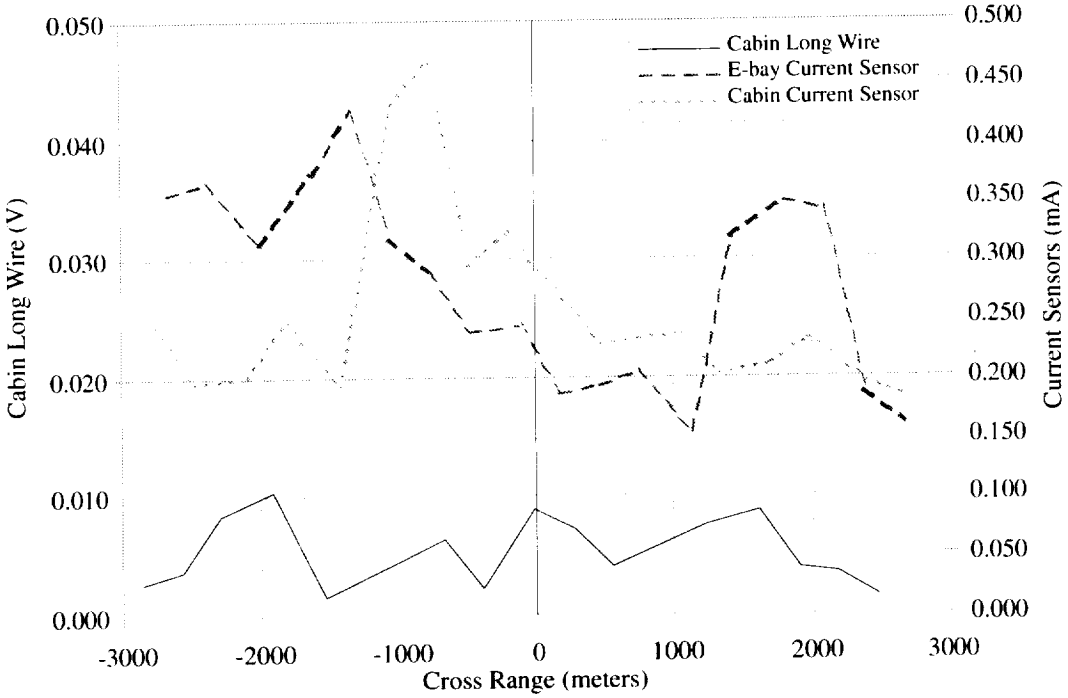

Figure A62. CLW and current measurements. 173 MHz; V-pol; crossbound; left incident; "clean."

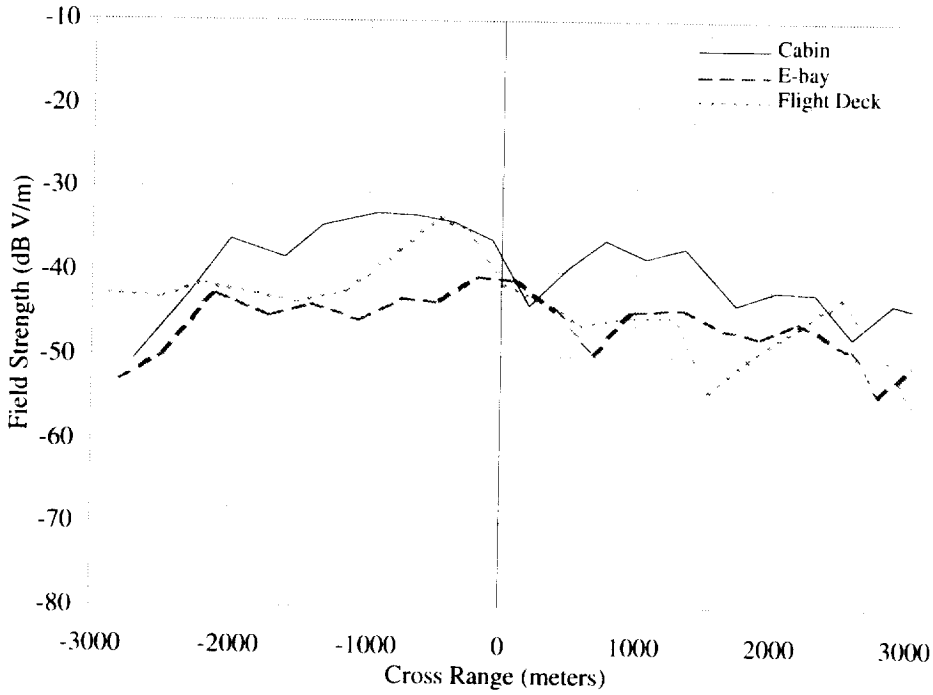

Figure A63. D-Dot measurements. 173 MHz; V-pol; crossbound; left incident; "flaps."

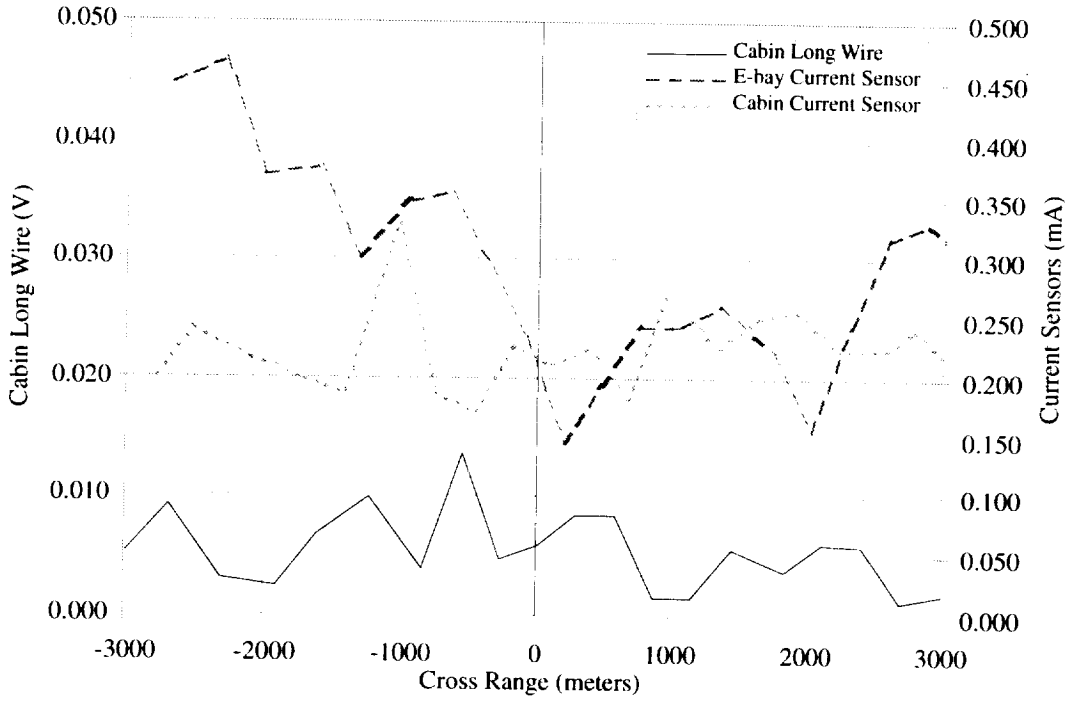

Figure A64. CLW and current measurements. 173 MHz; V-pol; crossbound; left incident; "flaps."

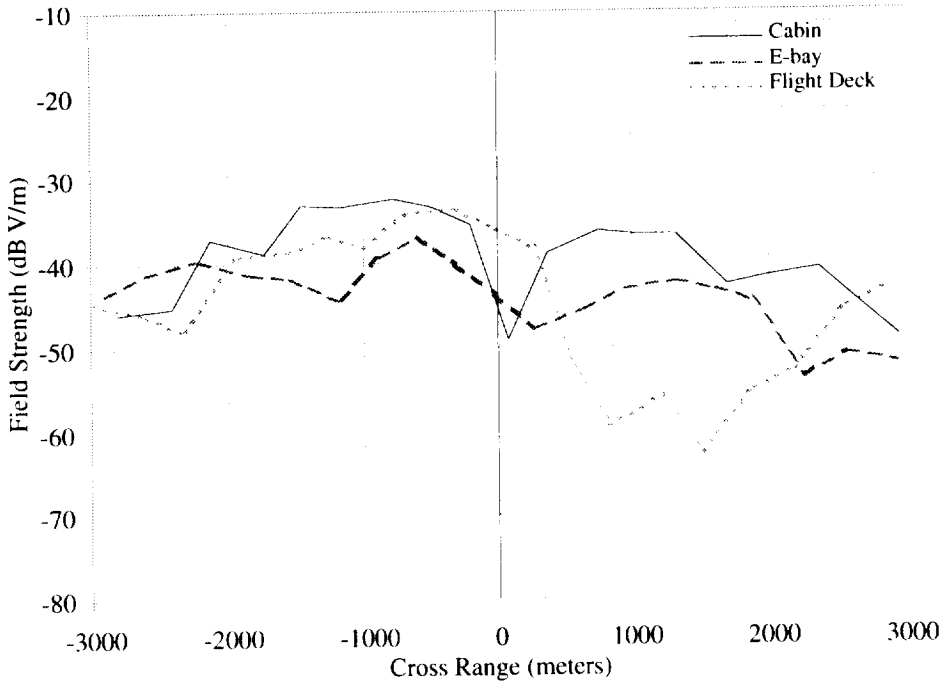

Figure A65. D-Dot measurements. 173 MHz; V-pol; crossbound; left incident; "flaps & gear."

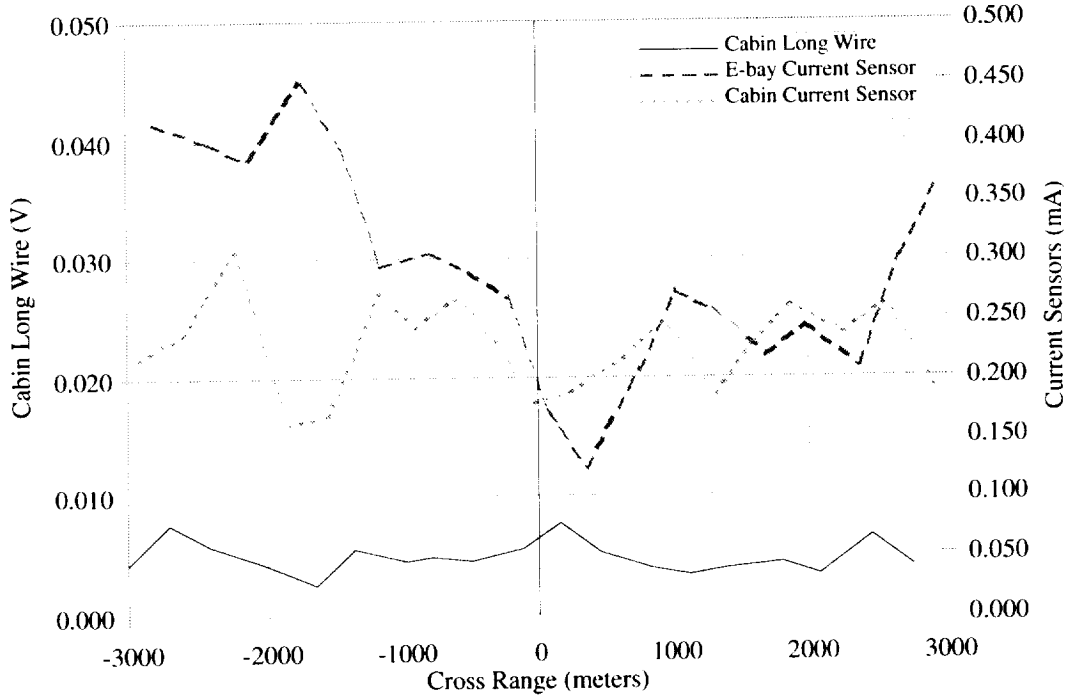

Figure A66. CLW and current measurements. 173 MHz; V-pol; crossbound; left incident; "flaps & gear."

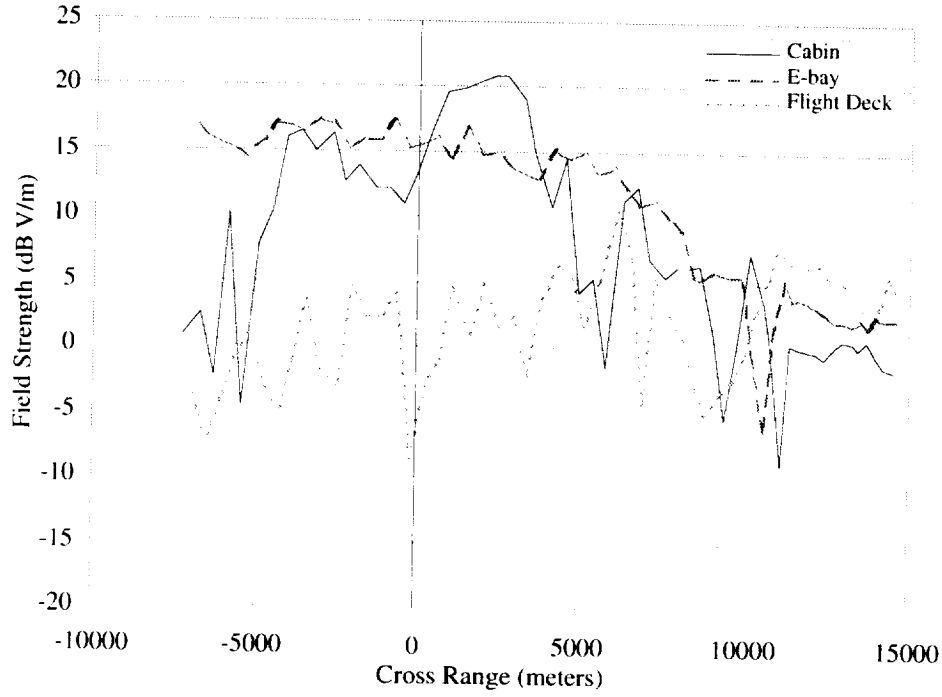

Figure A67. D-Dot measurements. 430 MHz; V-pol; inbound to crossbound; right incident; "clean."

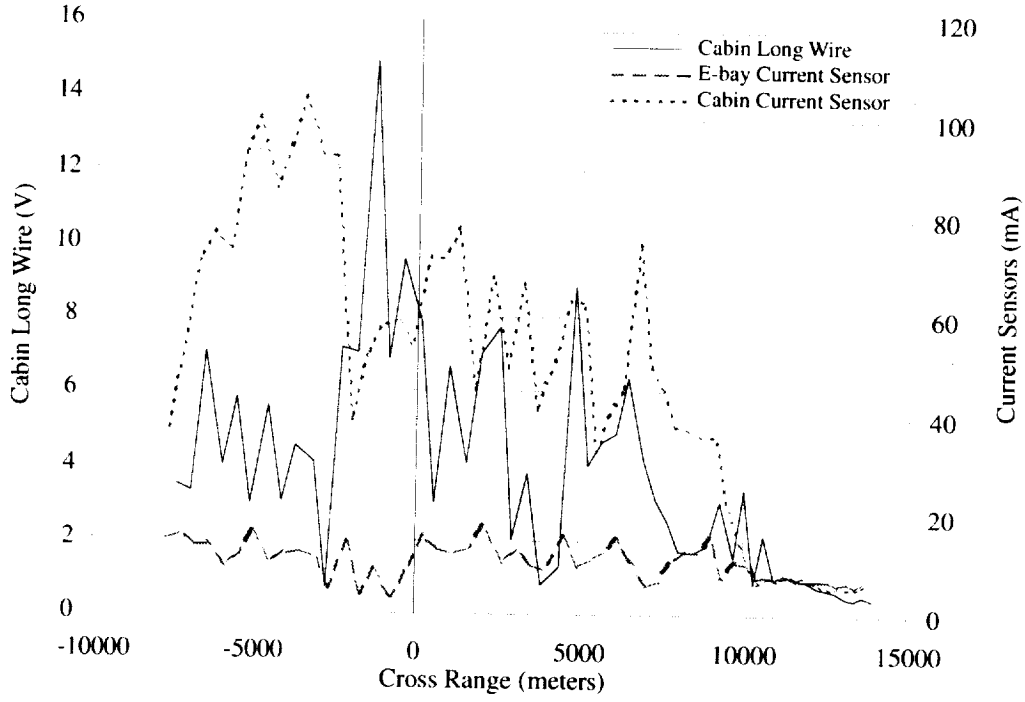

Figure A68. CLW and current measurements. 430 MHz; V-pol; inbound to crossbound; right incident; "clean."

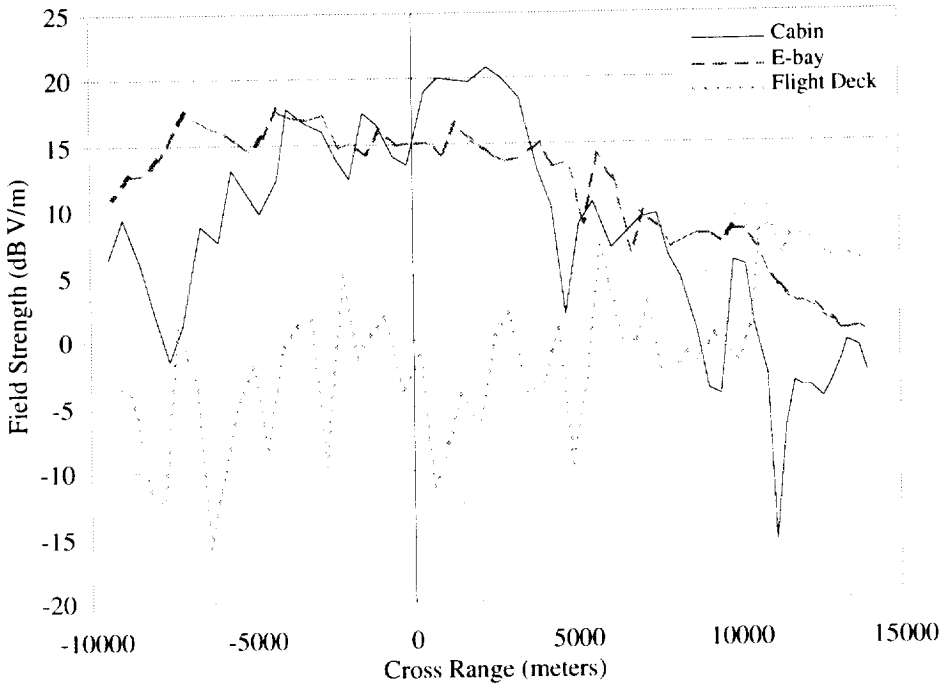

Figure A69. D-Dot measurements. 430 MHz; V-pol; inbound to crossbound; right incident; "flaps."

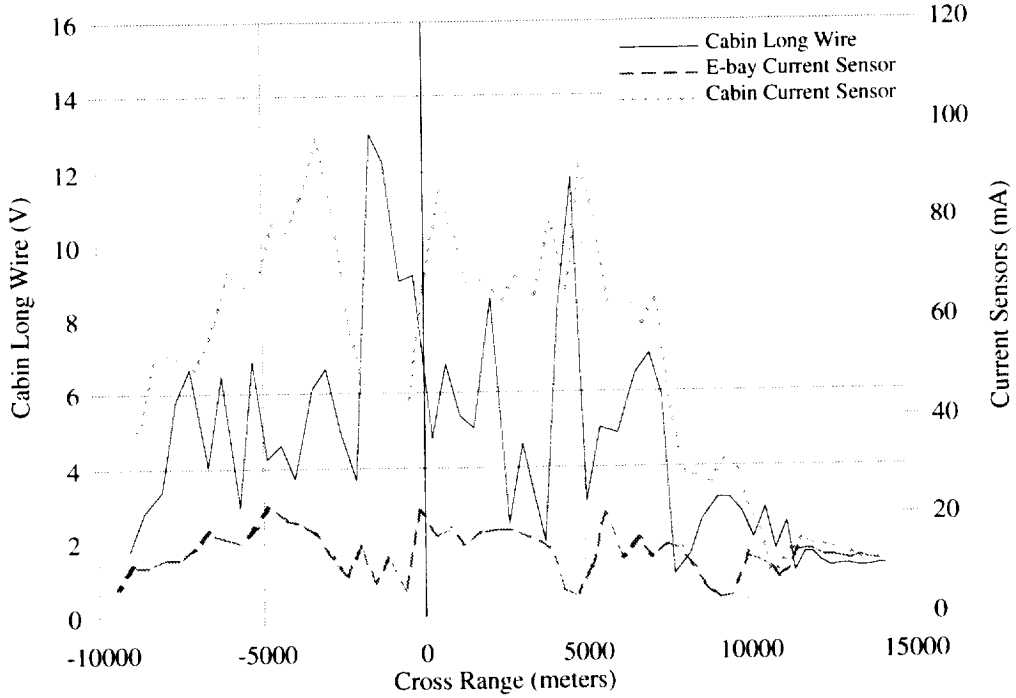

Figure A70. CLW and current measurements. 430 MHz; V-pol; inbound to crossbound; right incident; "flaps."

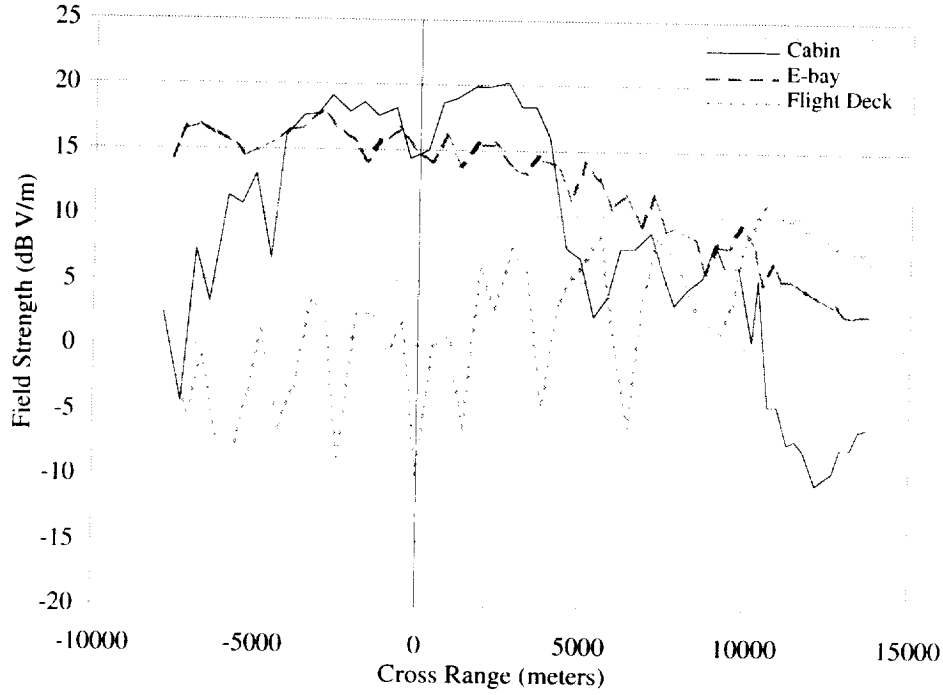

Figure A71. D-Dot measurements. 430 MHz; V-pol; inbound to crossbound; right incident; "flaps & gear."

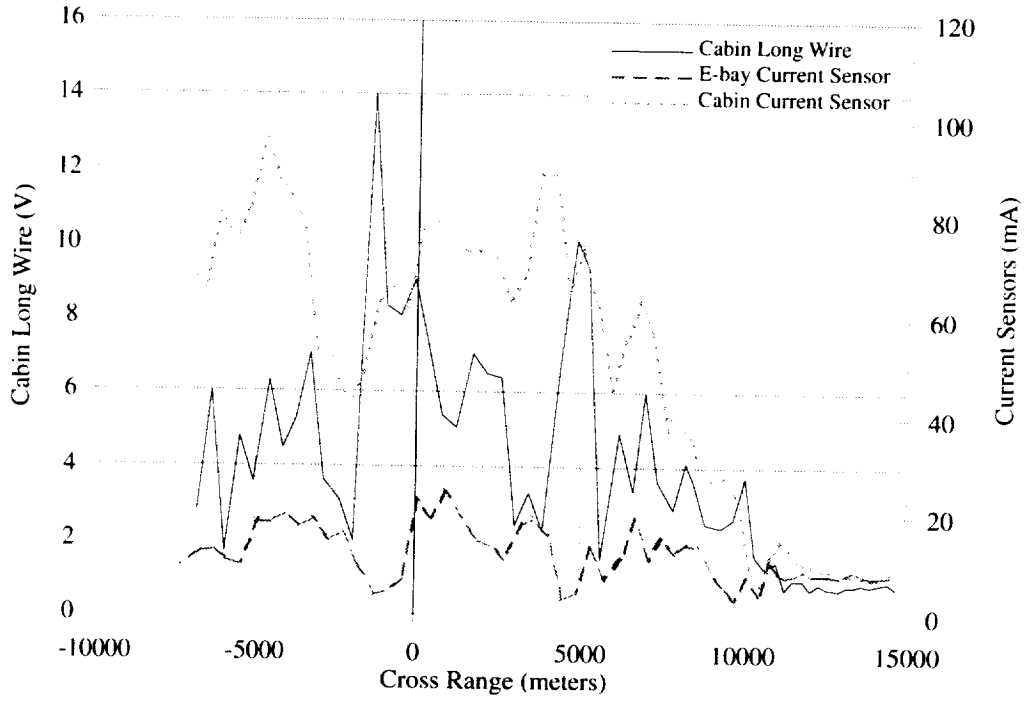

Figure A72. CLW and current measurements. 430 MHz; V-pol; inbound to crossbound; right incident; "flaps & gear."

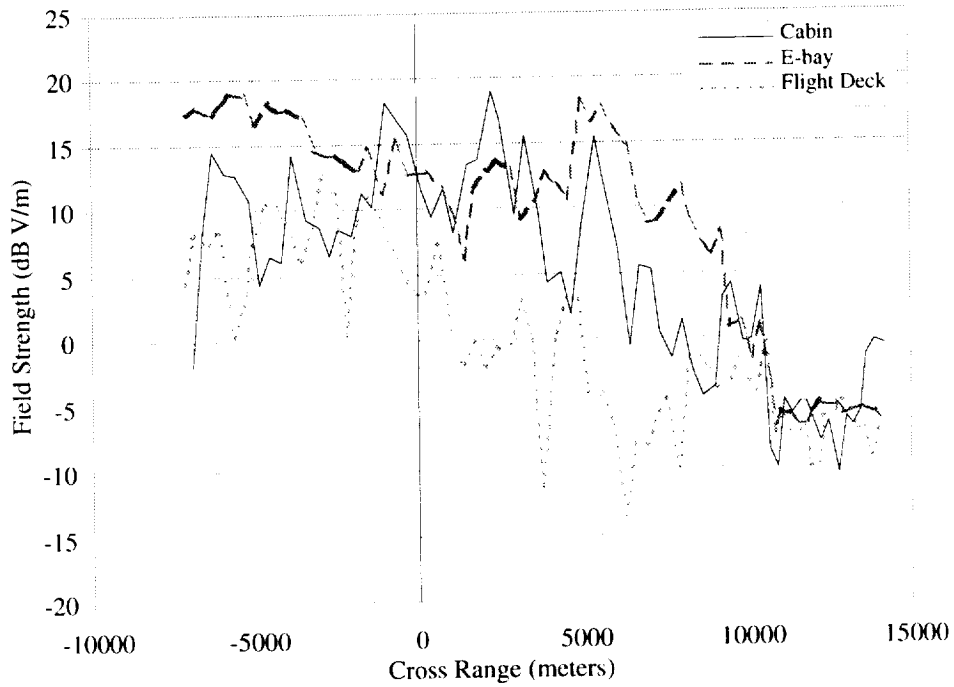

Figure A73. D-Dot measurements. 430 MHz; V-pol; crossbound; left incident to outbound; "clean."

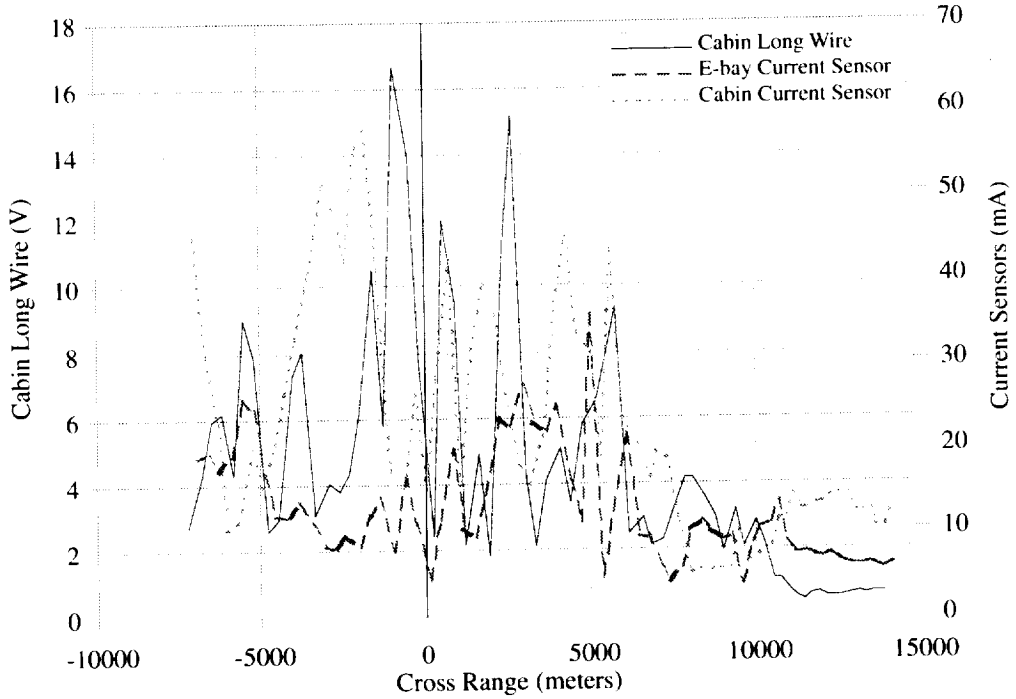

Figure A74. CLW and current measurements. 430 MHz; V-pol; crossbound; left incident to outbound; "clean."

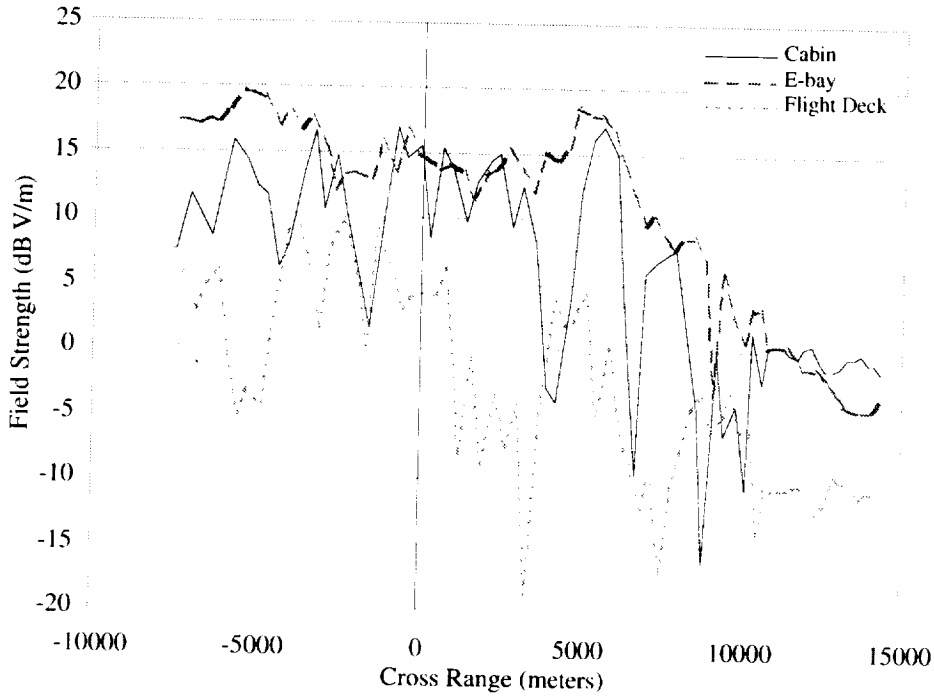

Figure A75. D-Dot measurements. 430 MHz; V-pol; crossbound; left incident to outbound; "flaps."

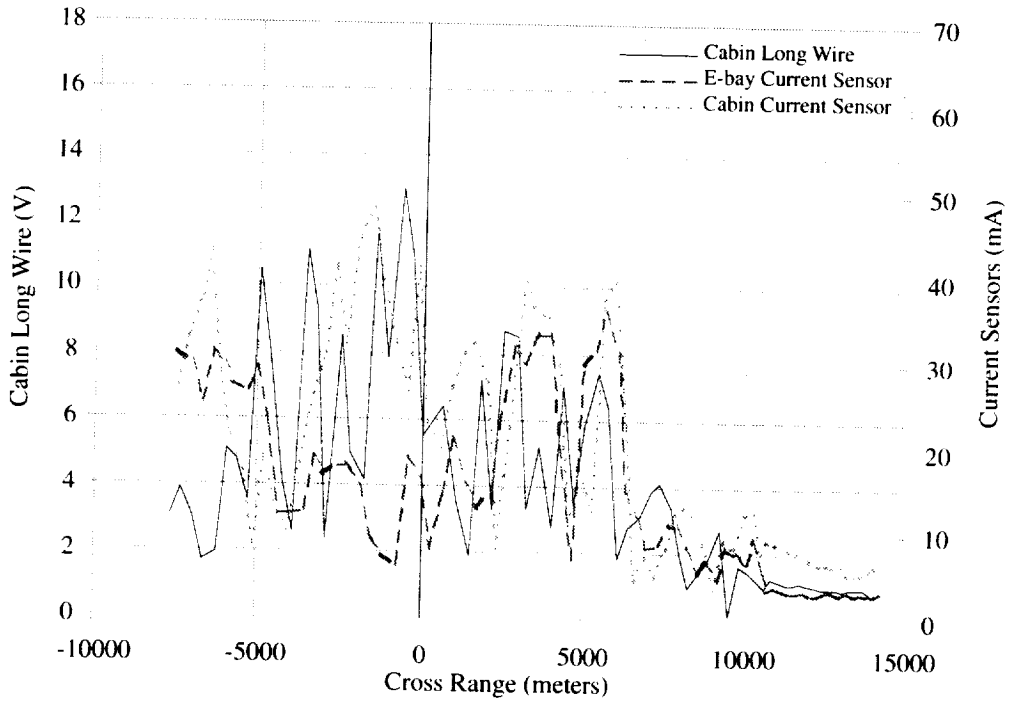

Figure A76. CLW and current measurements. 430 MHz; V-pol; crossbound; left incident to outbound; "flaps."

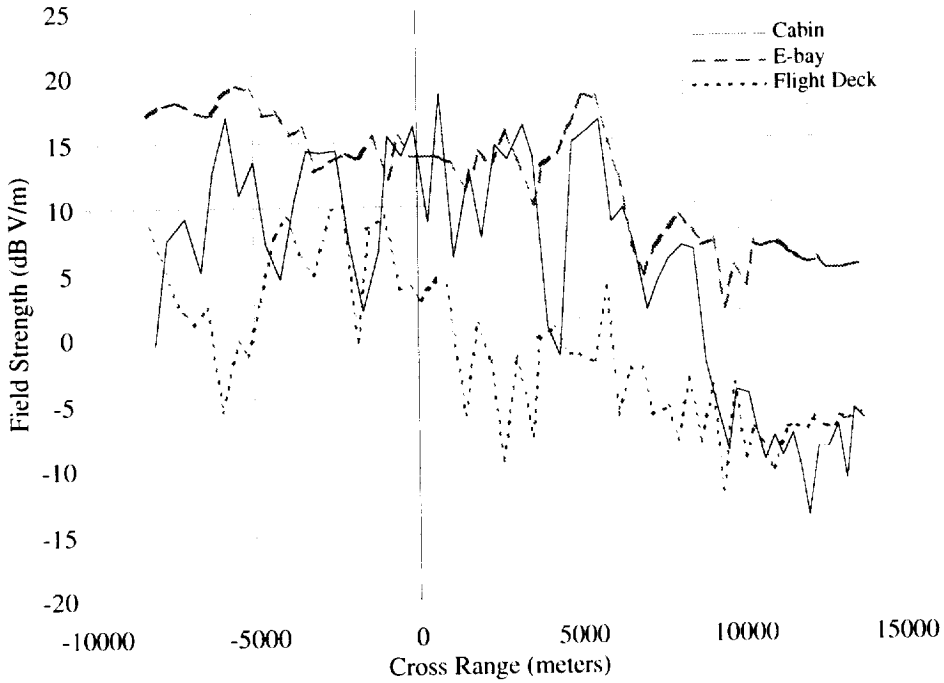

Figure A77. D-Dot measurements. 430 MHz; V-pol; crossbound; left incident to outbound; "flaps & gear."

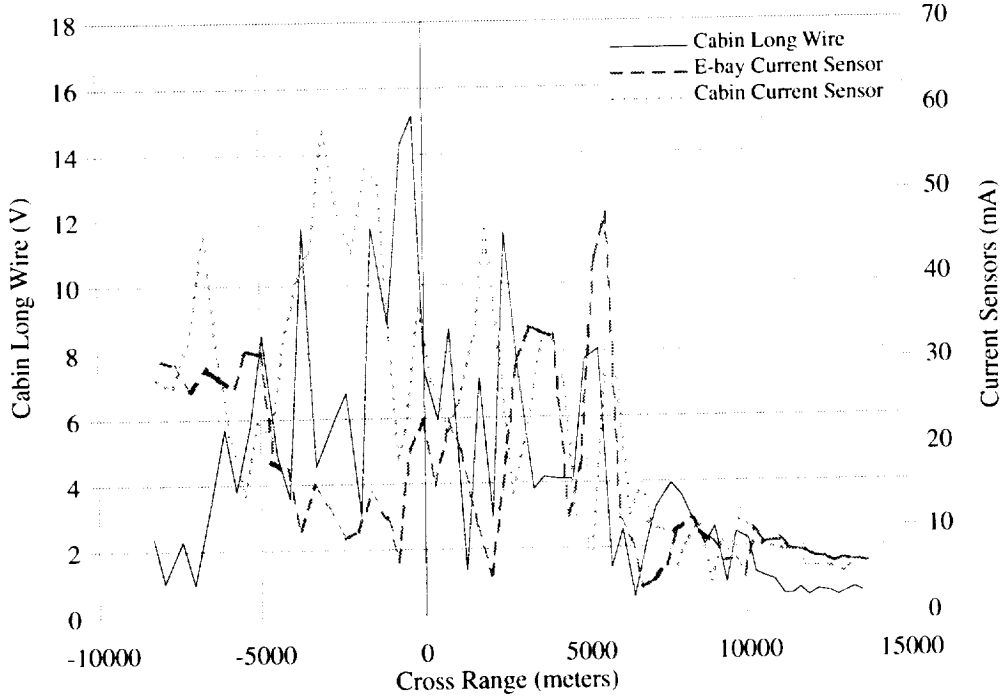

Figure A78. CLW and current measurements. 430 MHz; V-pol; crossbound; left incident to outbound; "flaps & gear."

Appendix B

Computed External Fields

This appendix documents the external field encountered by the aircraft during the 26, 173, and 430 MHz flight tests. For each flight, a plot of the external incident field is presented along with a table of incident angles giving the direction from which the incident field approaches the aircraft. Only incidence angles at selected range positions are given. The flights are arranged first by frequency of illumination, then by flight path (inbound, outbound, crossbound), and finally by aircraft configuration ("clean," "flaps," "flaps & gear"). Table B1 cross-references the illumination parameters to the sensor measurements. Note that the 430 MHz data are plotted against cross-range position even though flight paths at this frequency contain both side- and end-on exposure. As a result, the end-on portion of these flights is projected to a disproportionately short part of the plot in Figures B34 through B39.

Table B1. Organization of This Appendix

Test Frequency	Antenna Polarization	Flight Path	Figure and Table
26 MHz	Horizontal	Inbound	Figures B1 to B3 Tables B2 to B4
		Outbound	Figures B4 to B6 Tables B5 to B7
		Right Crossbound	Figures B7 to B9 Tables B8 to B10
173 MHz	Horizontal	Inbound	Figures B10 to B12 Tables B11 to B13
		Outbound	Figures B13 to B15 Tables B14 to B16
		Right Crossbound	Figures B16 to B18 Tables B17 to B19
		Left Crossbound	Figures B19 to B21 Tables B20 to B22
	Vertical	Inbound	Figures B22 to B24 Tables B23 to B25
		Outbound	Figures B25 to B27 Tables B26 to B28
		Right Crossbound	Figures B28 to B30 Tables B29 to B31
		Left Crossbound	Figures B31 to B33 Tables B32 to B34
430 MHz	Vertical	Inbound to Right Crossbound	Figures B34 to B36 Tables B35 to B37
		Left Crossbound to Outbound	Figures B37 to B39 Tables B38 to B40

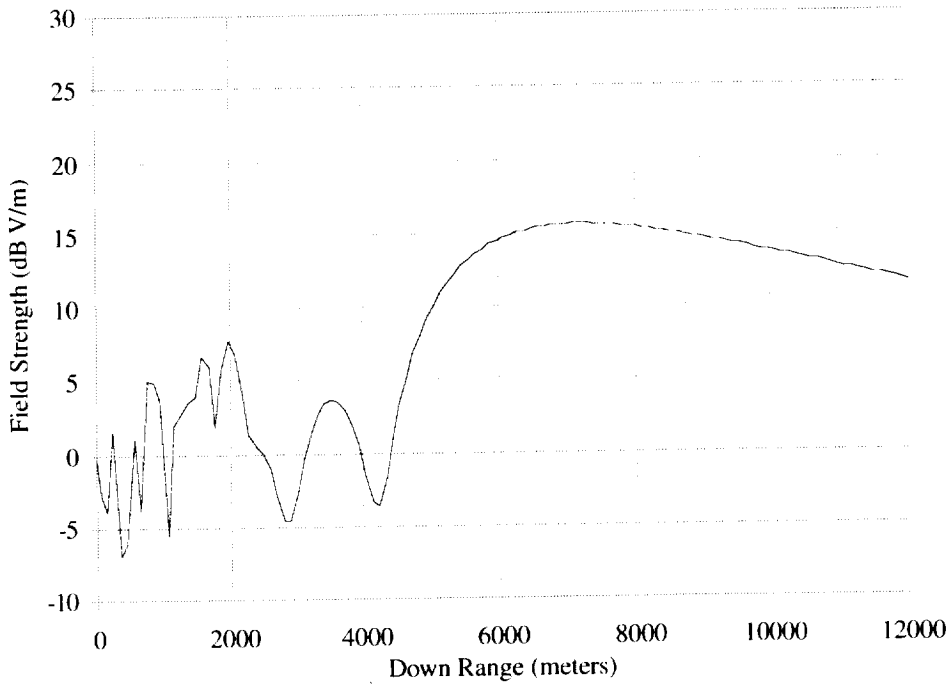

Figure B1. External field. 26 MHz; inbound; "clean."

Table B2. Incident Angles
[26 MHz; inbound; "clean"]

Down range (meters)	θ (degree)	ϕ (degree)	α (degree)
0	169.1	126.7	50.9
1000	146.6	10.1	88.4
2000	127.3	4.2	89.7
3000	118.6	2.1	90.0
4000	113.7	1.2	89.8
5000	110.3	0.8	89.9
6000	108.1	0.4	90.3
7000	106.6	0.6	89.7
8000	104.9	0.1	90.1
9000	104.3	0.0	90.1
10000	103.6	1.4	88.5
11000	103.0	1.0	89.9
12000	102.5	1.9	89.4

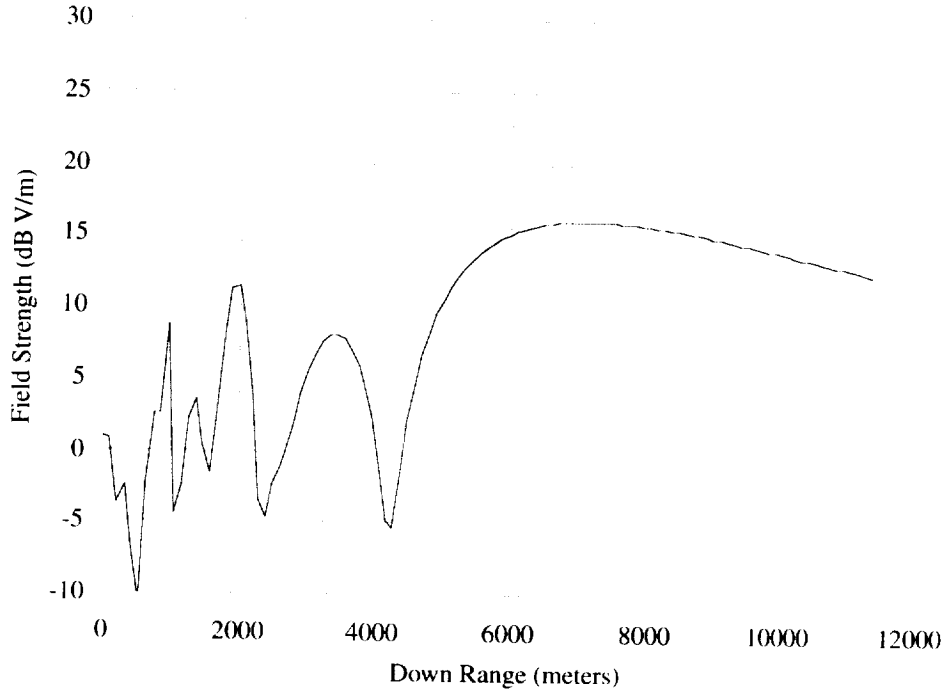

Figure B2. External field. 26 MHz; inbound; "flaps."

Table B3. Incident Angles
[26 MHz; inbound; "flaps"]

Down range (meters)	θ (degree)	ϕ (degree)	α (degree)
0	173.6	-118.3	116.8
1000	143.1	-8.8	91.3
2000	123.9	-4.4	90.2
3000	114.7	-3.3	90.3
4000	109.8	-3.0	90.4
5000	106.4	-2.3	90.0
6000	104.3	-2.0	90.2
7000	102.9	-2.6	90.5
8000	101.3	-2.5	90.4
9000	100.5	-2.0	90.2
10000	100.1	-1.8	89.7
11000	99.3	-1.0	89.9
12000			

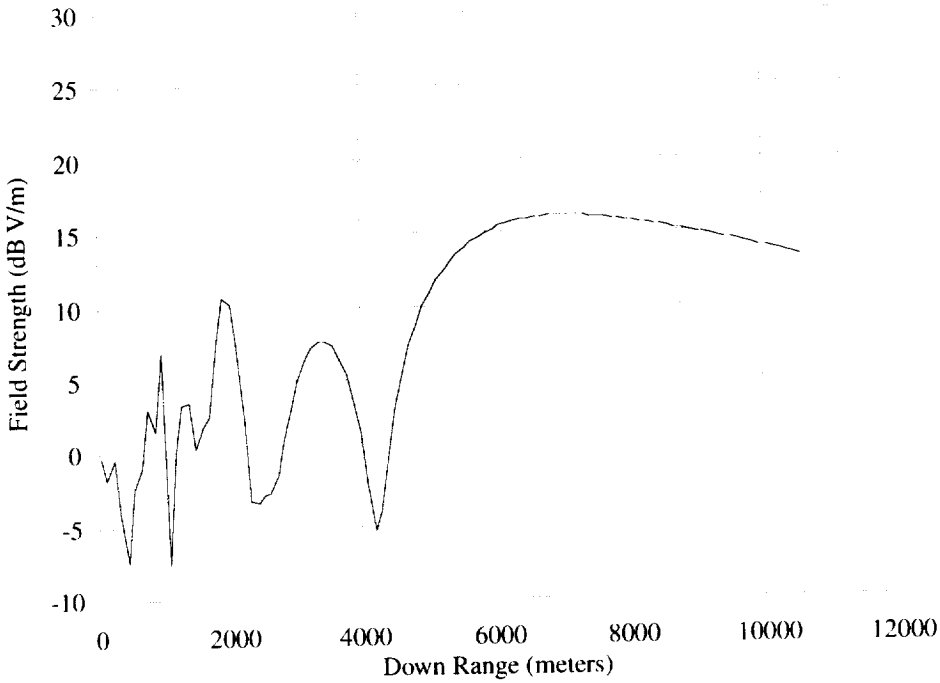

Figure B3. External field. 26 MHz; inbound; "flaps & gear."

Table B4. Incident Angles
[26 MHz; inbound; "flaps & gear"]

Down range (meters)	θ (degree)	ϕ (degree)	α (degree)
0			
1000	142.7	-9.3	90.8
2000	123.6	-5.0	90.8
3000	114.5	-3.7	90.6
4000	109.6	-1.9	89.9
5000	106.3	-2.2	90.5
6000	104.1	-1.9	90.3
7000	102.5	-1.6	90.3
8000	101.1	-1.7	90.5
9000	100.4	-1.4	90.2
10000	99.7	-1.0	89.1
11000			
12000			

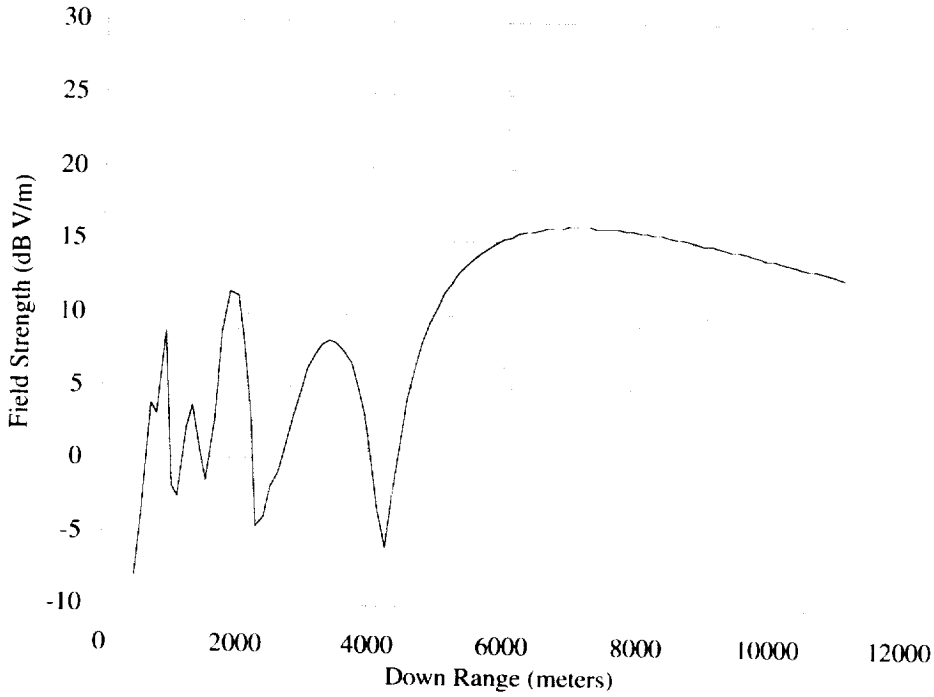

Figure B4. External field. 26 MHz; outbound; "clean."

Table B5. Incident Angles
[26 MHz; outbound; "clean"]

Down range (meters)	θ (degree)	ϕ (degree)	α (degree)
0			
1000	133.1	174.2	89.9
2000	114.2	177.6	89.3
3000	105.1	178.6	89.3
4000	100.1	179.0	89.4
5000	96.9	179.5	89.7
6000	94.7	179.5	90.0
7000	93.1	179.9	89.7
8000	92.0	-179.9	89.7
9000	90.8	-179.9	89.0
10000	90.2	-179.9	90.0
11000	89.8	-179.5	90.2
12000			

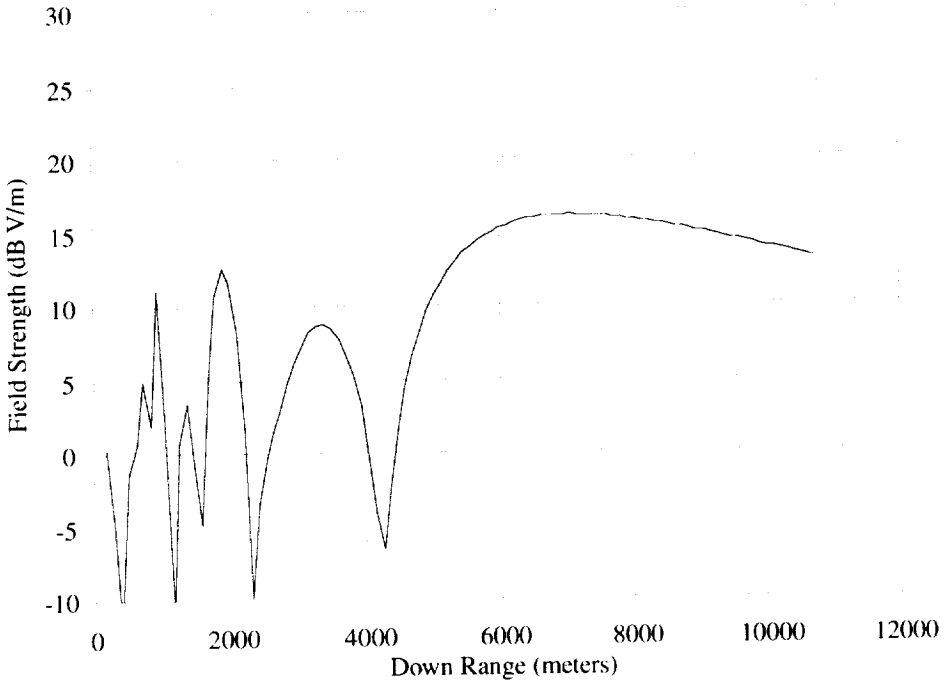

Figure B5. External field. 26 MHz; outbound; "flaps."

Table B6. Incident Angles
[26 MHz; outbound; "flaps"]

Down range (meters)	θ (degree)	ϕ (degree)	α (degree)
0			
1000	136.9	177.3	92.2
2000	117.8	179.7	89.9
3000	108.8	179.8	90.1
4000	103.7	179.8	90.3
5000	100.4	179.9	90.1
6000	98.2	-179.8	89.8
7000	96.6	-179.3	90.1
8000	95.7	-179.7	89.8
9000	94.4	-179.5	90.0
10000	93.6	-179.8	89.5
11000			
12000			

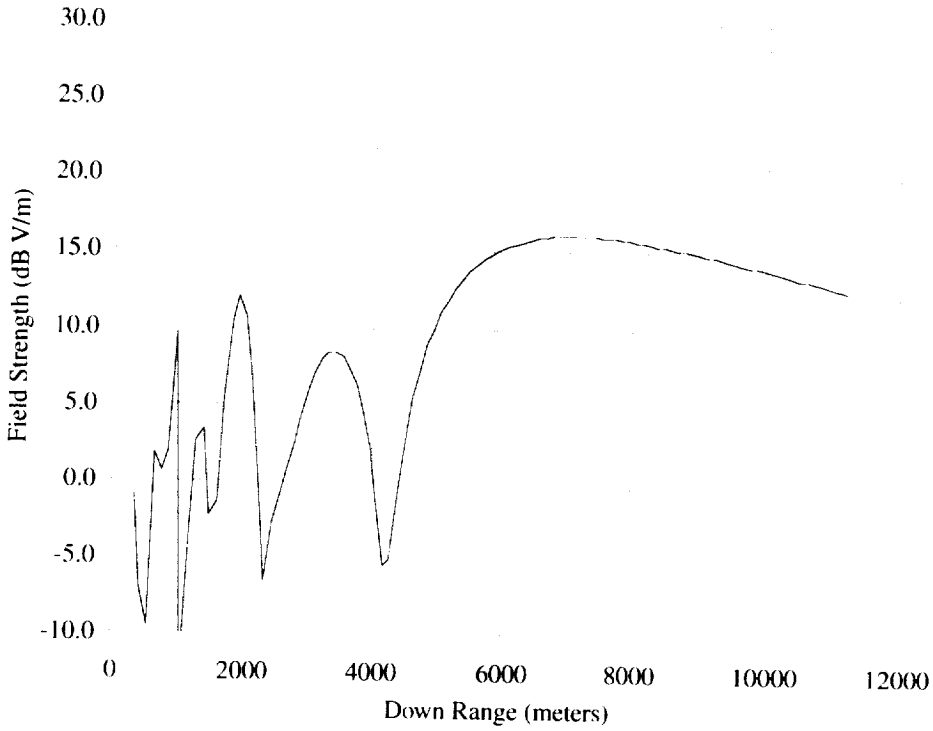

Figure B6. External field. 26 MHz; outbound; "flaps & gear."

Table B7. Incident Angles
[26 MHz; outbound; "flaps & gear"]

Down range (meters)	θ (degree)	ϕ (degree)	α (degree)
0			
1000	136.9	174.9	90.9
2000	117.6	177.7	89.8
3000	109.1	179.3	89.6
4000	103.8	179.7	89.8
5000	100.6	-179.9	89.6
6000	98.3	-179.4	89.6
7000	97.3	179.8	89.6
8000	96.0	-179.5	89.9
9000	94.8	-179.7	89.6
10000	93.9	-179.5	89.9
11000	93.2	-179.4	90.0
12000			

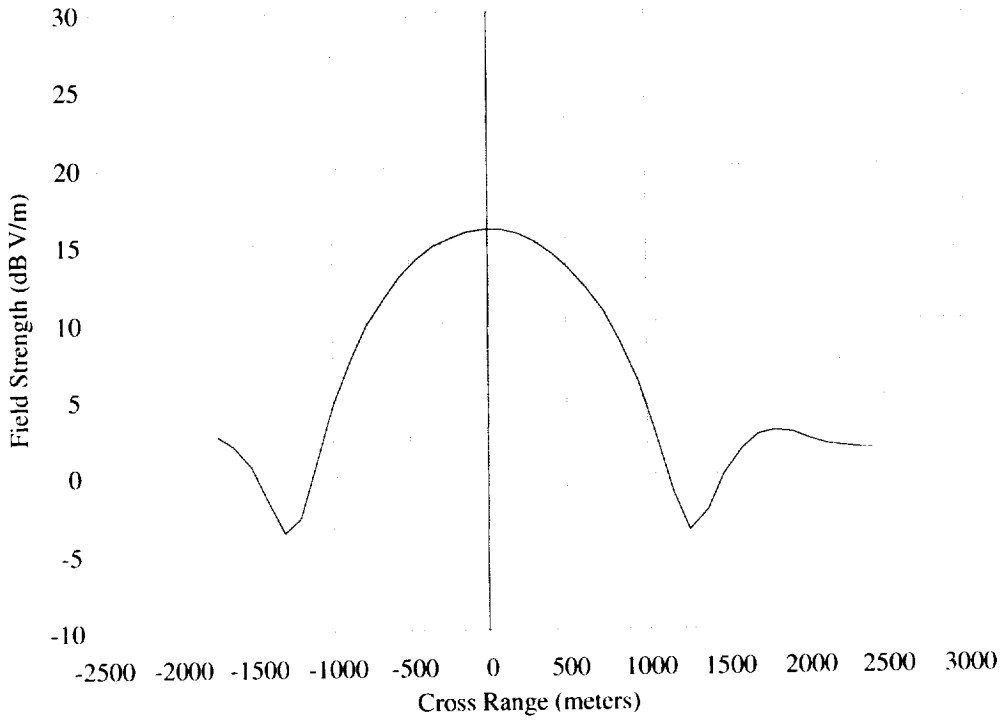

Figure B7. External field. 26 MHz; crossbound; "clean."

Table B8. Incident Angles
[26 MHz; crossbound; "clean"]

Cross range (meters)	θ (degree)	ϕ (degree)	α (degree)
-3000			
-2500			
-2000			
-1500	97.9	-104.0	95.7
-1000	98.1	-99.9	95.7
-500	98.5	-96.2	96.1
0	99.6	-91.8	95.9
500	99.6	-88.3	96.2
1000	100.7	-83.7	96.1
1500	101.3	-78.9	96.2
2000	100.6	-75.1	96.3
2500			
3000			

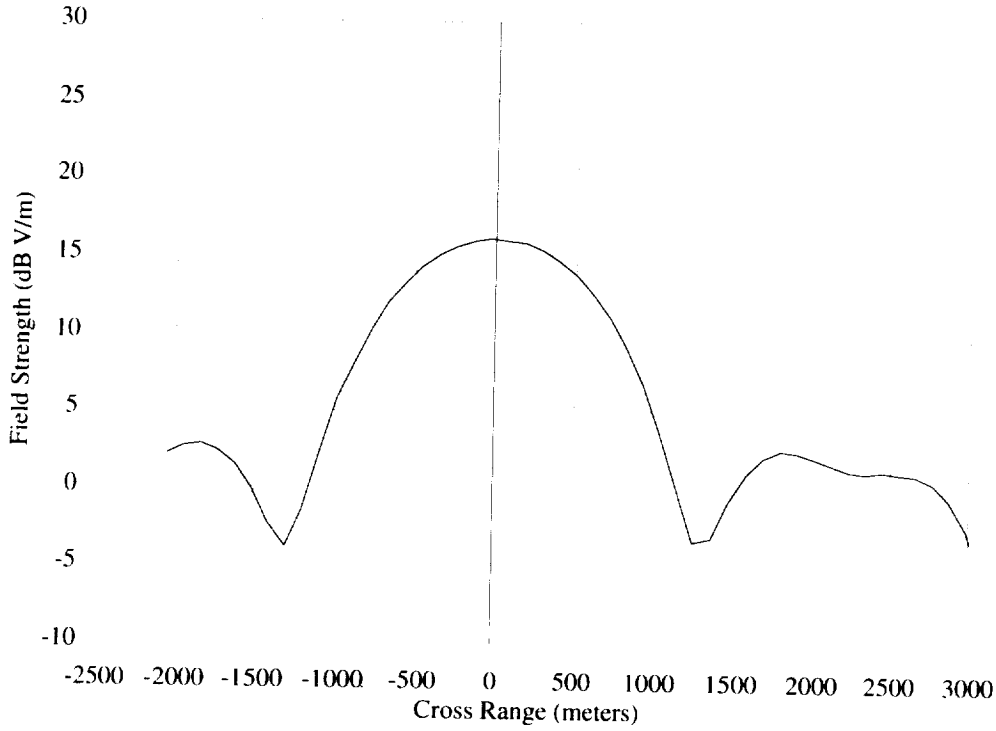

Figure B8. External field. 26 MHz; crossbound; "flaps."

Table B9. Incident Angles
[26 MHz; crossbound; "flaps"]

Cross range (meters)	θ (degree)	ϕ (degree)	α (degree)
-3000			
-2500			
-2000	98.8	-107.0	92.7
-1500	98.8	-103.4	92.7
-1000	98.9	-99.3	92.6
-500	98.8	-95.2	92.5
0	99.5	-91.2	92.6
500	100.2	-86.5	92.5
1000	100.4	-82.2	92.4
1500	100.9	-77.9	92.4
2000	100.1	-74.0	92.8
2500	99.7	-70.4	92.8
3000	99.8	-67.0	92.8

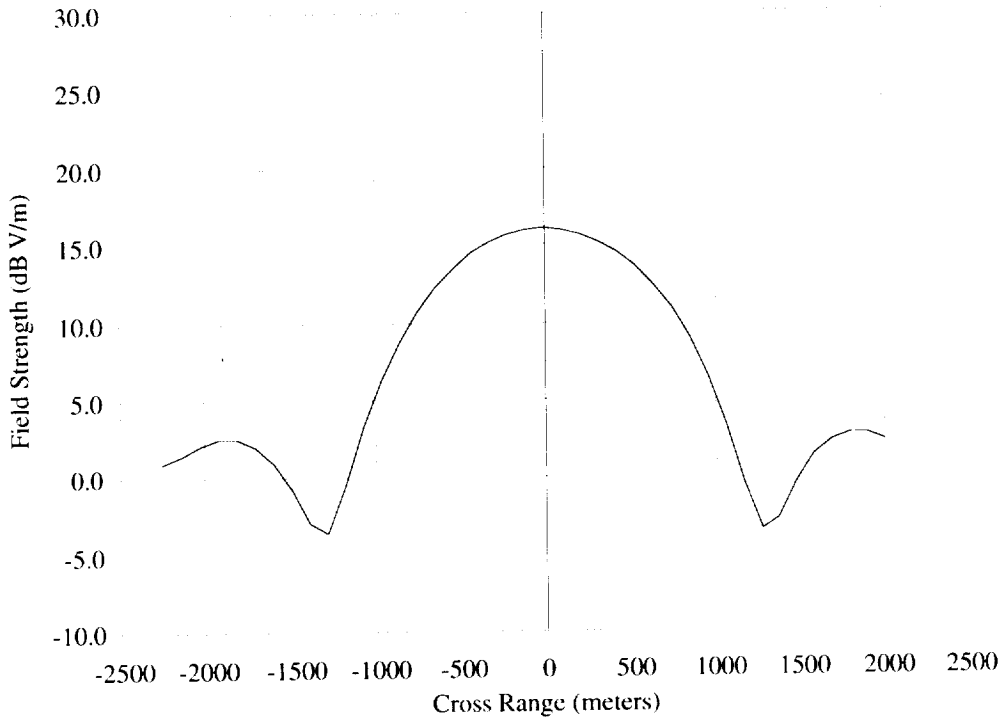

Figure B9. External field. 26 MHz; crossbound; "flaps & gear."

Table B10. Incident Angles
[26 MHz; crossbound; "flaps & gear"]

Cross range (meters)	θ (degree)	ϕ (degree)	α (degree)
-3000			
-2500			
-2000	98.1	-108.1	92.3
-1500	98.0	-104.6	92.2
-1000	97.6	-100.8	92.1
-500	97.5	-97.4	92.2
0	98.0	-93.9	92.4
500	98.5	-89.9	92.4
1000	98.2	-86.0	92.4
1500	98.0	-82.7	92.8
2000	97.4	-79.4	93.1
2500			
3000			

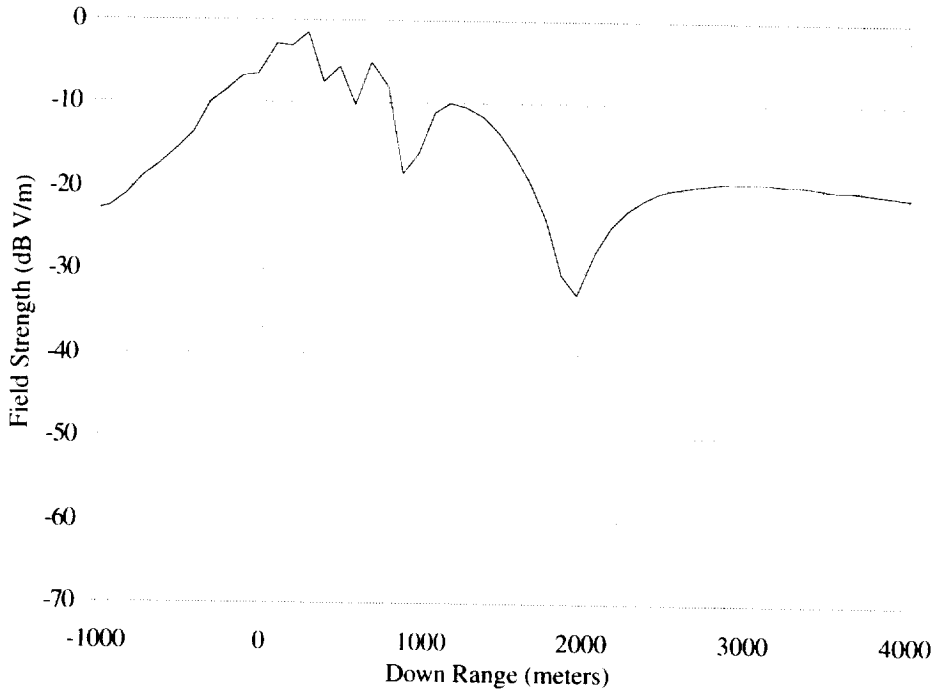

Figure B10. External field. 173 MHz; H-pol; inbound; "clean."

Table B11. Incident Angles
[173 MHz; H-pol; inbound; "clean"]

Down range (meters)	θ (degree)	ϕ (degree)	α (degree)
-1000	102.5	174.3	89.5
-500	117.8	172.4	89.0
0	169.1	107.4	68.0
500	129.8	2.5	84.5
1000	114.6	-0.4	86.2
1500	108.7	-3.0	90.6
2000	105.6	-4.2	91.2
2500	103.7	-5.5	92.1
3000	102.4	-6.5	92.3
3500	101.7	-6.8	90.8
4000	100.8	-7.4	91.8

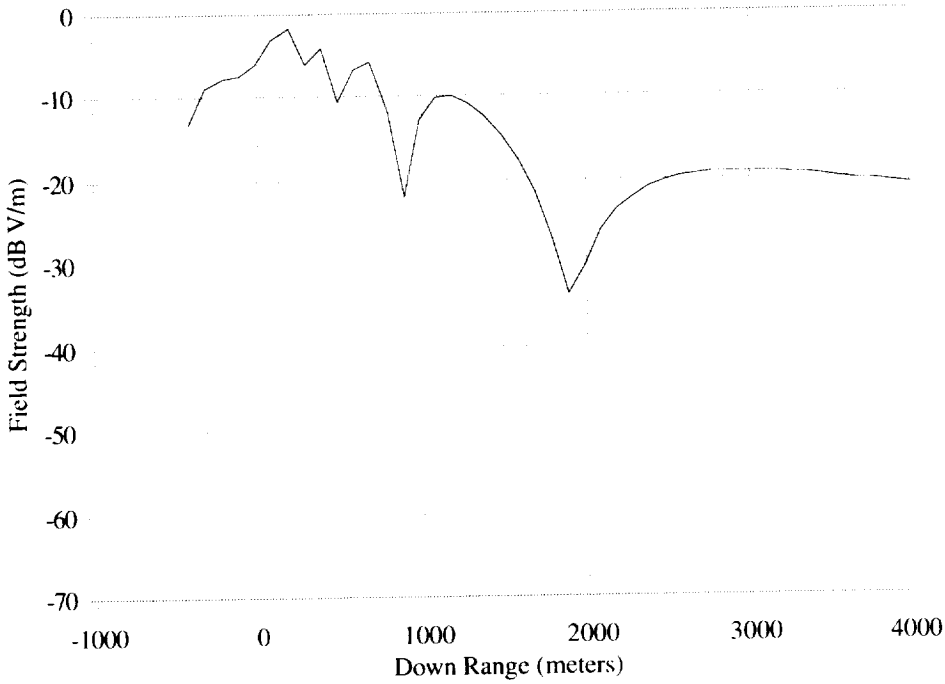

Figure B11. External field. 173 MHz; H-pol; inbound; "flaps."

Table B12. Incident Angles
[173 MHz; H-pol; inbound; "flaps"]

Down range (meters)	θ (degree)	ϕ (degree)	α (degree)
-1000			
-500			
0	165.4	95.5	80.5
500	125.6	5.7	87.5
1000	110.7	0.1	88.2
1500	104.9	-0.9	88.5
2000	101.9	-1.9	89.1
2500	99.9	-3.0	89.7
3000	98.9	-3.7	89.9
3500	98.0	-4.0	89.7
4000	97.2	-3.9	88.9

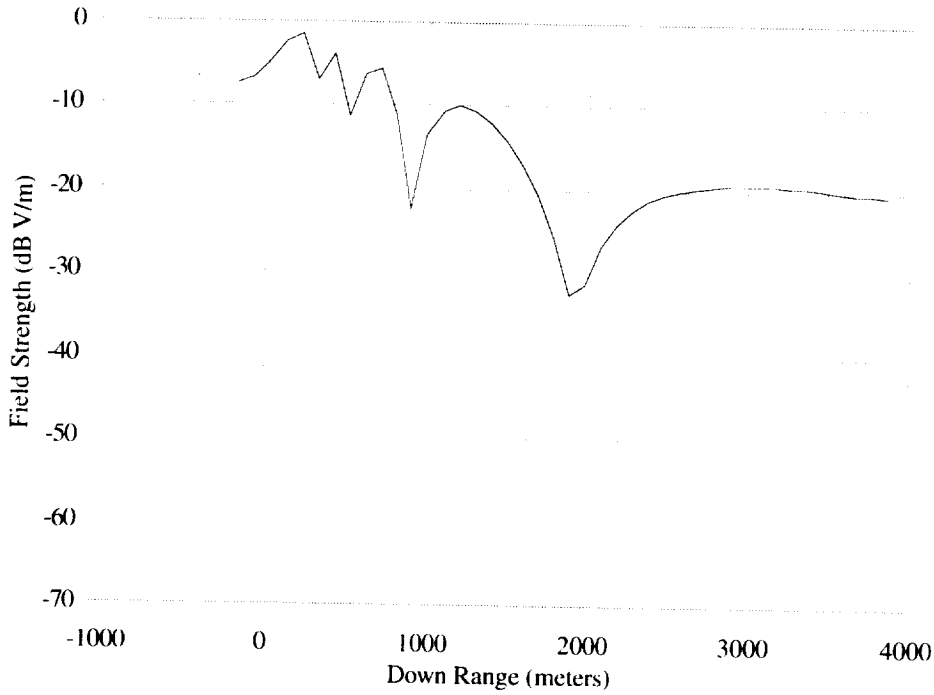

Figure B12. External field. 173 MHz; H-pol; inbound; "flaps & gear."

Table B13. Incident Angles
[173 MHz; H-pol; inbound; "flaps & gear"]

Down range (meters)	θ (degree)	ϕ (degree)	α (degree)
-1000			
-500			
0	172.4	98.8	70.1
500	126.1	1.3	89.3
1000	110.5	-0.8	89.0
1500	104.9	-2.1	89.3
2000	101.9	-3.0	90.9
2500	99.9	-3.9	91.4
3000	98.7	-4.6	91.0
3500	97.5	-4.9	90.6
4000			

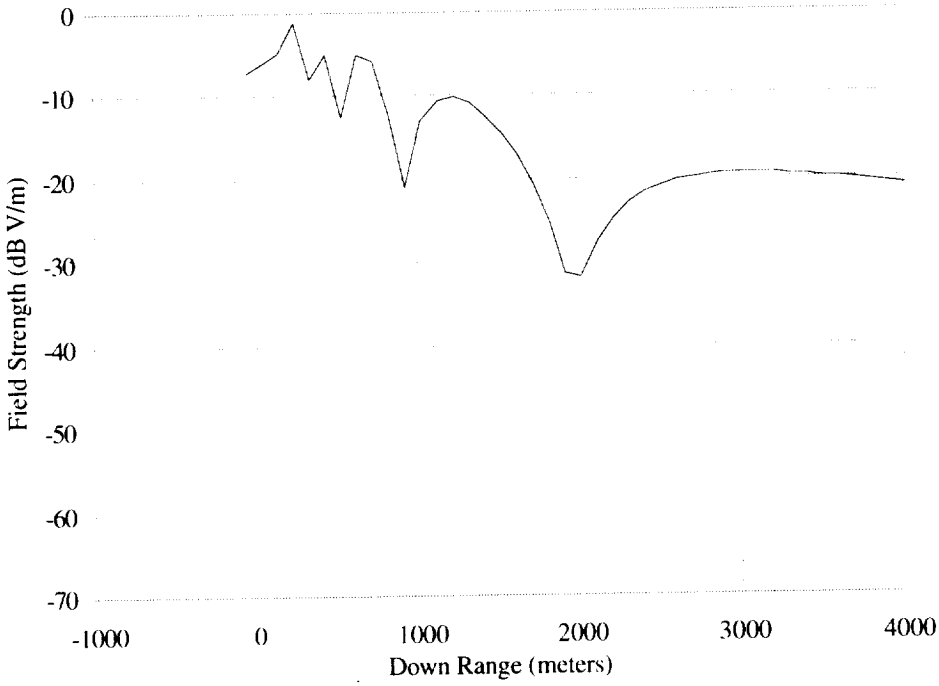

Figure B13. External field. 173 MHz; H-pol; outbound; "clean."

Table B14. Incident Angles
[173 MHz; H-pol; outbound; "clean"]

Down range (meters)	θ (degree)	ϕ (degree)	α (degree)
-1000			
-500			
0	159.7	103.7	73.9
500	118.8	169.4	87.7
1000	103.0	175.1	90.0
1500	97.1	176.7	90.8
2000	94.0	177.3	90.6
2500	92.0	178.2	90.8
3000	90.6	178.6	90.2
3500	89.9	179.1	88.2
4000	89.1	-179.7	88.8

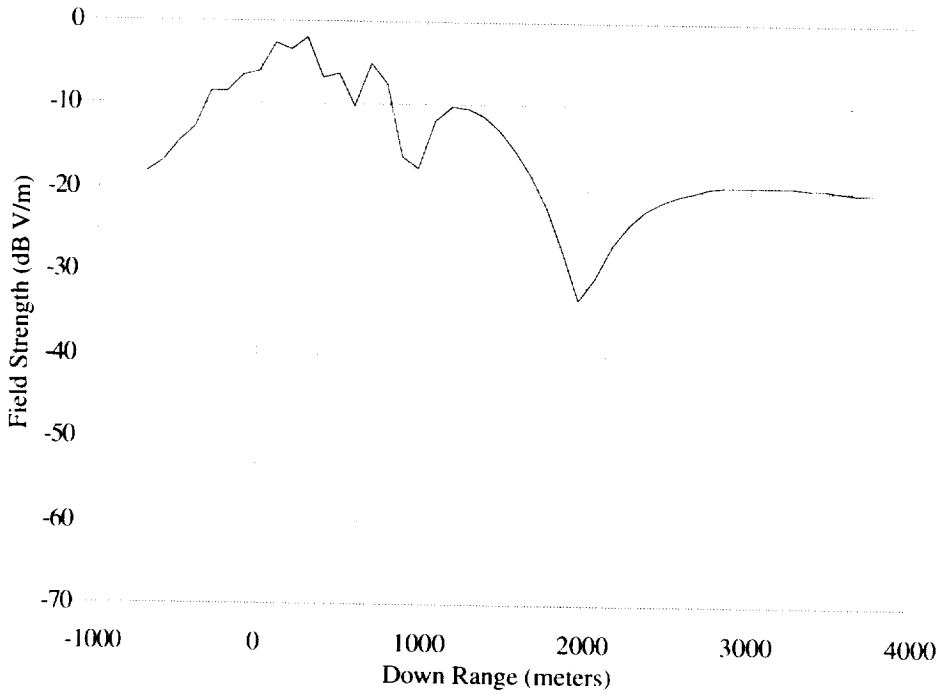

Figure B14. External field. 173 MHz; H-pol; outbound; "flaps."

Table B15. Incident Angles
[173 MHz; H-poll; outbound; "flaps"]

Down range (meters)	θ (degree)	ϕ (degree)	α (degree)
-1000			
-500			
0	175.3	68.4	72.6
500	122.2	179.4	91.5
1000	106.6	-179.9	90.7
1500	100.4	179.9	91.2
2000	97.5	179.8	91.6
2500	95.7	179.7	90.7
3000	94.4	-179.7	90.5
3500	93.4	-179.3	90.2
4000			

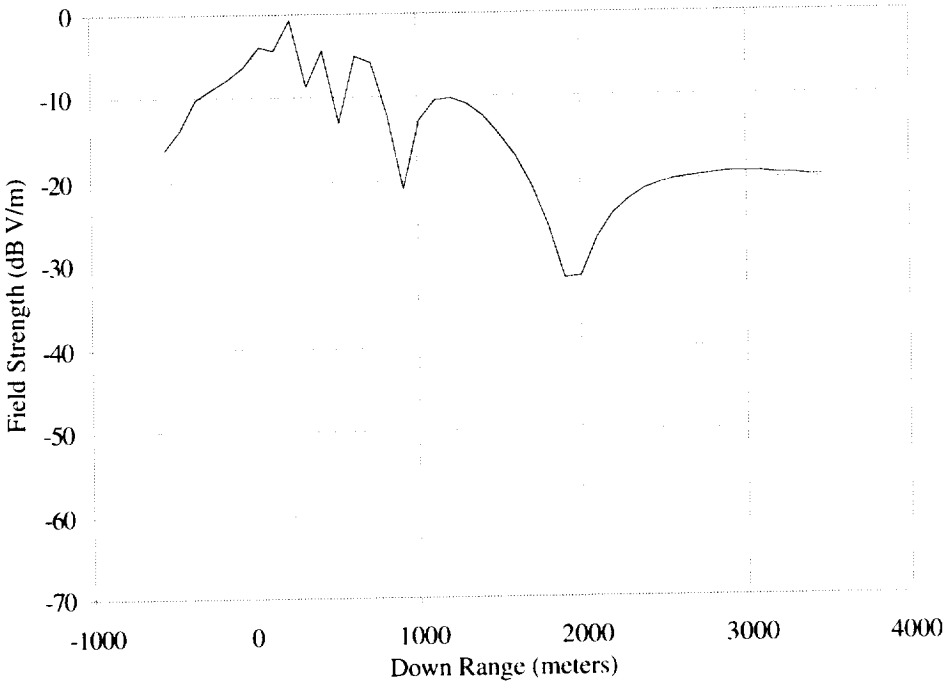

Figure B15. External field. 173 MHz; H-pol; outbound; "flaps & gear."

Table B16. Incident Angles
[173 MHz; H-pol; outbound; "flaps & gear"]

Down range (meters)	θ (degree)	ϕ (degree)	α (degree)
-1000			
-500	125.7	10.2	88.3
0	166.0	99.7	82.7
500	121.9	174.4	90.4
1000	106.2	178.2	90.4
1500	100.7	179.3	90.1
2000	97.8	179.9	90.8
2500	95.6	-179.6	90.6
3000	94.2	-179.3	90.4
3500			
4000			

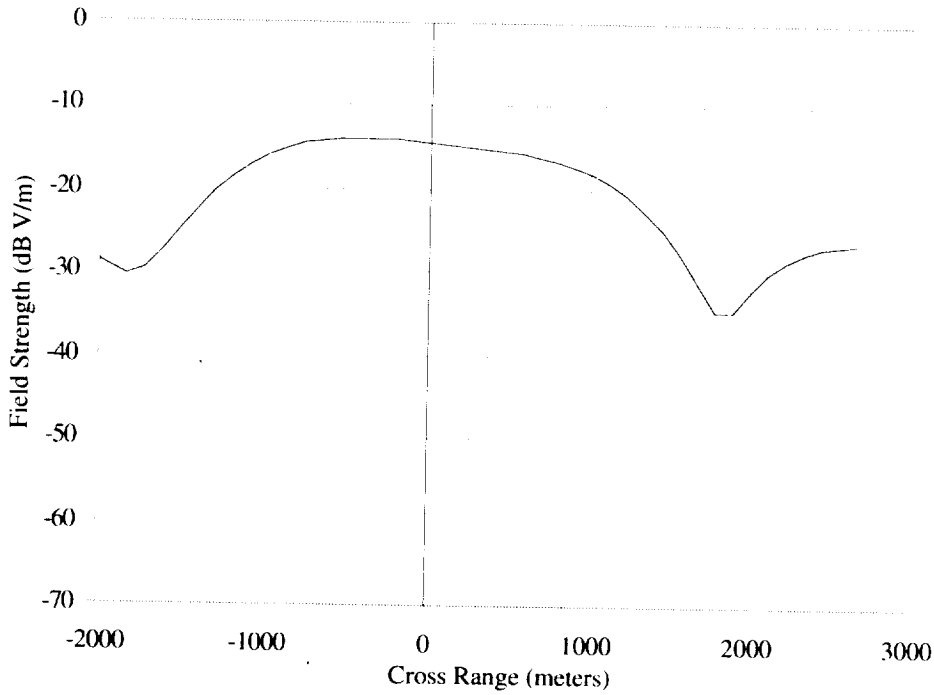

Figure B16. External field. 173 MHz; H-pol; crossbound; right incident; "clean."

Table B17. Incident Angles
[173 MHz; H-pol; crossbound; right incident; "clean"]

Cross range (meters)	θ (degree)	ϕ (degree)	α (degree)
-2000	104.6	-141.4	94.9
-1500	108.1	-133.5	95.6
-1000	111.7	-123.4	96.1
-500	115.0	-111.3	97.0
0	117.4	-97.3	97.4
500	118.3	-82.8	97.3
1000	118.0	-69.4	96.5
1500	116.8	-58.3	95.6
2000	115.5	-48.9	94.3
2500	113.2	-42.4	94.4
3000			

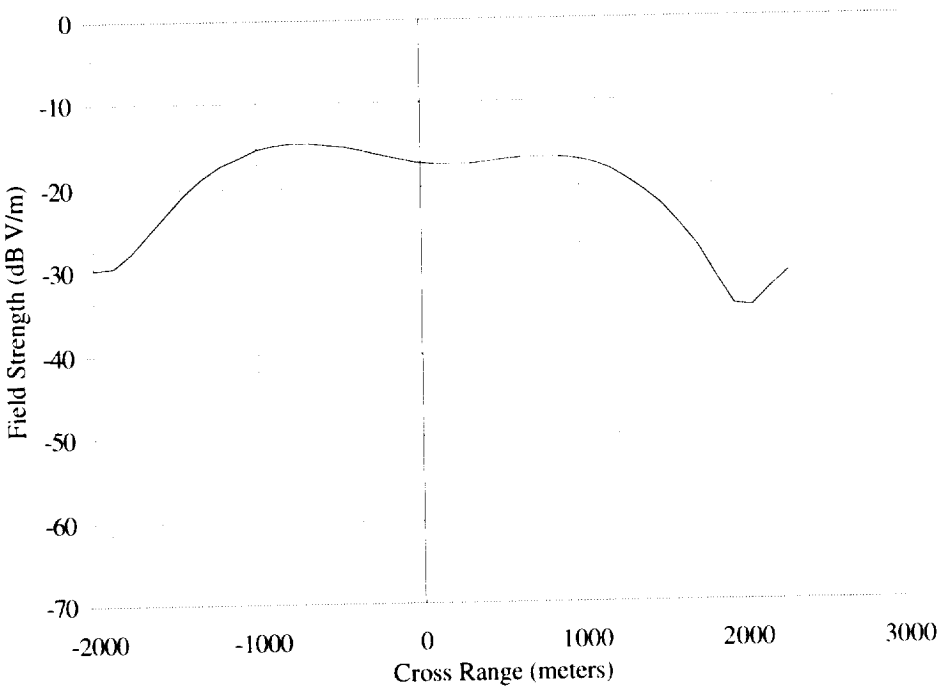

Figure B17. External field. 173 MHz; H-pol; crossbound; right incident; "flaps."

Table B18. Incident Angles
[173 MHz; H-pol; crossbound; right incident; "flaps"]

Cross range (meters)	θ (degree)	ϕ (degree)	α (degree)
-2000	108.7	-143.3	92.6
-1500	112.0	-135.0	92.6
-1000	115.3	-124.7	92.7
-500	118.2	-111.3	93.2
0	119.9	-96.4	93.5
500	120.3	-79.9	93.1
1000	119.0	-65.3	92.4
1500	116.7	-53.9	91.9
2000	113.6	-45.2	91.6
2500			
3000			

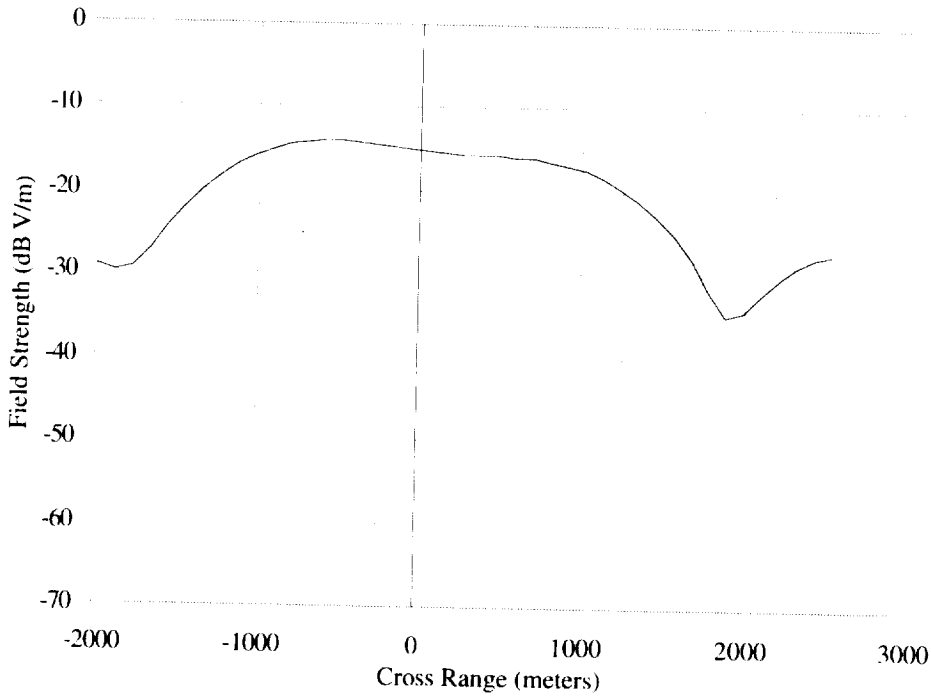

Figure B18. External field. 173 MHz; H-pol; crossbound; right incident; "flaps & gear."

Table B19. Incident Angles
[173 MHz; H-pol; crossbound; right incident; "flaps & gear"]

Cross range (meters)	θ (degree)	ϕ (degree)	α (degree)
-2000	108.2	-141.6	92.3
-1500	111.1	-133.7	92.4
-1000	114.3	-123.6	92.8
-500	117.0	-110.4	93.3
0	118.7	-95.4	93.4
500	118.8	-80.2	93.2
1000	117.4	-66.3	92.5
1500	115.4	-54.6	91.7
2000	112.8	-45.9	91.2
2500	110.5	-39.5	91.1
3000			

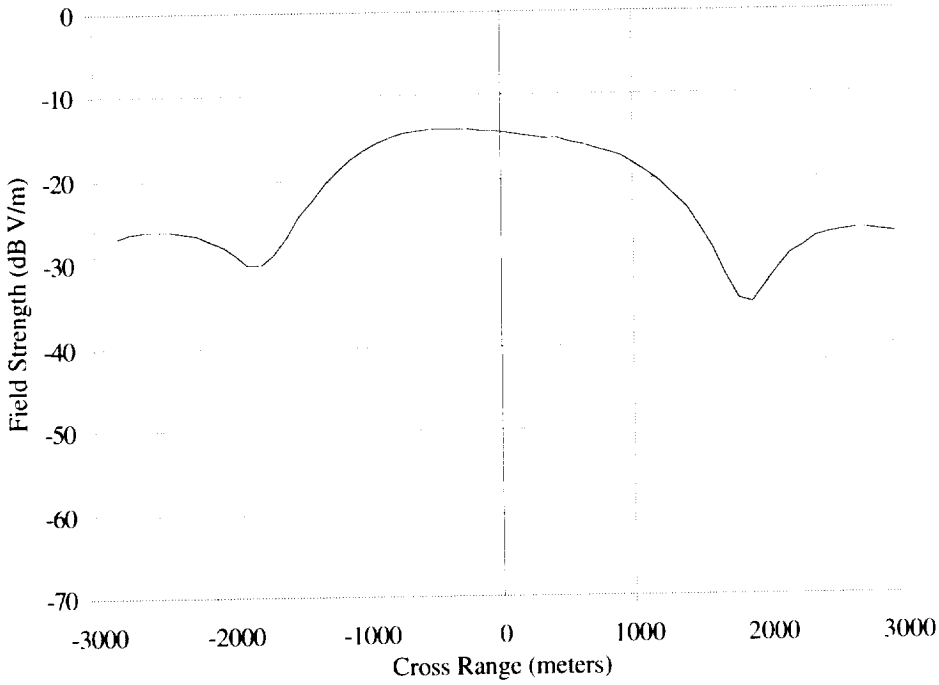

Figure B19. External field. 173 MHz; H-pol; crossbound; left incident; "clean."

Table B20. Incident Angles
[173 MHz; H-pol; crossbound; left incident; "clean"]

Cross range (meters)	θ (degree)	ϕ (degree)	α (degree)
-2000	113.0	48.2	84.3
-1500	115.3	55.9	84.0
-1000	116.6	66.9	83.4
-500	117.5	79.6	82.9
0	117.1	94.1	82.8
500	114.4	108.7	83.5
1000	111.0	120.9	84.6
1500	107.7	130.7	85.3
2000	104.8	138.5	86.0
2500	102.2	144.5	86.5
3000			

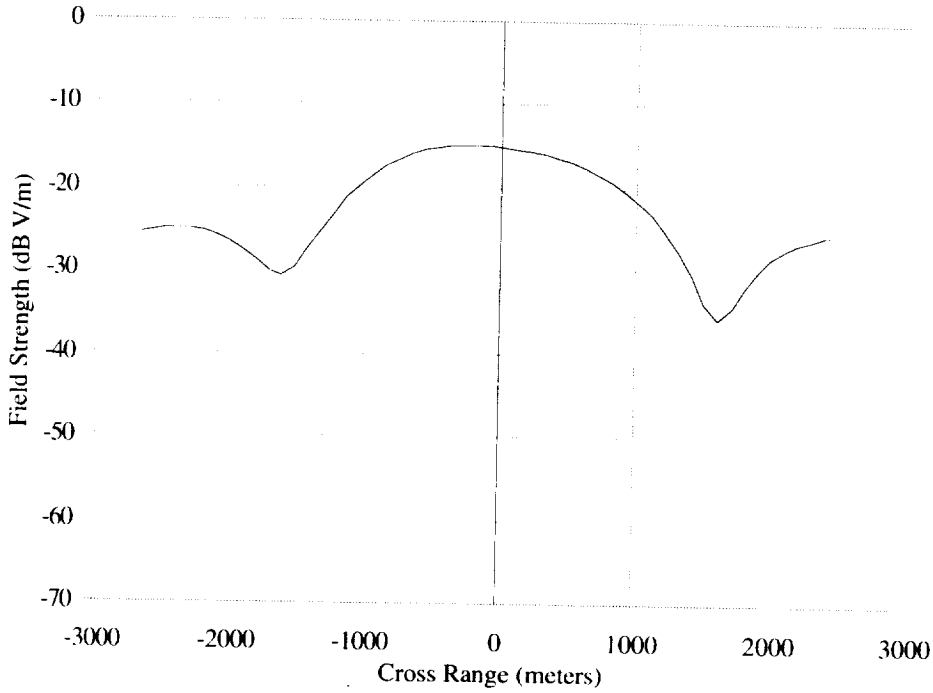

Figure B20. External field. 173 MHz; H-pol; crossbound; left incident; "flaps."

Table B21. Incident Angles
[173 MHz; H-pol; crossbound; left incident; "flaps"

Cross range (meters)	θ (degree)	ϕ (degree)	α (degree)
-2000	109.7	49.6	86.7
-1500	111.8	57.3	86.9
-1000	113.7	67.0	86.8
-500	114.9	78.9	86.7
0	114.8	92.2	86.9
500	113.4	105.3	87.2
1000	111.5	117.3	87.5
1500	109.1	127.6	87.9
2000	106.6	135.6	88.3
2500			
3000			

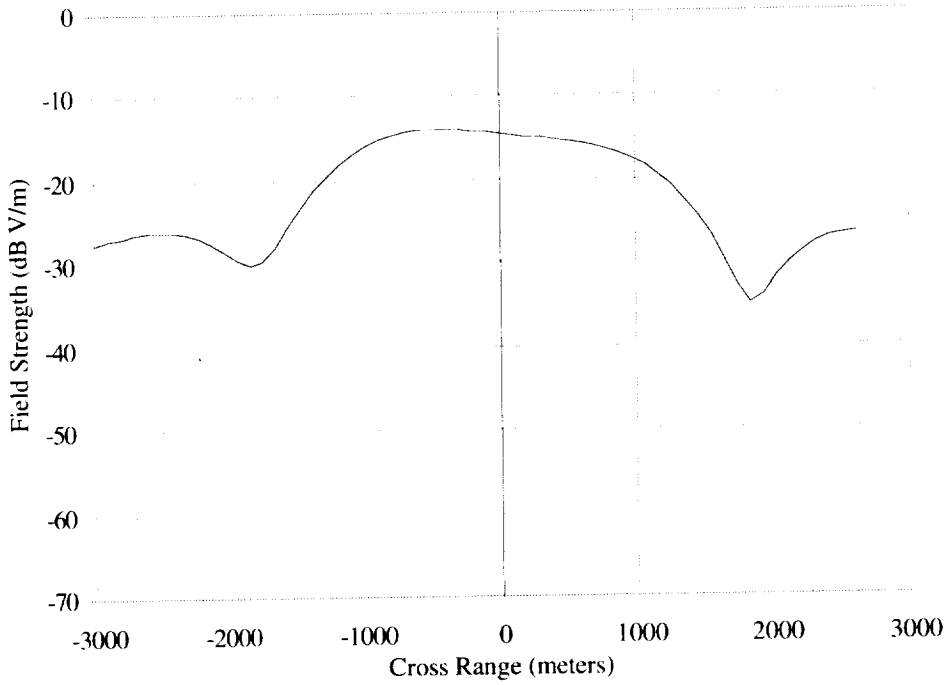

Figure B21. External field. 173 MHz; H-pol; crossbound; left incident; "flaps & gear."

Table B22. Incident Angles
[173 MHz; H-pol; crossbound; left incident; "flaps & gear"]

Cross range (meters)	θ (degree)	ϕ (degree)	α (degree)
-2000	110.9	47.6	86.8
-1500	113.2	55.5	86.6
-1000	115.8	65.8	86.6
-500	117.5	78.6	86.7
0	117.4	93.3	86.7
500	115.7	108.1	87.0
1000	113.1	121.0	87.8
1500	110.4	131.4	88.5
2000	107.6	139.5	88.7
2500	105.2	145.6	89.1
3000			

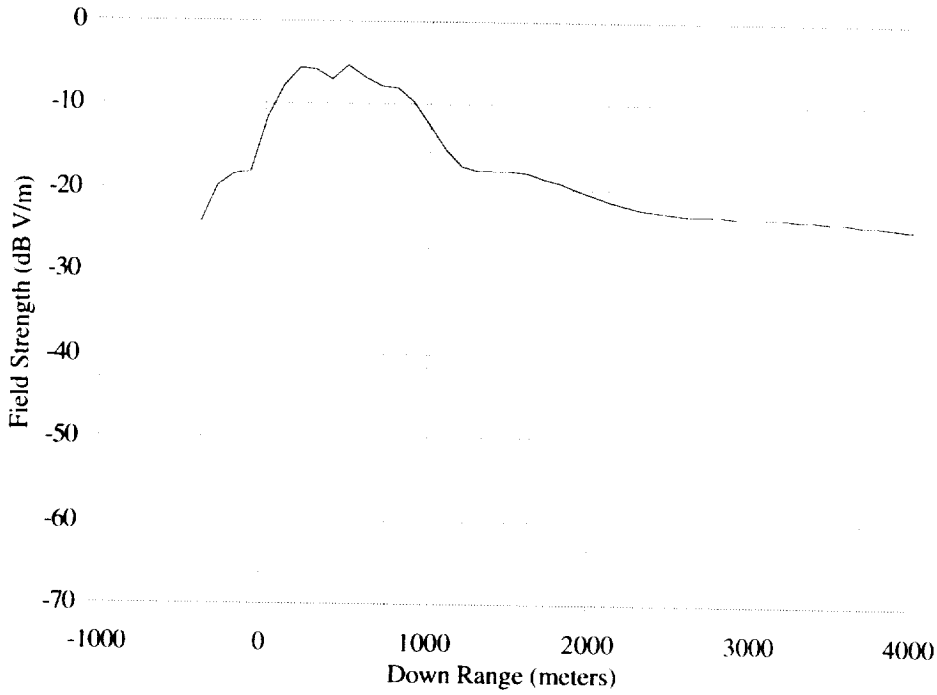

Figure B22. External field. 173 MHz; V-pol; inbound; "clean."

Table B23. Incident Angles
[173 MHz; V-pol; inbound; "clean"]

Down range (meters)	θ (degree)	ϕ (degree)	α (degree)
-1000			
-500			
0	171.0	-130.7	126.2
500	130.2	-8.5	2.3
1000	113.8	-9.2	5.4
1500	108.5	-7.1	0.2
2000	105.4	-6.1	0.3
2500	103.6	-5.9	0.2
3000	102.4	-2.1	7.3
3500	101.4	-1.8	1.1
4000	100.5	-2.4	0.4

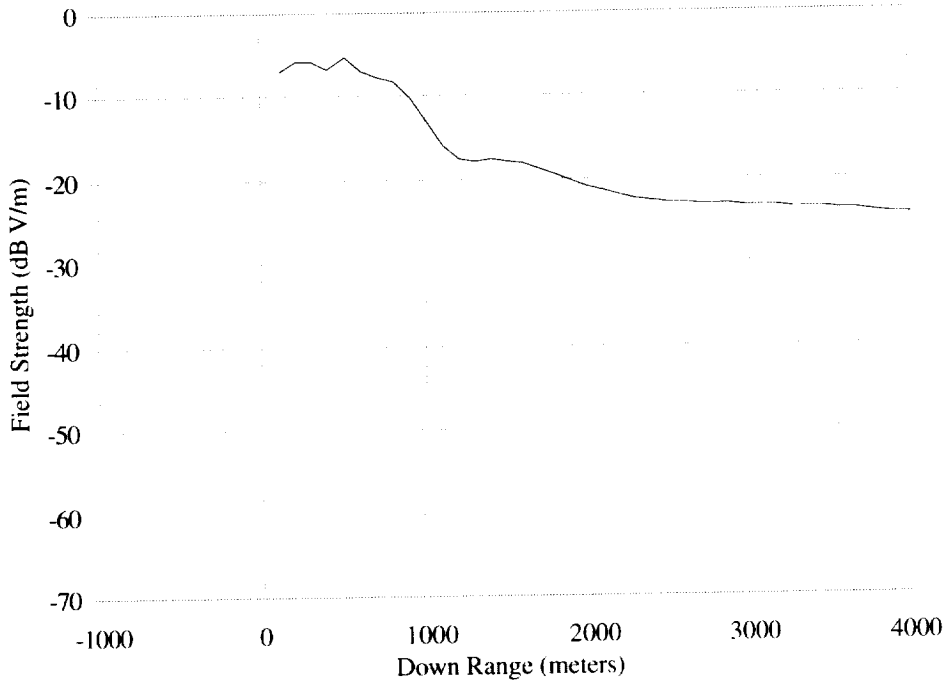

Figure B23. External field. 173 MHz; V-pol; inbound; "flaps."

Table B24. Incident Angles
[173 MHz; V-pol; inbound; "flaps"]

Down range (meters)	θ (degree)	ϕ (degree)	α (degree)
-1000			
-500			
0			
500	126.4	-7.0	0.7
1000	110.7	-6.3	0.0
1500	104.7	-5.9	0.6
2000	101.9	-5.4	1.5
2500	100.0	-4.8	0.2
3000	98.5	-5.3	1.2
3500	97.6	-5.4	0.3
4000	97.0	-4.7	2.1

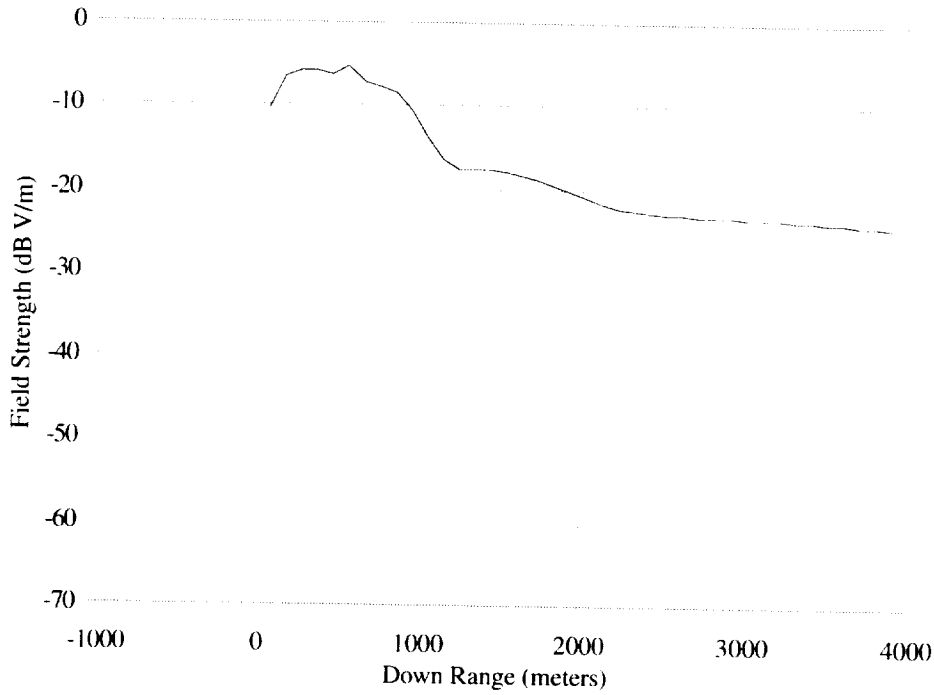

Figure B24. External field. 173 MHz; V-pol; inbound; "flaps & gear."

Table B25. Incident Angles
[173 MHz; V-pol; inbound; "flaps & gear"]

Down range (meters)	θ (degree)	ϕ (degree)	α (degree)
-1000			
-500			
0			
500	125.6	-9.4	2.0
1000	110.4	-6.6	0.5
1500	104.7	-6.7	0.5
2000	101.5	-5.2	2.5
2500	99.6	-5.3	0.2
3000	98.5	-4.2	2.9
3500	97.3	-4.4	1.1
4000			

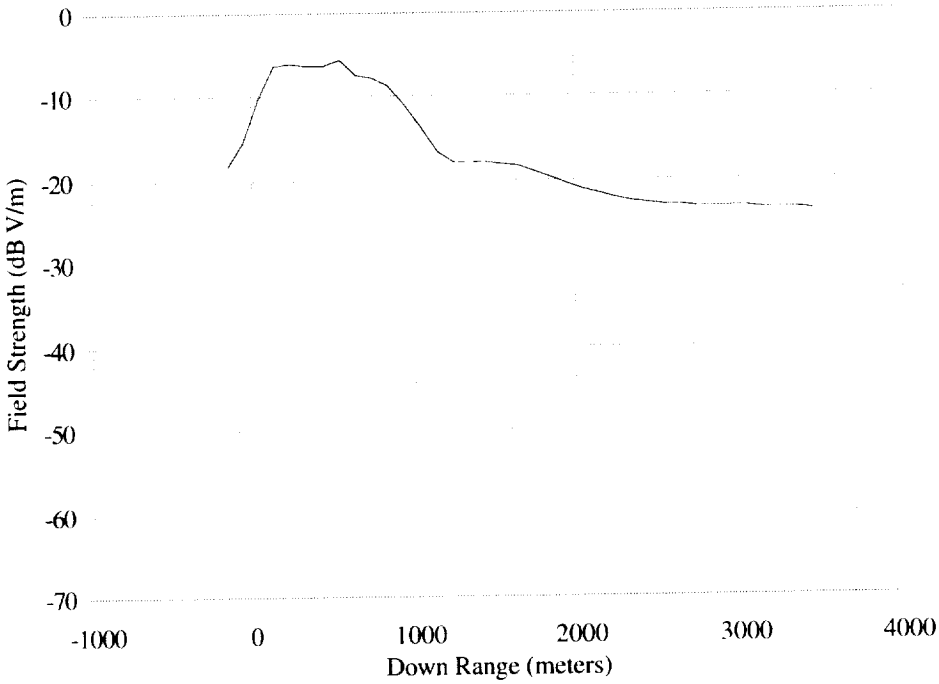

Figure B25. External field. 173 MHz; V-pol; outbound; "clean."

Table B26. Incident Angles
[173 MHz; V-pol; outbound; "clean"]

Down range (meters)	θ (degree)	ϕ (degree)	α (degree)
-1000			
-500			
0	169.3	114.6	67.2
500	119.0	-13.4	1.7
1000	103.7	-178.0	0.4
1500	97.6	-177.4	1.0
2000	94.3	-176.8	0.1
2500	92.2	-176.4	0.1
3000	91.2	-176.1	0.9
3500			
4000			

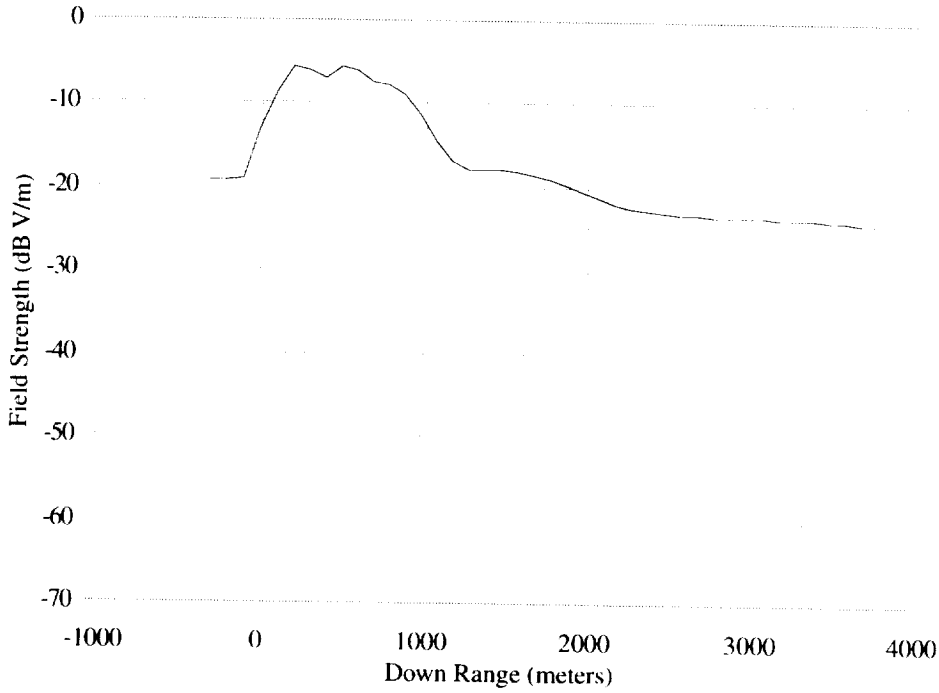

Figure B26. External field. 173 MHz; V-pol; outbound; "flaps."

Table B27. Incident Angles
[173 MHz; V-pol; outbound; "flaps"]

Down range (meters)	θ (degree)	ϕ (degree)	α (degree)
-1000			
-500			
0	169.1	97.2	86.6
500	122.2	-179.7	1.3
1000	106.9	-178.5	2.5
1500	100.9	-176.6	1.9
2000	98.0	-176.1	0.7
2500	95.7	-176.0	0.6
3000	94.6	-175.1	0.9
3500	93.5	-175.2	0.5
4000			

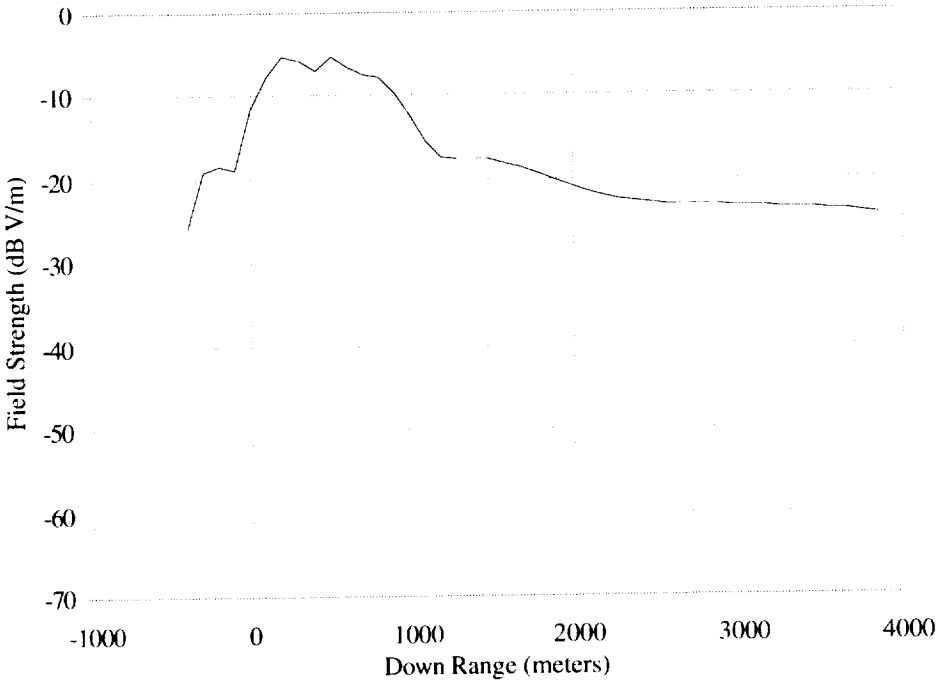

Figure B27. External field. 173 MHz; V-pol; outbound; "flaps & gear."

Table B28. Incident Angles
[173 MHz; V-pol; outbound; "flaps & gear"]

Down range (meters)	θ (degree)	ϕ (degree)	α (degree)
-1000			
-500			
0	161.8	97.8	86.5
500	122.0	177.1	6.2
1000	106.7	-178.1	0.2
1500	100.8	-176.6	0.4
2000	98.0	-177.5	3.2
2500	95.7	-176.0	1.6
3000	94.6	-176.2	2.0
3500	93.5	-176.0	0.1
4000			

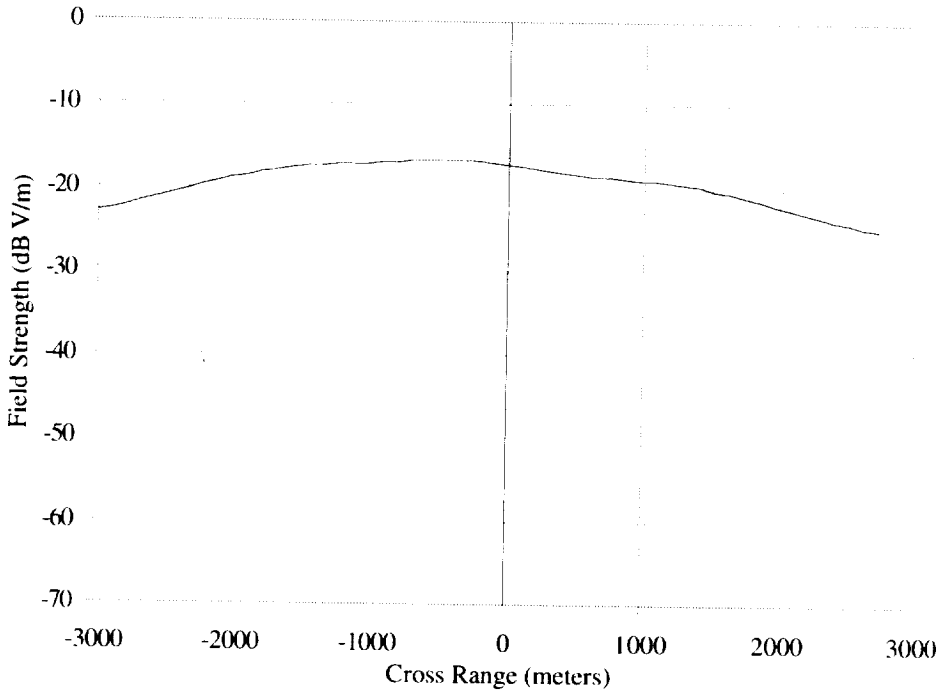

Figure B28. External field. 173 MHz;V-pol; crossbound; right incident; "clean."

Table B29. Incident Angles
[173 MHz; V-pol; crossbound; right incident; "clean"]

Cross range (meters)	θ (degree)	ϕ (degree)	α (degree)
-2000	104.5	-139.6	22.7
-1500	107.5	-132.4	20.8
-1000	111.0	-122.5	17.4
-500	114.3	-110.5	13.2
0	116.5	-97.3	7.5
500	117.4	-83.6	1.6
1000	117.0	-70.6	5.0
1500	116.4	-59.5	9.9
2000	114.9	-50.4	14.2
2500	112.8	-43.7	16.3
3000			

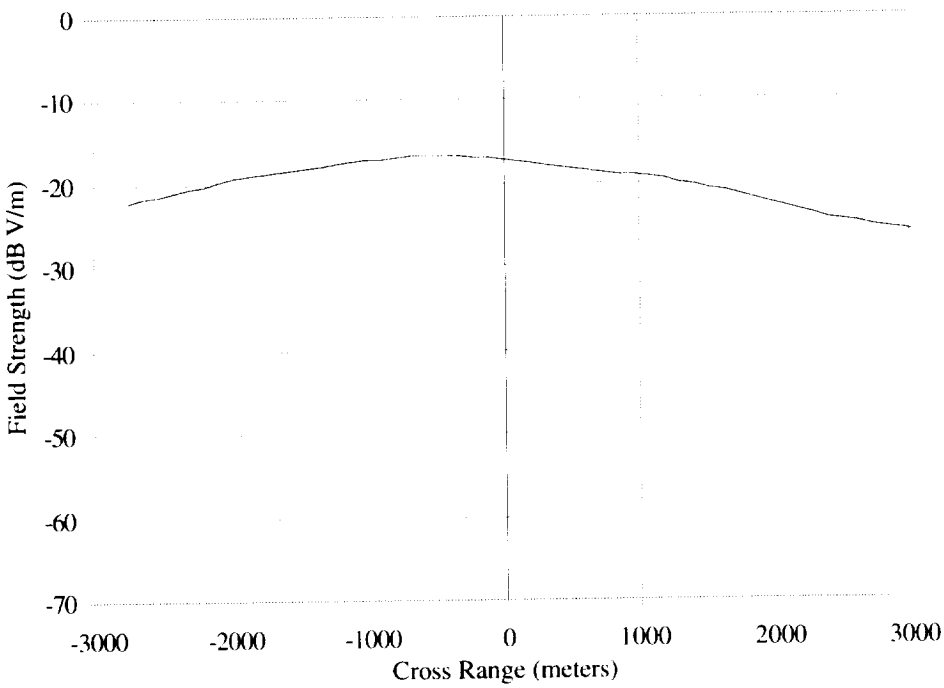

Figure B29. External field. 173 MHz; V-pol; crossbound; right incident; "flaps."

Table B30. Incident Angles
[173 MHz; V-pol; crossbound; right incident; "flaps"

Cross range (meters)	θ (degree)	ϕ (degree)	α (degree)
-2000	107.2	-136.5	18.7
-1500	109.7	-128.8	16.3
-1000	112.2	-119.1	12.8
-500	114.2	-107.9	8.2
0	115.5	-95.1	2.9
500	115.8	-81.6	2.6
1000	114.9	-69.5	7.7
1500	113.6	-59.4	11.9
2000	112.1	-51.0	15.0
2500	109.9	-44.4	17.1
3000	108.3	-39.1	18.9

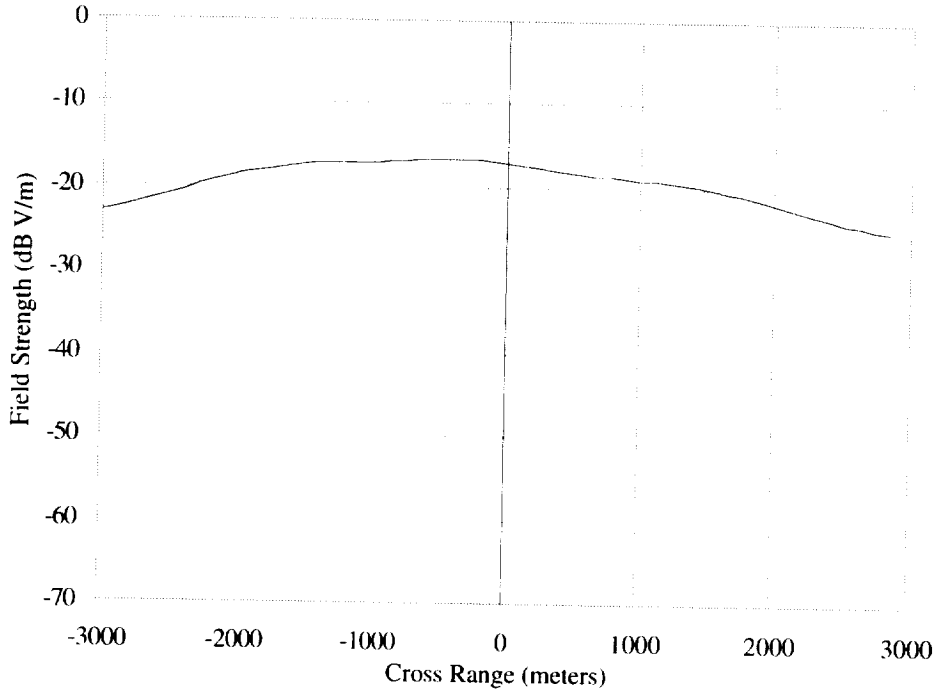

Figure B30. External field. 173 MHz; V-pol; crossbound; right incident; "flaps & gear."

Table B31. Incident Angles
[173 MHz; V-pol; crossbound; right incident; "flaps & gear"]

Cross range (meters)	θ (degree)	ϕ (degree)	α (degree)
-2000	107.3	-140.2	21.1
-1500	110.1	-132.3	18.6
-1000	113.1	-122.3	14.7
-500	115.7	-110.0	10.0
0	117.2	-95.9	3.5
500	117.5	-81.4	2.8
1000	116.7	-68.1	8.9
1500	115.1	-56.8	14.2
2000	113.1	-47.8	17.9
2500	110.5	-41.3	19.7
3000			

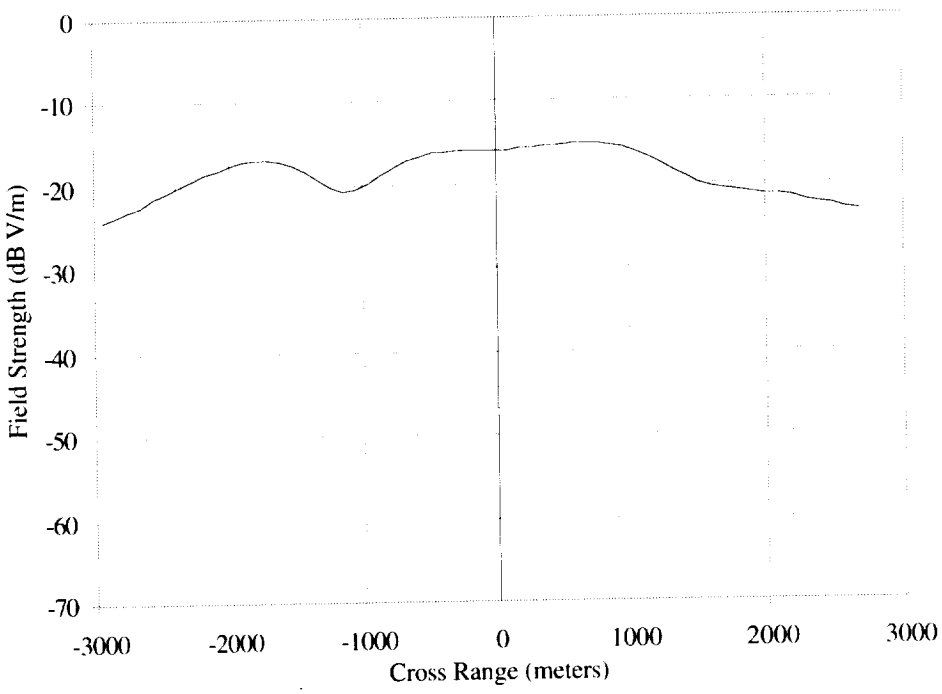

Figure B31. External field. 173 MHz; V-pol; crossbound; left incident; "clean."

Table B32. Incident Angles
[173 MHz; V-pol; crossbound; left incident; "clean"]

Cross range (meters)	θ (degree)	ϕ (degree)	α (degree)
-2000	117.4	40.3	24.2
-1500	121.0	48.2	20.6
-1000	124.6	60.2	14.3
-500	127.3	77.7	3.9
0	127.0	98.4	8.9
500	122.6	118.6	20.7
1000	116.9	134.0	28.3
1500	111.1	144.7	32.5
2000	107.1	151.8	35.1
2500	103.3	157.2	36.5
3000			

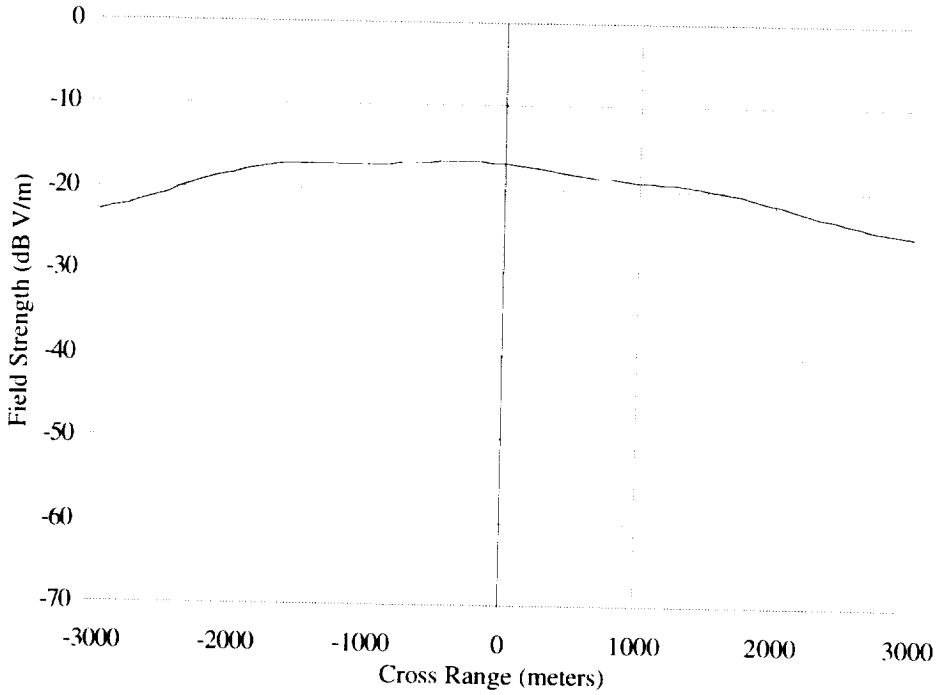

Figure B32. External field. 173 MHz; V-pol; crossbound; left incident; "flaps."

Table B33. Incident Angles
[173 MHz; V-pol; crossbound; left incident; "flaps"]

Cross range (meters)	θ (degree)	ϕ (degree)	α (degree)
-2000	110.9	48.6	15.9
-1500	113.4	56.4	13.2
-1000	115.8	66.9	9.1
-500	117.5	80.0	3.5
0	117.4	94.7	3.1
500	116.0	109.2	9.6
1000	113.5	122.1	15 1
1500	110.4	132.5	19
2000	107.3	140.4	21.9
2500	105.2	146.6	23.6
3000	103.3	151.7	25.3

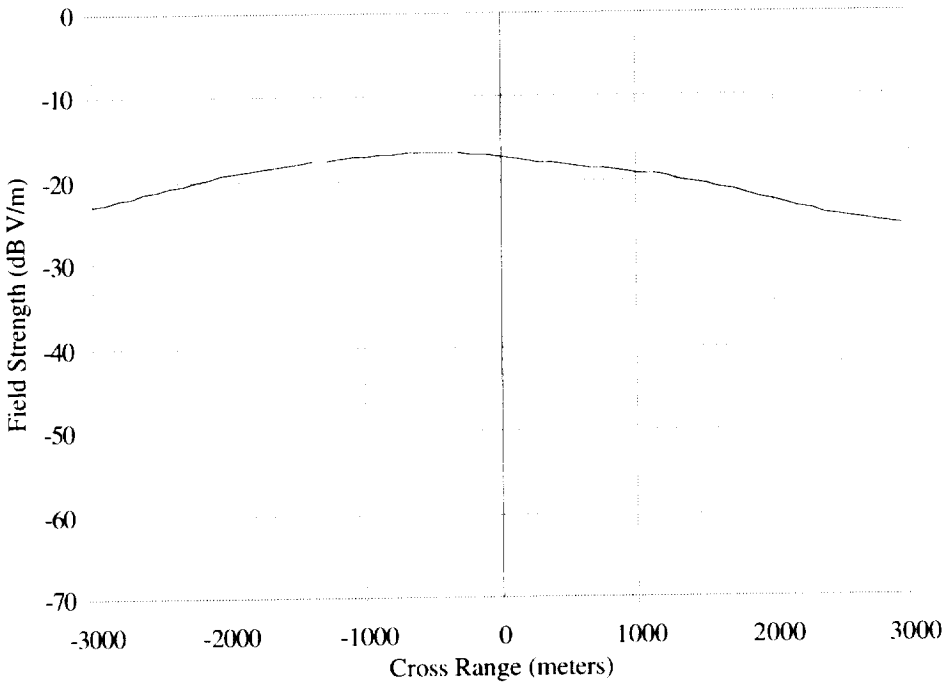

Figure B33. External field. 173 MHz; V-pol; crossbound; left incident; "flaps & gear."

Table B34. Incident Angles
[173 MHz; V-pol; crossbound; left incident;
"flaps & gear"]

Cross range (meters)	θ (degree)	ϕ (degree)	α (degree)
-2000	109.9	51.3	13.8
-1500	111.7	59.2	10.9
-1000	113.6	69.0	7.0
-500	114.6	80.9	2.5
0	114.4	94.3	3.3
500	113.5	107.4	9.1
1000	111.3	118.9	13.2
1500	109.1	129.0	16.9
2000	106.2	136.9	19.5
2500	104.4	143.1	21.3
3000			

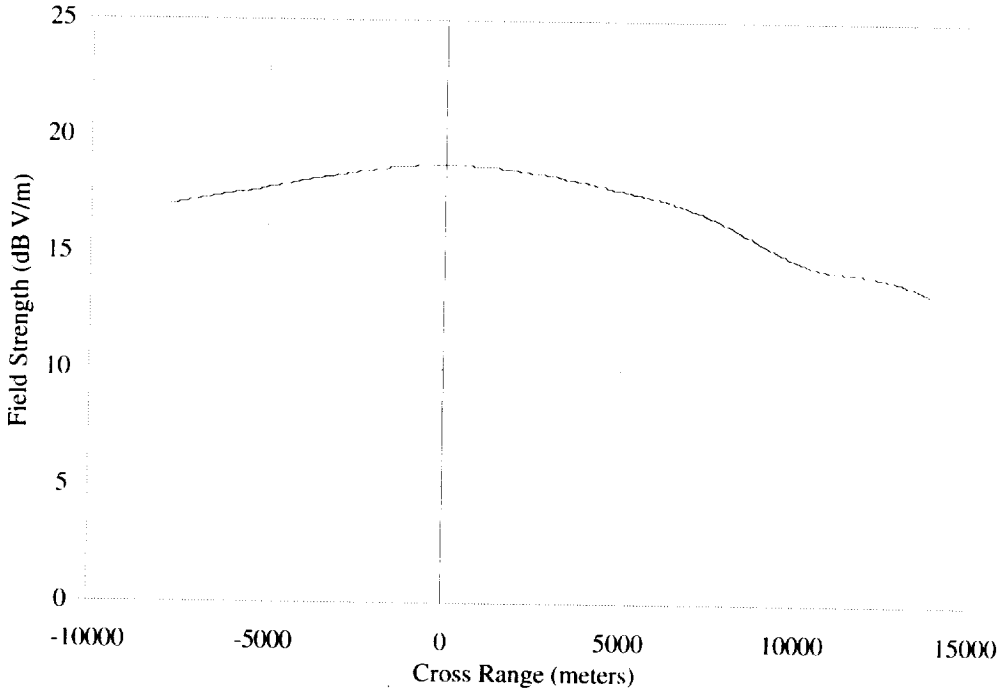

Figure B34. External field. 430 MHz; V-pol; inbound to crossbound; right incident; "clean."

Table B35. Incident Angles
[430 MHz; V-pol; inbound to crossbound;
right incident; "clean"]

Cross range (meters)	θ (degree)	ϕ (degree)	α (degree)
-8000			
-6000	90.3	-119.6	7.3
-4000	91.1	-111.1	7.1
-2000	92.4	-101.2	6.8
0	93.5	-90.7	6.2
2000	94.8	-80.0	5.5
4000	95.0	-69.9	4.5
6000	108.0	-41.9	8.2
8000	98.3	-29.5	0.3
10000	101.2	-11.1	12.3
12000	98.3	-3.3	1.3

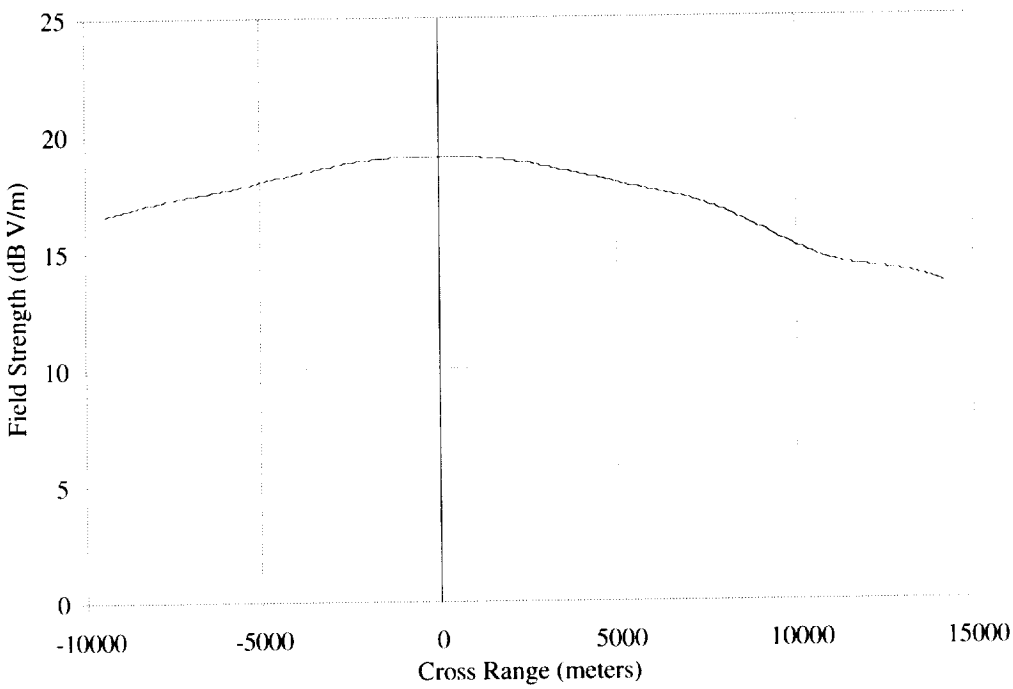

Figure B35. External field. 430 MHz; V-pol; inbound to crossbound; right incident; "flaps."

Table B36. Incident Angles
[430 MHz; V-pol; inbound to crossbound;
right incident; "flaps"]

Cross range (meters)	θ (degree)	ϕ (degree)	α (degree)
-8000			
-6000	91.8	-120.8	4.1
-4000	92.4	-111.8	3.8
-2000	93.1	-101.7	3.3
0	93.6	-91.0	2.6
2000	93.9	-80.3	2.0
4000	94.7	-69.8	0.8
6000	106.4	-53.7	8.0
8000	95.8	-28.9	1.7
10000	98.6	-22.7	9.5
12000	94.8	-2.1	1.6
14000	94.4	-2.3	1.3

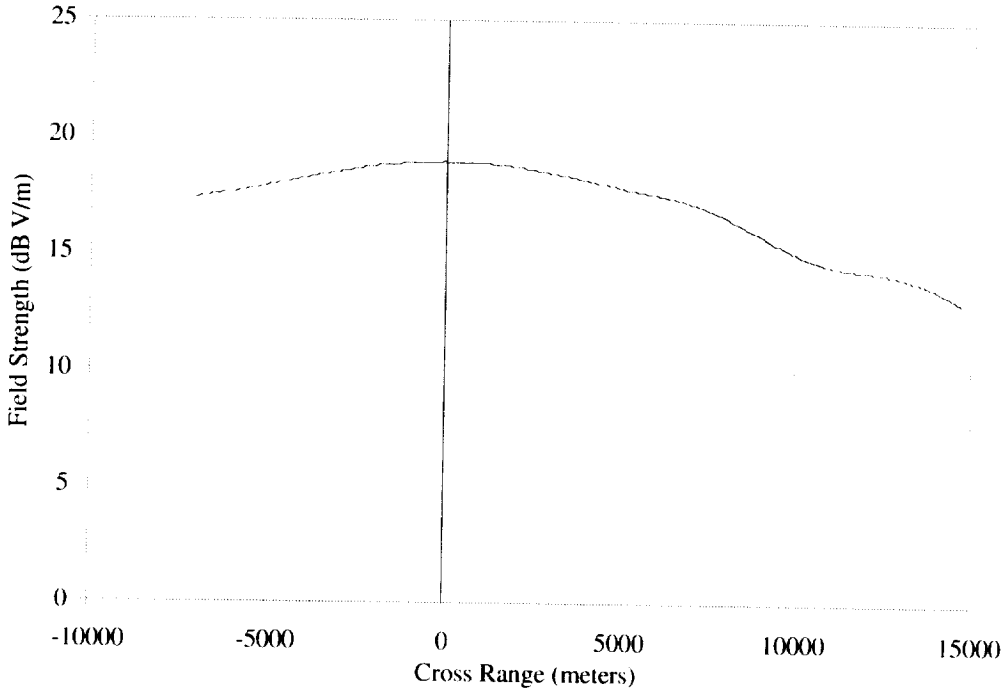

Figure B36. External field. 430 MHz; V-pol; inbound to crossbound; right incident; "flaps & gear."

Table B37. Incident Angles
[430 MHz; V-pol; inbound to crossbound;
right incident; "flaps & gear"]

Cross range (meters)	θ (degree)	ϕ (degree)	α (degree)
-8000			
-6000	92.0	-120.4	4.0
-4000	92.6	-111.2	3.8
-2000	93.1	-101.0	3.3
0	93.6	-90.4	2.6
2000	93.9	-79.6	1.8
4000	94.4	-69.0	0.8
6000	105.9	-51.2	8.3
8000	95.1	-28.9	0.6
10000	99.0	-19.7	11.5
12000	94.7	-2.1	1.6
14000	94.3	-2.7	0.5

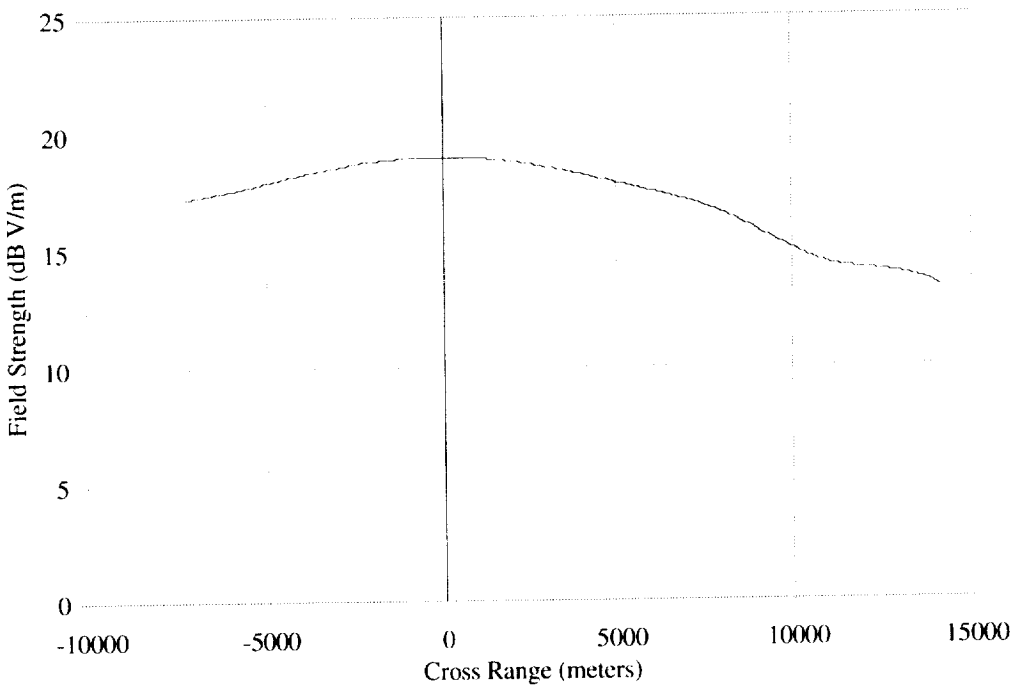

Figure B37. External field. 430 MHz: V-pol; crossbound; left incident to outbound; "clean."

Table B38. Incident Angles
[430 MHz; V-pol; crossbound; left incident to outbound; "clean"]

Cross range (meters)	θ (degree)	ϕ (degree)	α (degree)
-8000			
-6000	97.4	60.5	4.4
-4000	95.9	69.7	5.6
-2000	94.9	80.0	6.5
0	93.4	91.2	7.5
2000	92.3	102.1	7.7
4000	90.7	112.1	8.2
6000	97.5	133.8	16.7
8000	87.0	153.9	6.2
10000	87.9	165.4	15.1
12000	84.9	-178.1	1.4
14000	84.5	-177.8	0.6

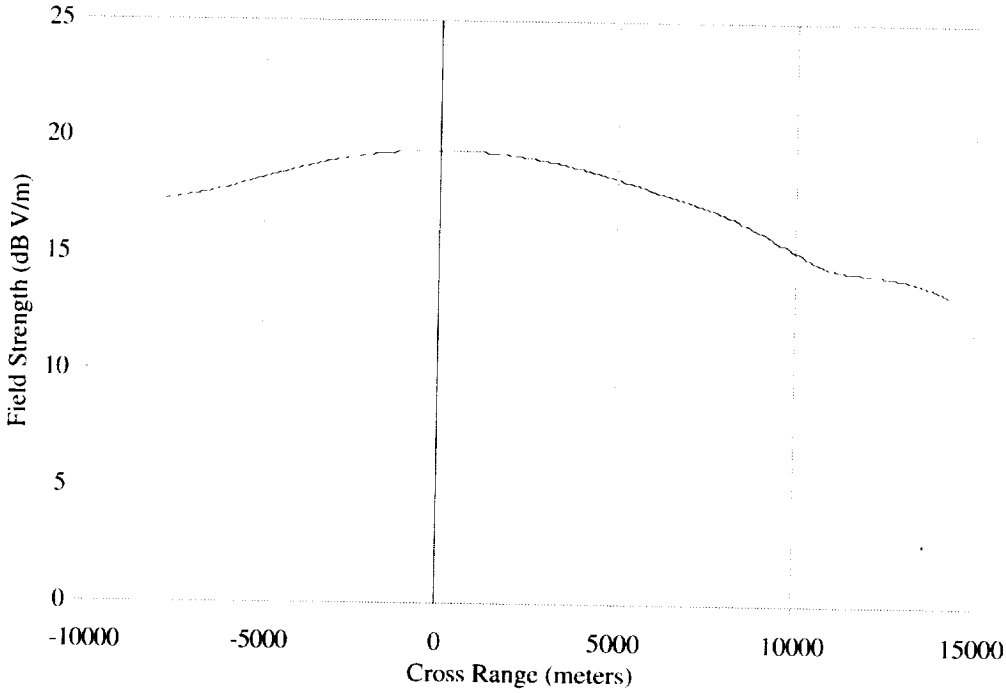

Figure B38. External field. 430 MHz; V-pol; crossbound; left incident to outbound; "flaps."

Table B39. Incident Angles
[430 MHz; V-pol; crossbound; left incident to outbound; "flaps"]

Cross range (meters)	θ (degree)	ϕ (degree)	α (degree)
-8000			
-6000	95.5	59.3	0.4
-4000	94.8	69.0	1.5
-2000	94.6	79.5	2.3
0	93.9	91.0	3.1
2000	93.2	102.5	3.9
4000	92.4	113.3	4.4
6000	99.9	139.2	14.8
8000	90.4	155.3	3.8
10000	91.1	170.8	15.3
12000	89.0	-177.9	1.5

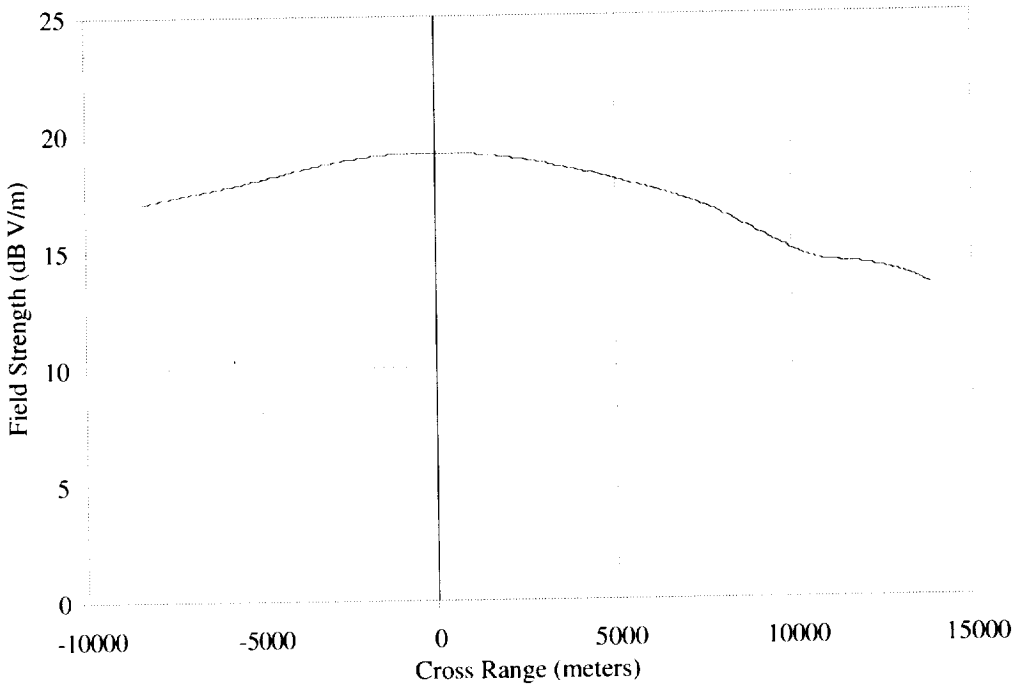

Figure B39. External field. 430 MHz; V-pol; crossbound; left incident to outbound; "flaps & gear."

Table B40. Incident Angles
[430 MHz; V-pol; crossbound; left incident to outbound; "flaps & gear"]

Cross range (meters)	θ (degree)	ϕ (degree)	α (degree)
-8000	94.9	51.7	0.2
-6000	94.9	60.6	0.5
-4000	94.6	70.0	1.3
-2000	94.4	80.4	2.0
0	93.8	91.2	2.9
2000	93.1	102.2	3.5
4000	92.6	112.5	4.2
6000	99.3	144.3	15.9
8000	90.5	155.1	3.5
10000	89.9	176.5	14.5
12000	89.1	-177.6	1.7

References

1. Perry, T. S.; and Geppart, L.: Do Portable Electronics Endanger Flight? *IEEE Spectr.*, Sept. 1996, pp. 26–33.

2. Helfrick, A.: Avionics and Portable Electronics: Trouble in the Air? *Avion. News Mag.*, Sept. 1996.

3. Fisher, F. A.; Plummer, J. A.; and Perala, R. A.: *Lightning Protection of Aircraft.* Lightning Technol., Inc., Pittsfield, MA, 1990.

4. Malnic, E.: Cockpit Confusion Preceded Airliner Crash in Guam. *Los Angeles Times*, Mar. 25, 1998.

5. Schwartau, W.: Information Warfare: *Chaos on the Electronic Superhighway.* Thunders Mouth Press, New York, 1994.

6. Anon.: City Surrenders to £ 400 Million Gangs. *The Sunday Times*, London, June 2, 1996.

7. Thompson, M.: Ordinary Radio Waves Allegedly Can Knock Down Combat Copter. *Los Angeles Times*, Nov. 9, 1987.

8. *Review of the Army UH-60 (Black Hawk) Electromagnetic Environment Issues.* Dept. of Defense, Office of Inspector General Rept. 88-151, June 1, 1988.

9. Mordoff, K. P.: UH-60 Helicopters to be Modified for Increased EMI Protection. *Aviat. Week & Space Technol.*, Oct. 10, 1988, pp. 75–77.

10. Thompson, M.: F-111 Downed by EMI? *Los Angeles Times*, Jan. 20, 1989.

11. Phillips, E. H.: Malibu Tests to Probe Effect of Radiated Fields. *Aviat. Week & Space Technol.*, Sept. 2, 1991, p. 30.

12. Lee, L.: *The Day the Phones Stopped—The Computer Crisis: The What and Why of It, and How We Can Beat It.* Donald I. Fine, Inc., New York, 1991.

13. Shooman, M. L.: *A Study of Occurrence Rates of Electromagnetic Interference (EMI) to Aircraft With a Focus on HIRF (External) High Intensity Radiated Fields.* NASA CR-194895, Apr. 1994.

14. Fuller, G.: *Understanding HIRF.* Avion. Comm. Inc., Leesburg, VA, 1995.

15. National Transportation Saftey Board (NTSB) Accident File No. 90-F-A099, Sept. 21, 1991.

16. Scarry, E.: The Fall of TWA 800The Possibility of Electromagnetic Interference. *The New York Rev. of Books*, Apr. 9, 1998, pp. 59–76.

17. NPRM *Applicable to FAR Part 25: Transport Category Airplanes.* FAA ARAC EEHWG Doc. WG-278, Draft 6, Mar. 1998.

18. Baum, C. E.: From the Electromagnetic Pulse to High-Power Electromagnetics. *Proceedings of the IEEE*, vol. 80, June 1992, pp. 789–817.

19. Kunz, K. S.; Breakall, J. K.; and Ludwigsen, A. P.: A Simple Interior Decomposition Model—Its Development and Application. *IEEE Trans. on EMC*, vol. 29, Feb. 1987.

20. Bacon, L. D.; Aurand, J. F.; Toth, R. F.; King, R. J.; Hudson, H. G.; McLeod, R.; and Knight, D. A.: *An Experimental Investigation of Microwave Coupling Into Realistic Objects.* Sandia Natl. Lab. Rept. SAN87-2196, Dec. 1987.

21. Baker, R. L.; and Pitts, F. L.: Fly-by-Light/Power-by-Wire Requirements and Technology Workshop. NASA CP-10108, Sept. 1992.

22. Edgel, W. R.: *Electric and Magnetic Field Sensor Application.* Prodyn Application Note 192, Prodyn Technol., Albuquerque, NM, Jan. 1995.

23. Dudley, K. L.: A Description of the Hardware Element of the NASA EME Flight Tests. *AIAA/IEEE Digital Avionics Systems Conference Proceedings*, Oct. 1996.

24. Koppen, S. V.: *A Description of the Software Element of the NASA EME Flight Tests.* NASA CR-201636, Dec. 1996.

25. Kaplan, E. D.: *Understanding GPS Principals and Applications.* Artech House, Norwood, MA, 1996.

26. Craig, J. J.: *Introduction to Robotics–Mechanics and Control.* Addison-Wesley, Reading, MA, 1989.

27. Arfken, G.: *Mathematical Methods for Physicists.* Academic Press, Orlando, FL, 1985.

28. Poggio, A. J.; Zacharias, R. A.; Pennock, S. T.; Avalle, C. A.; and Carney, H. L.: NASA Boeing 757 HIRF Test Series, *Low Power On-The-Ground Tests.* Lawrence Livermore Natl. Lab. Rept. &CRL-CR-122799, Aug. 1996.

29. Hatfield, M. O.; Johnson, D. M.; Freyer, G. J.; and Slocum, M. B.: *NASA Boeing 757 Cavity Field Variability Based on Bowing 757 and Boeing 707 Test Data.* Naval Surface Warfare Center, Dahlgren Division Rept. NSWCDD/TR-97/ 25, Jan. 1997.

30. Moeller, K. J.; and Dudley, K. L.: The NASA B-757 HIRF Test Series, Flight Test Results. *AIAA/IEEE Digital Avionics Systems Conference Proceedings*, Oct. 1997.

31. Johnson, R. C.; and Jasik, H.: *Antenna Engineering Handbook.* McGraw-Hill, New York, 1961.

32. Blanis, C. A.: Advanced Engineering Electromagnetics. John Wiley & Sons, New York, 1989.

33. Richmond, J. H.: Digital Computer Solutions of the Rigorous Equations for Scattering Problems. *Proceedings of the IEEE*, vol. 53, 1965, p. 796.

34. Harrington, R. F.: *Field Computation by Moment Methods.* MacMillian Co., New York, 1968.

35. Burke, G. J.: *Numerical Electromagnetics Code—NEC-4.* Lawrence Livermore Natl. Lab. Rept., UCRL-MA-109338, Jan. 1992.

36. Anon.: *An Experimenters Guide to the NASA Atmospheric Sciences Research Facility. NASA Wallops Flight Facility*, Mar. 1994.

37. Lee, T. H.; and Rudduck, R. C.: *OSU Reflector Antenna Code—Version 3.0.* Report 318021-1, Ohio State Univ. ElectroScience Lab., Feb. 1994.

38. Lee, S. H.; and Rudduck, R. C.: Aperture Integration and GTD Techniques Used in the NEC Reflector Antenna Code. *IEEE Trans. Antennas & Propag.*, vol. AP-33, Feb. 1985, pp. 189–194.

39. Chang, Y. C.: *Analysis of Reflector Antennas With Array Feeds Using Multi-Point GTD and Extended Aperture Integration.* Report 715559-3, Ohio State Univ. ElectroScience Lab., Mar. 1984.

40. Balanis, C. A.: *Antenna Theory, Analysis and Design—Second Edition.* John Wiley & Sons, New York, 1997.

41. Hill, D. A.; Ma, M. T.; Ondrejka, A. R.; Riddle, B. F.; Crawford, M. L.; and Johnk, R. T.: Aperture Excitation of Electrically Large, Lossy Cavities. *IEEE Trans. Electromagnetic Compatibility*, vol. 36, Aug. 1994, pp. 169–178.

42. Scearce, S. A.; and Bunting, C. F.: Statistical Results for the UHF Data From the NASA EME Flight Tests. *AIAA/IEEE Digital Avionics Systems Conference Proceedings*, Oct. 1998.

REPORT DOCUMENTATION PAGE

Form Approved
OMB No. 0704-0188

1. AGENCY USE ONLY (Leave blank)	2. REPORT DATE	3. REPORT TYPE AND DATES COVERED
	March 2001	Technical Publication

4. TITLE AND SUBTITLE
In-Flight Characterization of the Electromagnetic Environment Inside an Airliner

5. FUNDING NUMBERS
WU 522-14-21-01

6. AUTHOR(S)
Karl J. Moeller, Kenneth L. Dudley, Cuong C. Quach, and Sandra V. Koppen

7. PERFORMING ORGANIZATION NAME(S) AND ADDRESS(ES)
NASA Langley Research Center
Hampton, VA 23681-2199

8. PERFORMING ORGANIZATION REPORT NUMBER
L-18041

9. SPONSORING/MONITORING AGENCY NAME(S) AND ADDRESS(ES)
National Aeronautics and Space Administration
Washington, DC 20546-0001

10. SPONSORING/MONITORING AGENCY REPORT NUMBER
NASA/TP-2001-210831

11. SUPPLEMENTARY NOTES
Moeller, Dudley, and Quach: Langley Research Center, Hampton, VA; Koppen: Lockheed Martin Engineering & Sciences, Hampton, VA.

12a. DISTRIBUTION/AVAILABILITY STATEMENT
Unclassified-Unlimited
Subject Category 62 Distribution: Standard
Availability: NASA CASI (301) 621-0390

12b. DISTRIBUTION CODE

13. ABSTRACT (Maximum 200 words)

In 1995, the NASA Langley Research Center conducted a series of experimental measurements that characterized the electromagnetic environment (EME) inside a Boeing 757 airliner while in flight. Measurements were made of the electromagnetic energy coupled into a commercially configured aircraft as it was flown in close proximity to ground-based radio frequency (RF) transmitters operating at approximately 26, 173, and 430 MHz. The goal of this experiment was to collect data for the verification of analytical predictions of the internal aircraft response to an external stimulus. This paper describes the experiment, presents the data collected by it, and discusses techniques used to compute both the magnitude of the electric field illuminating the aircraft and its direction of propagation relative to a coordinate system fixed to the aircraft. The latter is determined from Global Positioning System (GPS) and aircraft Inertial Reference Unit (IRU) data. The paper concludes with an examination of the shielding effectiveness of the test aircraft, as determined by comparison of the measured internal EME and computed external EME.

14. SUBJECT TERMS
Electromagnetic Environment (EME); High Intensity Radiated Fields (HIRF); Shielding effectiveness; Digital avionics

15. NUMBER OF PAGES
149

16. PRICE CODE
A07

17. SECURITY CLASSIFICATION OF REPORT	18. SECURITY CLASSIFICATION OF THIS PAGE	19. SECURITY CLASSIFICATION OF ABSTRACT	20. LIMITATION OF ABSTRACT
Unclassified	Unclassified	Unclassified	UL